



8-2001

Development of an Integrated Sensor for the Measurement of the Acoustic Local Volume Displacement of Vibrating Beams

Randall Rozema

Follow this and additional works at: https://scholarworks.wmich.edu/masters_theses



Part of the Aerospace Engineering Commons, and the Mechanical Engineering Commons

Recommended Citation

Rozema, Randall, "Development of an Integrated Sensor for the Measurement of the Acoustic Local Volume Displacement of Vibrating Beams" (2001). *Master's Theses*. 1409.

https://scholarworks.wmich.edu/masters_theses/1409

This Masters Thesis-Open Access is brought to you for free and open access by the Graduate College at ScholarWorks at WMU. It has been accepted for inclusion in Master's Theses by an authorized administrator of ScholarWorks at WMU. For more information, please contact wmu-scholarworks@wmich.edu.



DEVELOPMENT OF AN INTEGRATED SENSOR FOR THE
MEASUREMENT OF THE ACOUSTIC LOCAL VOLUME
DISPLACEMENT OF VIBRATING BEAMS

by

Randall Rozema

A Thesis
Submitted to the
Faculty of The Graduate College
in partial fulfillment of the
requirements for the
Degree of Masters of Science in Engineering (Mechanical)
Department of Mechanical and Aeronautical Engineering

Western Michigan University
Kalamazoo, Michigan
August 2001

DEVELOPMENT OF AN INTEGRATED SENSOR FOR THE MEASUREMENT OF THE ACOUSTIC LOCAL VOLUME DISPLACEMENT OF VIBRATING BEAMS

Randall Rozema, M.S.E.

Western Michigan University, 2001

Currently, the methods used for sensing the volume displacement of a vibrating structure entail the use of a polyvinylidene fluoride sensor that spans the entire length of the structure. However, this work shows that the surface behavior related to volume displacement can be measured through the use of a polyvinylidene fluoride sensor that spans only the area of interest. In this application it was shown that two-point sensors are required in addition to the distributed, polyvinylidene fluoride sensor to achieve an accurate measurement. As a result, a set of four beams with different end conditions were constructed so that the localized sensors developed could be examined. In designing the localized surface sensors, the polyvinylidene fluoride surface sensor shape was developed, the sensor shapes necessary to measure a localized area of interest were determined, the sensors were constructed, and subsequently, they were tested using a test fixture constructed for this specific purpose. Finally, a comparison between the theoretical and actual measured values was completed so as to determine the accuracy of these sensors. From the comparison it was discovered that the localized sensors developed were sufficiently accurate for sensing the volume displacement of the vibrating beam with minor variations.

ACKNOWLEDGMENTS

I would like to begin by thanking the individuals from the Noise and Vibration laboratory at Western Michigan University who have assisted me throughout this research. I would especially like to thank Brian Zellers for his time spent in the machine shop constructing the test fixture that was used throughout this research.

Next, I would like to thank the members of my committee, Dr. Koorosh Naghshineh, Dr. Philip Guichelaar, and Dr. Marcellin Zahui, for taking the time to review my work. I would especially like to thank Dr. Naghshineh for providing me with the tools necessary to clearly understand objectives and goals of my work. His time and experience were an invaluable resource throughout the duration of this research.

Finally, I would like to thank my fiancé, Kathy, for having the patience and spending the time to proofread my work. I would also like to thank her for her continuing support and understanding as I worked to complete this research.

Randall Rozema

Copyright by
Randall Rozema
2001

TABLE OF CONTENTS

ACKNOWLEDGEMENTS	ii
LIST OF TABLES	vi
LIST OF FIGURES.....	vii
INTRODUCTION.....	1
CHAPTER	
I. REVIEW OF LITERATURE	3
Baffled Piston	6
Vibrating Beam	9
Piezoelectric Sensing Material	17
II. THEORETICAL DEVELOPMENT	22
Theoretical Development of Localized Sensors	22
Verification Process for a Localized Sensor.....	30
III. EXPERIMENTAL SETUP	33
Overview	33
Calculation of Beam Lengths	34
Test Fixture Construction.....	39
Baffled Box Construction.....	47
Experimental Equipment.....	50
Beam Resonance Verification	56

Table of Contents – Continued

CHAPTER	
Sensor Construction	61
Preliminary Experiments	63
IV. VOLUME DISPLACEMENT MEASUREMENTS	73
Localized PVDF Sensor Verification Process	73
Volume Displacement Experiments	79
<i>Fixed-Fixed Beam</i>	80
<i>Fixed-Free Beam</i>	93
<i>Fixed-Simply Supported</i>	98
<i>Simply Supported-Simply Supported</i>	103
Sound Power Measurements	105
V. CONCLUSION AND RECOMMENDATIONS	116
Conclusion	116
Recommendations for Future Work	117
REFERENCES	120
APPENDICES	
A. Assembly Drawings of the Beams and Test Fixture	122
B. Assembly Drawings of the Baffled Enclosure	141
C. Volume Displacement per Unit Force, Phase, and Power Spectrum Plots for the Fixed-Free Beam	156
D. Volume Displacement per Unit Force, Phase, and Power Spectrum Plots for the Fixed-Simply Supported Beam	163

Table of Contents – Continued

APPENDICES

E. Volume Displacement per Unit Force, Phase, and Power Spectrum	
Plots for the Simply Supported-Simply Supported Beam	175

LIST OF TABLES

1. 6061-T6 Aluminum Material Properties (Gere and Timoshenko, 1997).....	35
2. Constants Used for Determining the Beam Natural Frequencies	38
3. Calculated Beam Lengths for a 250 Hz First Resonance.....	39
4. Theoretical and Measured Resonances for the Beams Under Test.....	61
5. Fixed-Fixed Beam and Box Top Maximum Vibration Per Unit Force (dB((m/s ²)/N))	107
6. Fixed-Free Beam and Box Top Maximum Vibration Per Unit Force (dB((m/s ²)/N))	108
7. Fixed-Simply Supported Beam and Box Top Maximum Vibration Per Unit Force (dB((m/s ²)/N))	108
8. Hinged-Hinged Beam and Box Top Maximum Vibration Per Unit Force (dB((m/s ²)/N))	108
9. Microphone Locations used in the Sound Power Measurements	112

LIST OF FIGURES

1. Two Single-Input Single-Output Control Systems	2
2. Sound Power Reduction Methods.....	5
3. Vibrating Disk Noise-Control System	7
4. Schematic of a Piston Ring Setup	8
5. Experimental Setup and Location of Measurement Points	9
6. Sound Pressure Level Reduction Achieved as a Function of Frequency.....	9
7. Sound Pressure Level Reduction Achieved as a Function of Angle.....	9
8. Concept Illustration of the Experimental Implementation of Active Control Using this Methodology	11
9. Beam to Be Examined With Section of Interest Shaded	11
10. Possible Clamped-Clamped Beam Sensor Shapes	14
11. Possible Clamped-Simply Supported Beam Sensor Shapes	14
12. Sensors on a Plate in the x and y Directions (Charett et al. 1998)	15
13. Possible Sensor Distribution on the Surface of a Plate (Johnson & Elliott, 1995).....	17
14. Comparison of Analytical and Actual Data for 2-3 Mode Sensor	21
15. Segmented Beam.....	23
16. General Shape Used for the Surface Sensor	29
17. Fixed End With Six Tapped Holes	40
18. Simply Supported End With a Connecting Pin.....	40

List of Figures – Continued

19. Machined Set of Beams (From the Top Down: Fixed-Free, Simply Supported-Simply Supported, Fixed-Simply Supported, Fixed-Fixed).....	41
20. Rubberized Leveling Feet	41
21. Base With Tapped Holes for Leveling and Mounting the Slides.....	42
22. Machined Base for the Test Fixture	42
23. Close Up View of the Slots Machined in the Slides	43
24. End View of the Slide Showing One of the Guides on the Base	43
25. Countersunk Holes for Mounting the Towers.....	43
26. One of the Towers Mounted on a Slide	44
27. Beam Support for a Fixed End Condition. (Left) Top, (Right) Bottom	46
28. Fixed End Condition With Material Removed	46
29. Simply Supported End Condition	47
30. Assembled Simply Supported End Condition	47
31. Simply Supported Pin	47
32. Plywood Box Constructed With the Simply Supported Beam Inside (Top Cover Removed)	49
33. Baffled Box Covers Constructed From Plywood. (a) Fixed-Fixed Cover, (b) Fixed-Free Cover, (c) Fixed-Simply Supported Cover, (d) Simply Supported-Simply Supported Cover	49
34. Seal Material and Connecting Stud.....	49
35. Simply Supported Beam in the Baffled Box, Such that the Cover and the Beam are Flush.....	50
36. Simply Supported Beam Sealed Along the Edges With Tape	50

List of Figures – Continued

37. Connectors Utilized to Link the Electrical Signals from Outside the Box to the Instruments Located Inside the Box.....	50
38. HP Analyzer and TEAC DAT Recorder Used for Data Collection.....	52
39. Techron Amplifier Used for Shaker Excitation	52
40. Seven Pound Shaker Used as an Excitation Source.....	52
41. Accelerometers Used for Sensing the Vibrations. (Left: Model U353B16, Right: Model 352C22)	52
42. Force Gauge With Stinger Used for Measuring the Excitation Force	53
43. Single Channel PCB Signal Conditioner	53
44. Test Setup Used for Taking the Accelerometer Measurements.....	53
45. Test Setup Used for Making the Integrated Sensor Measurements	54
46. Larson Davis Analyzer Used for Sound Power Measurements	55
47. Half-Inch Microphone Used for Sensing Sound Power.....	55
48. Multi-Channel Signal Conditioner.....	55
49. Schematic of the Test Setup Used for the Sound Power Measurements	56
50. Beam Resonance Verification Setup for Different Beam Boundary Conditions. (a) Fixed-Fixed Beam, (b) Fixed-Free Beam, (c) Fixed-Simply Supported, (d) Simply Supported-Simply Supported	58
51. Spectrum Analyzer and Amplifier Used for Beam Resonance Tests	58
52. Shaker and Accelerometer Setup For Measuring the Beam Resonances.....	58
53. Frequency Response for the Fixed-Fixed Beam	59
54. Frequency Response for the Fixed-Free Beam	60

List of Figures – Continued

55. Frequency Response for the Fixed-Simply Supported Beam	60
56. Frequency Response for the Simply Supported-Simply Supported Beam.....	61
57. Battery and Leads Used for Surface Sensor Shaping.....	63
58. Ruler With Full Length Piece of PVDF.....	64
59. PVDF Behavior for the Full Length Piece of PVDF	65
60. Etched PVDF Sensor	65
61. Chemically Etched and Cut PVDF Volume Displacement Measurement.....	66
62. Cut PVDF Sensor.....	66
63. Electrically Cut PVDF Sensor	66
64. Electrically Cut and Physically Cut PVDF Volume Displacement Measurement.....	67
65. PVDF Physically Cut at the Electrically Etched Location.....	67
66. Traceable Sensor Shape Template	68
67. Applying the PVDF to the Taped Surface	68
68. Template Taped in Place Over the PVDF.....	69
69. Black Marker Being Used to Color in an Electrical Lead on the Sensor.....	69
70. Shaded Sensor Shape and Lead Before Etching	69
71. (Left) Etchant Being Applied With a Foam Brush. (Right) Etchant After Application.....	71
72. Removing the Excess Etchant Solution With a Soft Cloth.....	71
73. Etched Sensor.....	72

List of Figures – Continued

74. Isopropyl Alcohol Being Used to Remove the Marker.....	72
75. Finished Sensor With Accelerometers.....	72
76. Volume Displacement Comparison With and Without Accelerometers	76
77. Simply Supported Beam Marked at Every Two Centimeters.....	78
78. Localized PVDF Sensors After They Have Been Isolated From Each Other	81
79. Sensor Shapes Used for the Total and Local Sensors.....	81
80. Fixed-Fixed Volume Displacement Magnitude for Section A of the Double Sensor.....	83
81. Fixed-Fixed Volume Displacement Phase for Section A of the Double Sensor.....	84
82. Power Spectrum for Section A of the Two Section Local Sensor	84
83. Fixed-Fixed Volume Displacement Magnitude for Section B of the Double Sensor.....	85
84. Fixed-Fixed Volume Displacement Phase for Section B of the Double Sensor.....	86
85. Power Spectrum for Section B of the Two Section Local Sensor	88
86. Fixed-Fixed Volume Displacement Magnitude for Section A of the Triple Sensor.....	88
87. Fixed-Fixed Volume Displacement Phase for Section A of the Three Section Sensor.....	89
88. Power Spectrum for Section A of the Three Section Local Sensor	89
89. Fixed-Fixed Volume Displacement Magnitude for Section B of the Triple Sensor.....	90

List of Figures – Continued

90. Fixed-Fixed Volume Displacement Phase for Section B of the Three Section Sensor.....	90
91. Power Spectrum for Section B of the Three Section Local Sensor	91
92. Fixed-Fixed Volume Displacement Magnitude for Section C of the Triple Sensor.....	91
93. Fixed-Fixed Volume Displacement Phase for Section C of the Three Section Sensor.....	92
94. Power Spectrum for Section C of the Three Section Local Sensor	92
95. Fixed-Fixed Total Volume Displacement Magnitude	94
96. Fixed-Fixed Total Volume Displacement Phase	94
97. Power Spectrum for the Total Sensor	95
98. Sensor Shapes Used for the Fixed-Free Beam.....	96
99. Fixed-Simply Supported Sensor Shapes	99
100. Simply Supported-Simply Supported Sensor Shapes	103
101. Fixed-Fixed Beam With the Test Grid Laid Out on the Box Top	107
102. Reverberation Chamber Setup for Sound Power Measurements.....	109
103. Reference Sound Source Used for Sound Power Measurements.....	110
104. Axis of Orientation and Color Coded Borders	112
105. Fixed-Fixed Beam Sound Power Comparison.....	114
106. Fixed-Free Beam Sound Power Comparison.....	114
107. Fixed-Simply Supported Beam Sound Power Comparison.....	115
108. Simply Supported-Simply Supported Beam Sound Power Comparison	115

INTRODUCTION

The foundation of this research is based on common active noise control methods that are in practice, where active control can be defined as the implementation of a secondary control actuator to reduce the sound power radiated from a structure. In this active control process a method for sensing the undesired sound or vibration is required to send a signal to a controller, which then drives a secondary control actuator. The secondary wave generated by the control actuator in turn cancels the undesired disturbance resulting in the reduction of unwanted noise or vibration. It is possible to achieve active control systems that affect a large surrounding area (global area) and are effective for a broad range of frequencies. However, these systems require that multiple sensors and multiple actuators be used in conjunction with a complex multi-input, multi-output controller for controlling undesired disturbances. The advantage to this method of control is that only one control device (be it complex) is required to affect a wide area. However, the disadvantages are that this type of a system is complex to implement and, as a result, are not cost effective.

Due to the complexity of such control systems, it is desired to devise an active control system which focuses on the reduction of broad band sound or vibration at a localized area. This method of control would entail a single localized sensor for sensing the disturbance at a desired location. In addition to the single sensor, a single cancellation device or secondary control actuator will be required. Both the sensor and cancellation device are connected through the implementation of a simple single-

input single-output controller. Figure 1 shows a schematic representation of the desired control system. This type of control system is advantageous because a simplified controller will be more cost effective and easier to implement. However, the desired control system will be limited in its frequency range and the cancellation area over which the controller is effective. As such, multiple single-input, single-output control systems will be required to reduce unwanted disturbances over a large area (global area).

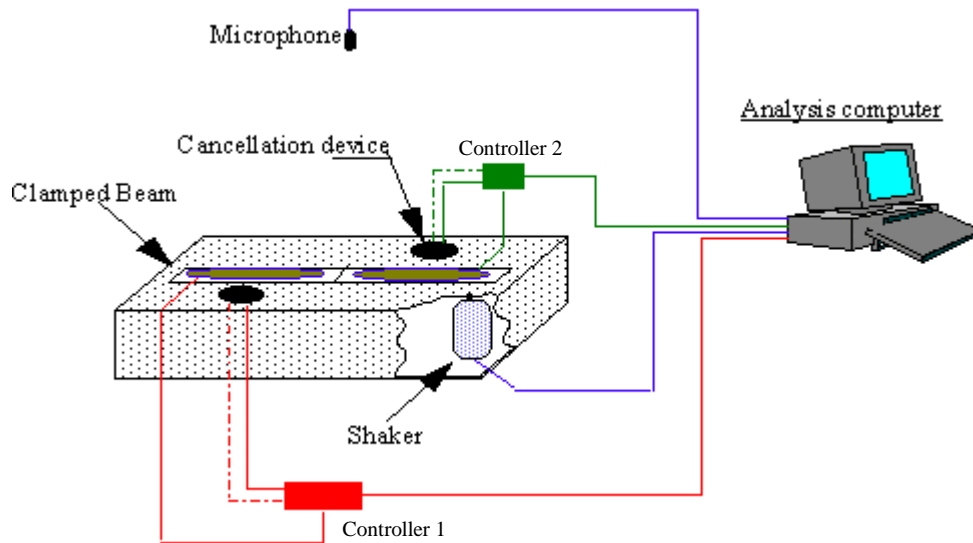


Figure 1. Two Single-Input Single-Output Control Systems.

In the development of a single-input single-output control system many components need to be researched and developed. These components include the sensor, controller, and cancellation device. Thus, the focus of the remainder of this research is on the development of single localized sensors. The final goal of this research is to develop a localized surface sensor which spans and measures the volume displacement of a specific area of interest on the surface of a vibrating structure.

CHAPTER I

REVIEW OF RELEVANT LITERATURE

One of the means of achieving noise control is to reduce the sound radiated from vibrating structures. Through an understanding of volume displacement and methods of controlling it, the desired sound reduction may be possible. The volume displacement is a measure of the total volume of air displaced as the result of surface vibrations. Simply stated, it is the displacement of the structure integrated over its surface. However, it is assumed that structures vibrate in a harmonic motion, and therefore, the volume displacement and the volume velocity of the structure are directly related. The volume velocity is proportional to the total sound power radiated from the structure at low frequencies (Rex, 1991). Therefore, at low frequencies, by reducing the volume velocity or volume displacement, it is possible to reduce the total sound power radiated from a vibrating structure. A flow chart of possible sound power reduction methods can be seen in Figure 2.

The sound power can be controlled in one of two ways. The first method is through passive control. In this application, passive control would reduce the sound power radiated from a structure by altering the dynamic properties of the structure through adding absorbing materials or by isolating the structure from its source of excitation. The other method of control, which is preferred at lower frequencies, is referred to as active control. Active control relies on the implementation of secondary control actuators that can be used for reducing the sound power radiated (Johnson &

Elliott, 1995). A recent publication by Zahui, Kamman, and Naghshineh (2001b) presented an example of active control in which the sound power of a beam was reduced through the use of acoustic actuators. The acoustic actuators were used to control the local volume displacement of a clamped vibrating beam.

In order for active control to be successful, effective implementation of three components are necessary as shown in Figure 2. These are a sensor, a controller, and an actuator. The sensor must be a structural sensor that informs the controller how and when to activate a secondary actuator. Therefore, in the case of a vibrating beam, the structure has to be outfitted with vibrational surface sensors. The vibrational sensors can be either point sensors or continuous sensors. An example of a typical point sensor is an accelerometer which is used to measure the vibration of a single point on a structure. However, a point sensor is not typically desired as multiple accelerometers would be required to measure the vibration of a surface, thereby adding to the complexity of the control system. In contrast, a continuous sensor is a sensor that spans over a section of a structural surface. Recently, continuous sensors used for measuring surface vibrations were formed from piezoelectric materials. Such sensors can be used as either a local (measuring over limited segment of a structural surface of interest) or a global sensor (measuring over the entire structural surface of interest), as the flow chart in Figure 2 demonstrates. For the implementation of a local sensor, the structure would have to be divided into finite sections. To confirm that the local sensors are measuring the surface movement properly, a summation of local

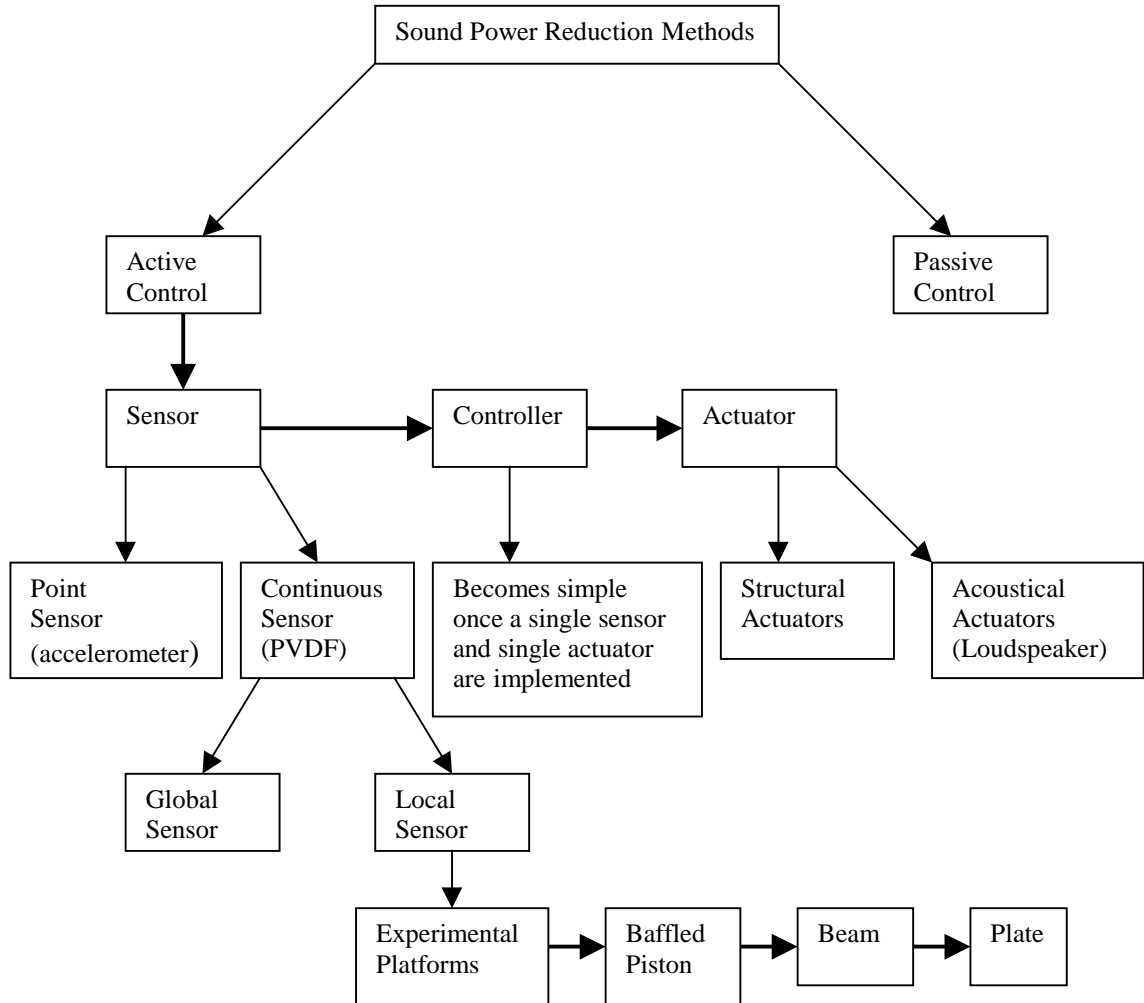


Figure 2. Sound Power Reduction Methods.

sensor measurements would be required. The summation would then yield the same values as a total or a global sensor measurement. Additionally, each finite structural segment would require its own sensor and controller. On the other hand, a global sensor would cover an entire structure with one continuous sensor and only require one controller. However, the drawback to the global sensor is that the entire structure is being controlled. This can be undesirable as at higher frequencies where the structural wavelength is smaller and the sound that is radiated may be coming from

many isolated smaller portions of the total structure. Thus, it is more desirable to use a local sensing method (multiple local sensors).

The research of Guigou et al. (1994 & 1996), Johnson and Elliott (1995), Naghshineh et al. (1998), and Zahui et al. (2001a) has demonstrated that the theory of controlling volume velocity to minimize radiated sound power has been tested in several applications. Some of the applications in which this theory has been applied are with a baffled piston, a vibrating beam, and a vibrating plate. However, in these applications, many assumptions are made, therefore, many variations are possible. Thus, examples of the sensors that can be used in these different applications were examined.

Baffled Piston

The first structure considered was a baffled piston. The baffled piston (uniformly vibrating circular disk surrounded by an infinite, rigid baffle) is a simple structure for which the theory and equations are readily available for analysis. In research presented by Naghshineh et al. (1998), the theory examined included the reduction of noise through the utilization of a noise-control device that acts over the surface of a radiating disk. In this application the device is controlled as the result of a motion sensor (an accelerometer) that informs the system when to be activated. An example of the system can be seen in Figure 3, where a vibrating disk is controlled by a loudspeaker placed near its center.

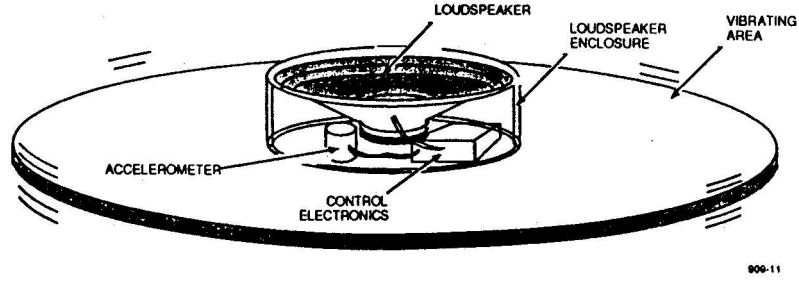


Figure 3. Vibrating Disk Noise-Control System.

The theory behind such a system is best described as a baffled piston of radius a_2 containing a noise-control device of radius a_1 , which acts as an inner piston. A diagram of a baffled piston model can be seen in Figure 4. The idea behind such an apparatus is that the inner piston will vibrate at a velocity such that the total sound radiated from the system will be minimized. A theoretical prediction for the radiation from such an apparatus can be represented by the following equation as presented by Junger and Feit (1993) as:

$$\hat{p}(r, \theta) \approx \frac{ik\rho c e^{-ikr}}{r} \left\{ \hat{v}_1 a_1^2 \frac{J_1(ka_1 \sin \theta)}{ka_1 \sin \theta} + \hat{v}_2 \left[a_2^2 \frac{J_1(ka_2 \sin \theta)}{ka_2 \sin \theta} - a_1^2 \frac{J_1(ka_1 \sin \theta)}{ka_1 \sin \theta} \right] \right\}, \quad (1)$$

where $\hat{p}(r, \theta)$ is the radiated pressure; r and θ are the coordinates of the observation point (Figure 4); \hat{v}_1 and \hat{v}_2 are the inner piston and outer ring surface velocities, respectively; k is the acoustic wave number; ρ is the air density; and c is the speed of sound through air. After simplification it is found that in order for the inner piston to cancel the outer ring, the velocity profile for the piston must be represented as:

$$\hat{v}_1 = -\hat{v}_2 \left(\frac{A_2}{A_1} \right), \quad (2)$$

where A_1 and A_2 are the areas of the inner piston and the outer ring.

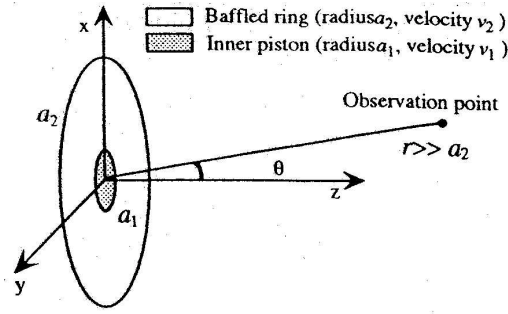


Figure 4. Schematic of a Piston Ring Setup.

Naghshineh et al. (1998) tested the system's performance by recording the output with a series of microphones located at many points. These measurements included both conditions when the control system was turned on and when it was turned off. Figure 5 shows the location of these measurements in the experimental setup. From the data collected, two plots were created which show the sound level reductions achieved. The first set of data was measured one meter away from the plate in 15 degree increments. This data can be seen in Figure 6, and shows that when the noise-control system is activated, a reduction of up to 20 dB can be achieved for a frequency range of 50- to 500-Hz. The next set of data displayed accounted for the system performance as a function of microphone angle. Figure 7 shows that the system consistently reduced the sound pressure level by 10 to 13 dB over all angles examined. As a result of these experiments, it was concluded that the new system for reducing the sound power radiated from a baffled piston was effective within a 50- to 100-Hz frequency band. However, in the area near the loudspeaker, the reduction was minimal since it was the dominant noise source.

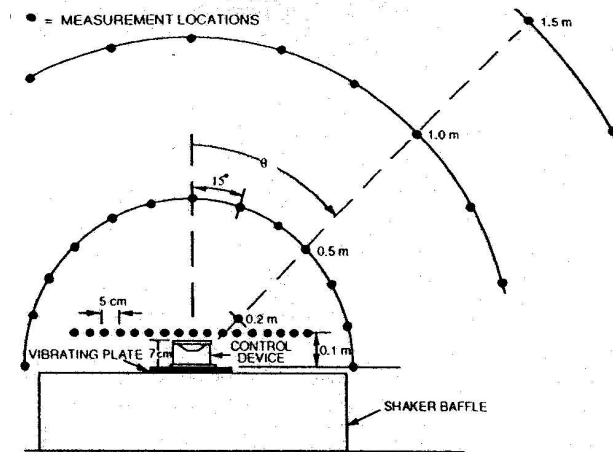


Figure 5. Experimental Setup and Location of Measurement Points.

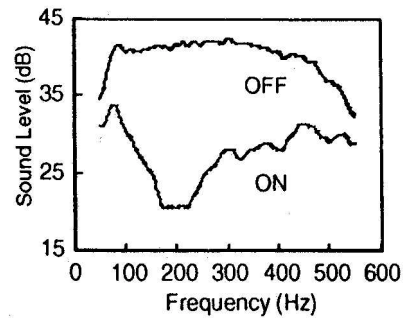


Figure 6. Sound Pressure Level Reduction Achieved as a Function of Frequency.

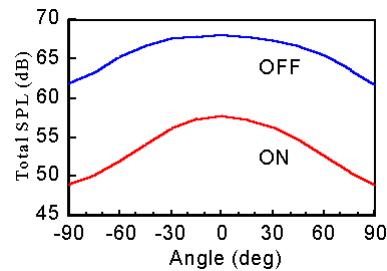


Figure 7. Sound Pressure Level Reduction Achieved as a Function of Angle.

Vibrating Beam

Since the baffled piston was a simple, uniformly vibrating system, the next step in progression was to study a beam that is a one-dimensional, non-uniformly vibrating system. Research has been completed in which the sound power radiated

from a vibrating beam was reduced (Zahui et al. 2001b). Unlike the baffled piston for which a single accelerometer served as an effective motion sensor, the vibrating beam experiments utilized a PolyVinyliDene Fluoride (PVDF) sensor. The PVDF on the beam was used to sense the beam's volume displacement and to provide the controller with the necessary information to excite the secondary actuators, thereby reducing the emitted sound power. This process could be thought of as the second generation of volume displacement control.

One method of control presented by Zahui et al. (2001b) implements loudspeakers as secondary actuators. In this application each loudspeaker reduces the local volume displacement of the nearby section of the vibrating structure. By reducing the volume displacement of the beam locally at multiple sections, the ability of the entire structure to radiate sound is reduced. In this example Zahui et al. (2001b) used a clamped-clamped aluminum beam vibrating non-uniformly. The vibration was a result of the beam being driven by a shaker, which was monitored by a force sensor mounted between the shaker and beam. The radiated sound pressure was then measured with a microphone placed above the beam. It was assumed that a reduction in overall sound power resulting from a minimization of the overall volume displacement could be sensed by measurements of the reduction in the sound pressure level radiated from the beam at multiple points surrounding the beam. Figure 8 shows the experimental setup used to verify that the sound power was reduced.

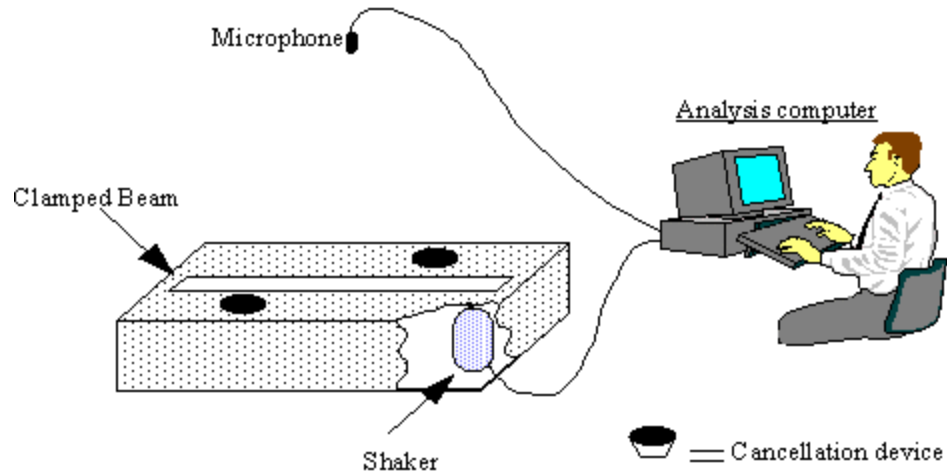


Figure 8. Concept Illustration of the Experimental Implementation of Active Control Using this Methodology.

Zahui et al. (2001a) continued to examine the use of local sensors since PVDF has the ability to sense changes in strain only. In designing the local sensors, it was noted that at least one non-vibrating beam boundary condition had to be included in the area covered by the PVDF. In other words, the sensor had to span the entire length of the beam and include a fixed or hinged boundary condition. With this in mind, a closer examination of the development of a sensor for any arbitrary portion of a beam was completed. The beam of interest spanned a range from $x = 0$ to $x = l$, and the section of interest was contained within that length and ranged from $x = a$ to $x = c$.

Figure 9 shows an illustration of how the beam was segmented.

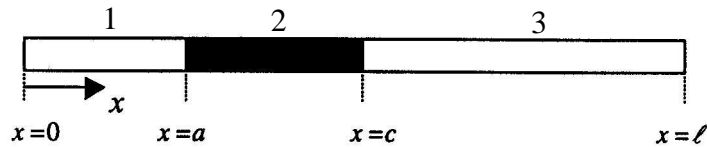


Figure 9. Beam to Be Examined With Section of Interest Shaded.

To account for the beam essentially being broken into three sections, the charge generated from the PVDF sensor will have to be calculated in three sections. The total electrical charge for the PVDF in this case becomes the sum of all the sections calculated. When written in its equation form, it appears as follows:

$$q = q_1 + q_2 + q_3, \quad (3)$$

where the subscripts refer to the sensor segment over sections 1, 2, and 3 ($0 \leq x \leq a$, $a \leq x \leq c$, $c \leq x \leq l$), respectively. Therefore, the general form of the equations for determining the sensor shape are as follows:

$$q_1 = -e_{31}(h_b + h_s) \left\{ [F_1(a)Z'(a) - F_1'(a)Z(a)] - [F_1(0)Z'(0) - F_1'(0)Z(0)] + \int_0^a F_1''(x)Z(x)dx \right\}, \quad (4a)$$

$$q_2 = -e_{31}(h_b + h_s) \left\{ [F_2(c)Z'(c) - F_2'(c)Z(c)] - [F_2(a)Z'(a) - F_2'(a)Z(a)] + \int_a^c F_2''(x)Z(x)dx \right\}, \quad (4b)$$

and

$$q_3 = -e_{31}(h_b + h_s) \left\{ [F_3(l)Z'(l) - F_3'(l)Z(l)] - [F_3(c)Z'(c) - F_3'(c)Z(c)] + \int_c^l F_3''(x)Z(x)dx \right\}, \quad (4c)$$

where $F_1(x)$, $F_2(x)$, and $F_3(x)$ describe the sensor shape over sections 1, 2, and 3, respectively. Since the area of interest for sensing is in the range $a \leq x \leq c$, $F_1''(x)$ and $F_3''(x)$ are set equal to zero (straight line) such that $F_2(x)$ is the only portion of the sensor measuring the strain in the beam. Imposing the continuity of shape and slope, a relationship between these functions is formed as follows:

$$F_1(a) = F_2(a), \quad (5a)$$

$$F_1'(a) = F_2'(a), \quad (5b)$$

$$F_2(c) = F_3(c), \text{ and} \quad (5c)$$

$$F_2'(c) = F_3'(c). \quad (5d)$$

Considering that $F_2(x)$ is the only section of the sensor being used to measure the volume displacement the three sensor shape functions that comprise the entire sensor shape can take the form of:

$$F_1(x) = A_1x + B_1, \quad (6a)$$

$$F_2(x) = \kappa x^2 + A_2x + B_2, \text{ and} \quad (6b)$$

$$F_3(x) = A_3x + B_3, \quad (6c)$$

such that through combinations of boundary conditions as specified by various beam mountings, the constants $A_1, B_1, A_2, B_2, A_3, B_3$, and κ can be found and the sensor shape determined. Due to the large degree of freedom in this problem, there are many possible solutions that satisfy the sensor shape constraints. Figure 10 shows an example of some of the possible sensor shapes for a clamped-clamped end condition when the sensor is calculated in three segments similar to the conditions that the above equations describe. Similarly, Figure 11 shows the sensor shapes for a clamped-simply supported beam. Clearly, it is observed that the development of sensors for measuring the volume displacement of a local area on a vibrating beam is possible.

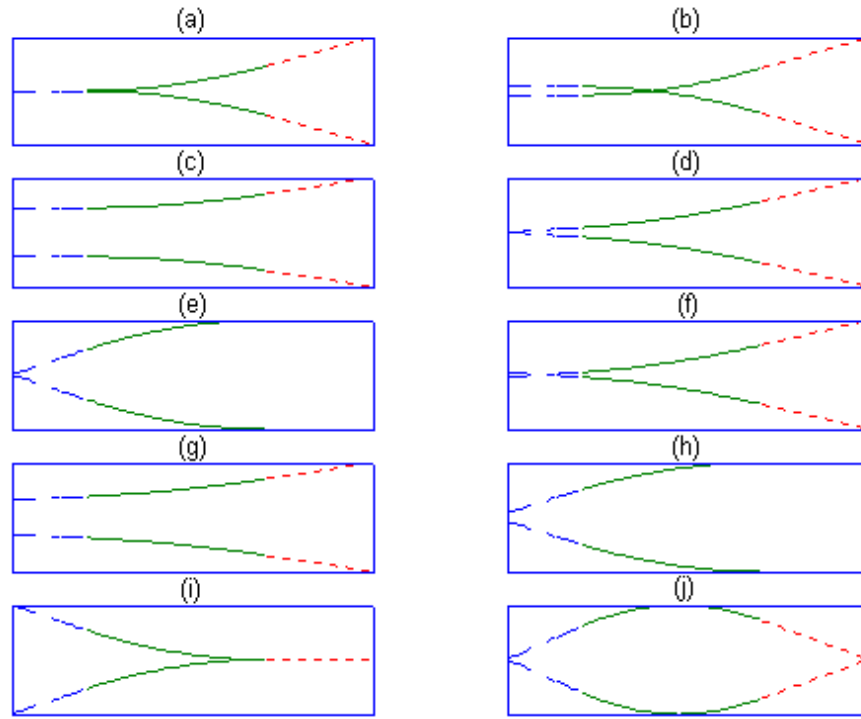


Figure 10. Possible Clamped-Clamped Beam Sensor Shapes
(The solid line represents area whose volume displacement is to be monitored).

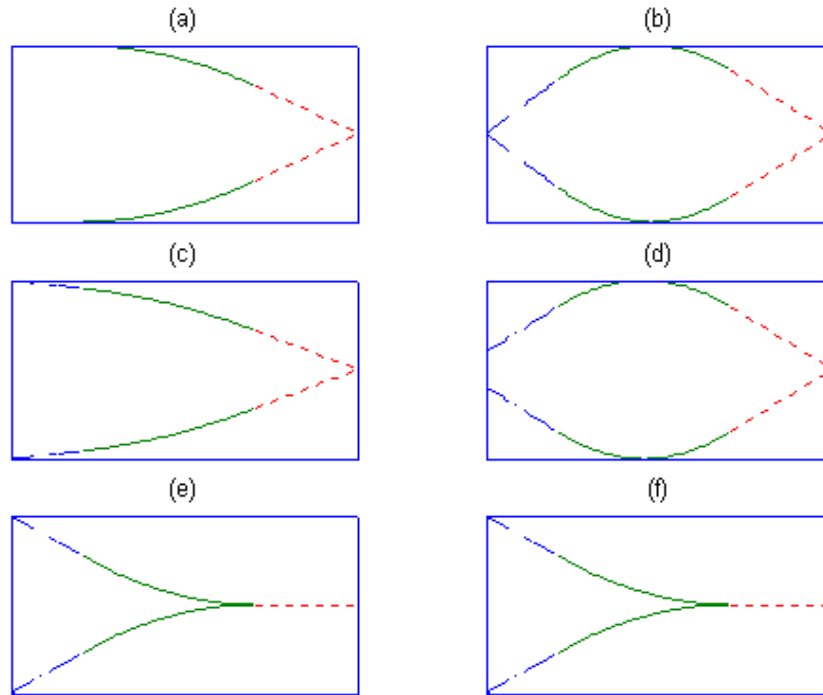


Figure 11. Possible Clamped-Simply Supported Beam Sensor Shapes
(The solid line represents area whose volume displacement is to be monitored).

Vibrating Plate

The next, more complex application in which surface sensors can be used to sense and potentially be used to reduce the sound power emitted is a vibrating rectangular plate. Like the vibrating beam, a PVDF film can be used to create the surface sensors instead of using multiple point sensors such as accelerometers. The plate is very similar to the beam except that there are two directions in which the sensors span. That is, instead of just spanning in the x direction, the sensor now has to span in both the x and the y directions. An example of this concept was given by Charette et al. (1998) as shown in Figure 12.

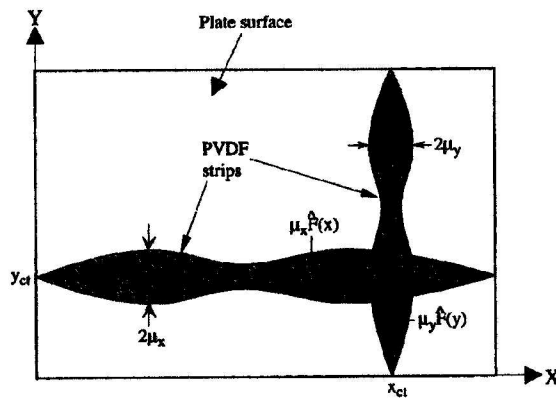


Figure 12. Sensors on a Plate in the x and y Directions (Charett et al. 1998).

One example of PVDF implementation on a plate was presented by Johnson and Elliott (1995). In this example a fixed plate was used and the general charge equation was presented as:

$$q = \int_0^{l_y} \int_0^{l_x} -hF(x, y) \left[e_{31} \frac{\partial^2 Z(x, y)}{\partial x^2} + e_{32} \frac{\partial^2 Z(x, y)}{\partial y^2} \right] dx dy, \quad (7)$$

where q is the total charge of the film, h is the film-neutral axis separation, $F(x,y)$ is the sensor shape of the film, e_{31} and e_{32} are piezoelectric constants, $Z(x,y)$ are the transverse displacement (i.e., deflections) of the plate, and $\frac{\partial^2 Z(x,y)}{\partial x^2}, \frac{\partial^2 Z(x,y)}{\partial y^2}$ are due to the strain caused by the bending in the plate. This equation can be broken into two components, one describing the x direction and the other describing the y direction such that $q = q_x + q_y$, where:

$$q_x = \int_0^{l_y} \int_0^{l_x} -hF(x,y)e_{31} \frac{\partial^2 Z(x,y)}{\partial x^2} dx dy \quad (8)$$

$$\text{and } q_y = \int_0^{l_y} \int_0^{l_x} -hF(x,y)e_{32} \frac{\partial^2 Z(x,y)}{\partial y^2} dx dy. \quad (9)$$

After some mathematical manipulation, Johnson and Elliott (1995) showed that the sensor output charge in the x direction is proportional to the integrated displacement of the surface as represented by

$$q_x = 2he_{31} \int_0^{l_y} \int_0^{l_x} Z(x,y) dx dy - he_{31} l_x [Z(l_x, y) + Z(0, y)] dy \quad (10)$$

It is recognized next that the output due to bending in the y direction needs to be zero; therefore, Eq. (9) is manipulated to become a function of the x direction as follows:

$$q_y = -he_{32} \int_0^{l_x} F(x) \left[\frac{\partial Z(x, l_y)}{\partial y} - \frac{\partial Z(x, 0)}{\partial y} \right] dx. \quad (11)$$

Since the plate has fixed edges, the deflections at $y=0$ and at $y=l_y$ will equal zero, and thus, q_y will equal to zero as well. Therefore, the total charge output from the sensor will equal q_x , which will represent the volume displacement of the entire plate.

Figure 13 shows how the sensor may be distributed on the surface of the plate. Consequently, this example showed how the sensor distribution might vary from one application to another. Likewise, it shows that there is more than one possible solution to the problem of measuring the volume displacement of a plate, as the sensor configurations in Figures 12 and 13, even though very different, still measure the same surface behavior.

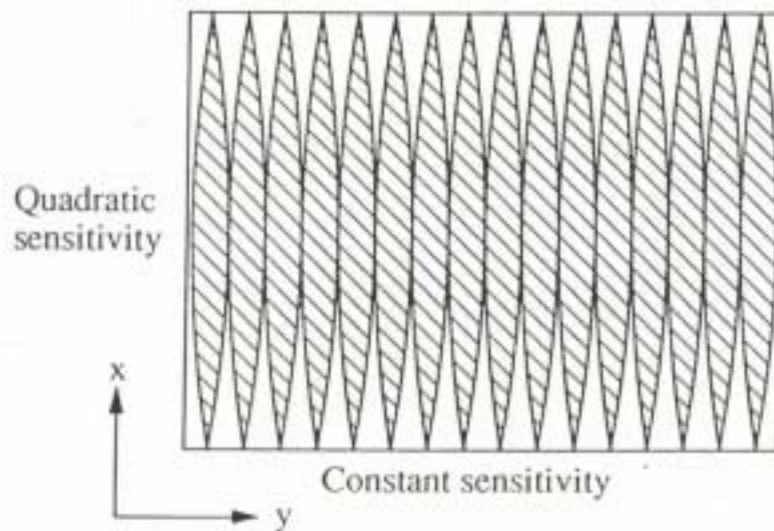


Figure 13. Possible Sensor Distribution on the Surface of a Plate (Johnson & Elliott, 1995).

Piezoelectric Sensing Material

As mentioned, vibrational sensors can be constructed from piezoelectric materials to sense the movement of a surface. Piezoelectric materials also maintain the ability to change their dimensions when subjected to an electrical field (Johnson & Elliott, 1993). With the ability to change dimensions under electrical fluctuations, piezoelectric materials can be used as actuation device in addition to sensing applications. In applications where vibrations of a large surface or portions of a large

surface need to be sensed, the desired material is PolyVinyliDene Fluoride (PVDF). PVDF is constructed in the form of a multi-layer polymeric film that can be shaped for use as a given application requires. Additionally, PVDF is a strain-sensitive material, and therefore, it is capable of providing the user with a local strain measurement (Zahui et al., 2001a). The PVDF senses strain in the material and produces an electrical charge potential to this strain. Thus, if such a sensor is bonded to a test structure, it can measure its strain over the portion of the structural surface covered by PVDF. Since an applied strain produces an electrical charge, it should be noted that the PVDF exhibits a characteristic of polarity. In addition to measuring the magnitude of strain applied, the direction of the movement can be sensed. Another advantage to using PVDF is that it provides the user with a distributed sensor for which spatial filtering techniques can be applied by tailoring the sensor shape (Chartette et al., 1998). In other words, the sensor can be formed to the optimal shape for the application in which it will be used.

The general equation for the charge generated by a PVDF sensor is used to determine the sensor shape. This equation varies depending on the PVDF application and assumptions made. From Zahui et al. (2001a), an example of an equation used for a PVDF sensor in one dimension is given as:

$$q = -(h_b + h_s)e_{31} \int_0^l F(x)Z''(x)dx, \quad (12)$$

where q is the PVDF charge, h_b and h_s are the beam and the PVDF sensor thicknesses, e_{31} is the PVDF sensor stress/charge coefficient, $Z''(x)$ is the second derivative of the

displacement field $Z(x)$, and $F(x)$ represents the function describing the shape of the PVDF sensor. Then, through integration by parts, the equation takes the form:

$$q = -e_{31}(h_b + h_s) \left\{ [F(l)Z'(l) - F'(l)Z(l)] - [F(0)Z'(0) - F'(0)Z(0)] + \int_0^l F''(x)Z(x)dx \right\}. \quad (13)$$

It is found that if the function $F(x)$ takes the form of a quadratic equation such as:

$$F(x) = \tilde{\kappa}x^2 + Ax + B, \quad (14)$$

where $\tilde{\kappa}$, A, and B are unknown coefficients, then the integral can be simplified as:

$$\int_0^l F''(x)Z(x)dx = \tilde{\kappa} \int_0^l Z(x)dx = \tilde{\kappa} \left(\frac{D}{b} \right). \quad (15)$$

In the above equation, b represents the beam width and D the total volume displacement of the beam. Solving for the constants $\tilde{\kappa}$, A, and B in Eq. 14 yields a total sensor shape $F(x)$, which can be fabricated. This can be tricky as the PVDF is sensitive enough that the slightest error in sensor construction can introduce significant errors in the desired sensor output. The two main sources of error in implementation of PVDF sensors are sensor forming and sensor placement. One method for forming sensors used by Johnson and Elliott (1995) was to chemically etch the PVDF using ferrous chloride and standard circuit board etching techniques. However, there is another etching approach that does not implement any chemicals. In this method, a power supply is used to pass a current through the film. The current is passed through two leads, one of which is grounded to the film's surface while the other is used to outline the desired sensor shape (AMP, 1994). On the other hand, a more conventional sensor forming technique used by Zahui et al. (2001a) was to

physically cut the material into shape. The advantage in using this method of cutting is that many methods can be used which range from a razor knife to a precision laser.

Once the sensor is formed to its desired shape, it has to be bonded to the surface on which it will be used. One method for adhering the sensors used by Clark and Burke (1996) was to place the sensor on double-sided carpet tape and then place it on the structure. However, another method that could be used to adhere the sensors to the structure is to use a liquid adhesive (AMP, 1994). The advantage to using a liquid adhesive is that it would allow the sensor to be relocated on the structure's surface before the adhesive dries, thus reducing placement error. The placement error can also be reduced by forming the sensor shape after the PVDF has been applied to the structure's surface and etching using the chemical process as opposed to the cutting process. Additionally, caution needs to be taken when using liquid adhesives to ensure that the PVDF is isolated from all metallic surfaces on which it is mounted. Finally, in research presented by Clark and Burke (1996), it was shown that the errors from forming inaccuracies are minimal compared to the errors from misalignment and placement. For example, Clark and Burke (1996) ran an experiment in which the theoretical response of a sensor designed to respond to the second and third modes of a simply-supported beam was compared to the same sensor with a placement error of 0.26 percent with respect to the beam length. That is, for a 380-millimeter beam, the sensor had a placement error of one millimeter. The results in Figure 14 show that the error can be on the magnitude of 10 to 20 decibels near the resonance of other

modes in the beam. As a result, when constructing sensors, special attention must be paid to where the sensor is placed.

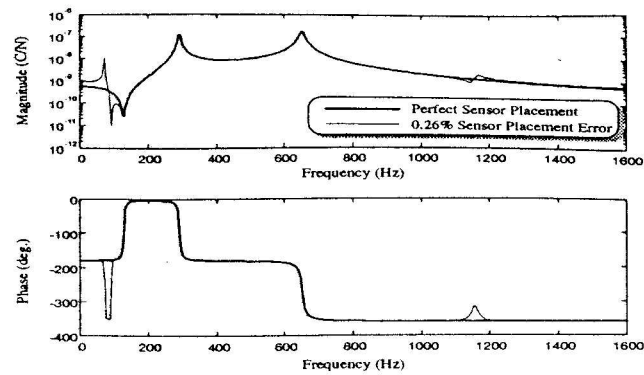


Figure 14. Comparison of Analytical and Actual Data for 2-3 Mode Sensor.

CHAPTER II

THEORETICAL DEVELOPMENT

Theoretical Development of Localized Sensors

Recognizing that it is possible to sense the local volume displacement of a beam with a sensor that traverses the entire length of a beam, it was desired to form a localized sensor that would be applied only over a desired length of a beam as opposed to over the entire length of a beam. Simply stated, it was desired to measure a local volume displacement while only monitoring the local surface area of interest. Figure 15 illustrates a beam segmented into three sections where the shaded area would represent the area covered by a local sensor. In other words, the sensor would span from the point $x=a$ to the point $x=c$ and only measure the beam volume displacement within the region $a \leq x \leq c$. By localizing the sensor in this manner, the sensor shape will be independent of the beam end conditions present. Instead, the sensor shape will be adjusted to the length of the localized area of interest. The possible beam end condition combinations examined in this work include fixed-fixed, fixed-free, fixed-simply supported, and simply supported-simply supported. The reason for examining all of these end conditions is that each end condition will produce different vibrational behavior which will in turn yield different beam volume displacement yielding a different radiated sound. Therefore, sensors for each set of end conditions were developed.

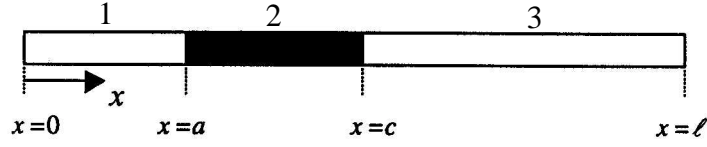


Figure 15. Segmented Beam.

The first step in the sensor development was to generate the equations for the localized sensors so that the sensor shapes for the areas of interest could be constructed. However, before progressing to the development of the localized sensor equations, the calculations for a total sensor performed by Johnson and Elliott (1993) were reviewed. In their work, Johnson and Elliott started with the PVDF charge equation:

$$q = -e_{31}(h_b + h_s) \int_a^c F(x)Z''(x)dx. \quad (16)$$

Then, through double partial integration a charge equation takes the form:

$$q = -e_{31}(h_b + h_s) \{ [F(l)Z'(l) - F'(l)Z(l)] - [F(0)Z'(0) - F'(0)Z(0)] + \int_0^l F''(x)Z(x)dx \}. \quad (17)$$

The new charge equation and the assumption that the sensor shape was a quadratic function in the form:

$$F(x) = \tilde{\kappa}x^2 + Ax + B \quad (18)$$

were used in conjunction with the beam's boundary conditions to develop an expression for the volume displacement of the beam and the shape of the sensor. The research also presented that the sensor shape shall meet the assumed conditions that $F(0) = F(l) = 0$ and $F'(0) = -F'(l)$ signifying that the sensor shape will be symmetric along the x axis and equal to zero at its ends. Thus, by differentiating the assumed

quadratic sensor shape function, Eq. (18), the derivatives and functions at the end conditions became:

$$F(x) = \tilde{\kappa}x^2 + Ax + B \Rightarrow F(0) = B, F(l) = \tilde{\kappa}l^2 + Al + B, \quad (19)$$

$$F'(x) = 2\tilde{\kappa}x + A \Rightarrow F'(0) = A, F'(l) = 2\tilde{\kappa}l + A, \text{ and} \quad (20)$$

$$F''(x) = 2\tilde{\kappa}. \quad (21)$$

Next, the differentiated equations, Eqs. (19, 20, and 21), are set equal to the sensor shape constraints and the resulting equations are solved for the constants A and B , thereby resulting in a new sensor shape function:

$$F(x) = \tilde{\kappa}x^2 - \tilde{\kappa}lx = \tilde{\kappa}(x^2 - lx). \quad (22)$$

The result of the new sensor shape equation is that the first and second derivatives for the sensor shape equation meet the required conditions for the sensor shape ($F(0) = F(l) = 0$ and $F'(0) = -F'(l) = -\tilde{\kappa}l$). Applying these sensor shape constraints to the charge equation, it takes the simplified form:

$$q = -e_{31}(h_b + h_s)\{-\tilde{\kappa}l[Z(l) + Z(0)] + 2\tilde{\kappa}\int_0^l Z(x)dx\}. \quad (23)$$

However, it is known that the volume displaced D can be represented as:

$$D = b\int_0^l Z(x)dx \quad (24)$$

where b is the beam width and can be rearranged to take the form:

$$\int_0^l Z(x)dx = \frac{D}{b}. \quad (25)$$

In its new form, the volume displacement can be substituted into Eq. (23), and the charge equation will take the form:

$$q = -e_{31}(h_b + h_s)\{-\tilde{\kappa}l[Z(0) + Z(l)] + 2\tilde{\kappa}\frac{D}{b}\}. \quad (26)$$

Solving the above expression for the volume displacement, D , an expression as a function of the sensor shape and charge results in the form:

$$D = \frac{-b}{2\tilde{\kappa}}\{-\tilde{\kappa}l[Z(0) + Z(l)]\} - q\left[\frac{b/2\tilde{\kappa}}{e_{31}(h_b + h_s)}\right], \quad (27)$$

where $Z(0)$ and $Z(l)$ are the displacement at the boundary of the beam, q is the charge generated by the PVDF. However, in the case where the beam is ideally clamped, $Z(0)$ and $Z(l)$ are zero, and the entire first term drops out of Eq. (27). Therefore, these calculations as performed by Johnson and Elliott (1993) will develop a total volume displacement sensor that spans the entire length of the beam.

Using a similar approach to the above by Johnson and Elliott (1993), a quadratically shaped localized surface sensor can be developed for a beam. This localized sensor would in fact span from $x = a$ to $x = c$ in Figure 15. Again, in developing the localized sensor shape and volume displacement equations, the initial equation used was the PVDF charge equation, Eq. (16), except the limits of integration are now changed from $x = 0$ and $x = l$ to $x = a$ and $x = c$. Therefore, the new general form of the charge equation in one dimension becomes:

$$q = -e_{31}(h_b + h_s)\int_a^c F(x)Z''(x)dx. \quad (28)$$

Once again, applying double partial integration, the charge equation takes the form of a localized charge equation (\hat{q}):

$$\hat{q} = -e_{31}(h_b + h_s)\{[F(c)Z'(c) - F'(c)Z(c)] - [F(a)Z'(a) - F'(a)Z(a)] + \int_a^c F''(x)Z(x)dx\}. \quad (29)$$

Like before, the sensor shape, $F(x)$ is assumed to take the form:

$$F(x) = \tilde{\kappa}x^2 + Ax + B \quad (30)$$

and the sensor shape constraints of $F(a) = F(c) = 0$ and $F'(a) = -F'(c)$ are being applied again. In meeting these conditions the localized charge equation can be simplified to:

$$\hat{q} = -e_{31}(h_b + h_s)\{F'(a)[Z(a) + Z(c)] + 2\tilde{\kappa} \int_a^c Z(x)dx\}, \quad (31)$$

where $Z(a)$ and $Z(c)$ are the displacements of the beam at locations coinciding with the ends of the sensor. Each of these values can be measured with an accelerometer.

Since the localized volume displacement (\hat{D}) can be represented as:

$$\int_a^c Z(x)dx = \frac{\hat{D}}{b}, \quad (32)$$

and substituted back into the local charge equation, Eq. (31), then local charge can be expanded as a function of local volume displacement as:

$$\hat{q} = -e_{31}(h_b + h_s)\{F'(a)[Z(a) + Z(c)]\} + -e_{31}(h_b + h_s)\frac{2\tilde{\kappa}\hat{D}}{b}. \quad (33)$$

This equation can be solved for the local volume displacement (\hat{D}) as:

$$\hat{D} = \frac{-b}{2\tilde{\kappa}}\{F'(a)[Z(a) + Z(c)]\} - \hat{q}\left[\frac{b/2\tilde{\kappa}}{e_{31}(h_b + h_s)}\right], \quad (34)$$

where $F'(a)$ is the slope of the sensor shape, $Z(a)$ and $Z(c)$ are the displacements at the ends of the sensor, and \hat{q} is the charge generated by the localized PVDF sensor. As a result, if PVDF is applied only to the area between a and c , and the charge \hat{q} as well as the displacements $Z(a)$ and $Z(c)$ are measured, the local volume displacement (\hat{D}) can be calculated.

Using the above generalized sensor shape equation, the specific sensor shape can be determined. Assuming that $\tilde{\kappa}$ is given and the sensor shape is a function of a and c , the coefficients A and B can be calculated. Substituting a and c in for x , the generalized equation takes the form:

$$F(a) = \tilde{\kappa}a^2 + Aa + B = 0, \quad (35)$$

$$F(c) = \tilde{\kappa}c^2 + Ac + B = 0. \quad (36)$$

Satisfying the boundary condition $F'(a) = -F'(c)$, the expression for the constant A can be found to be:

$$A = -\tilde{\kappa}(a + c). \quad (37)$$

Substituting the above equation into either Eq. (35) or Eq. (36), the expression for the constant B can be derived as:

$$B = \tilde{\kappa}ac. \quad (38)$$

Thus, substituting the constants A and B into Eq. (30), the sensor shape becomes the following function of x :

$$F(x) = \tilde{\kappa}[x^2 - (a + c)x + ac], \quad (39)$$

where a , c and $\tilde{\kappa}$ are all constants. Using this expression, it is possible to determine the location of the maximum value on the curve. This is calculated by taking the first derivative of Eq. (39) with respect to x and setting it equal to zero. It was found that the maximum occurs at the midpoint between a and c ,

$$x = \frac{a + c}{2}. \quad (40)$$

Therefore, replacing x in Eq. (39) with the expression in Eq. (40), the maximum point on the curve can be represented as:

$$F(x)_{\max} = \tilde{\kappa}[(\frac{a+c}{2})^2 - (a+c)(\frac{a+c}{2}) + ac]. \quad (41)$$

Simplifying the above equation, we can write:

$$F(x)_{\max} = \tilde{\kappa}[-\frac{(a-c)^2}{4}]. \quad (42)$$

However, the maximum point on the curve also occurs at the midpoint along the length of the beam:

$$F(x)_{\max} = \frac{b}{2}. \quad (43)$$

Setting these two expressions equal, one can solve for the constant $\tilde{\kappa}$ as:

$$\tilde{\kappa} = \frac{-2b}{(a-c)^2}, \quad (44)$$

and the sensor shape function can be expressed purely as a function of x :

$$F(x) = \frac{-2b}{(a-c)^2}[x^2 - (a+c)x + ac] \quad a \leq x \leq c. \quad (44)$$

Upon inspection it is recognized that the sensor shape is not unique to any specific set of boundary conditions as the local sensor is designed to span a fraction of a beam instead of an entire beam. In other words, the origin of the sensor shape is free to traverse the length of the beam between $x = 0$ and $x = l$. This signifies that the localized sensor shapes are independent of boundary conditions and are only unique to the length of the section of interest on the test specimen. Figure 16 depicts the general shape that represents sensor shape used. This shape includes the plotting of both $F(x)$ and $-F(x)$.

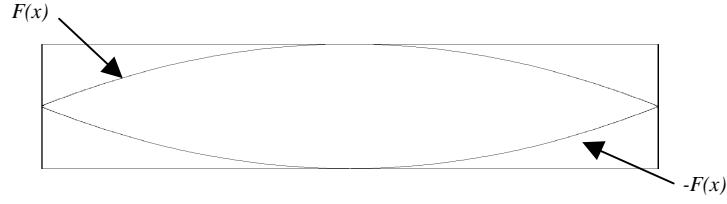


Figure 16. General Shape Used for the Surface Sensor.

With the generation of a specific sensor shape equation, it is possible to generate a specific expression for the localized volume displacement. However, before any substitutions are possible, an expression for $F'(a)$ is needed. This expression can be obtained by differentiating Eq. (45) and letting $x = a$ such that after simplification:

$$F'(a) = \frac{2b}{(c-a)}. \quad (46)$$

Thus, by substituting k from Eq. (44) and $f'(a)$ from above into Eq. (34) the result yields:

$$\hat{D} = \left[\frac{(c-a)b}{2} \right] [Z(a) + Z(c)] + \hat{q} \left[\frac{(a-c)^2}{4e_{31}(h_b + h_s)} \right]. \quad (47)$$

In the above equation, $Z(a)$ and $Z(c)$ are displacements, but the measurements being acquired are taken with accelerometers and are measures of acceleration. Therefore, if harmonic motion is assumed, the time harmonic equivalent to the displacement is:

$$Z = X e^{i\omega t}. \quad (48)$$

However, in the time domain, acceleration is simply the second derivative of the displacement; thus, the accelerometer measurement can be represented as:

$$\ddot{Z} = -\omega^2 X e^{i\omega t}. \quad (49)$$

By substituting the displacement into the acceleration expression, the acceleration can be represented as a function of the displacement:

$$\ddot{Z} = -\omega^2 Z. \quad (50)$$

Rearranging the above, the required displacement can be expressed as a function of the measured acceleration as:

$$Z = -\frac{\ddot{Z}}{\omega^2}, \quad (51)$$

which can be substituted into Eq. (47) to express the local volume displacement as a function of frequency, measured acceleration at two sensor ends, and local charge as:

$$\hat{D} = \frac{-(c-a)b}{2\omega^2} [\ddot{Z}(a) + \ddot{Z}(c)] + \hat{q} \left[\frac{(a-c)^2}{4e_{31}(h_b + h_s)} \right]. \quad (52)$$

Therefore, when a local PVDF sensor with two accelerometers at its ends is applied to a vibrating beam, the data acquired can be used to compute the local volume displacement of the beam under this integrated sensor.

Verification Process for a Localized Sensor

With a hypothesis developed, a plan as to how it will be verified was needed. The technique used was based on a known measurement technique such as the use of many accelerometers to compute the local volume displacement as a means of comparison to measurements taken with the integrated surface sensor. Additionally, since the beam will be radiating sound, the sound power of the beam can be measured and compared to a theoretically predicted sound power. As a result, a systematic approach was required for the integrated sensor verification process.

The first step in the verification process was to construct an integrated sensor using the developed localized equations. This sensor was developed to contain a PVDF surface sensor which works in conjunction with the two accelerometers at the sensor's ends to measure the total volume displacement for the beam. Once the total volume displacement was measured with the integrated sensor, a set of accelerometer measurements were taken at finite, equally spaced points along the length of the beam covered by the sensor. Then, the accelerometer data was compiled using the trapezoidal rule integration technique to determine the volume displacement per beam width, which was then multiplied by the beam width to obtain the volume displacement for the beam. Lastly, the volume displacement measured by the integrated sensor was compared with the volume displacement measured using the multiple accelerometers. When the volume displacements area compared, it is said that the data shows an acceptable correlation if the two measurements match.

After the total sensor was checked and the correlation was acceptable, a series of local sensors were constructed to span the length of the entire beam. The local volume displacement was then gathered for each individual local sensor, and the local sensors were combined to compute the beam's total volume displacement. This total volume displacement was then compared to the volume displacement measured by the total sensor that was fabricated per the verification process described in the previous paragraph. Finally, the compiled volume displacement from the local sensors was compared to the volume displacement as determined using the trapezoidal rule and accelerometer measurements.

The final verification method for the data was to measure the sound power emitted from the beam. In this process the procedure for the ANSI S12-31 1990 standard was followed, and the sound power was directly measured. After measuring the actual sound power, the theoretical sound power was calculated using the volume displacement measurements from the previous verification steps. More details for the processes followed in the experimental verification can be found in a later chapter.

CHAPTER III

EXPERIMENTAL SETUP

Overview

Before the experimental setup was constructed the facilities within which the research was to be conducted were examined. The facilities were checked for any limitations that may dictate how the experimental setup was to be constructed. The only major constraint that was encountered was the fact that the reverberation chamber that was to be used for the sound power measurements had a lower cutoff frequency of 125 Hz. Meaning that any sound power measurements made below 125 Hz in the chamber were invalid. As a result, it was determined that all of the beams would be designed to have a 250 Hz first resonance. This way the lower cutoff of the reverberation chamber was not a concern. Additionally, due to limitations in the source excitation the frequency range of interest was given an upper limit of 1600 Hz. With the effective measuring range from 0 to 1600 Hz, the first two modes of resonance were excited and measured for all the beams, and the third mode was excited and sensed for the fixed-fixed and fixed-simply supported beams.

It was also discovered that an apparatus was required in which only the sound from the vibrations of the top surface of the beam would be radiated. Therefore, a baffled box was constructed in which the top of the beam was to lie in the same plane as the top of the box and the sides of the beam were covered by the thickness of the baffle. In addition to constructing a baffled box a test fixture was required to hold the

test beams in place while the experiments were completed. However, this fixture had to be designed in such a manner that it would fit inside the baffled box and adjust in such a manner that each of the beams could be examined from the one test platform. As a result, the test beams were designed, the test fixture was constructed, and the baffled box was assembled.

Calculation of Beam Lengths

Before the experimental verification of the sensor shapes could begin and based on the variety of end conditions to be analyzed, a systematic approach to the problem was required. The first step in the analysis was to determine the effective lengths for the various beams being analyzed since each pair of end conditions contributes to different vibrational modes within the beams. Therefore, each beam had its own unique length. However, before the effective beam lengths could be calculated, the beam material, the material properties, the beam cross section, and the cross-sectional properties had to be chosen. After considering several materials such as brass, bronze, nickel, steel, and titanium, it was decided that 6061-T6 aluminum exhibited the most desirable material properties for a 0.0127 m (0.5 inch) by 0.0381 m (1.5 inches) rectangular cross section. The material and cross-sectional properties used for the calculations are listed in Table 1 below. In addition to the material properties, the desired frequency at which the first resonant frequency was to occur had to be decided, as this is one of the main factors that helps justify the length of the beams. For this research, due to equipment limitations, it was determined that the

first resonance for all the beams should occur at a frequency of approximately 250 Hz.

Knowing the beam's material and cross-sectional properties, the effective lengths could now be determined for the various end conditions. However, due to the varying end conditions, the beam lengths will not all be identical since the set of

Table 1.

6061-T6 Aluminum Material Properties (Gere and Timoshenko, 1997).

6061-T6 Aluminum
$E = 70 \text{ GPa}$
$\rho = 2700 \text{ kg/m}^3$
$\nu = 0.33$
$A = 483.9 \text{ mm}^2$
$I = 6503.6 \text{ mm}^4$

boundary conditions will change for each beam. For example, Hayek (2001) states that the fixed end condition will exhibit a displacement and a slope both equal to zero

($Z|_{x=0} = 0, \frac{dZ}{dx}|_{x=0} = 0$), while a simply supported end condition will have a

displacement and a moment both equal to zero ($Z|_{x=0} = 0, \frac{d^2Z}{dx^2}|_{x=0} = 0$). Similarly, the

free end condition will have a shear and a moment both equal to zero

($\frac{d^2Z}{dx^2}|_{x=L} = 0, \frac{d^3Z}{dx^3}|_{x=L} = 0$). Thus, by using the general equation for the transverse

vibration of a prismatic beam and the boundary conditions for each beam end condition, the resonant frequencies can be derived. From this derivation, the effective

beam lengths can be determined if the first resonant frequency is known. Therefore, using a fixed free beam as an example, the beam length equation will be derived.

In deriving the expression for the fixed-free beam, the general equation for transverse vibration of a prismatic beam is expressed as:

$$y = A \cos k_f x + B \sin k_f x + C \cosh k_f x + D \sinh k_f x, \quad (53)$$

where A , B , C , and D are constants, k_f is a constant that is dependent on the beam's boundary conditions, x is the point along the length of the beam of interest, and y is the vertical displacement of the point of interest. Then, from the boundary conditions, it can be recognized that the first, second, and third derivatives of Eq. (53) are required and can be expressed as:

$$\frac{dy}{dx} = y' = k_f (B \cos k_f x - A \sin k_f x + C \sinh k_f x + D \cosh k_f x), \quad (54)$$

$$\frac{d^2 y}{dx^2} = y'' = k_f^2 (-B \sin k_f x - A \cos k_f x + C \cosh k_f x + D \sinh k_f x), \text{ and} \quad (55)$$

$$\frac{d^3 y}{dx^3} = y''' = k_f^3 (A \sin k_f x - B \cos k_f x + C \sinh k_f x + D \cosh k_f x). \quad (56)$$

Applying the fixed boundary conditions at $x = 0$, it can be found that:

$$y|_{x=0} = 0 = A + C \quad \therefore A = -C, \text{ and} \quad (57)$$

$$\left. \frac{dy}{dx} \right|_{x=0} = 0 = k_f (B + D) \quad \therefore B = -D. \quad (58)$$

Thus, if Eqs. (53), (54), (55), (56) are rewritten with the above constant relationships, these equations take the form:

$$y = A(\cos k_f x - \cosh k_f x) + B(\sin k_f x - \sinh k_f x), \quad (59)$$

$$y' = k_f (A(\sin k_f x + \sinh k_f x) + B(\cos k_f x - \cosh k_f x)), \quad (60)$$

$$y'' = k_f^2 (-A(\cos k_f x + \cosh k_f x) - B(\sin k_f x + \sinh k_f x)), \text{ and} \quad (61)$$

$$y''' = k_f^3 (A(\sin k_f x - \sinh k_f x) - B(\cos k_f x + \sinh k_f x)). \quad (62)$$

Next, the boundary conditions for the free end $x = l$ are applied, producing:

$$0 = k_f^2 (-A(\cos k_f l + \cosh k_f l) - B(\sin k_f l + \sinh k_f l)), \text{ and} \quad (63)$$

$$0 = k_f^3 (A(\sin k_f l - \sinh k_f l) - B(\cos k_f l + \cosh k_f l)). \quad (64)$$

Rearranging Eqs. (63) and (64) to a form in which the coefficient A is divided by the coefficient B , the following expression:

$$\frac{B}{A} = \frac{-(\cos k_f l + \cosh k_f l)}{(\sin k_f l + \sinh k_f l)} = \frac{(\sin k_f l - \sinh k_f l)}{(\cos k_f l + \cosh k_f l)} \quad (65)$$

is obtained. Cross-multiplying the sine and cosine functions yields:

$$-(\cos k_f l + \cosh k_f l)^2 = \sin^2 k_f l - \sinh^2 k_f l. \quad (66)$$

By expanding the cosine squared terms and rearranging the terms, the equation results in:

$$-2\cos k_f l \cosh k_f l = \sin^2 k_f l + \cos^2 k_f l + \cosh^2 k_f l + \sinh^2 k_f l. \quad (67)$$

Now simplifying the above equation, the expression becomes $\cos k_f l \cosh k_f l = -1$, and the solution for $k_f l$ becomes:

$$k_f l \approx (n - \frac{1}{2})\pi. \quad (68)$$

Having solved for the expression of $k_f l$, the expression for the resonant frequency can be expressed as:

$$f_f = \frac{(k_f l)^2}{2\pi l^2} \sqrt{\frac{EI}{\rho A}} = \frac{((n - \frac{1}{2})\pi)^2}{2\pi l^2} \sqrt{\frac{EI}{\rho A}}, \quad (69)$$

where f_f is the resonant frequency, $(k_f l)^2$ is a constant that is dependent on the end conditions, l is the beam length, E is Young's Modulus for the material, I is the moment of inertia, ρ is the material density, A is the cross-sectional area, and f is the mode number. Thus, using the same approach laid out from Eq. (53) to Eq. (69) each of the other boundary conditions can be analyzed and the values for $(k_f l)^2$ determined. It should also be noted that the values of $(k_f l)^2$ are independent of the material used and have been predetermined by Thompson (1993). They can be found in Table 2 for each of the beams analyzed.

Table 2.

Constants Used for Determining the Beam Natural Frequencies.

Beam Configuration	$(k_1 l)^2$ Fundamental	$(k_2 l)^2$ Second Mode	$(k_3 l)^2$ Third Mode
Simply Supported	9.87	39.5	88.9
Cantilever	3.52	22	61.7
Clamped-Clamped	22.4	61.7	121
Clamped-Hinged	15.4	50	104

Having developed an expression for the resonant frequency as a function of the material and cross-sectional properties as well as the beam length, the beam lengths required to achieve a first resonance at 250 Hertz can be calculated. This can be done by rearranging Eq. (69) such that the equation takes the form:

$$l = \sqrt{\frac{(k_f l)^2}{2\pi f_f}} \sqrt{\frac{E \left(\frac{1}{12}\right) h^2}{\rho}}. \quad (70)$$

Note that the beam length is independent of the beam width and beam cross section. Therefore, using the material properties in Table 1 and the $(k_{rl})^2$ values in Table 2, the beam lengths can be calculated. The resulting beam lengths can be found in Table 3.

Test Fixture Construction

With the required beam lengths analytically determined, the construction of the test specimens could begin. The design and construction of the test fixture used to support the test specimens was initialized as well. The test fixture was designed such

Table 3.

Calculated Beam Lengths for a 250 Hz First Resonance.

Support	L_1 (m)	L_1 (ft)
Simply Supported	0.34	1.12
Cantilever	0.20	0.67
Clamped-Clamped	0.52	1.68
Clamped-Hinged	0.43	1.39

that it could be disassembled and reassembled to accommodate different beam end conditions. The different setups had to be capable of supporting a fixed-fixed, a fixed-free, a fixed-simply supported, and a simply supported-simply supported beam. Therefore, in addition to the beams themselves, the different components of the test fixture included the base, two slides, two towers, two fixed end conditions, and two simply supported end conditions.

In constructing the beams, several factors had to be considered. The first item was that the beam lengths calculated were the effective beam lengths. In other words, all the beams needed to be slightly longer than the calculated length so that the beams

could be mounted in the test fixture and still effectively resonate at 250 Hz. As a result, depending on the end conditions, a set length was added to each beam. For all the fixed end conditions, an extra 0.1016 meters (4 inches) was added to the length of the beam, while for all the simply supported end conditions, 0.0127 meters (0.5 inches) was added to each of the beams. Also, the method by which the fixed and simply supported end conditions were going to be modeled had to be considered. This issue was resolved by simply drilling and tapping a set of six $\frac{1}{4}$ -20 holes in the end of the beam for the fixed end conditions (Figure 17). Similarly, for the simply supported end conditions, a dimple was put on the side of the beam and a pin was machined to sit in the dimple and hold the end condition in place (Figure 18). The complete set of machined beams is shown below in Figure 19.



Figure 17. Fixed End With Six Tapped Holes.



Figure 18. Simply Supported End With a Connecting Pin.



Figure 19. Machined Set of Beams (From the Top Down: Fixed-Free, Simply Supported-Simply Supported, Fixed-Simply Supported, Fixed-Fixed).

Like the beams, the design of the base had to be carefully planned because the base had to be constructed in such a way that the force used to excite the beam did not vibrate the test fixture. In other words, the base had to be designed in such a way that the vibrations it experienced would not influence the vibration of the beam under examination. To prevent this several things were done. First, the base was designed to have a large mass such that it would require a large force to create disturbing vibrations in it. Next, a large slot was machined in the center of the base so that the structure that supported the shaker (excitation force) was isolated from the entire test fixture. The final preventative measure taken was to put adjustable rubberized feet under the base (Figure 20). Therefore, multiple tapped holes were drilled in the base to allow it to be leveled and to provide a connecting point for the slides (Figure 21). The finished base without the feet can be seen in Figure 22.



Figure 20. Rubberized Leveling Feet.

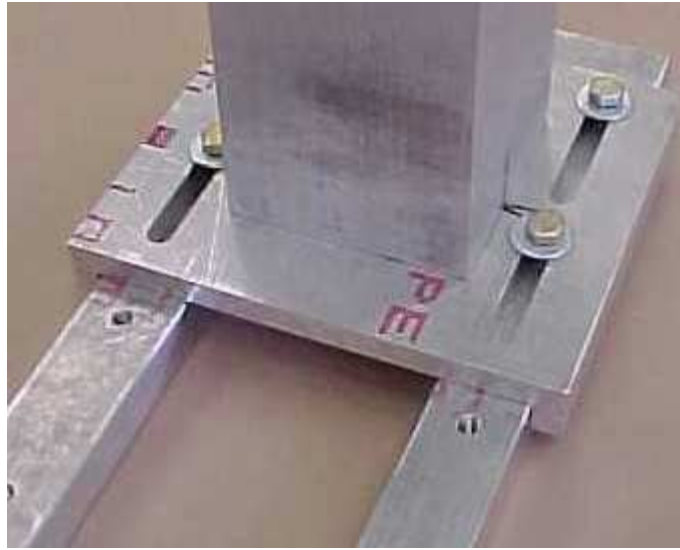


Figure 21. Base With Tapped Holes for Leveling and Mounting the Slides.



Figure 22. Machined Base for the Test Fixture.

Once the base was constructed, two slides were designed and fabricated. The purpose of these slides was to allow for adjustments to be made. The adjustments necessary included the ability to accommodate the different beam lengths. Since every beam tested had a unique length, machined slots were placed on each side that allowed for fine adjustments in length (23). The slides were also designed in such a way that they had guides that were used to assist in aligning the slots and the holes in the base when the slides were moved (Figure 24). The guides were also used to assist in keeping the fixture assembled squarely. The slides also had a series of four holes drilled into their centers. These holes were countersunk on the bottom side and were

intended for attaching the towers (Figure 25). The reason the holes are countersunk is that the bottom of the slides remain level, and there are no bolt heads protruding.



Figure 23. Close Up View of the Slots Machined in the Slides.

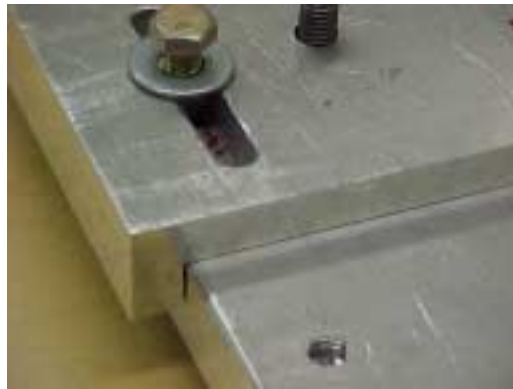


Figure 24. End View of the Slide Showing One of the Guides on the Base.



Figure 25. Countersunk Holes for Mounting the Towers.

After the slides were machined, construction on a pair of towers began. The purpose of the towers was to merely act as an extension and to elevate the beam to a height at which the shaker could be placed under it. The towers were designed to provide approximately 0.2032 meters (8 inches) of elevation. Since the towers were

so tall, it was decided that a solid cross section of 0.1016 meters (4 inches) would provide stable support. The solid cross section was used instead of a hollow cross section for two reasons. First, the solid cross section provided more mass to the test fixture for damping undesired vibrations, and second, the solid cross section would allow the tower to be easily bolted to the slide. The bolts used to connect the tower and the slide were a tapered 3/8-16 socket head screw. Figure 25 depicts one of the screws used, while Figure 26 illustrates one of the towers mounted on a slide.



Figure 26. One of the Towers Mounted on a Slide.

Completing the towers, the foundation for the test fixture was complete. Next, the end conditions had to be designed and fabricated. The end conditions are referred to as theoretical since it is very difficult to exactly model a fixed and a simply supported end condition. In an attempt to model a fixed end condition as accurately as possible, a pair of fixed end condition blocks were constructed. These blocks contained four countersunk holes on their corners which were used to connect the

blocks to the towers. They also included six holes positioned 0.0254 meters (1 inch) apart along the center line. These holes were positioned in such a way that the blocks could be bolted to the fixed ends of the test beams (Figure 27). After constructing the fixed end condition blocks, it was realized that the some of the material along the edge had to be removed because it was interfering with the vibration at the end of the beams (Figure 28). The removal of this material also affected the effective length of the beams and, as a result, lowered the resonant frequencies of the beams containing fixed end conditions.

The simply supported end conditions were constructed in a similar manner as the fixed end conditions. Again the block contained countersunk holes for attaching it to the tower. However, since the simply supported beam was to be held on the sides, the block had to be designed such that the beam could be moved freely. Therefore, a opening for the beam was machined and holes for the simply supported pins were positioned such that the top of the beam was flush with the top of the block when it was in use (Figures 29, 30). The pins used were machined to a point and threaded so that the force they applied to the beam could be regulated (Figure 31). With the ability to adjust the applied force as necessary, the theoretical simply supported end condition could be accurately modeled. After completing the interchangeable blocks it was now possible to sufficiently model all the beams being investigated and the verification process could begin. (Note: A set of detailed drawings associated with the fixture components is located in Appendix A.)

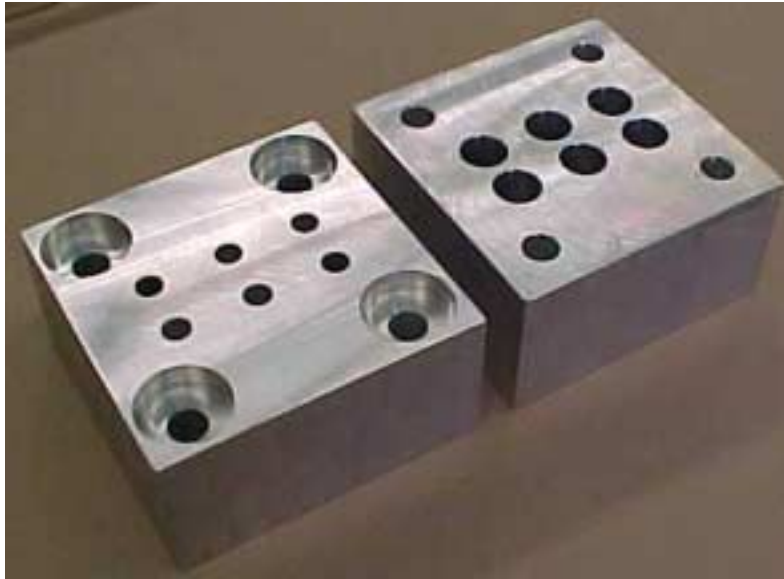


Figure 27. Beam Support for a Fixed End Condition. (Left) Top, (Right) Bottom.



Figure 28. Fixed End Condition With Material Removed.



Figure 29. Simply Supported End Condition.



Figure 30. Assembled Simply Supported End Condition.

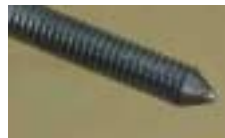


Figure 31. Simply Supported Pin.

Baffled Box Construction

While in the design and construction process, a baffled box was constructed to house the test fixture for testing the surface sensors. The purpose of the baffled box is to isolate the source of the sound being radiated. In other words, the baffled box was used to mask undesired sounds that may be generated by the test fixture, the shaker, and the underside of the beam. As a result, a box was constructed that was large

enough to house the test fixture, the shaker, and some vibrational dampening materials.

In the construction, 0.01905 meter (0.75 inch) plywood was used for the sides of the box (Figure 32). However, the box bottom and box top for each of the beams were fabricated from 0.0127 meter (0.5 inch) plywood (Figure 33). Also, when connecting the sides and bottom, all the joints were sealed with silicone to prevent air leaks. In a similar manner the top of the sides was designed in such a way that all the tops would be airtight when in use. This was accomplished by using strips of airtight foam around the perimeter of the sides where the tops were bolted on (Figure 34). Each of the tops was constructed in such a way that the beam fit flush with the surface of the tops when they were in use (Figure 35). By having the top and the beam lie flush with one another, the box could be totally sealed by applying tape over the gaps between the beam and the box (Figure 36). In this way, all the volume displacement measured by the surface sensor is known to be only the result of the beam's surface vibrations. Finally, since the box was designed to be airtight, a set of connectors was mounted in the front face of the box (Figure 37). These connectors were used for connecting the shaker and force gauge to their respective excitation and measurement devices. A set of detailed drawings for the construction of the baffled box can be found in Appendix B.

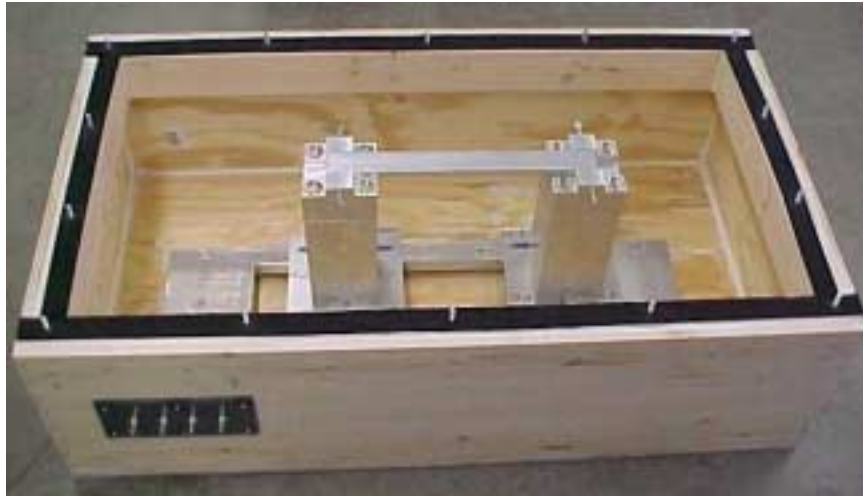


Figure 32. Plywood Box Constructed With the Simply Supported Beam Inside (Top Cover Removed).

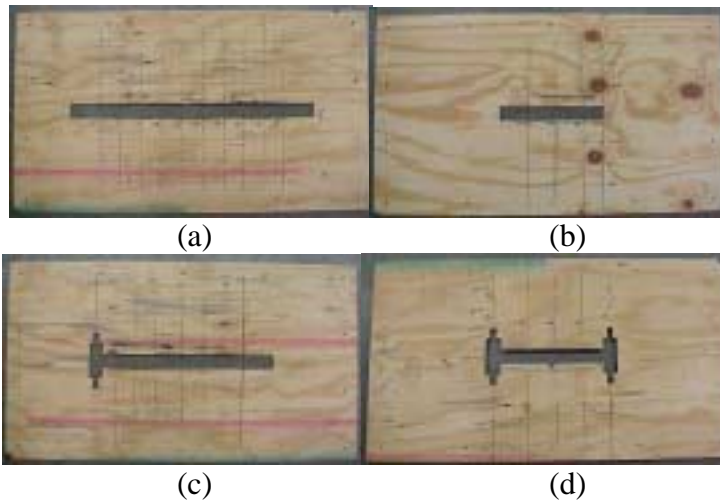


Figure 33. Baffled Box Covers Constructed From Plywood. (a) Fixed-Fixed Cover, (b) Fixed-Free Cover, (c) Fixed-Simply Supported Cover, (d) Simply Supported-Simply Supported Cover



Figure 34. Seal Material and Connecting Stud.

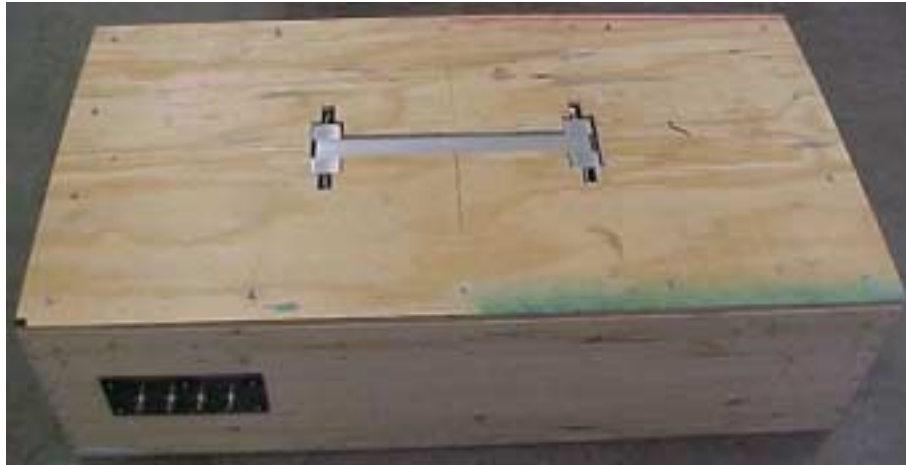


Figure 35. Simply Supported Beam in the Baffled Box, Such that the Cover and the Beam are Flush.



Figure 36. Simply Supported Beam Sealed Along the Edges With Tape.



Figure 37. Connectors Utilized to Link the Electrical Signals from Outside the Box to the Instruments Located Inside the Box.

Experimental Equipment

With the construction of the test fixture and the baffled box, the equipment required for the testing portion of this sensor verification study had to be set up. Locating the equipment required for the testing process, learning how to assemble it, and learning to operate it properly were the first steps to successfully testing the

developed integrated surface sensors. The components used for gathering the vibrational data throughout this research were a Hewlett Packard (HP) Dynamic Signal Analyzer (model 35670 A) and a TEAC Digital Audio Tape (DAT) recorder (model RD-135T) (Figure 38). In addition to data acquisition, the HP dynamic signal analyzer was used in conjunction with a Techron power amplifier (model 5507) and a Labworks seven pound electrodynamic shaker (model ET-132-2) to provide the beam a vibratory source of excitation (Figures 39 and 40). This excitation was transmitted to the beam through a short piece of threaded rod, referred to as a stinger (Figure 40). Consequently, several instruments were considered for measuring the excitation force and vibrations of the beam. In the cases where point sensors were used to sense the vibrations, PCB Piezotronics accelerometers (models U353B16 and 352C22) were used (Figure 41). Similarly, the excitation force was measured using a PCB Piezotronics force gauge (model 208B02) (Figure 42). The signals generated by the accelerometer and the force gauge were passed through a set of PCB signal conditioners (model 480E09) before being routed to the TEAC DAT recorder (Figure 43). By passing the signal through a PCB signal conditioner, the signal was filtered and amplified before it reached the TEAC DAT recorder. A schematic of the test setups used for the accelerometer and the integrated sensor measurements can be seen in Figures 44 and 45.



Figure 38. HP Analyzer and TEAC DAT Recorder Used for Data Collection.

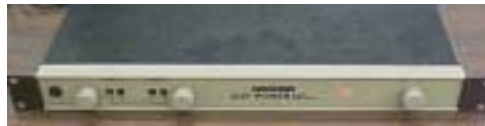


Figure 39. Techron Amplifier Used for Shaker Excitation.



Figure 40. Seven Pound Shaker Used as an Excitation Source.



Figure 41. Accelerometers Used for Sensing the Vibrations.
(Left: Model U353B16, Right: Model 352C22)



Figure 42. Force Gauge With Stinger Used for Measuring the Excitation Force.



Figure 43. Single Channel PCB Signal Conditioner.

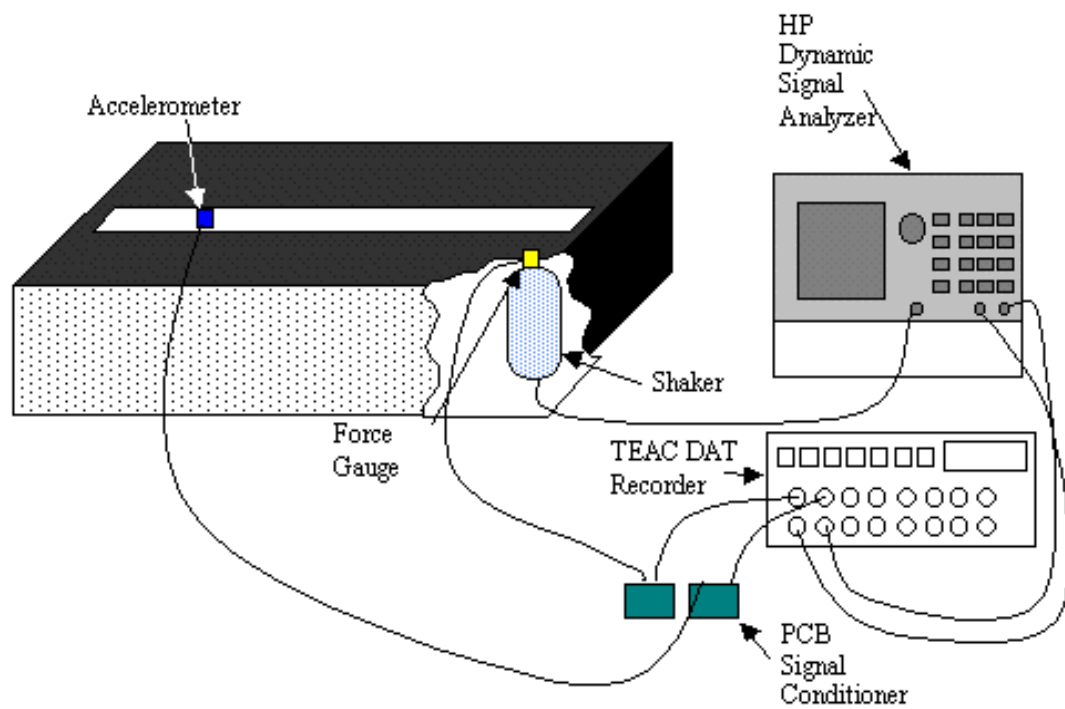


Figure 44. Test Setup Used for Taking the Accelerometer Measurements.

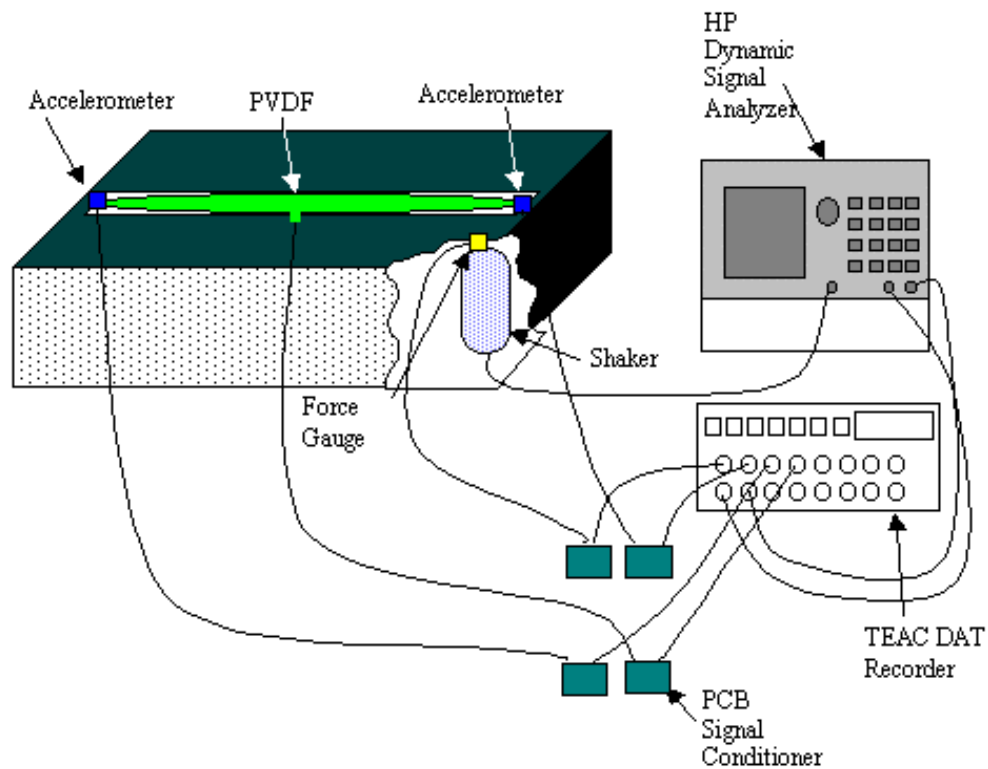


Figure 45. Test Setup Used for Making the Integrated Sensor Measurements.

In a similar manner to the vibrational data collected, sound data collection required much of its own unique equipment. However, the excitation process was the same for the sound power measurements as it was for the vibrational measurements. Also, the signal measured was initially recorded by the TEAC DAT recorder in much the same manner as the vibrational signal. Then, the DAT recording was played back to a Larson Davis Spectrum Analyzer (model 2900B) for completing the sound power analysis (Figure 46). However, the signal that was recorded was sensed through a set of six half inch TMS microphones (model 140AQ) with preamplifiers (model 426A01) instead of accelerometers and a force gauge (Figure 47). The microphone signal was then passed through a multi-channel PCB signal conditioner (model 481)

similar to the PCB signal conditioners used for the vibrational data (Figure 48). A schematic of this setup can be seen in Figure 49.



Figure 46. Larson Davis Analyzer Used for Sound Power Measurements.



Figure 47. Half-Inch Microphone Used for Sensing Sound Power.



Figure 48. Multi-Channel Signal Conditioner.

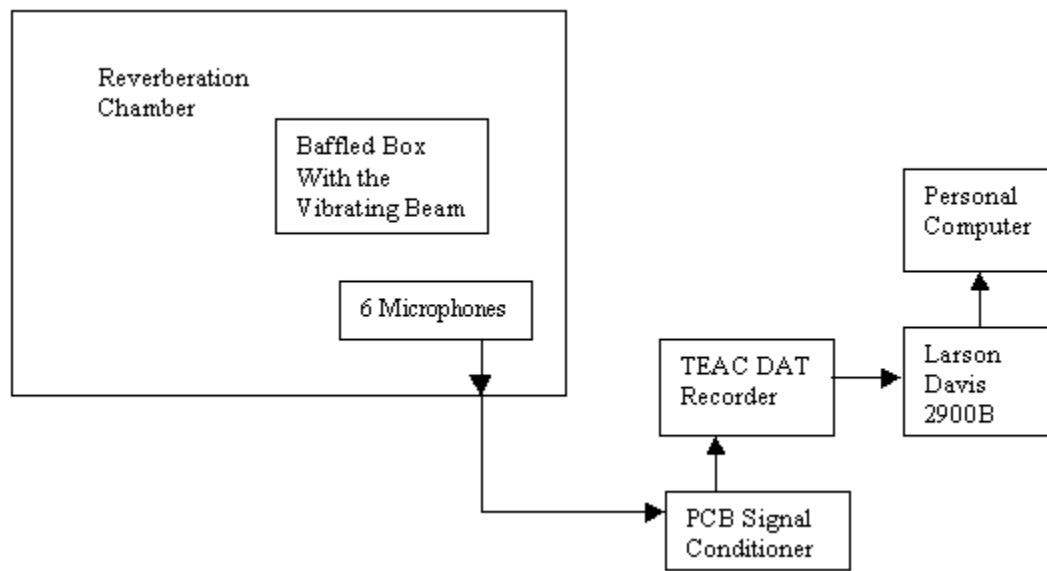


Figure 49. Schematic of the Test Setup Used for the Sound Power Measurements.

Beam Resonance Verification

With the test fixture and the test specimens completed, the next logical step was to verify that the beam's first mode of resonance was indeed at the theoretically designed value of 250 Hz. This process of verification was completed by mounting the beams in the test fixture one at a time and exciting them with a random excitation produced by a LDS (Ling Dynamic Systems L.T.D.) four pound shaker (model V203) (Figure 50). The shaker was driven at 2.2 Volts peak to peak by the HP spectrum analyzer; however, the signal from the spectrum analyzer was later amplified by the amplifier at a setting of four on the volume knob (Figure 51). In addition to driving the shaker with a random signal, the location at which it was placed was critical. The driving location had to be in such a place that nothing interfered with the modes of the first three resonances of the beams, which were the modes of interest. In other words, the stinger had to be located in such a way that it was not on a node of any of the

modes of interest. As a result, the stinger was located at a distance of 0.1524 meters (6 inches) from the end of the beam for the fixed-fixed, the fixed-simply supported, and the simply supported-simply supported cases and 0.0254 meters (1 inch) from the free end on the fixed-free beam (Figure 50).

Once the method and location of the excitation was set up, the required measurements had to be determined. It was decided that the best measurement for depicting the resonances in the beams was to show the frequency response using an accelerometer and force gauge. In setting up for such a measurement, an accelerometer and a force gauge are required to be placed in the same plane as one another such that they essentially lie directly on top of each other (Figure 52). Then, the signals from the two sensors are brought into the spectrum analyzer where the accelerometer measurement is automatically divided by the force measurement, thereby producing the frequency response spectrum.

After setting up the test fixture, the beam was excited and the frequency response function between an accelerometer located on the beam (above or close to the stinger attachment point) and the force gauge was measured and saved for each beam. Figures 53, 54, 55, and 56 show a representation of this frequency response spectrum as it was displayed on the spectrum analyzer for the fixed-fixed, the fixed-free, the fixed-simply supported, and the simply supported-simply supported beams, respectively. From these spectra, the actual beam resonant frequencies can be identified by locating the peak values of the spectrum. Once the experimental resonances are measured, they can be compared to the theoretical resonances

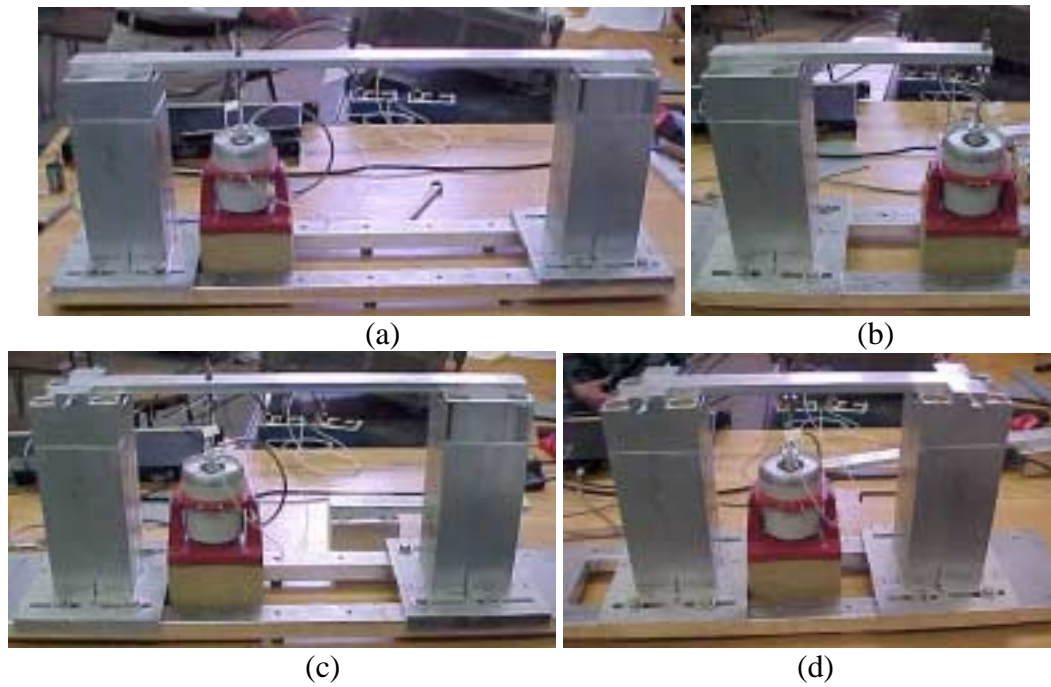


Figure 50. Beam Resonance Verification Setup for Different Beam Boundary Conditions. (a) Fixed-Fixed Beam, (b) Fixed-Free Beam, (c) Fixed-Simply Supported, (d) Simply Supported-Simply Supported

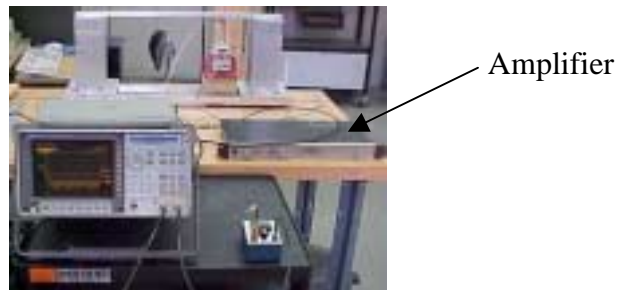


Figure 51. Spectrum Analyzer and Amplifier Used for Beam Resonance Tests.



Figure 52. Shaker and Accelerometer Setup For Measuring the Beam Resonances.

calculated based on the effective beam lengths. Table 4 represents the comparison between the theoretical and experimental resonant frequencies for the first three modes of the fixed-fixed and the fixed-simply supported beams, and the first two modes for the fixed-free and the simply supported-simply supported beams. In comparing the calculated and measured first resonant frequency for the fixed-free beam, it was recognized that a large variation occurred. This difference was realized to be a result of the fixed end condition being modified and effectively lengthening the fixed-free beam. However, based on the comparison of the resonant frequencies for the remaining beams, it was believed that the end conditions were being satisfactorily modeled. Therefore, it was believed that the integrated sensors designed should be able to measure the volume displacement of the beams accurately.

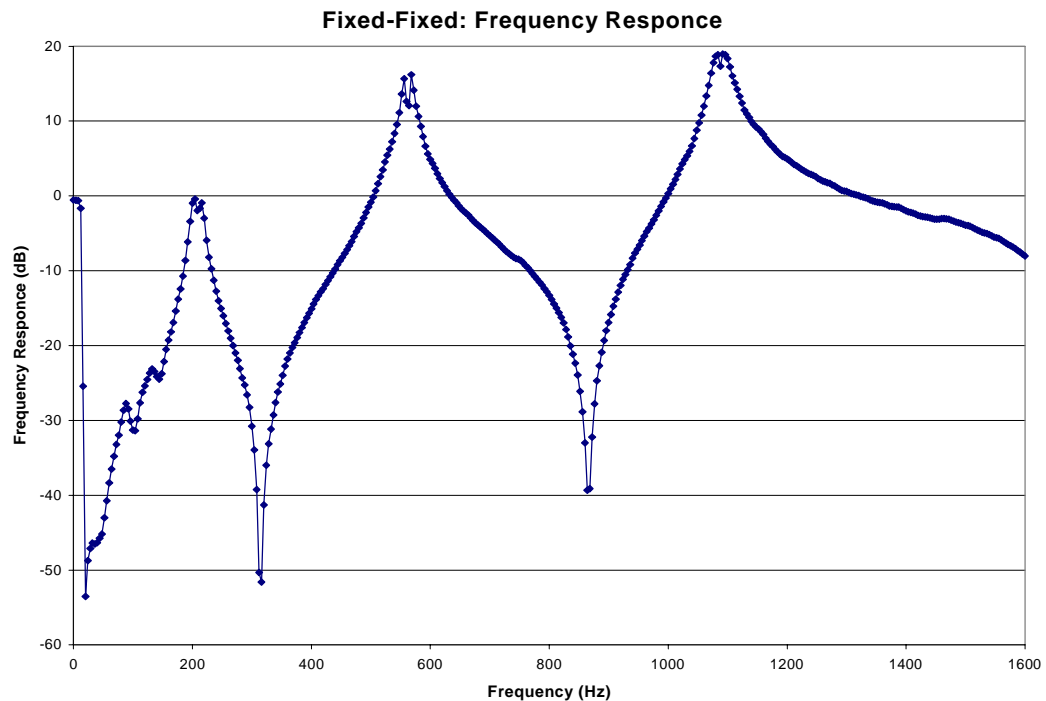


Figure 53. Frequency Response for the Fixed-Fixed Beam.

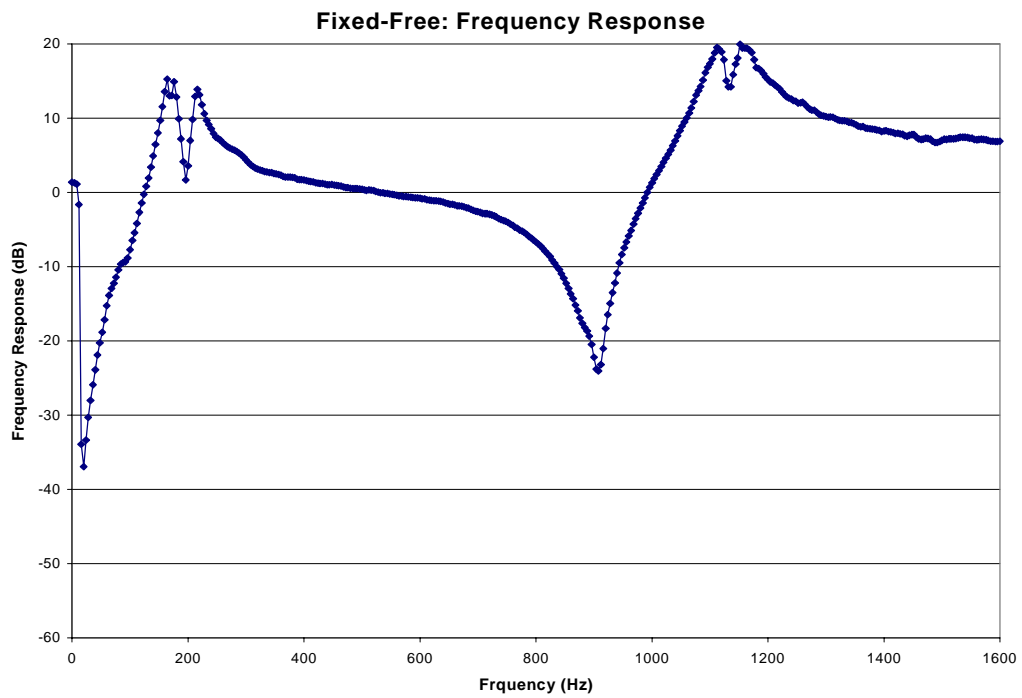


Figure 54. Frequency Response for the Fixed-Free Beam.

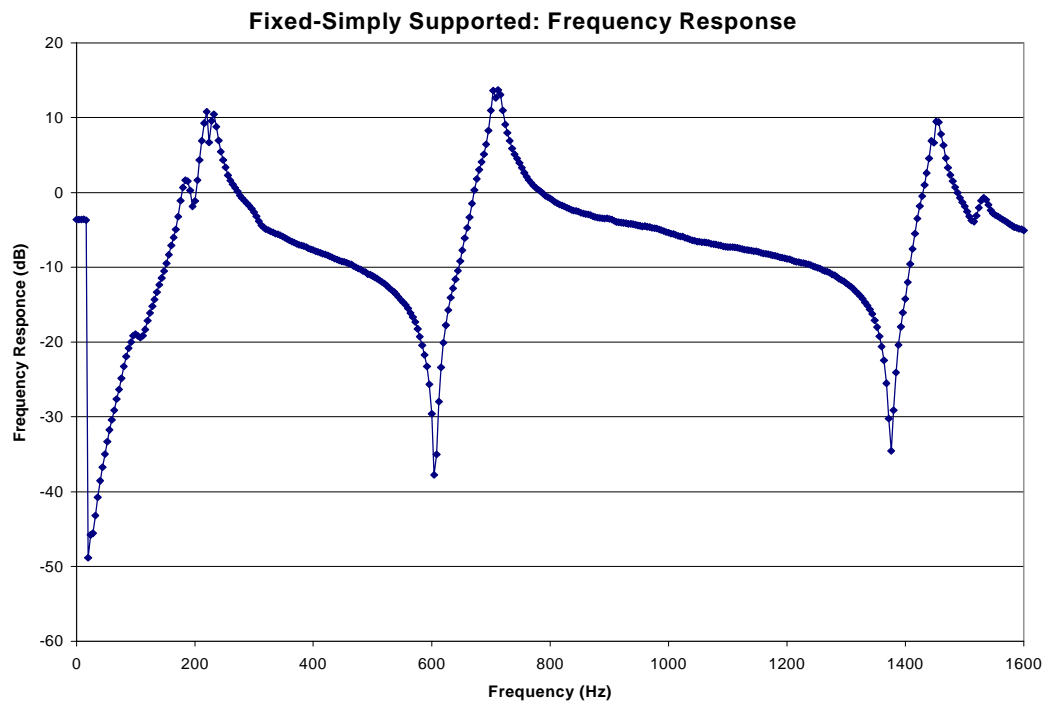


Figure 55. Frequency Response for the Fixed-Simply Supported Beam.

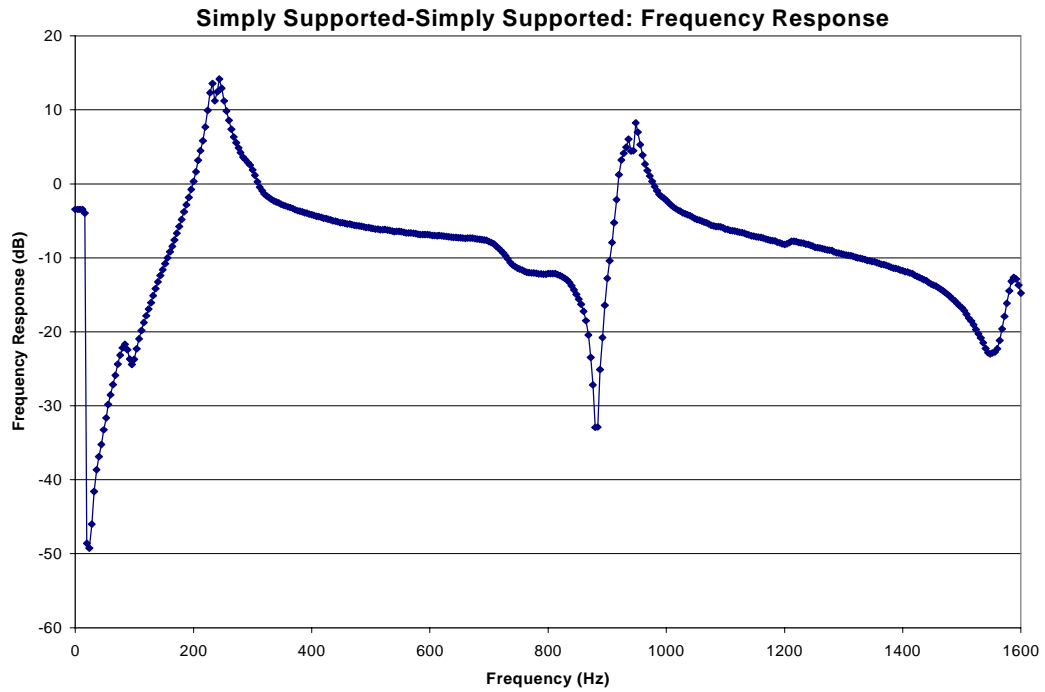


Figure 56. Frequency Response for the Simply Supported-Simply Supported Beam.

Table 4.

Theoretical and Measured Resonances for the Beams Under Test.

Support Type	f_1 (Hz)	f_1 (Hz)	f_2 (Hz)	f_2 (Hz)	f_3 (Hz)	f_3 (Hz)
Simply Supported	252.50	244	1010.52	948	2274.31	N/A
Fixed-Free	230.41	156	1440.05	1152	4038.67	N/A
Fixed-Fixed	223.19	204	614.76	568	1205.60	1092
Fixed-Hinged	233.15	232	756.98	712	1574.53	1460
Key		Theoretical	Measured			

Sensor Construction

Once the sensor layout had been analytically determined and the beam lengths experimentally verified, the PVDF sensors had to be constructed. The shaping process can be performed using one of several methods. The first method is to cut the PVDF into its desired shape with a razor blade, scissors, or a form of precision cutting

laser. This method was used by Zahui et al. (2001a) and proved to be somewhat inaccurate. The second method was to electrically cut the film (AMP, 1994). In this process, the ground of a nine volt battery is connected to the surface of the PVDF, and the positive lead of the battery is connected to a wire that comes to a sharp point and is used to trace the sensor shape (Figure 57). While tracing the sensor shape, the voltage of the battery is passed through the PVDF and the material on the surface of the PVDF is “melted” away, thus producing an isolated shape that is to be used as a sensor. This method proved to be a clean and effective approach to sensor shaping except the sensor shape was hard to see after it was formed due to the fine point on the electrode. However, the third method is etching the surface with a dilute solution of printed circuit board solution (ferrous chloride). This process was developed by Johnson and Elliott (1993). Through personal communications with Dr. Steve Elliott (2000) of the Institute for Sound and Vibration Research at the University of Southampton, U.K. and consulting with Dr. John Miller (2000) in the chemistry department at Western Michigan University, it was found that the process used for etching the PVDF is very much like that used for etching electrical circuit boards. In the electrical circuit board etching process, the area that is to carry a current is marked off. Then, the etching solution is applied to the unmasked material. The solution removes the unmasked material, forming an accurate sensor shape. Unfortunately, the PVDF etching process had not been used at Western Michigan University before. Experimentation was required to perfect an effective etching process for sensor formation.



Figure 57. Battery and Leads Used for Surface Sensor Shaping.

In the process of constructing the PVDF sensors, the PVDF had to be adhered to the surface of the beam. This could be achieved using one of two methods. The first method was to use double-sided tape, and the second method was to use a glue or epoxy. One of the advantages to using the glue or epoxy was that the sensor could be repositioned without harming the sensor before the adhesive hardened. However, when using a glue or epoxy, caution had to be used so that the PVDF was electrically isolated from the structure. On the other hand, by using the tape, the sensor was to be isolated from the structure as the tape added a membrane layer between the beam and the sensor. Therefore, it was better to use the tape as long as the sensor could be positioned properly. Consequently, since it was possible to etch the sensor shape with the PVDF already mounted on the beam, the errors associated with locating the sensor on the structure were minimized.

Preliminary Experiments

Before constructing any surface sensors, some experiments were conducted in order to characterize the behavior of the PVDF when it was formed. This experiment was conducted using a wooden ruler as a beam and using different PVDF configurations. For example, the first experiment that was run involved applying a

rectangular piece of PVDF to the surface of the ruler (Figure 58). The ruler was then excited with a shaker, and the resulting beam characteristics were measured for a frequency range from zero to 800 hertz (Figure 59). Then, the PVDF on the ruler was etched to half of its original length (Figure 60). The PVDF behavior was once again measured for a frequency range from zero to 800 hertz when the ruler was excited by the shaker (Figure 61). After the etched PVDF was measured, it was cut with a razor knife along the etched line (Figure 62). Again the ruler was excited by the shaker, and the behavior of the PVDF was measured for a frequency range from zero to 800 hertz (Figure 61). The reason for cutting the PVDF at the etched line was to prove that the etching had indeed had an effect on the PVDF. Therefore, the results of this set of tests confirmed that the PVDF could in fact be formed into the desired sensor shape.



Figure 58. Ruler With Full Length Piece of PVDF.

In addition to examining the chemical etching process, the method of electrically forming the PVDF was also examined. In this set of tests the piece of PVDF that had been chemically etched in half was electrically separated in half again (Figure 63). The ruler was excited and the PVDF behavior was measured for a frequency range from zero to 800 hertz (Figure 64). Then, once the PVDF behavior was documented, the PVDF was physically cut at the same point that the electrical cut was made (Figure 65). Now with one quarter of the original length actually being

measured, the beam was excited again. The PVDF behavior was once again measured

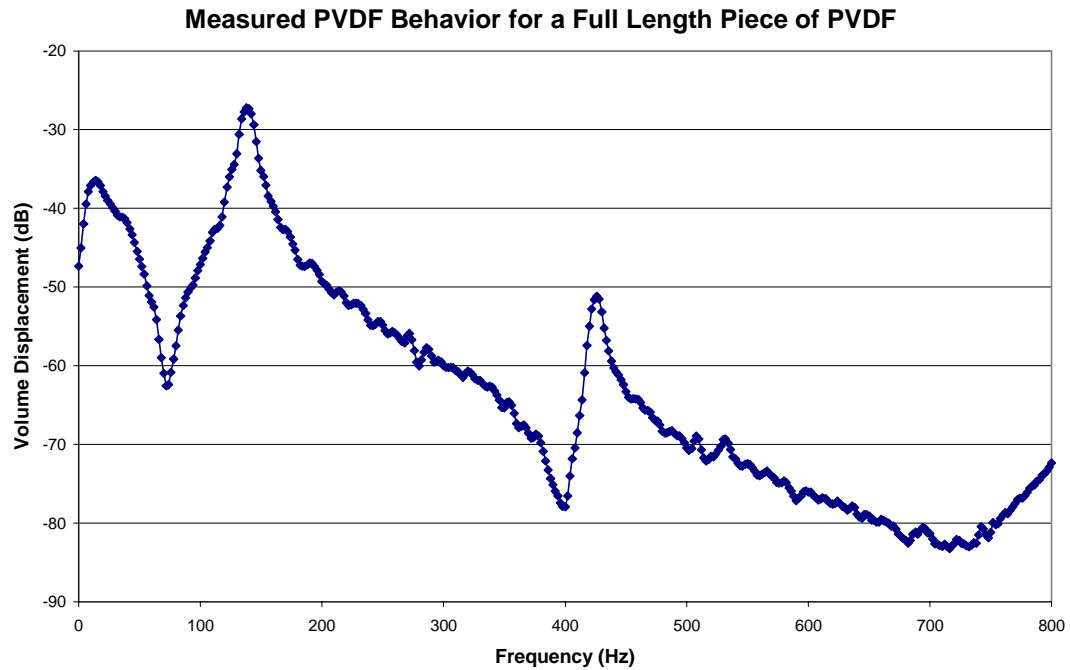


Figure 59. PVDF Behavior for the Full Length Piece of PVDF.



Figure 60. Etched PVDF Sensor.

for a frequency range from zero to 800 hertz and compared to the behavior measured when the PVDF was electrically cut (Figure 64). The results showed that the PVDF behaved as if it had been actually cut when it was electrically etched, therefore proving that this was also a viable option for etching the surface sensors.

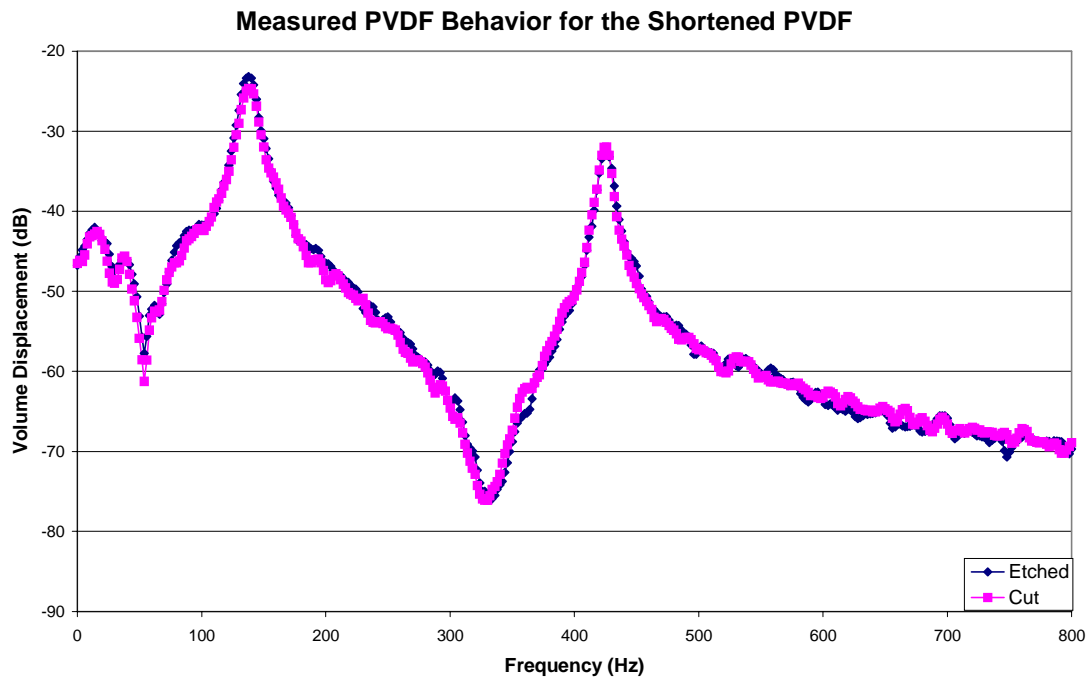


Figure 61. Chemically Etched and Cut PVDF Volume Displacement Measurement.



Figure 62. Cut PVDF Sensor.



Figure 63. Electrically Cut PVDF Sensor.

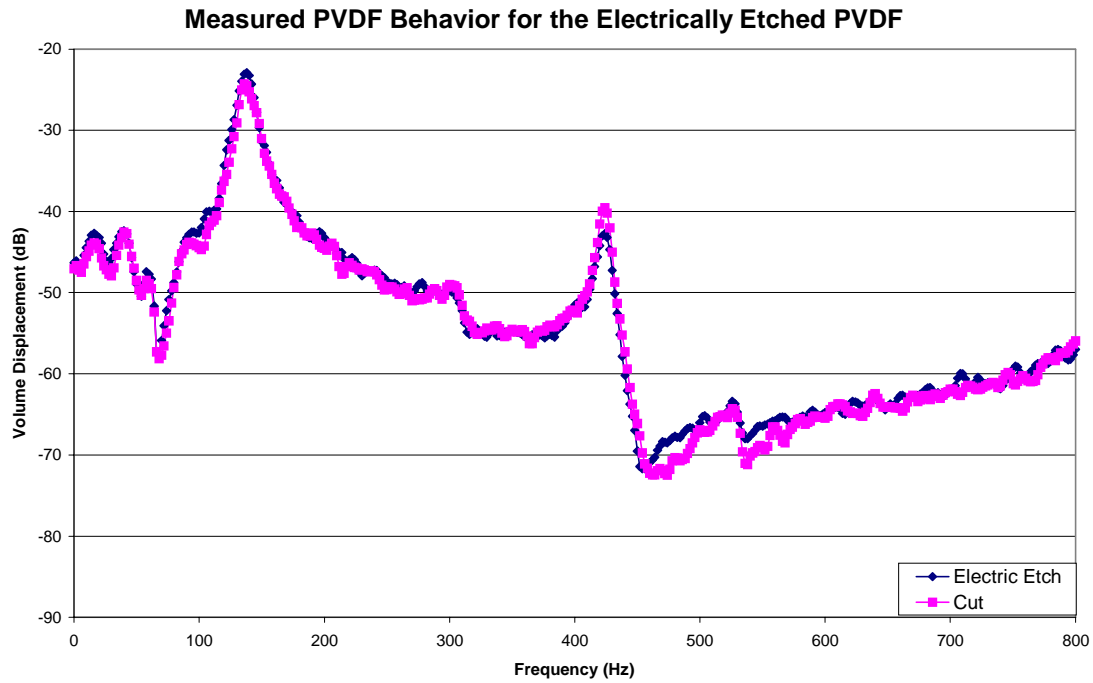


Figure 64. Electrically Cut and Physically Cut PVDF Volume Displacement Measurement.



Figure 65. PVDF Physically Cut at the Electrically Etched Location.

Understanding the PVDF etching process more, a procedure for forming and constructing surface sensors from PVDF was developed. The first step in the sensor formation process was to formulate the sensor shape equation, $F(x)$, based on the beam's dimensions and material properties. The next step was to program the sensor shape equation into MATLAB such that it would generate a plot of $F(x)$ and $-F(x)$ on the set of coordinate axes. This plot was then scaled in such a way that when it was printed, it would be on a one to one scale with the beam of interest. After the scaled

plot was printed, it was carefully cut out with a razor blade, thereby producing a traceable template (Figure 66).



Figure 66. Traceable Sensor Shape Template.

The third step in the sensor construction process was to clean the surface of the beam where the sensor was to be applied. This cleaning process includes the removal of any dirt or residue on the surface with white board cleaning solvent and, the removal of any deformations or discontinuities with a razor blade. Once the surface was cleaned, a layer of 0.0381 meter (1.5 inch) wide double-sided tape was applied to the surface. The tape was applied carefully so that no bubbles or wrinkles were formed on the surface. After the tape was in place, it was trimmed to the effective length of the beam of which was to be measured. The next step after applying the tape was to apply a layer of PVDF to this tape (Figure 67). When applying the PVDF, care was used again to prevent the formation of bubbles and wrinkles.



Figure 67. Applying the PVDF to the Taped Surface.

Once the PVDF was in place and the sensor template was made, the template was taped in place over the PVDF (Figure 68). Then, a black permanent marker was used to trace the shape of the sensor onto the PVDF (Figure 69). Next, the marker was used to fully shade in the area of the sensor and a lead which was used for making the necessary electrical connections to the sensor (Figure 70). The area that was shaded was to be the effective area of the sensor which was to be used for making the beam volume displacement measurements.



Figure 68. Template Taped in Place Over the PVDF.



Figure 69. Black Marker Being Used to Color in an Electrical Lead on the Sensor.

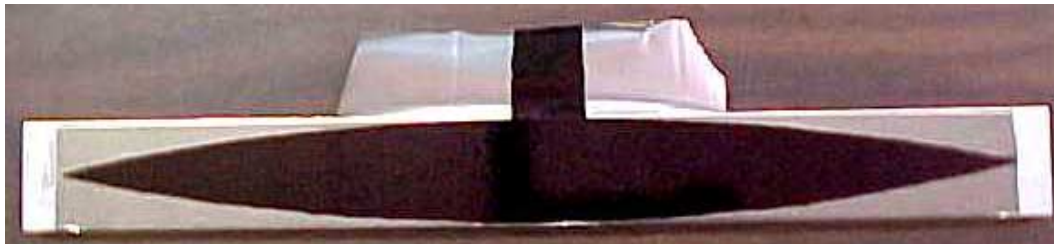


Figure 70. Shaded Sensor Shape and Lead Before Etching.

The next step after the shading was completed was to use a foam brush to apply a small amount of Radio Shack Printed Circuit Board etchant along the edges of the shaded sensor shape (Figure 71). This etchant solution, once in contact with the unprotected PVDF, removes the surface layer of the PVDF and results in an etched sensor shape. The excess etchant solution on the surface was later removed by drying it with a soft cloth or towel (Figure 72). At this point the sensor could be used; however, the sensor would be colored in with marker, and the condition of the sensor surface would not be known (Figure 73). Therefore, it is recommended that the marker be removed from the surface. The marker removal was achieved by using a soft cloth and applying isopropyl alcohol (rubbing alcohol) to the surface (Figure 74). By cleaning the surface with the alcohol, the sensor that remains can be inspected for scratches and discontinuities which indicate that the sensor is bad. At this point, the beam can be placed in the test fixture and preparation can be made to begin testing.

Once the inspected beam had been placed in the test fixture and in the baffled box, the electrical leads had to be attached to the sensor. This was completed by soldering copper leads to a shielded wire which was used to protect against outside noise, such as the 60 and 120 Hz signals generated by electrical currents. The other end of the shielded wire contained a BNC connector which was used to connect the sensor to the TEAC DAT recorder and from there, connected to the HP analyzer. Once connected to the HP analyzer, the sensor was ready to take measurements. Therefore, the only remaining steps in testing a surface sensor are to place the

accelerometers at the ends of the sensors and to excite the beam with the shaker (Figure 75).



Figure 71. (Left) Etchant Being Applied With a Foam Brush.
(Right) Etchant After Application.



Figure 72. Removing the Excess Etchant Solution With a Soft Cloth.

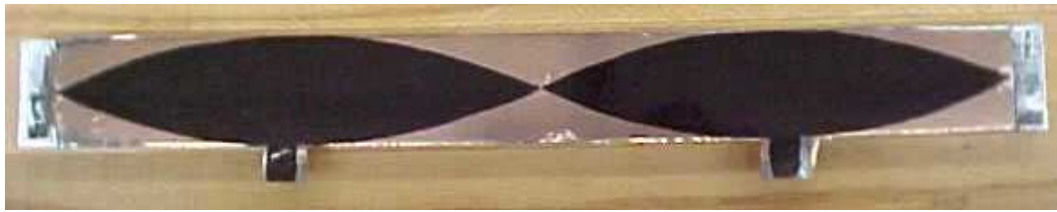


Figure 73. Etched Sensor.



Figure 74. Isopropyl Alcohol Being Used to Remove the Marker.

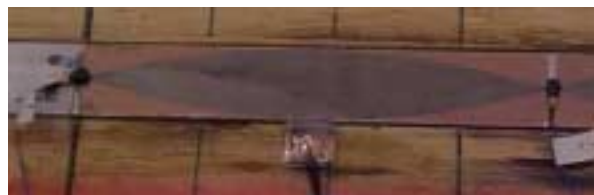


Figure 75. Finished Sensor With Accelerometers.

CHAPTER IV

VOLUME DISPLACEMENT MEASUREMENTS

Localized PVDF Sensor Verification Process

With the PVDF sensor construction process developed, it was necessary to verify that the integrated PVDF and accelerometer sensors correctly measured the beams' volume displacement. The process used for verifying the integrated sensors included measuring the local and total volume displacements for a given beam with different integrated sensors. After comparing the integrated sensor volume displacement measurements, a set of accelerometer measurements (predicted) were taken at finite points, and the volume displacement was again calculated and compared to the local and total integrated sensor measurements. However, for the purpose of active control, measuring the magnitude of the volume displacement is not as important as sensing the frequencies at which the maximum volume displacements occur. Thus, the measurements made by the local sensors are considered sufficient for control purposes if the resonances (maximum volume displacement) for both the predicted and actual measurements coincide with respect to frequency. Finally, the sound power of the beam being examined was measured and compared to the theoretical sound power calculated using the volume displacement.

The first step in the verification process was to develop a baseline; therefore, the first sensor constructed was a total sensor. This total sensor was used to measure the volume displacement over the entire surface of the beam. After measuring the

beam's volume displacement, the raw data, in volts, as output by the PVDF charge and the accelerometer were collected with the dynamic signal analyzer had to be processed. In the processing of the raw data, a correction factor needed to be applied to the data, which converted the data from a volt per volt measurement to a volume per unit force measurement. In achieving this unit conversion, the first step was to multiply the raw data by the calibration factor for the force gauge. This correction factor was 51.5 mV/lb_f (manufacturer's calibrated value). However, since the metric unit system measurement was desired, the correction factor had to be divided by a conversion factor of 4.448 N/lb_f. Thereby, a final correction factor of 0.1164 V/N was produced.

By applying this correction factor, the new units on the calculation became volts per newton, so another conversion factor was necessary to form the units of cubic meters per newton. To account for the volume portion of the measurement, it was recalled that the total charge (q) was proportional to the total volume displacement (D). Therefore, if the measured PVDF voltage was converted to a charge (q), the charge could be set equal to the volume displaced. As a result, the voltage measurement was divided by the internal resistance of the dynamic signal analyzer, which was measured to be 1.006 M Ω , and a measure of the current resulted. This measure of current was in reality equal to the charge, as current is actually a measure of charge flowing per second. Thus, the final correction factor accounting for both the volume displaced and the excitation force for all the PVDF measurements was $1.157 \times 10^{-8} \text{ m}^3/\text{N}$.

Additionally, when the total volume displacement is measured by the PVDF, it was found through experimentation that the measurements taken by the accelerometers on the ends of the sensor are insignificant for the fixed-fixed, fixed-simply supported, and simply supported-simply supported end conditions. In other words, the expression in Eq. (34) containing the accelerometer measurements can be ignored as their effect on the measurement in these cases was minimal (Figure 76). Upon further investigation, it was realized that those accelerometer measurements should be insignificant as they are positioned such that they are taking measurements at locations where ideally there is no movement (fixed and simply supported end conditions). The reason these measurement locations are ideally motionless is due to the beam end conditions. Thus, for all cases where a simply supported or a fixed end condition were at the end of a sensor, the accelerometer measurement at that point was deemed insignificant and the total volume displacement (D) was measured strictly with the PVDF sensor.

The second step in verifying the PVDF sensors was to construct the localized sensors. The localized sensors varied in length as the beam lengths were not all identical, and the sensor sizes were determined by dividing the beams into halves and thirds. So, the resulting sensor lengths were related to the effective length of the beams as opposed to being a predetermined length. Also, the local sensor measurement required that the accelerometer data be incorporated into the local volume displacement (\hat{D}). The accelerometers were required now as the local

surface sensors utilized measurement points that were no longer at the ends of the beams.

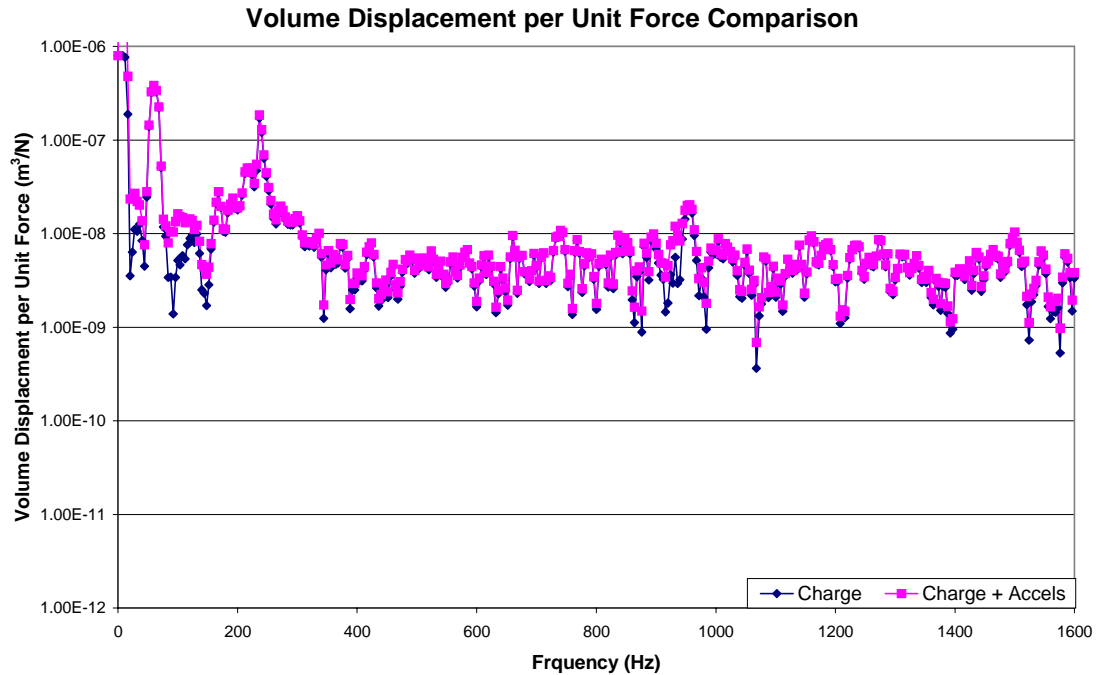


Figure 76. Volume Displacement Comparison With and Without Accelerometers.

When including the accelerometer measurements, an additional correction factor was needed. This new correction factor was used in conjunction with the one used for the total PVDF sensors. This additional correction factor was also used to account for the accelerometers and resulted from calibrating the accelerometers. In the calibration process, the accelerometer was excited with a known acceleration of 10 m/s^2 at 1000 Hz, and the number of millivolts present at 1000 Hz was measured. After taking the measurement, a ratio of the measured millivolts was created with the excitation acceleration. The ratio calculated was then multiplied by the voltage measured using the accelerometer while testing the localized PVDF sensor. This resulted in a unit

conversion from volts to a unit of acceleration in m/s^2 . Then, by multiplying the first half of Eq. (34) by the correction factors for the accelerometer and the force gauge a measure of volume displaced per unit force in m^3/N was obtained. Then, after the localized volume displacement had been measured for each of the localized sensors that comprised the entire length of the beam, the total volume displacement was calculated by summing the local volume displacement of all the sections of the beam. This compiled total volume displacement was then compared to the total volume displacement which was directly measured by the total PVDF sensor, thus, producing the first confirmation that the local sensors were measuring the data accurately.

Continuing the verification process, a series of accelerometer measurements was taken to verify that the local and total PVDF sensors are accurately measuring the beam volume displacement. A series of accelerometer measurements was taken along the center line of a vibrating beam. These measurement points were spaced at an increment of two centimeters apart along the entire effective length of the beam (Figure 77). Since each beam had a different length, the number of data points measured changed with the beam end conditions tested. These accelerometer measurements were converted to a measure of volume displacement through the use of the trapezoidal rule of integration. By using the trapezoidal rule of integration, the volume per width of air moved along the center line of the beam can be quantified. By multiplying the volume per width moved by the beam width, the volume of air moved can be obtained (i.e., volume displacement). Thus, the general form of the

trapezoidal rule expression for the volume displacement of the localized or total PVDF surface sensor area would be:

$$\hat{D} = \frac{-(c-a)b}{n(2\pi f)^2} [0.5\ddot{Z}(a) + \ddot{Z}(x_1) + \ddot{Z}(x_2) + \dots + 0.5\ddot{Z}(c)], \quad (71)$$

where a and c are the sensor end points, n is the number of finite divisions between points a and c , f is the frequency of a particular measurement, and \ddot{Z} is the accelerometer measurements at the two centimeter finite divisions. This volume displacement calculation can be considered accurate since care was taken to ensure that the stinger connected to the shaker driving the beam is threaded into the beam at the midpoint of its width. Therefore, by driving the beam along its centerline, the deflection throughout the beam width is considered to be uniform. Thus, the volume displacement calculated by the trapezoidal rule can be compared to the volume displacement measured by the PVDF sensors. This comparison will act as a second verification that the localized PVDF sensors are measuring these values accurately.



Figure 77. Simply Supported Beam Marked at Every Two Centimeters.

The final verification method used was to compare the measured sound power radiated from the beam to the theoretical sound power that was calculated from the total volume displacement. The reason for comparing both the total volume displacement per unit force and the sound power measurements is that at low

frequencies, the total sound power radiated into the far field by a baffled vibrating surface is proportional to the squared magnitude of the volume displacement of the surface (Rex, 1991). Therefore, it is possible to calculate this sound power and confirm the validity of the sensor through the use of the volume displacement in the following equation:

$$W = \frac{\omega^4 \rho_o}{4\pi c} |\tilde{V}|^2, \quad (72)$$

where W is the sound pressure, ω is the circular frequency in rad/s, c is the speed of sound, ρ_o is density, and \tilde{V} is the complex volume displacement. With the sound pressure calculated, the sound power can be computed by:

$$dB_{power} = 10 \log_{10} \left(\frac{W}{10^{-12}} \right), \quad (73)$$

where dB_{power} is the sound power level (Lord et al., 1987). However, when comparing the sound power data, caution had to be used to ensure that the major contributions to the total sound power radiated were strictly from the beam. Therefore, the difference in vibration between the beam and the baffled box top was measured. By quantifying the vibrational difference, it was possible to show that the box top vibration was not a significant contributor to the total measured sound power from the box.

Volume Displacement Experiments

In order to verify the accuracy of the integrated sensors designed, a sequence of experiments was conducted. This sequence included testing the fixed-fixed, the fixed-free, the fixed-simply supported, and the simply supported-simply supported beam end conditions. Unfortunately, since each beam was a different length, the

sensors used in the verification process were unique as they all varied in length. However, even though each sensor shape and set of results obtained are unique, the steps taken in the analysis of the results is the same. For the sake of brevity, the full analysis for the fixed-fixed beam is presented here along with the data used to perform this analysis. However, only a discussion is given of the data acquired on other beam end conditions and the graphs and depictions of the data are given in Appendices C, D, and E. In all cases, the conclusions drawn and the problem encountered are similar to those discussed for a fixed-fixed beam.

Fixed-Fixed Beam

The fixed-fixed beam was the longest beam analyzed, so three different surface sensors were designed and tested on this beam. The first sensor was a single, total surface sensor which spanned from one fixed end to the other fixed end. Then, a second surface sensor, which was the first set of the localized sensors, was examined. This set of sensors was designed in such a way that each sensor measured volume displacement of one half of the beam's effective length. These two local sensors also shared a common intersecting point in the center of the beam where an accelerometer was located. Since both of these sensors were constructed from one long piece of PVDF, these sections were physically cut at their intersection (middle of the beam) so as to isolate the individual sensors from each other, thus preventing the possibilities of errors (Figure 78). Finally, a third set of local sensors was constructed that divided the beam into three equal lengths. These sensors contained the same general shape as the previous sensors except their individual length was shorter. The PVDF was again

cut to ensure these sensors were isolated from one another while sharing two common accelerometer points on the beam. Figure 79 depicts the different sensor shapes as they were designed for use on the fixed-fixed beam. Once the integrated sensor measurements were collected, the set of accelerometer measurements required for calculating the local and the total volume displacement from the trapezoidal rule were taken over 28 equally spaced points along the length of the beam. After the accelerometer and integrated sensor data was analyzed using Eq. (34), the volume displacement per unit force was plotted as a function of the excitation frequency. These results were compared to determine if the integrated sensor designed accurately measured the beam local and total volume displacement.



Figure 78. Localized PVDF Sensors After They Have Been Isolated From Each Other.

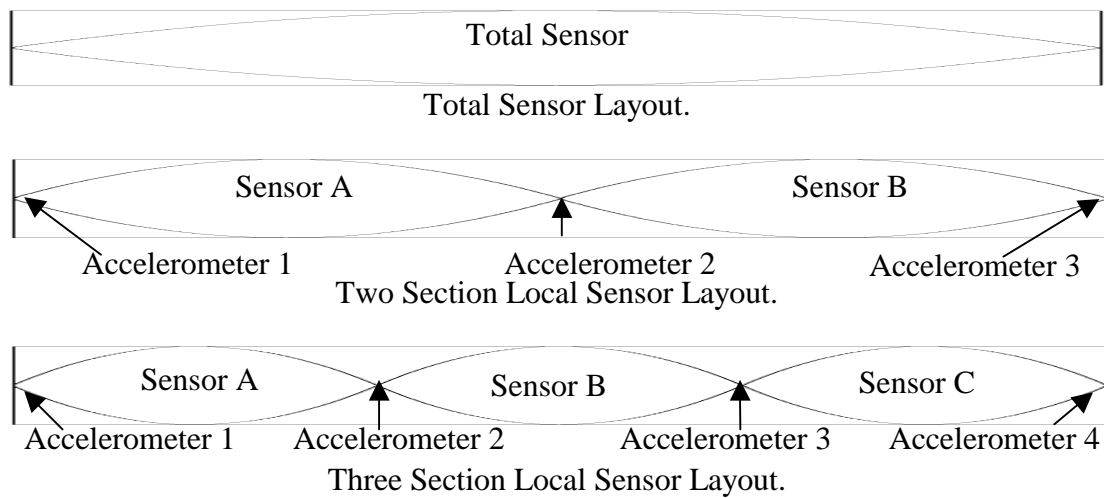


Figure 79. Sensor Shapes Used for the Total and Local Sensors.

The first set of plots constructed were for the two sectioned localized sensors. This set of plots included both the volume displacement per unit force and the phase of volume displacement as computed using Eq. (34), for both the accelerometer and the PVDF measurements of the left side and the right side sensors. Examining the volume displacement per unit force for the local sensor on the left side, section A, it was found that the frequencies at which the resonances occurred corresponded almost exactly for the accelerometer and the integrated sensor measurements (Figures 80). Additionally, when the phase measured by the accelerometer and integrated sensor were examined with respect to frequency, the results were found to behave in much the same manner (Figure 81). The only major difference between the two sets of data was that the magnitude of the volume displacement measured using the integrated PVDF and accelerometer sensors was higher than expected at frequencies above approximately 800 Hz. This error may be due to a poor signal-to-noise-ratio measured by the PVDF, so the power spectrum of the PVDF sensor was compared to background noise to ensure that a sufficient signal was measured (Figure 82). In checking the power spectrum, it was found that the signal was sufficiently above the background noise to be free of errors. As a result, the magnitude difference was considered to be real, and it was concluded that the PVDF sensor on section A was in fact measuring the beam's resonant response accurately. This dominant response is the main source of the sound power being radiated from the vibrating beam.

Similar to the left side sensor, the local sensor on the right side of the beam, section B, was examined. From the volume displacement per unit force and phase

plots (Figures 83, 84), it was again concluded that the sensor on section B was accurately measuring the behavior of the beam's movement. Like the sensor on section A, at frequencies above approximately 800 Hz, the magnitude of the accelerometer and the integrated PVDF and accelerometer sensor measurements varied as the integrated sensor was measuring a larger volume displacement than the accelerometers. Once again, the power spectrum was checked to see if the variations may have been the result of a bad PVDF measurement (Figure 85). However, the difference did not result from the PVDF sensor based on the signal-to-noise-ratio measured in the power spectrum. Therefore, having checked the most logical sources of the magnitude differences and not being able to fully explain these differences at this time, the local sensor on the right half of the beam was determined to be measuring the beam resonances precisely.

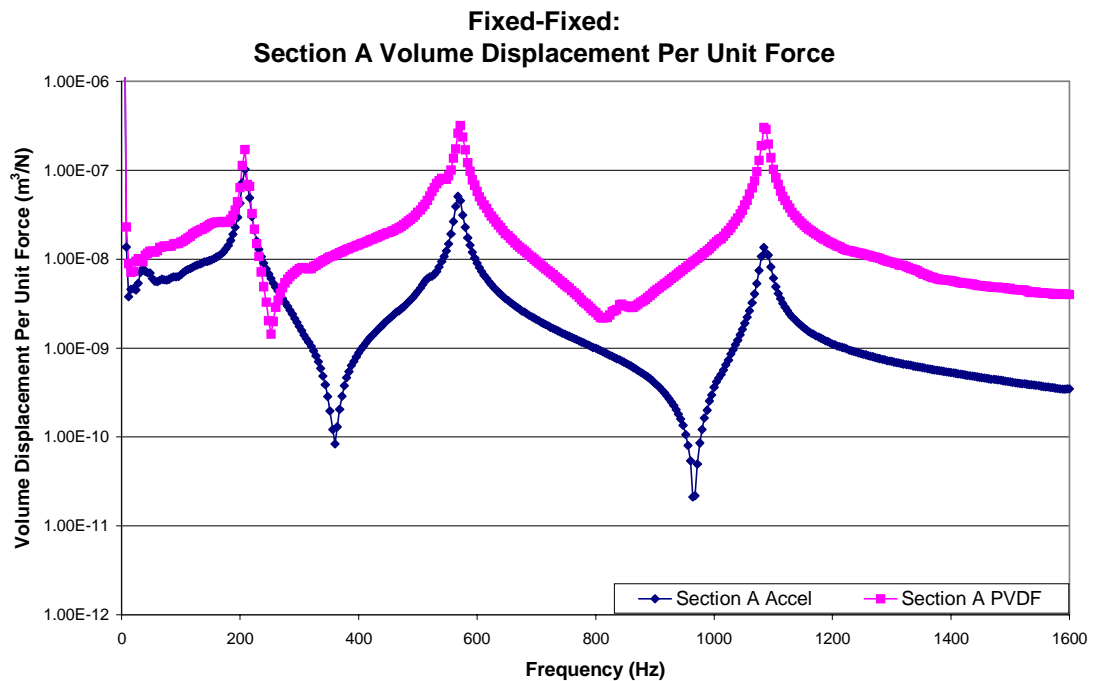


Figure 80. Fixed-Fixed Volume Displacement Magnitude for Section A of the Double Sensor.

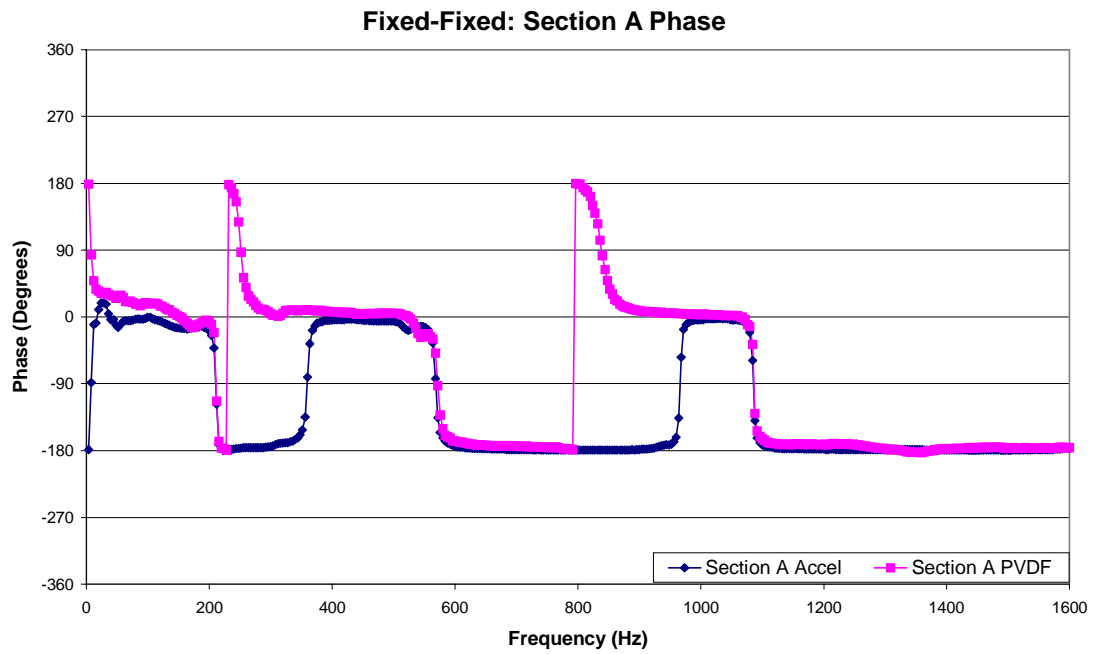


Figure 81. Fixed-Fixed Volume Displacement Phase for Section A of the Double Sensor.

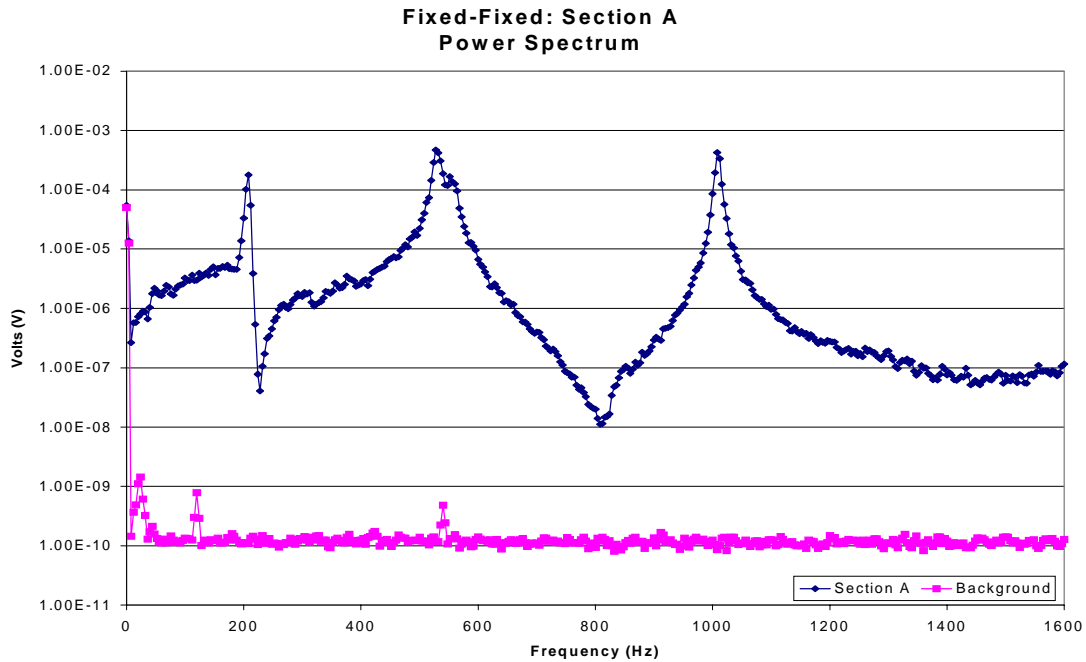


Figure 82. Power Spectrum for Section A of the Two Section Local Sensor.

The second set of plots was constructed for the data collected for the three section sensor. This data was plotted in the same fashion as the two section sensor data. In examining the extreme left hand local sensor, section A, it was found that the accelerometer and integrated sensor measurements were almost identical to those measured using discrete accelerometer measurements at frequencies below 800 Hz and that some discrepancies occurred at frequencies above 800 Hz (Figures 86, 87). However, there are two factors that can contribute to some of the discrepancies present. First, the phases do not match at the higher frequencies where the variations in the volume displacement occur. In fact, in some instances, the phases are almost a full 180 degrees different, signifying that the volume displacement measured by the

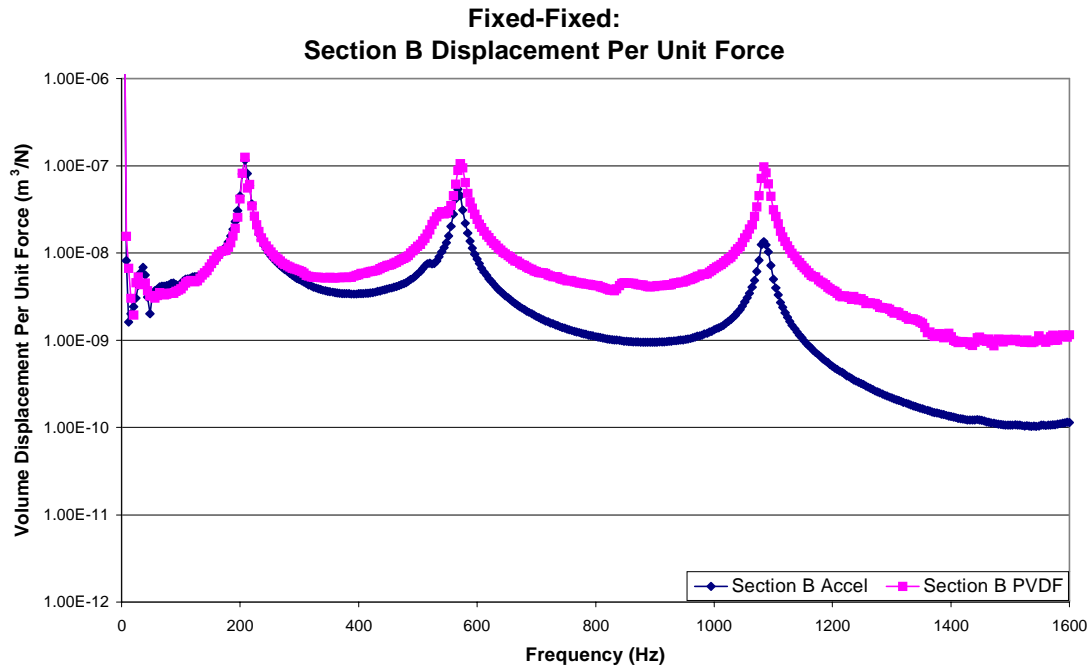


Figure 83. Fixed-Fixed Volume Displacement Magnitude for Section B of the Double Sensor.

two measuring devices is different. Also, the power spectrum for the PVDF sensor shows some low points where the signal measured is less than a factor of ten greater than the background signal. This weak signal may signify that the measurement includes erroneous data measured from an outside source. However, since the peaks that represent the resonances (the frequencies the radiate sound power most efficiently) are accurately measured, the sensor was concluded to be sufficient for sensing the frequencies at which the sound power should be reduced for the leftmost portion of the excited beam.

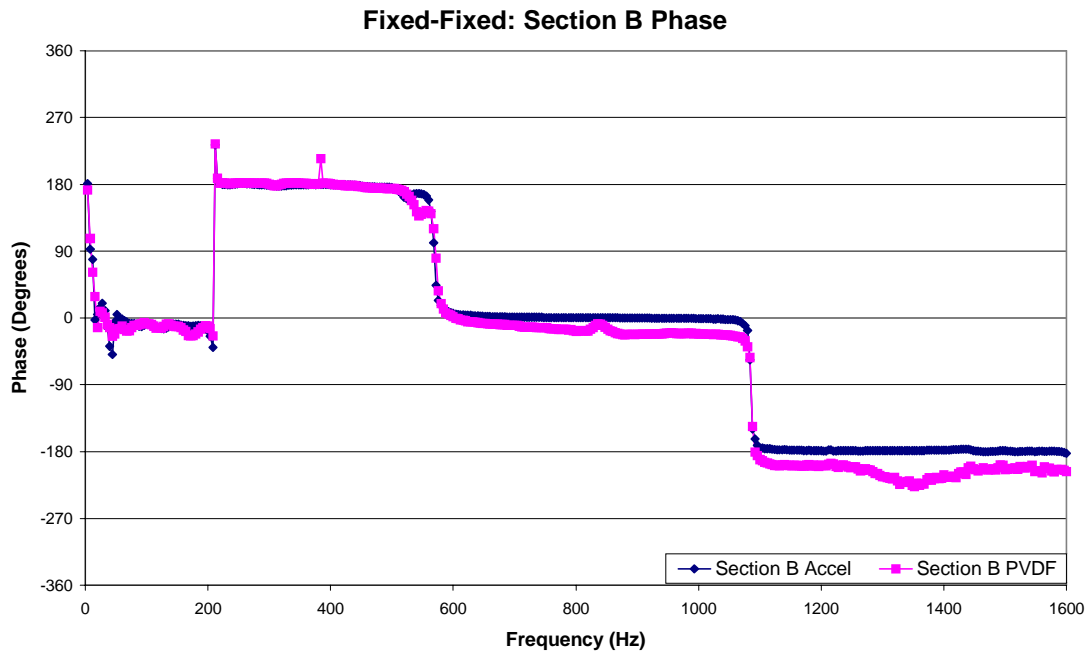


Figure 84. Fixed-Fixed Volume Displacement Phase for Section B of the Double Sensor.

Next, the middle integrated sensor, section B, was analyzed. The phase and the volume displacement per unit force were found to share the same trends in both the integrated sensor and accelerometer measurements (Figures 89, 90). However, like many of the previous integrated sensors, at the higher frequencies there is a magnitude variation the volume displacement per unit force measurements. In considering the source of the variations, the power spectrum was checked and found to be free from errors (Figure 91). Thus, the local PVDF sensor was considered to be sufficient for representing the behavior and the resonances of the middle portion of the beam.

The final local sensor analyzed was the sensor furthest to the right, section C. This data showed the best correlation of all the sensors examined, as the volume

displacement per unit force almost exactly matched a frequency of approximately 800 Hz for both the accelerometer and the integrated sensor (Figure 92). At the frequencies greater than 800 Hz, some variation occurred, but it was so small that it could be declared insignificant. Then, looking at the phase of the accelerometer and integrated sensor measurements, it was recognized that at frequencies greater than 800 Hz, the two data sets are out of phase (Figure 93). Thus, the phase could be contributing to the variations in the magnitude. However, the power spectrum for the PVDF sensor was also checked to insure that there was no contribution to the error as the result of a bad signal (Figure 94). Since the signal-to-noise-ratio was sufficient, the variation in the volume displacement per unit force was deemed acceptable, and the PVDF sensor was determined to sufficiently represent the behavior of section C of the three sectioned local sensor. Consequently, having examined each of the localized sensors that comprised this test individually, it was decided that the measurements taken by the PVDF did represent the behavior of the beam effectively.

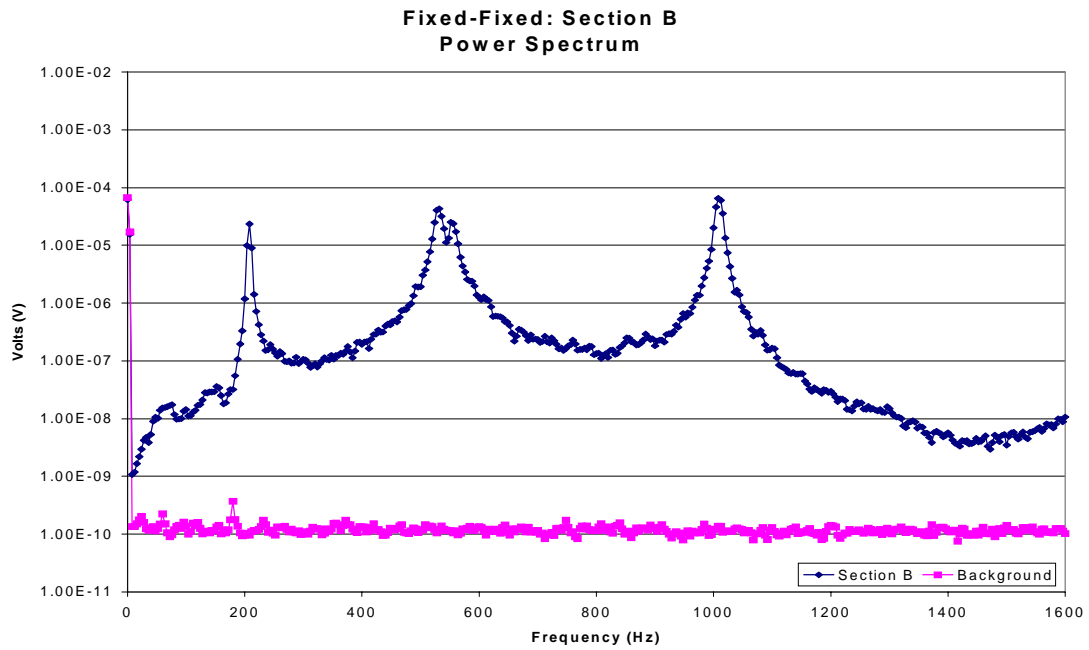


Figure 85. Power Spectrum for Section B of the Two Section Local Sensor.

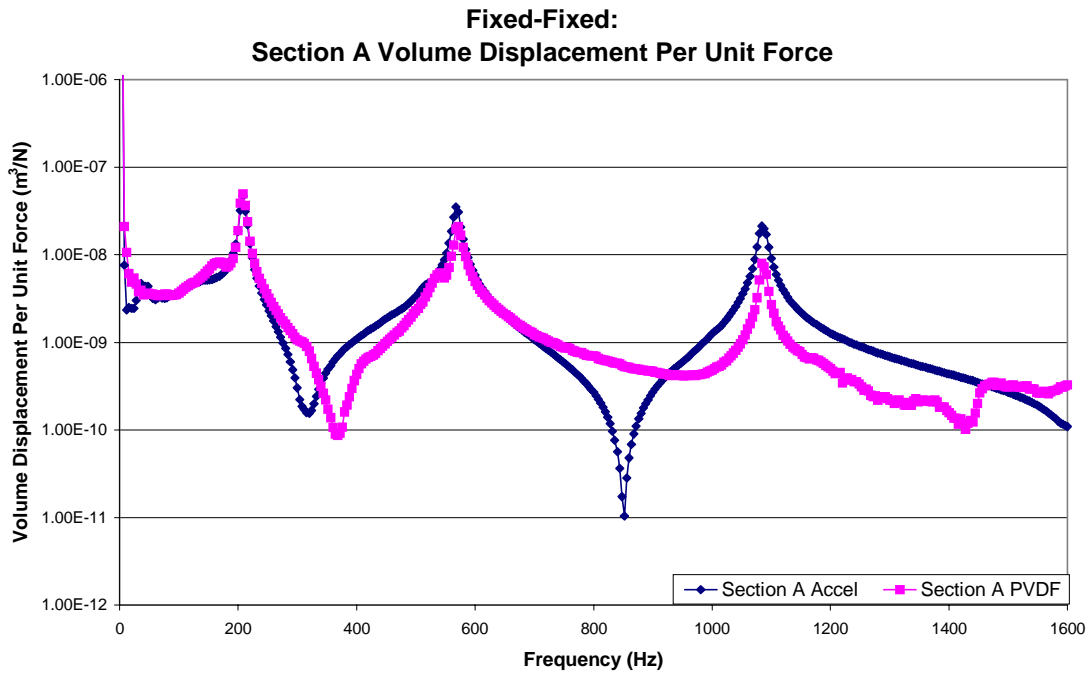


Figure 86. Fixed-Fixed Volume Displacement Magnitude for Section A of the Triple Sensor.

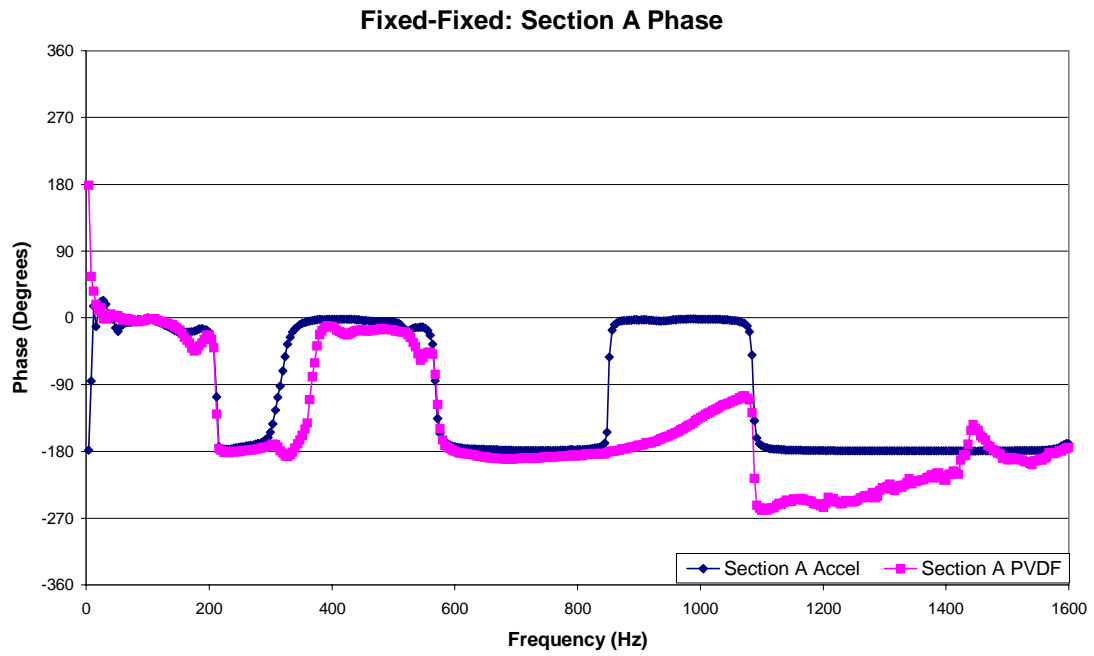


Figure 87. Fixed-Fixed Volume Displacement Phase for Section A of the Three Section Sensor.

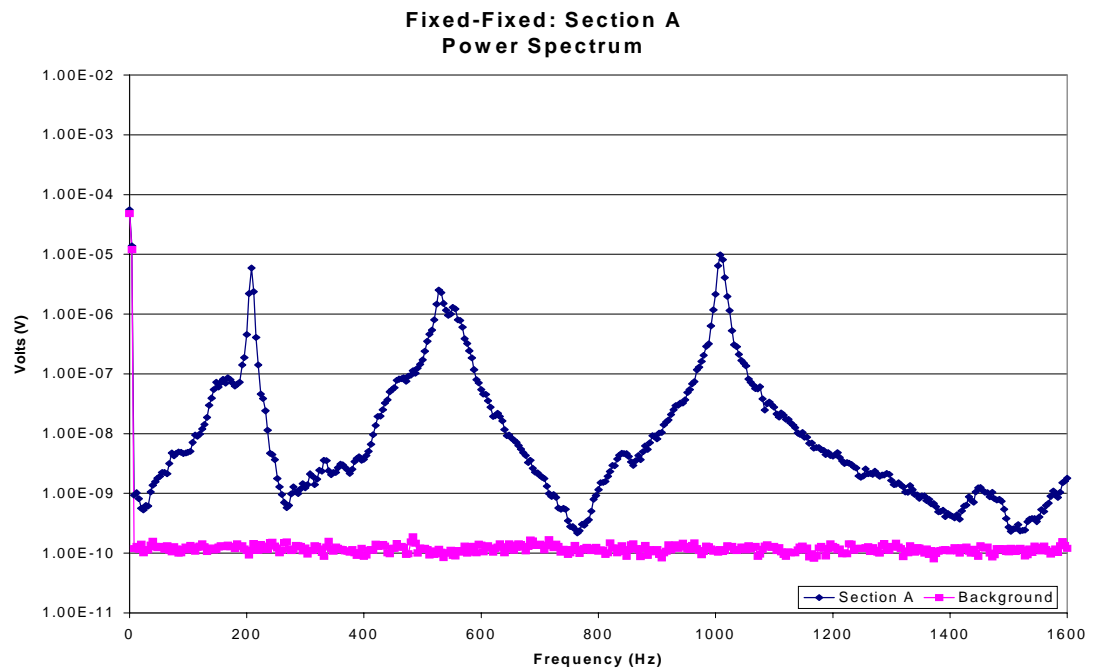


Figure 88. Power Spectrum for Section A of the Three Section Local Sensor.

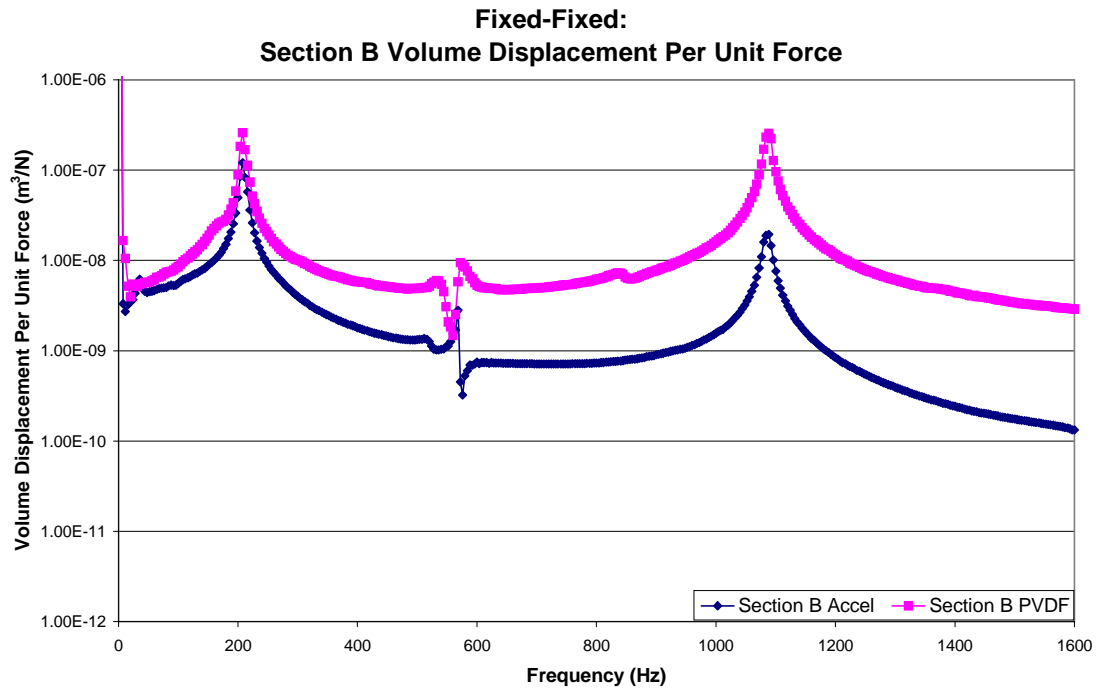


Figure 89. Fixed-Fixed Volume Displacement Magnitude for Section B of the Triple Sensor.

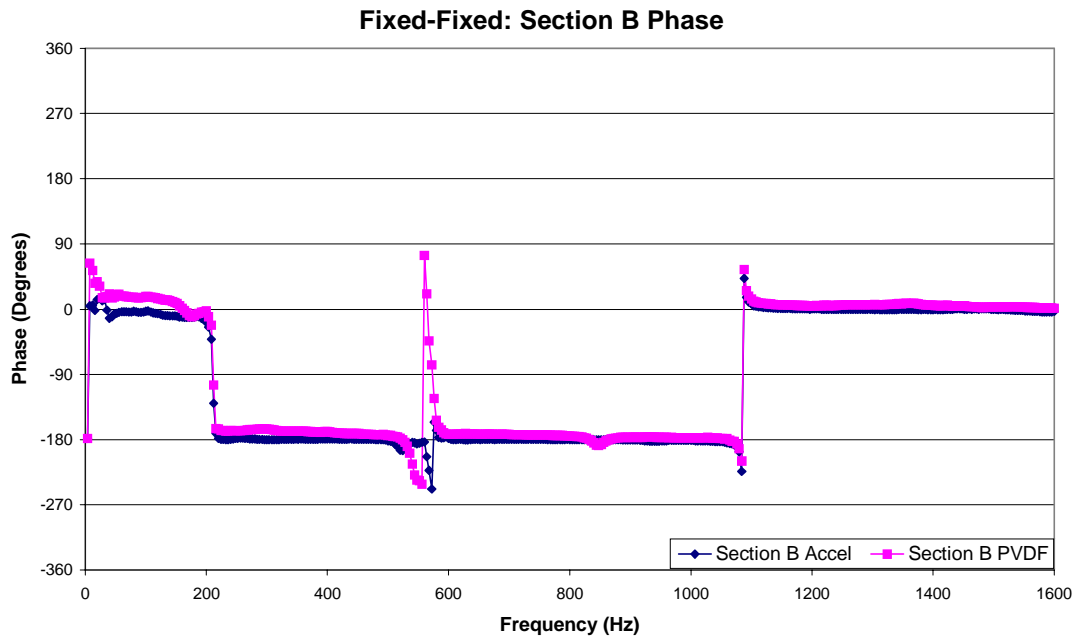


Figure 90. Fixed-Fixed Volume Displacement Phase for Section B of the Three Section Sensor.

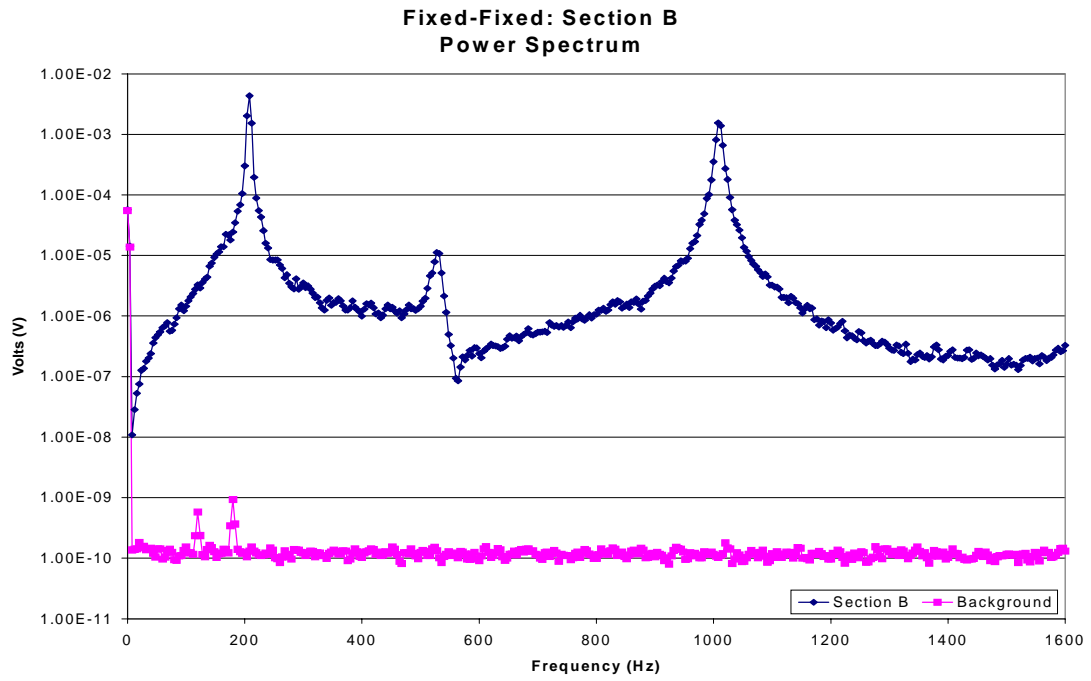


Figure 91. Power Spectrum for Section B of the Three Section Local Sensor.

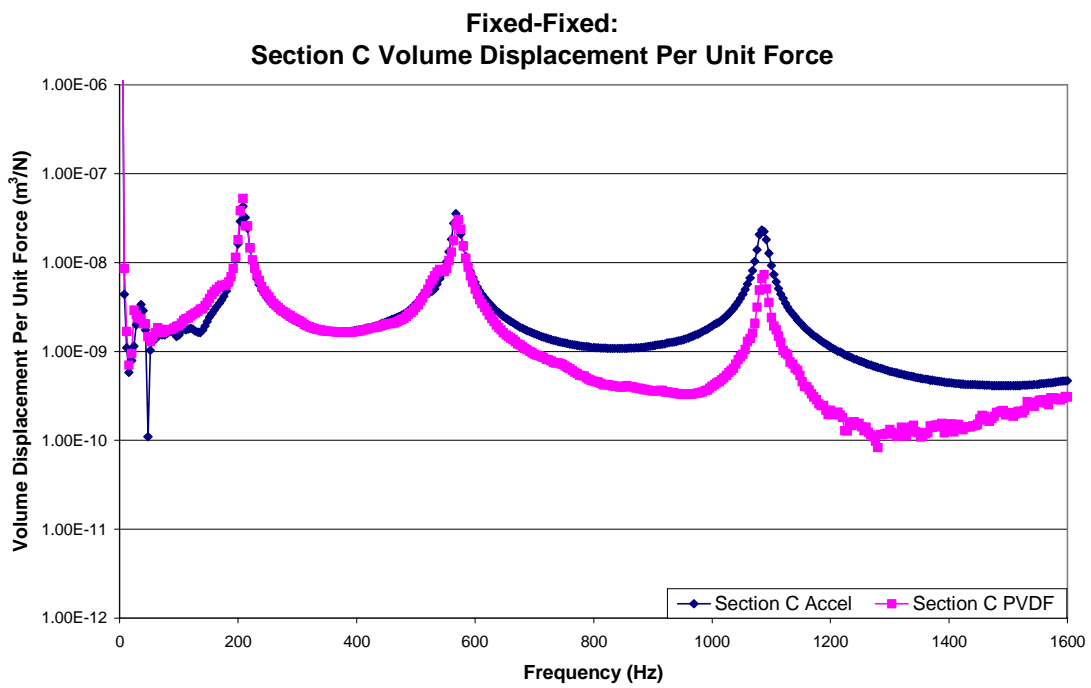


Figure 92. Fixed-Fixed Volume Displacement Magnitude for Section C of the Triple Sensor.

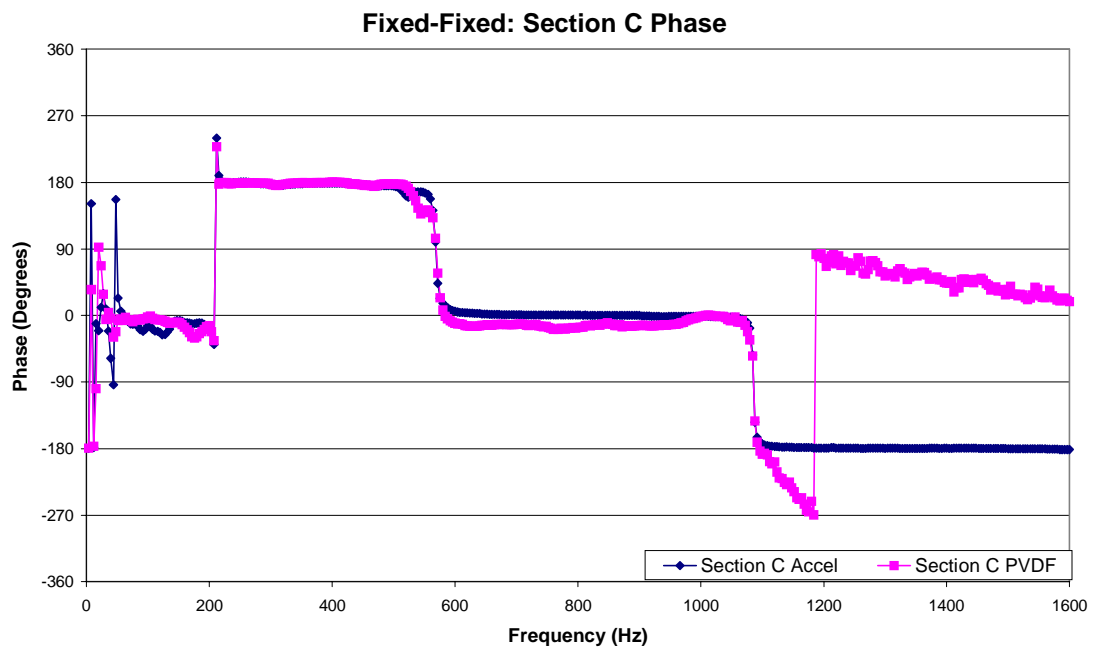


Figure 93. Fixed-Fixed Volume Displacement Phase for Section C of the Three Section Sensor.

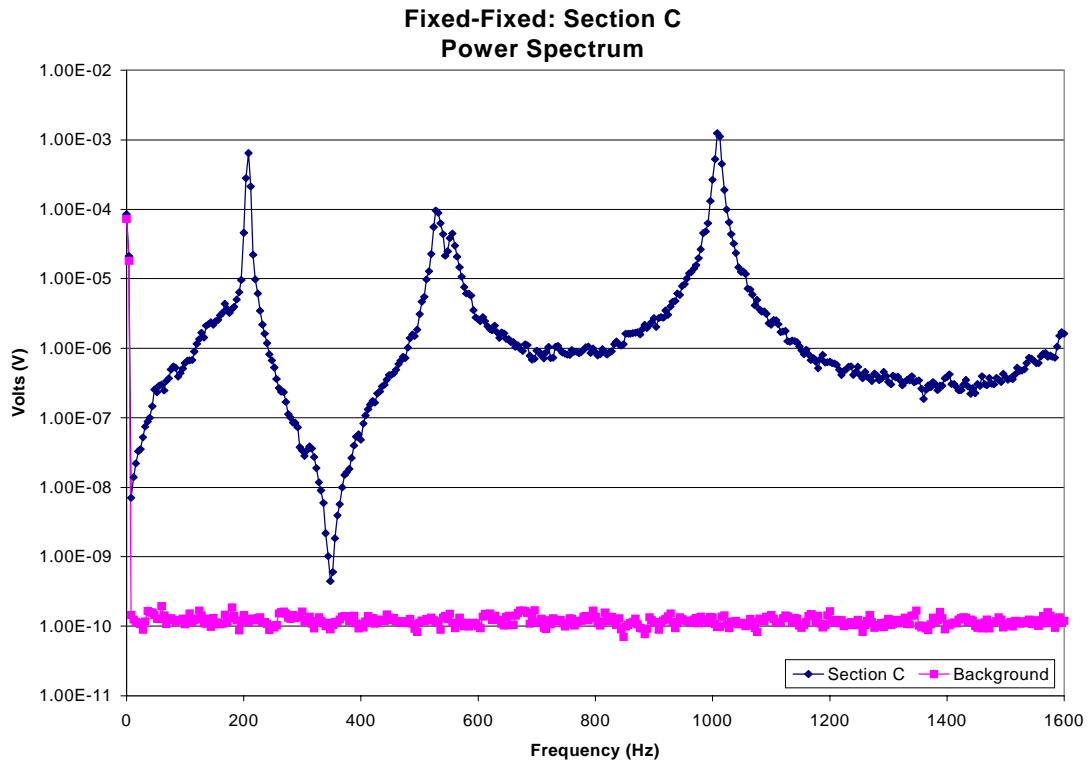


Figure 94. Power Spectrum for Section C of the Three Section Local Sensor.

Finally, a set of plots was constructed that compared the total volume displacement per unit force. These plots included measurements from the accelerometer, the total surface sensor, and the two sets of localized integrated PVDF and accelerometer sensors (Figures 95, 96). Comparing the volume displacement per unit force measurements, the observations showed that the accelerometer measurements predicted a lower volume displacement than the integrated sensor measured at frequencies greater than the first resonance. However, even though the predicted magnitude was lower, the frequencies at which the anti-resonances and resonances occurred are still aligned. Therefore, the many deviations that occurred in the phase of the integrated sensor in comparison to the accelerometer and the

possibility of erroneous data in the power spectrum will be the major contributors to the magnitude variations. Investigating the power spectrum for the total sensor, it was found that the signal measured by the PVDF was more than strong enough to be free from errors (Figure 97). As a result, if the magnitude differences are concluded to be insignificant, the total and local PVDF sensors constructed for the fixed-fixed beam are considered to accurately depict the behavior of the beam for both global and localized measurements.

Fixed-Free Beam

The second set of sensors examined were for the fixed-free end condition, and since this was the shortest beam analyzed, only two different surface sensors were tested, one total sensor and one set of two localized sensors. First, the total surface sensor which spanned the entire length of the beam was tested. Since one end was

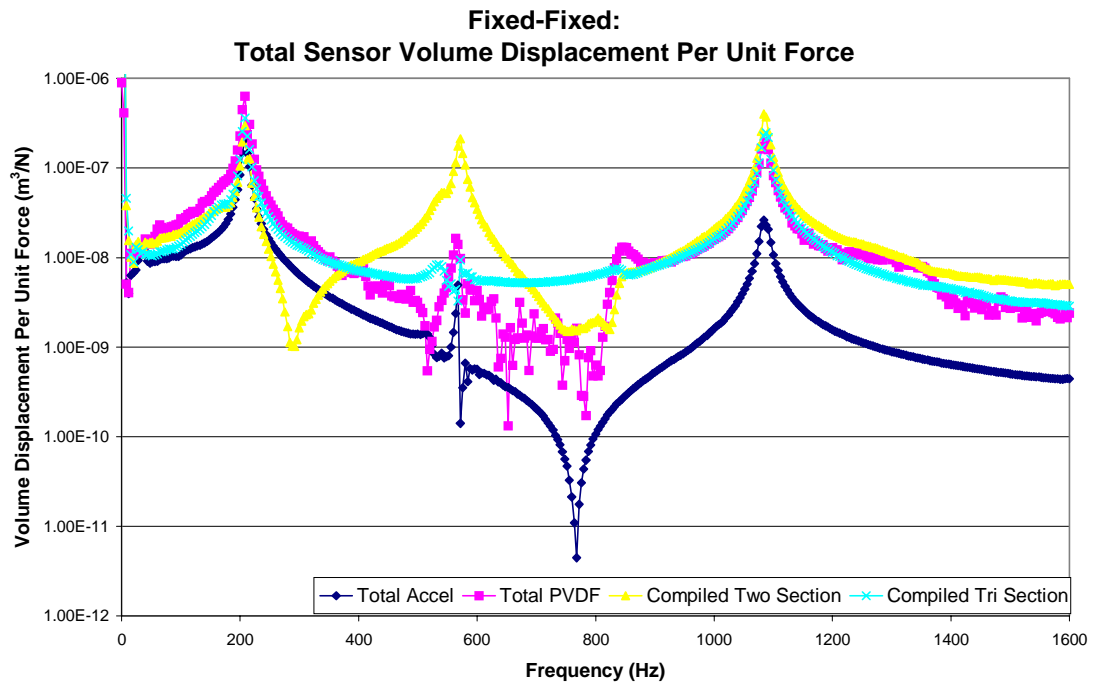


Figure 95. Fixed-Fixed Total Volume Displacement Magnitude.

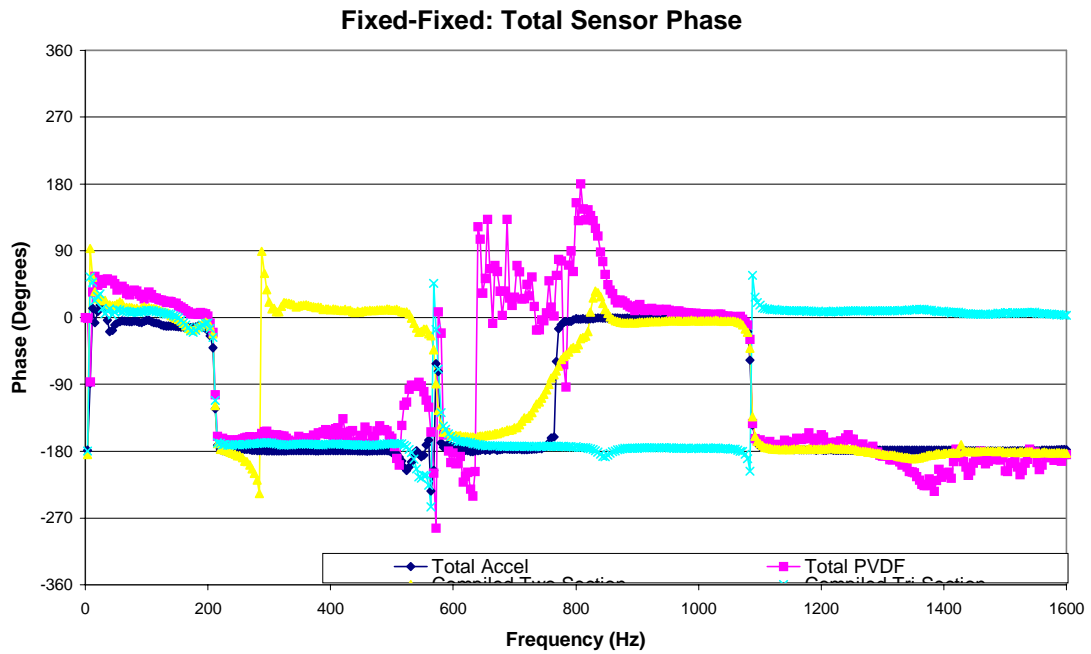


Figure 96. Fixed-Fixed Total Volume Displacement Phase.

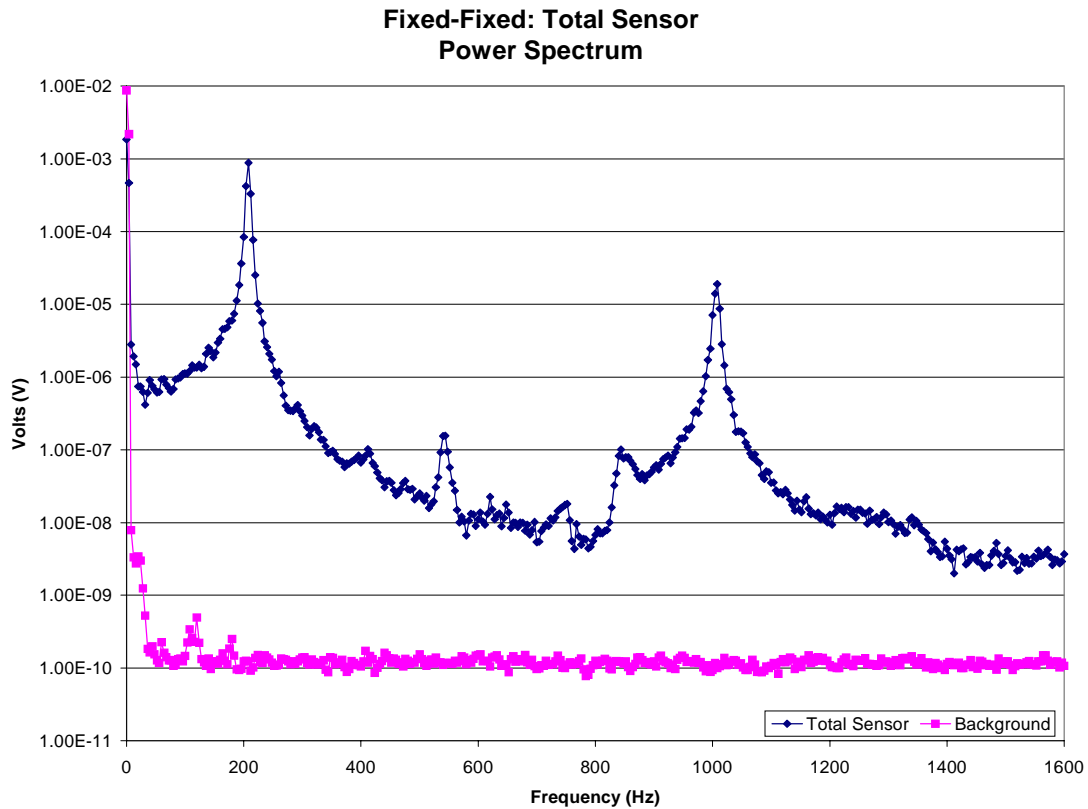


Figure 97. Power Spectrum for the Total Sensor.

free, an accelerometer was required at that end. Next, the set of localized surface sensors were examined. This set of sensors was designed in such a way that each sensor spanned one half of the beam's effective length. These individual local sensors then shared a common intersection at the midpoint of the effective length of the beam where an accelerometer was located, just as in the case of the fixed-fixed beam. The PVDF also had to be cut so as to insure that the individual PVDF sensors were isolated. Figure 98 depicts the different sensor shapes used, as they were specifically designed for use on the fixed-free beam. Once the integrated PVDF and accelerometer sensor measurements were taken, the set of accelerometer measurements necessary for calculating the volume displacement were taken along

the centerline of the beam. Then, the integrated sensor and the accelerometer volume displacement per unit force measurements were plotted as a function of frequency, and the results were compared (Appendix C).

During the data analysis, the volume displacement per unit force was plotted as a function of the excitation frequency for both the accelerometer and the integrated sensor measurements. The first set of plots generated from these measurements included the volume displacement and phase for the both the left and the right local sensors. Examining the volume displacement measured by the local sensor on the left side, section A, it was found that the accelerometer and PVDF measurements were almost identical in phase and magnitude. The few discrepancies that did occur in the volume displacement per unit force can be traced back to changes that occurred in the phase.

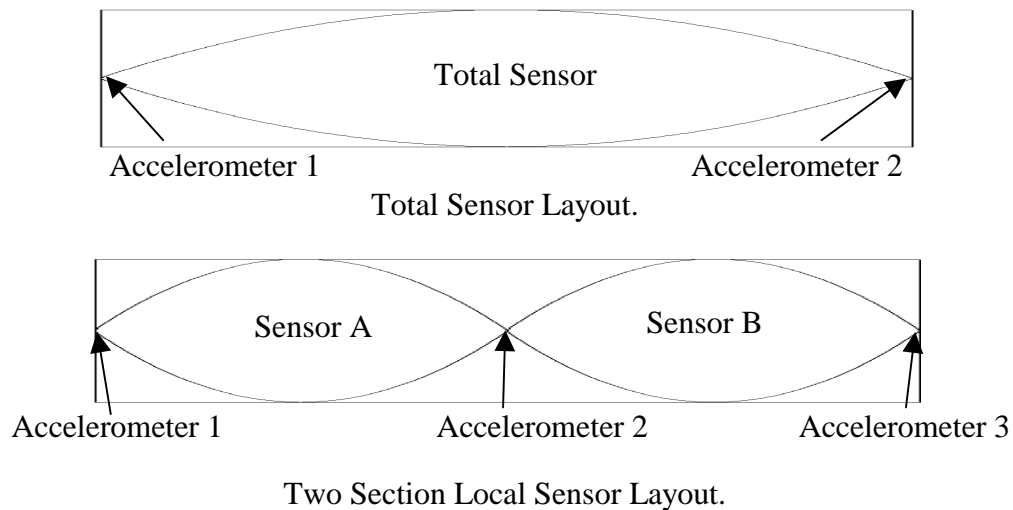


Figure 98. Sensor Shapes Used for the Fixed-Free Beam.

In a similar manner, the local sensor on the right side of the beam, section B, was examined. Inspecting the volume displacement per unit force and phase plots, it was concluded that the sensor on section B was measuring accurately for the first 400 Hz, after which the volume displacement per unit force measurement became overwhelmed with excessive noise. This noise that appeared in the volume displacement plot also appeared in the phase plot, leading to a suspicion of a insufficient signal or large amounts of noise. Therefore, the power spectrum measurements for this local sensor were examined to ensure that a strong signal was being measured. The power spectrum measurements for the local sensor, on section B, showed that indeed there existed a low signal-to-noise-ratio, thus producing the inaccuracies in the measurement.

Finally, after finding that only one local sensor measured accurately, a set of plots was constructed that compared the total volume displacement per unit force for all the sensors. These plots included data from the accelerometer measurements, the total surface sensor, and the set of combined localized integrated sensors. Comparing the all volume displacement per unit force measurements, it was noticed that the accelerometer measurements had predicted a lower volume displacement than those made by the integrated PVDF sensor. These discrepancies in the magnitude of the volume displacement per unit force can be traced back to poor power spectrum measurements. However, the frequency and magnitude for the first resonance coincide, and the frequency at which the second resonance occurs is aligned even though the volume displacement does not coincide. Therefore, considering that the

signal is not sufficient for some of the frequencies measured, the integrated sensors were considered adequate for measuring the volume displacement behavior for the vibrating fixed-free beam.

Fixed-Simply Supported Beam

The third beam examined was for the fixed-simply supported end condition, and since it was the second longest beam analyzed, three different configurations of surface sensors were tested on this beam as they were for the case of the fixed-fixed beam. First, a total surface sensor that spanned the entire length of the beam was tested. The next surface sensor was a set of two localized sensors each covering half of the beam. As a result, the two local sensors shared a common end point at the middle of the beam where an accelerometer was located. However, like the other local sensors, the PVDF was cut at this intersection to isolate the individual sensors from each other. Finally, a set of three local sensors each covering a third of the beam were constructed and tested. These PVDF sensors were also cut so that they were isolated from one another, while sharing two common intersections where accelerometers were located on the beam. Figure 99 depicts the different sensors as they were designed for use on the fixed-simply supported beam. Like the other beams, once the PVDF sensors were constructed and tested, a set of accelerometer measurements were taken. Using the trapezoidal rule, the total and local volume displacements were calculated. After the trapezoidal rule was applied to the accelerometer measurements and the necessary correction factors were applied to the

PVDF data, the resulting volume displacement per unit force was plotted as a function of the excitation frequency (Appendix D).

The first set of data that was plotted represented the two sectioned localized sensors. This set of plots included both the volume displacement per unit force and the phase of the beam as measured by both the local sensor on the left side and the local sensor on the right side of the beam. The resulting volume displacement per unit force for the local sensor on the left side, section A, was found to be identical to the volume displacement per unit force obtained using the accelerometers with only slight variations in the magnitude. Additionally, the phase measured by the accelerometer and integrated sensor shared the same general trends. Therefore, with the exception of the slight deviations at some of the higher frequencies, the local sensor output on section A shows a good correlation to the true (accelerometer) measurements.

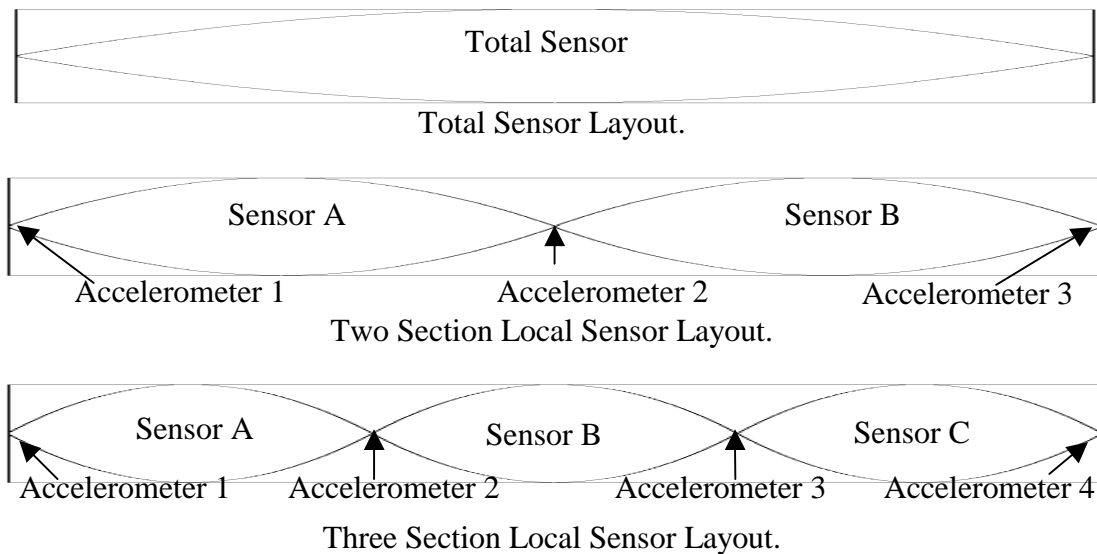


Figure 99. Fixed-Simply Supported Sensor Shapes.

Next, the local sensor for the right side of the beam, section B, was examined. From the volume displacement per unit force plot, it was recognized that the frequency at which the resonances occurred was measured accurately. However, the magnitude of the volume displacement per unit force measurements demonstrated variations in which the integrated sensor measured larger volume displacements than were predicted. In a similar fashion, the phase plot contained many variations between 200 and 400 Hz and again at frequencies above 1000 Hz. Therefore, the magnitude difference can be partly attributed to the difference in phase, meaning that the accelerometer and the integrated sensor were not accurate. However, for the purpose of active control, measuring the magnitude of the volume displacement is not as important as sensing the frequencies at which the maximum volume displacements occur. Thus, the measurements made by the local sensors are considered sufficient for control purposes.

The data collected for the three section sensor was analyzed in the same fashion as the double section sensor. In examining the extreme left hand sensor, section A, it was found that the accelerometer and integrated sensor measurements were almost identical for the frequencies below 800 Hz, and some magnitude discrepancies occurred above 800 Hz. However, some of these discrepancies can be attributed to the fact that the phases have a difference associated with them at higher frequencies. Additionally, the power spectrum measured for this sensor contains a low signal-to-noise-ratio throughout most of the measurement. In other words, the

signal measured is less than a factor of ten greater than the background signal for much of the frequency measured. Therefore, if the phase differences and a poor signal-to-noise-ratio account for the variations present in the magnitude, the sensor can be considered accurate for the purpose of measuring the fixed-simply supported beam's volume displacement.

Following the inspection of the PVDF sensor on section A, the middle sensor, section B, was analyzed. It was found that like many of the other sensors, the vibrational movement of the beam was being depicted accurately with respect to the frequency. On the other hand, the magnitude of the volume displacement per unit force measurement for the integrated sensor differed from the accelerometers at frequencies higher than 800 Hz, at which point the integrated sensor was measuring a larger volume displacement than was predicted. However, this variation in magnitude was not the result of a phase change or a bad signal being generated by the PVDF. As a result, the only logical explanation for the magnitude difference can be the fact that the accelerometer measurements were taken at finite locations every two centimeters along the beam, whereas the PVDF measurements were continuous.

Finally, the local sensor furthest to the right, section C, was examined. From this data, it was found that the volume displacements per unit force measurements matched extremely well except at the anti-resonance at approximately 1100 Hz. At this frequency there are some discrepancies in the data. However, from the power spectrum for this sensor, it was recognized that from approximately 800 Hz to 1100 Hz, the signal measured contained a large amount of noise producing a low signal-to-

noise-ratio, and the variations may be the result of an outside disturbance.

Consequently, the three local sensors measured the volume displacement and the resonances of the beam precisely for frequencies below 800 Hz, while representing the behavior at higher frequencies with some magnitude variations.

The final set of plots created for the fixed-simply supported beam were for the total volume displacement per unit force and the total phase. These plots included the accelerometer, the total PVDF surface sensor, and the two sets of localized PVDF sensors measurements. In comparing the volume displacement per unit force measurements, it was observed that the accelerometer volume displacement measurements have a large variation from the PVDF measurements at frequencies greater than 600 Hz. However, even though the magnitudes vary, the resonances still appear at the same frequencies for the accelerometer and the PVDF. Therefore, the PVDF sensors are measuring the frequencies at which the behavior is occurring accurately, while the variations in magnitude will be explained below.

First, the phase measured by the PVDF may be affecting the volume displacement measured since it exhibits many variations from the phase predicted by the accelerometer. Thus, during the time in which the measurements were made by the accelerometer and the PVDF, something may have happened to the force that was exciting the beam. Second, the signal generated by the PVDF may not have been strong enough to be free of outside disturbances. Thus, the variation in the magnitude can be attributed to experimental error.

Simply Supported-Simply Supported Beam

The final set of sensors examined was for the simply supported-simply supported end condition, and since it was the second shortest beam analyzed, only two surface sensor configurations were tested, one total sensor and one set of two equal-length localized sensors. The total surface sensor which spanned the entire length of the beam was investigated. Then, after testing the total sensor, the set of the localized sensors were examined. This set of sensors was designed such that each sensor spanned one half of the beam's effective length. These two local sensors then shared a point of intersection where an accelerometer was located and a piece of PVDF was removed to isolate the two local sensors. Figure 100 depicts the total and the local sensors as they were designed for use on the simply supported-simply supported beam. Then, after testing the integrated sensors, the accelerometer measurements were collected, and the total and local volume displacements were calculated for the accelerometer and integrated sensor. Finally, the volume displacement per unit force and the phase were plotted as functions of the frequency for each of the setups examined.

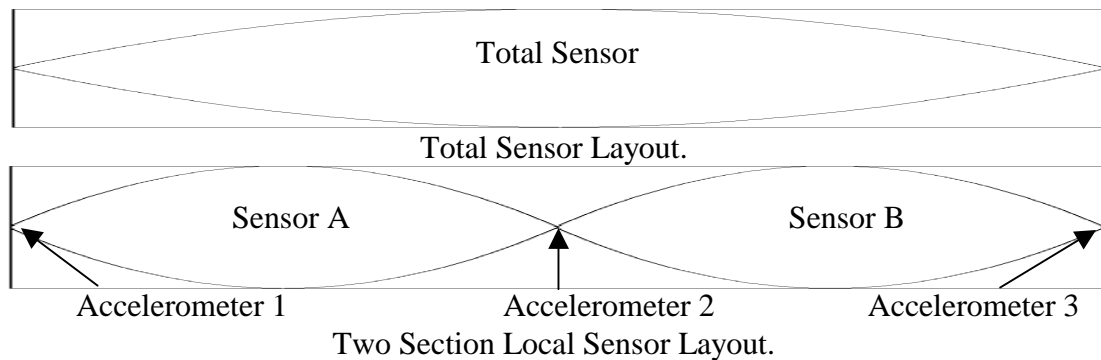


Figure 100. Simply Supported-Simply Supported Sensor Shapes.

First, the volume displacement per unit force was measured by the local sensor on the left side, section A, and it was found that the accelerometer and integrated sensor measurements were nearly identical in phase and magnitude up to a frequency of 800 Hz. After 800 Hz, the accelerometer and the integrated PVDF and accelerometer sensor measurements no longer share any similarities except at the point where a resonant frequency is present. The discrepancies that occur in the volume displacement per unit force can be traced back to changes that occurred in the phase and to the fact that the power spectrum shows that a weak signal-to-noise-ratio was generated by the PVDF surface sensor used in the integrated sensor. Therefore, it could be concluded that the integrated sensor on section A was measuring the vibrational volume displacements of the beam for frequencies up to 800 Hz sufficiently.

In a similar manner, the local sensor on the right side of the beam, section B, was examined. Inspecting the volume displacement per unit force and phase plots, it was concluded that the sensor on section B was measuring accurately for the first 800 Hz after which the integrated surface sensor measurement of volume displacement per unit force became filled with noise and deviated from the behavior predicted by the accelerometer. This noise that appeared in the volume displacement per unit force plot also appeared in the phase plot, leading to a suspicion of a bad signal. Therefore, the power spectrum measurements for this local sensor was examined to ensure that the suspicion was correct. The power spectrum measurements for the local sensor on section B showed that indeed there was a poor signal-to-noise-ratio, thus producing

the inaccuracies and noise in the measurement. The local sensors for the simply supported-simply supported beam were then declared to be accurate for frequencies below 800 Hz, while being questionable at frequencies above 800 Hz.

Finally, after finding that the local sensor measured accurately up to 800 Hz, a pair of plots was constructed that compared the total volume displacement per unit force and the phase for all the sensors. These plots included data from the accelerometer measurements, the total surface sensor, and the two localized integrated surface sensors. Comparing the volume displacement per unit force measurements for all the sensors, it was noticed that the accelerometer measurement and the localized integrated surface sensor measurement were comparable, while the total sensor contained some variation. However, from the power spectrum of the total sensor, it was noticed that not only was the signal weak but it was filled with noise as the variations in the plot show. Therefore, the total sensor cannot be used to accurately compare the data from the local sensors. However, since the accelerometer and the localized integrated surface sensor measurements are comparable, it can be tentatively concluded that the localized sensors are measuring accurately to at least a frequency of 800 Hz.

Sound Power Measurements

After all the beam vibrational data was collected and analyzed for each beam end condition, the final phase of the sensor verification process was performed. This final verification entailed quantifying the maximum vibrations on the beam and on the top of the baffled box, setting up and measuring the sound power of the vibrating

beam, and analyzing these results. The first experiment conducted on each of the beams and box tops was to measure the maximum vibration per unit force that occurred at finite points on their surfaces. These points of interest were measured at approximately every fourth accelerometer measurement point, which is an average of eight centimeters apart, along the length of the beam and at an average of every 0.0635 meters (2.5 inches) across the top of the box. Thus, a grid was formed on each box top. An example of the grid for the fixed-fixed beam and box top can be viewed in Figure 101. By making these measurements, it was possible to check and ensure that the box top was not vibrating at an excessive level, thus, representing an insignificant contribution to the overall sound radiated from the box. To be considered an excessive vibration per unit force, the difference between the vibration per unit force of the beam and the vibration per unit force of the box top had to a difference of 10 dB((m/s²)/N) or less over a frequency range of 60 to 1600 Hz. Therefore, if the data is examined for each of the beams, it can be observed that for each box top, the maximum level of vibrational excitation is not great enough to create a disturbing sound power (Tables 5, 6, 7, 8). However, in each set of data, it was noticed that with the fixed and simply supported end conditions, the maximum vibrations of the beam, over a range from 60 to 1600 Hz, were not a factor of ten greater than those for the box top. In these instances, the beam measurements were taken at the end conditions where the vibrations are naturally small, and therefore, the small differences are to be expected as the box top should not be vibrating a great deal in these areas. Therefore, the experiment performed insured that the vibrations from

the baffled box did not contribute to the sound power radiated or interfere with the beam vibrations at a significant level.

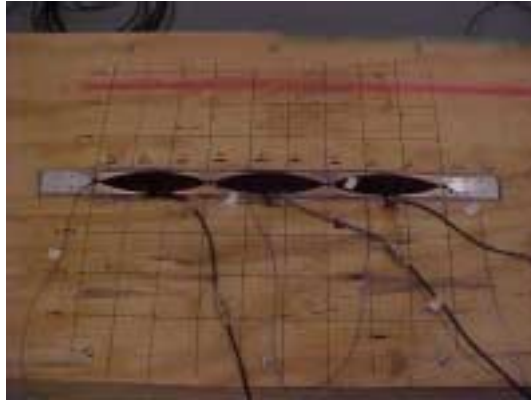


Figure 101. Fixed-Fixed Beam With the Test Grid Laid Out on the Box Top.

Table 5.

Fixed-Fixed Beam and Box Top Maximum Vibration Per Unit Force ($\text{dB}((\text{m/s}^2)/\text{N})$).

	Node 1	Node 4	Node 7	Node 10	Node 13	Node 16	Node 19	Node 22	Node 25	Node 28
row1	-3.47	-2.09	-2.23	-1.99	-3.01	-2.35	-3.04	-3.07	-2.70	-1.81
row2	-2.13	-3.01	-2.22	-2.45	-3.66	-1.92	-2.50	-1.88	-1.07	-1.68
row3	-2.34	-2.56	-2.75	-2.07	-2.21	-3.00	-2.09	-2.62	-2.44	-2.95
beam	-0.14	23.98	25.81	18.64	26.38	25.29	18.26	27.95	24.07	-0.98
row4	-1.67	-2.27	-3.31	-2.83	-2.63	-2.30	-2.63	-1.98	-1.95	-2.66
row5	-2.91	-3.13	-2.76	-2.75	-2.17	-2.45	-2.41	-1.80	-2.53	-1.84
row6	-1.39	-2.79	-2.20	-2.49	-1.85	-1.55	-2.52	-2.49	-1.88	-3.09

Table 6.

Fixed-Free Beam and Box Top Maximum Vibration Per Unit Force ($\text{dB}((\text{m/s}^2)/\text{N})$).

	Node 1	Node 5	Node 9	Node 12
row1	-1.21	-0.95	-2.09	-1.78
row2	-1.64	-2.08	-2.59	-2.37
row3	-0.77	-0.76	-0.29	-1.30
beam	0.09	22.47	19.59	21.73
row4	-2.00	-0.67	-1.34	-1.59
row5	-1.48	-0.84	-1.30	-3.41
row6	0.00	-1.33	-1.71	-2.25

Table 7.

Fixed-Simply Supported Beam and Box Top Maximum Vibration Per Unit Force ($\text{dB}((\text{m/s}^2)/\text{N})$).

	Node 1	Node 4	Node 7	Node 10	Node 14	Node 17	Node 20	Node 23
row1	-3.26	-2.66	-3.27	-1.74	-3.81	-2.26	-3.60	-2.46
row2	-3.40	-2.65	-2.72	-2.17	-3.35	-2.04	-2.35	-2.05
row3	2.16	-1.55	-2.78	-2.57	-2.50	-2.57	-2.94	-2.84
beam	1.15	27.32	27.07	24.36	24.26	25.07	24.48	-2.48
row4	-0.34	-2.16	-2.33	-2.67	-2.42	-2.79	-2.50	-2.76
row5	-2.83	-3.24	-1.82	-2.10	-1.74	-2.97	-2.38	-2.85
row6	-2.29	-3.16	-2.27	-3.20	-3.01	-2.34	-2.99	-2.45

Table 8.

Hinged-Hinged Beam and Box Top Maximum Vibration Per Unit Force ($\text{dB}((\text{m/s}^2)/\text{N})$).

	Node 1	Node 5	Node 9	Node 13	Node 18
row1	-1.92	-2.57	-2.77	-2.22	-2.54
row2	-1.07	-1.99	-2.30	-2.15	-2.57
row3	-1.62	-2.41	-2.37	-1.96	-2.38
beam	-1.33	25.31	19.82	26.21	5.34
row4	-2.13	-1.64	-1.64	-1.94	-2.14
row5	-1.99	-2.33	-2.48	-1.91	-2.09
row6	-1.81	-2.48	-2.31	-2.43	-2.59

Next, the method used for calculating the sound power had to be determined because there is more than one approach that can be used to calculate the sound power of a test object. Thus, it was decided that for this process, the comparison method of measuring sound power would be used. In the comparison method, the sound pressure level of the subject under test along with the sound pressure level of a known reference source are measured and used in conjunction with the known sound power for the reference sound source. This information was used in the following expression:

$$L_w = L_p + (L_{wr} - L_{pr}), \quad (74)$$

to calculate the sound power radiated by a test subject, L_w , where L_p is the sound pressure of the test subject averaged over the six microphones, L_{wr} is the sound power of a reference sound source and L_{pr} is the sound pressure of the reference sound source averaged over the six microphones (ANSI, 1990). Having decided what method to use for testing the sound power, the reverberation chamber (Figure 102) was set up to make the required measurements from the baffled beams and reference sound source.



Figure 102. Reverberation Chamber Setup for Sound Power Measurements.

In setting up the reverberation chamber for the sound power measurements, the locations of the microphones and sound source within the chamber had to be determined. Therefore, the ANSI S12.31 – 1990 standard was used to determine the required limitations and locations for the sound power equipment. The standard required that the sound source not fill more than 1% of the room's total volume. Since the volume of the Western Michigan University reverberation chamber is 74.9 m^3 ($2,646 \text{ ft}^3$), the sound source needed to fill a volume less than 0.749 m^3 (26.46 ft^3). This requirement was fulfilled as the reference sound source used was contained a volume of approximately 0.0425 m^3 (1.5 ft^3), and the baffled box was approximately 0.198 m^3 (7 ft^3). Figure 103 shows the G&G Acoustic Reference Sound Source (model GA60) which was used as a known sound power source.



Figure 103. Reference Sound Source Used for Sound Power Measurements.

Additionally, the sound source was required to be at least 1.5 meters away from any wall or diffuser as specified by the standard. Thus, the sound source was

positioned inside a rectangle identifying the acceptable source placement area that was marked using red tape on the floor of the chamber. Figure 104 shows a section of the outlined area within which the sound source could be placed. Once placed within this area, the source was oriented such that it was not parallel to any nearby walls.

Consequently, according to the standard for any sound power measurements conducted within the Western Michigan University reverberation chamber, the microphones must be at least one meter from all reflective surfaces, including the ceiling and floor. Thus, the microphones were placed within an outlined area that was marked using green tape on the floor of the reverberation chamber (Figure 104).

Also, the ANSI standard required that the microphones be a minimum of a one half of a wavelength of the lowest frequency of interest apart at all times. The wavelength is frequency dependent; therefore, the distance of separation will depend on the lower cutoff frequency for the reverberation chamber. In this case, the lower cutoff frequency was 125 Hz, so the microphones had to be at least 1.372 meters (4.5 feet) apart as determined by:

$$x = \frac{\lambda}{2} = \frac{c}{2f}, \quad (75)$$

where x is the distance of separation, λ is the wavelength, c is the speed of sound in air, and f is the frequency of the wavelength (Lord et al., 1987). As a result, the microphones were placed, and their locations were recorded in case one was bumped during the baffled beam testing (Table 9).



Figure 104. Axis of Orientation and Color Coded Borders.

Table 9.

Microphone Locations used in the Sound Power Measurements.

Microphone	Location (meters)		
	X	Y	Z
1	3.20	2.91	1.44
2	1.14	3.09	1.68
3	5.38	1.02	1.67
4	2.88	1.23	1.74
5	5.08	3.07	1.71
6	1.31	1.30	1.39

Confident that the baffled box is not significantly contributing to the sound power radiated by the beam and that the reverberation chamber was set up properly for making the sound power measurements, the sound power for the fixed-fixed, the fixed-free, the fixed-simply supported, and the simply supported-simply supported beams was measured. Then, the theoretical sound power was calculated for the accelerometer, total surface sensor, and local integrated sensors using their volume displacement measurements using Eqs. (72) and (73). The results of the actual

measured and the theoretically calculated sound powers were then plotted for the 1/3 octave band frequencies from 160 Hz to 1250 Hz (Figures 105, 106, 107, 108).

From the resulting graphs, a comparison study could be completed for each of the beams. However, since the trends that appear tend to do so in each of the graphs, the sound power conclusions will be presented all at once. First, it is recognized that the sound power measured and the sound power calculated from the accelerometer volume displacements share the same sound power magnitude fluctuations throughout the majority of the frequency spectrum analyzed for each beam. Also, the sound power represented by the PVDF sensors shares the same general trends as the sound power that was directly measured. However, in most cases, the calculated sound power does not have the same magnitude as the measured sound power. When the overall sound power was calculated, it was found that the sound power calculated from the volume displacement measurements matched quite closely to that which was measured directly from the beam. As a result, if the discrepancies that occurred in the volume displacement measurements are considered to be one of the major sources of error, it can be concluded that the total and local PVDF sensors developed for the beams are capable of sensing the beam's volume displacement and sound power radiated.

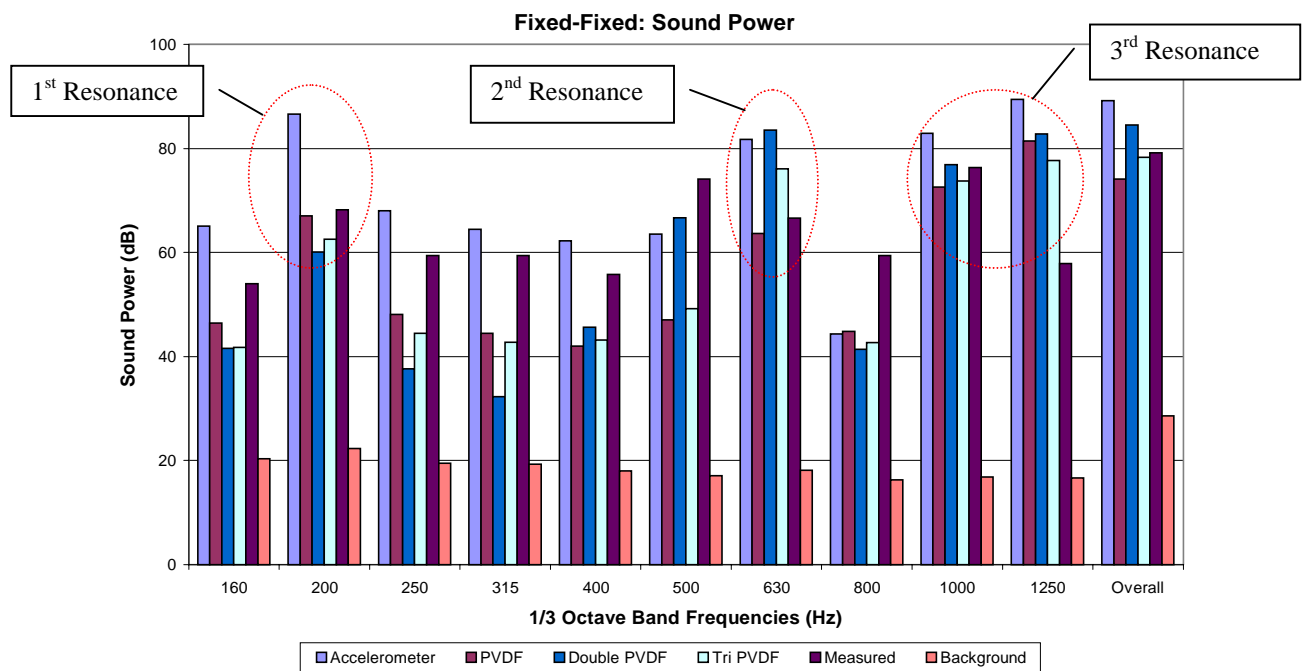


Figure 105. Fixed-Fixed Beam Sound Power Comparison.

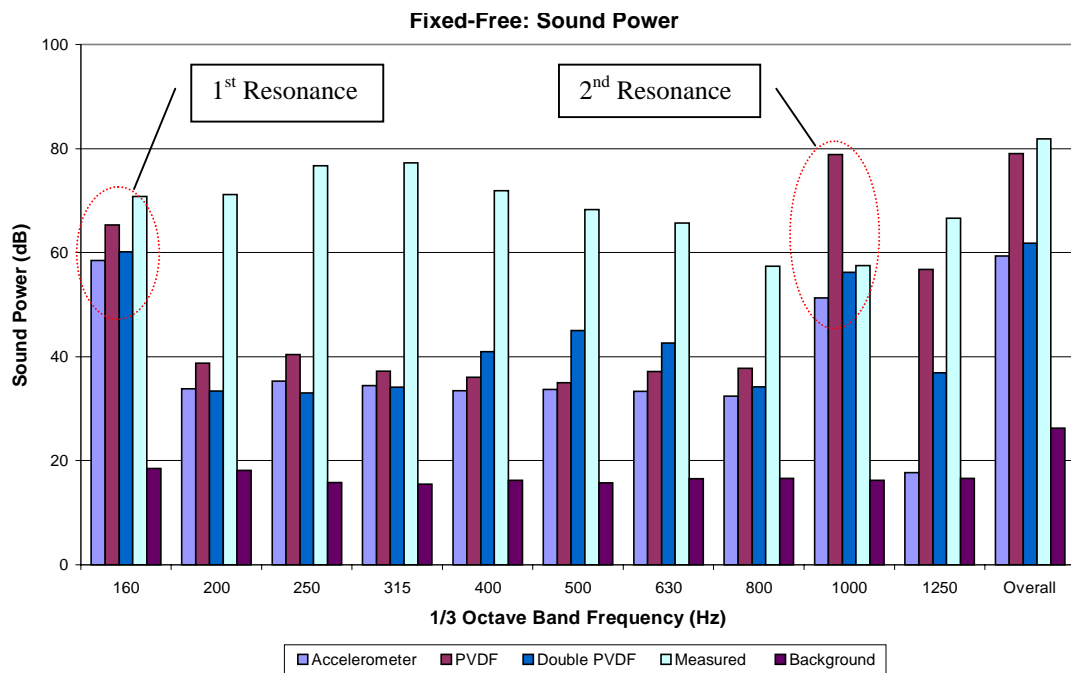


Figure 106. Fixed-Free Beam Sound Power Comparison.

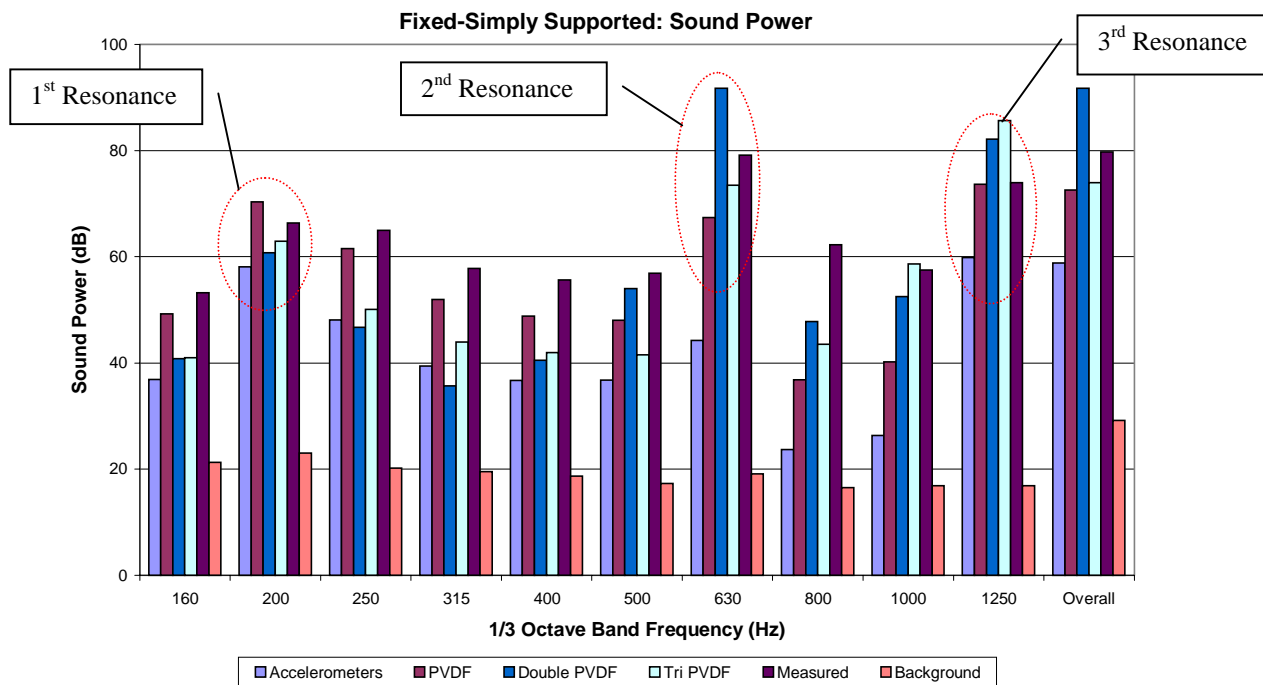


Figure 107. Fixed-Simply Supported Beam Sound Power Comparison.

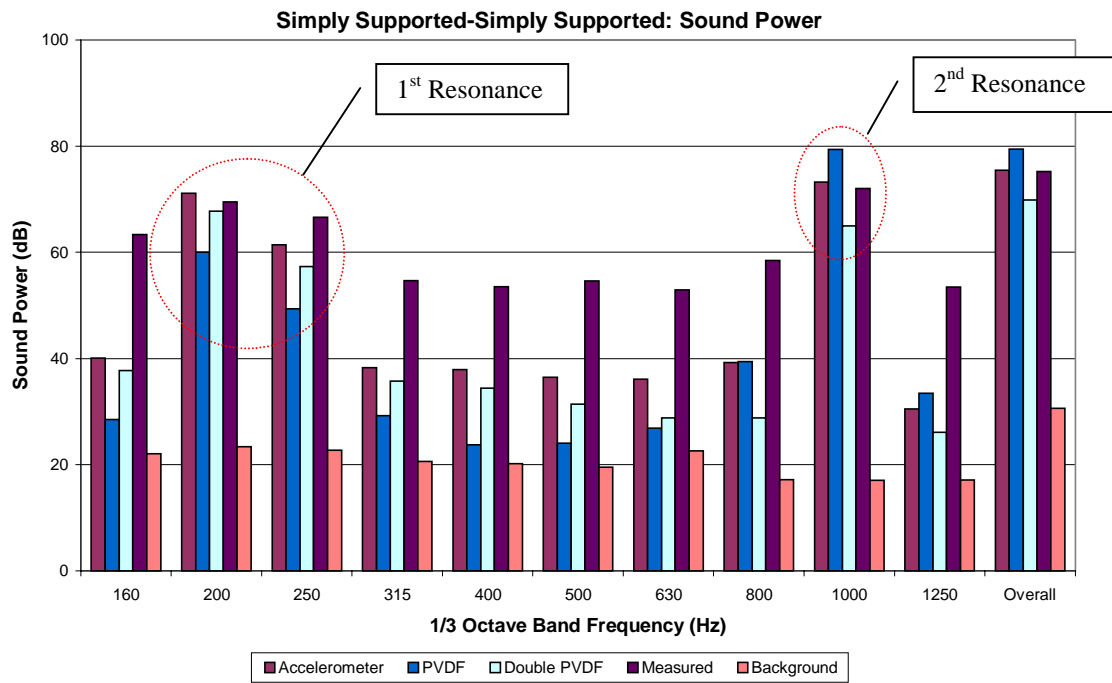


Figure 108. Simply Supported-Simply Supported Beam Sound Power Comparison.

CHAPTER V

CONCLUSION AND RECOMMENDATIONS

Conclusion

As mentioned before, the ultimate goal of this research is to use surface sensors to measure the volume velocity or volume displacement of a vibrating structural surface. As the background information has shown, there are three different types of structures for which similar research has already been completed. These are a baffled piston, a beam, and a plate. In this background research, different methods and approaches were described in which the surface vibrations of a structure could be measured. Also, local sensors used for sensing the local volume displacement of a radiating structure, and total sensors that sensed the volume displacement of an entire structure and operated on a global level for noise reduction were investigated. However, only the local sensors were examined in detail as they could be focused on one particular section of an entire structure and potentially be used to reduce the sound power radiated from particular areas of interest. Ultimately, some existing local and total sensor shapes were presented for a vibrating beam and plate. Therefore, it was believed more practical localized sensors could be developed for a vibrating beam.

Believing that it was possible to simplify the design of local sensors used on beams, a test platform was designed and constructed, and a verification process was developed to test the sensors designed. Therefore, by performing multiple tests to verify the integrated PVDF and accelerometer sensors that were developed for sensing the vibrational modes of multiple beam end conditions, it was discovered that in each case, it was feasible to accurately measure the desired volume displacement. In an effort to show that this theory was practical for implementation in active control systems, a set of volume displacement (per unit force) and sound power measurements were performed. In each case, the integrated PVDF and accelerometer sensors developed showed some discrepancies in the magnitude of the measurements taken; however, the general trends of the beams' volume displacement were accurately measured with respect to the frequencies. The integrated PVDF and accelerometer sensors were indeed capable of measuring the resonant frequencies and many of the other movements that occurred as a function of frequency. However, it was determined that the variations in the magnitudes could be the result of using an excitation force that was too small for driving the beam. Additionally, in the case of the sound power, the variations in the 1/3 octave frequencies may have resulted from the fact that there were inaccuracies in the magnitude of the measured volume displacement used for calculating the theoretical sound power from the volume displacement.

Recommendations for Future Work

Having worked with PVDF for this research, some of the limitations in its behavior were discovered and explored while many other questions were developed as a result. The first question encountered involved how to most effectively attach electrical leads to the PVDF for the purpose of taking a measurement. Some of the methods explored included soldering the wire for the lead to copper tape and using the copper tape to stick to the PVDF for making the measurements. Next, simply using the copper tape to stick the wire leads to the PVDF was explored and found to still produce inconsistent signals like the previous method. Therefore, it is believed that through some future exploration, a method for attaching electrical leads to the PVDF can be developed in which the measurements can be made on a consistent basis.

The next question that was raised throughout this work was with respect to the value of the stress per charge coefficient (e_{31} , e_{32} , and e_{33}) of the PVDF and a possible method for obtaining the exact values for this property. This became an issue as the PVDF being used ran out on one roll and a new roll of PVDF had to be used to finish the measurements. In switching from one roll of material to another, the possibility existed that the values of the stress per charge coefficient may have changed and caused some of the data to be skewed as a result. Therefore, the idea of developing a method by which the PVDF could be tested and the stress per charge coefficient determined was discussed. When calling the manufacturer of the PVDF, the technical support representative claimed that he did not know of any commercially available

apparatus that could be used to measure the PVDF stress per charge coefficient and confirmed that the PVDF can have up to a 20% variation in the stress per charge constant from one roll to another. Therefore, it is recommended that a device for experimentally measuring the stress per charge constant and strain constants of the PVDF be developed.

Another unknown property of the PVDF is whether the stress per charge coefficient (e_{31} , e_{32} , and e_{33}) is a linear value or if it is a function of frequency. The reason that this is of interest is that if the stress per charge coefficient is a function of frequency or responds in a non-linear manner, many of the magnitude variations at higher frequencies may be explained. Thus, it is suggested that some investigation be done to determine if the stress per charge coefficient is linear under the conditions used for measuring the volume displacement.

The final question that was developed was related to the work that was performed for the localized PVDF sensors. This question was based on the fact that for most radiating structures, the main source of sound radiation occurs in the form of end and edge radiation. In other words, the majority of the undesirable sound radiated in this application would be produced along the edge of the beam. Therefore, rather than sensing the behavior for the entire beam or even a localized portion of a beam, it would be more beneficial to measure the behavior at the ends and along the edges of the beam. Thus, there is room for future improvements in the development of sensors for measuring the localized sources of radiated sound for the purpose of the active control of sound.

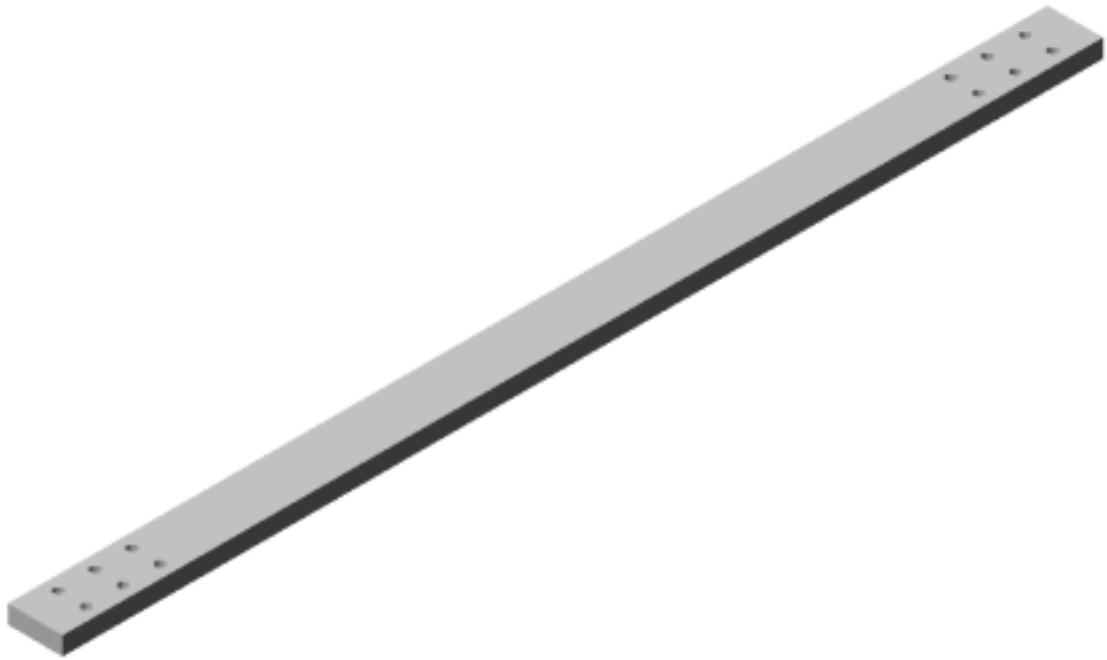
REFERENCES

- American National Standard Institute. *Precision Methods for the Determination of Sound Power Levels of Broad-Band Noise Sources in Reverberation Rooms (ANSI S12.31-1990)*. New York: Acoustical Society of America.: August 2, 1990
- AMP. (1994). *Basic Design Kit*. AMP Incorporated, P/N 0-1004308-0 REV:E.
- Charette, F., Berry, A., Guigou, C. (1998). *Active Control of Sound Radiation from a Plate using a Polyvinylidene Fluoride Volume Displacement Sensor*. Journal of Acoustical Society of America, 103(3), 1493-1503.
- Clark, R.L. and Burke, S.E. (1996). *Practical Limitations in Achieving Shaped Model Sensors with Induced Strain Materials*. ASME Journal of Vibration and Acoustics, 118(4), 668-675.
- Elliott, S. (December 11, 2000). personal correspondence via electronic mail. From sje@isvr.soton.ac.uk to naghshineh@wmich.edu.
- Gere, J.M. and Timoshenko, S.P. (1997). *Mechanics of Materials 4th Edition*. PWS Publishing Company. Boston, Massachusetts.
- Guigou, C., Charrette, F., Berry, A. (1994). *Active Control of Sound by Minimization of Volume Velocity on Finite Beam*. Third International Congress on Air- and Structure-Borne Sound and Vibration, June 13-15 Montreal, Canada, 1507-1514.
- Guigou, C., Berry, A., Charette, F., Nicolas, J., (1996). *Active Control of Finite Beam Volume Velocity using Sshaped PVDF Sensor*. Acustica, 82, 772-783.
- Hayek, S.I., (2001). *Advanced Mathematical Methods in Science and Engineering*. Marcel Dekker Incorporated. New York.

- Johnson, M.E. and Elliott, S.J. (1993). *Volume Velocity Sensors for Active Control*. Proceedings of Institute of Acoustics, 15(3), 411-420.
- Johnson, M.E. and Elliott, S.J. (1995). *Experiments on the active control of sound radiation using a volume velocity sensor*. SPIE, 2443, 658-669.
- Junger, M.C. and Feit, D. (1993). *Sound, Structures, and Their Interactions*. Acoustical Society of America.
- Lee, C.K. and Moon, F.C. (1988). *Laminated Piezopolymer Plates for Torsion and Bending Sensors and Actuators*. IBM Research Division. Yorktown Heights, New York.
- Lord, H.W., Gatley, W.S, Eversen, H.A. (1987). *Noise Control for Engineers*. Robert E. Krieger Publishing Co., Inc.. Malabar, Florida.
- Naghshineh, K., Mason, V.B., Kamman, J.W. (1998). *Active Reduction of Radiated Noise From a Baffled Piston Using a Volume Velocity, Feedforward Controller*. ASME Journal of Vibrations and Acoustics, 120, 484-490.
- Miller, J. (January 8, 2001). personal interview at Western Michigan University.
- Rex, J. (1991). *The Use of Integrated Transducers for the Active Control of Structural Vibration*. University of Southampton.
- Thompson, W.T. (1993). *Theory of Vibration with Applications 4th Edition*. Prentice-Hall Incorporated. Upper Saddle River, New Jersey.
- Zahui, M.B., Naghshineh, K., Kamman, J.W. (2001a). *Narrow band active control of sound radiated from a baffled beam using local volume displacement minimization*. Journal of Applied Acoustics, 62(1), 17-64.
- Zahui, M.B., Kamman, J.W., Naghshineh, K. (2001b). *Measurement of Local Displacement Sensors for a Vibrating Beam*. ASME Journal of Vibration and Acoustics, 123.

Appendix A

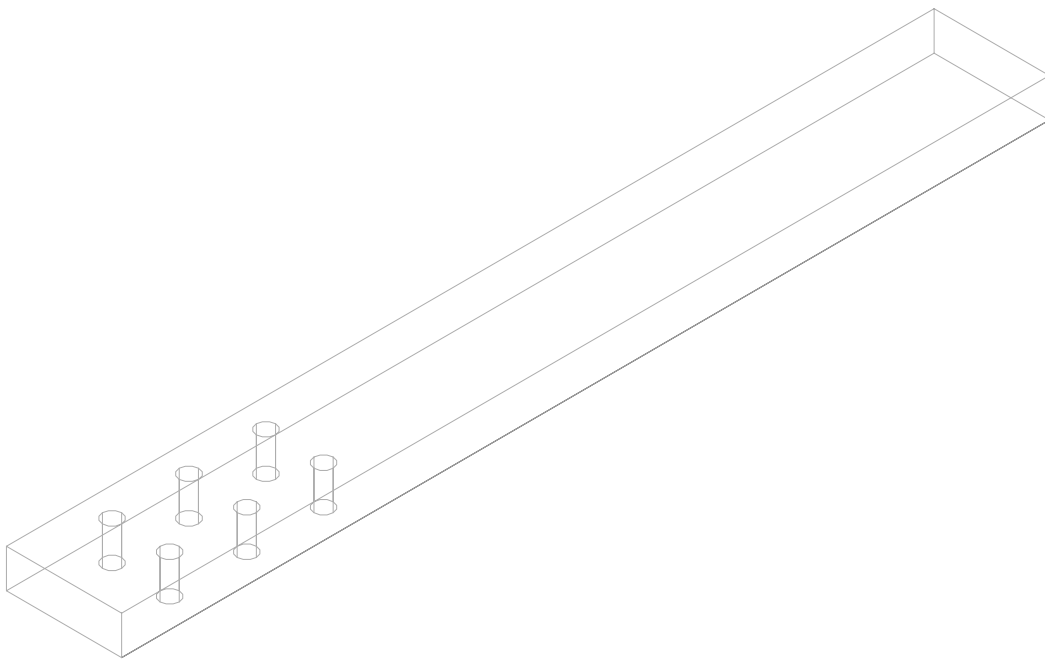
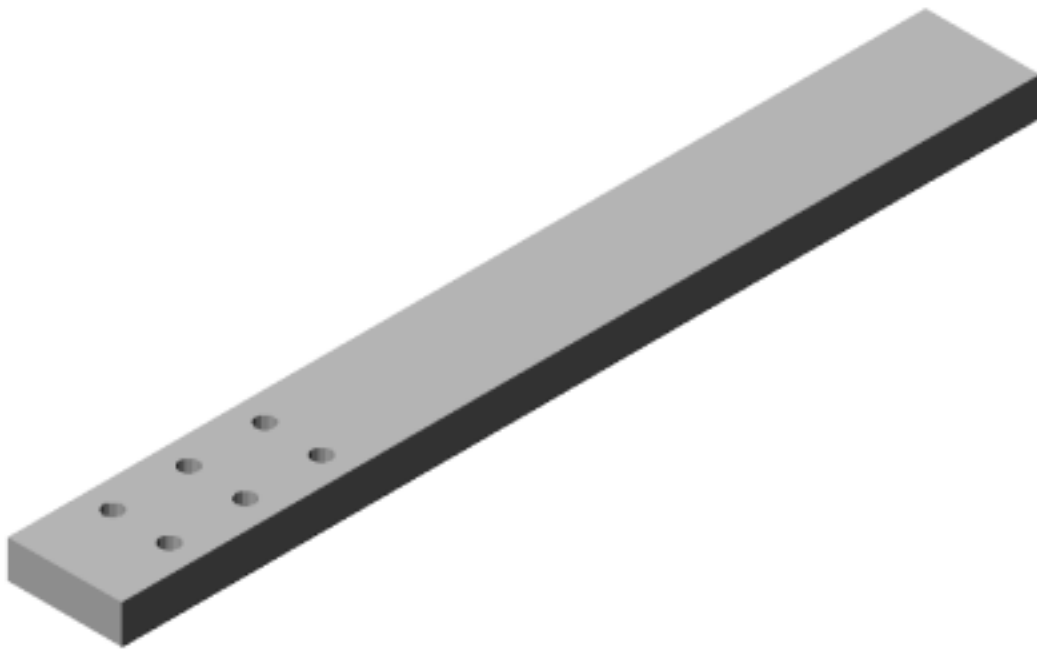
Assembly Drawings of the Beams and Test Fixture



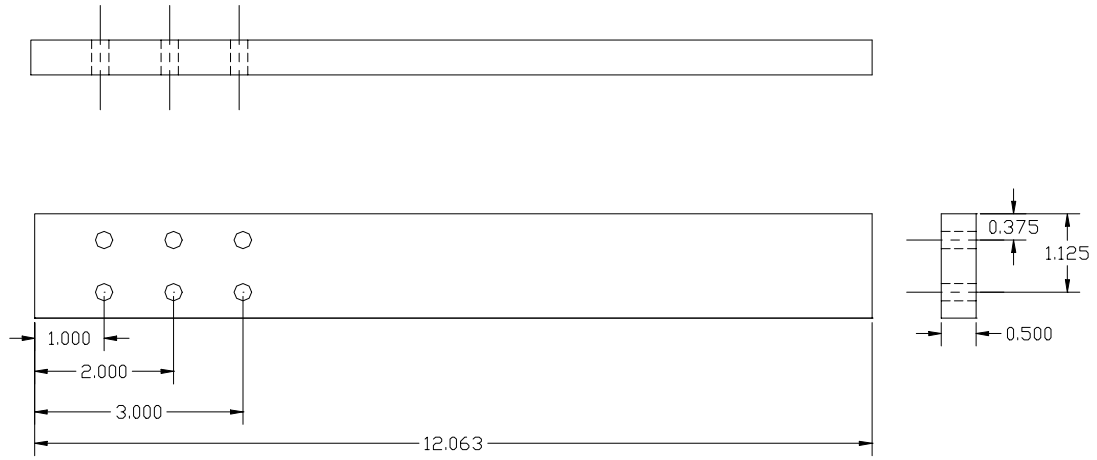
A1. 3-Dimensional Drawings of the Fixed-Fixed Beam.



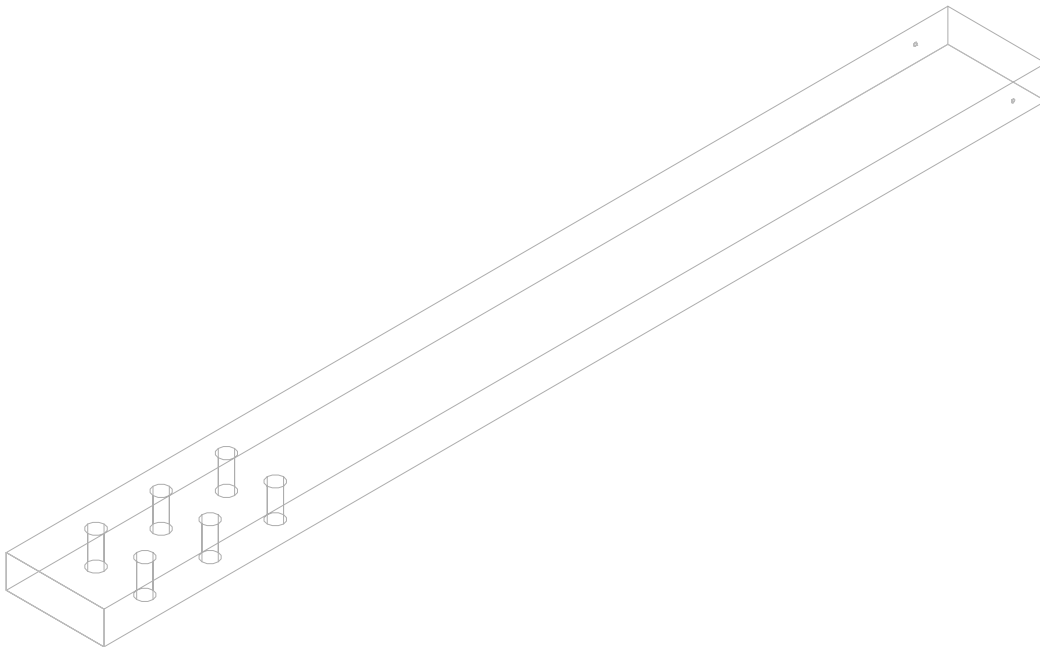
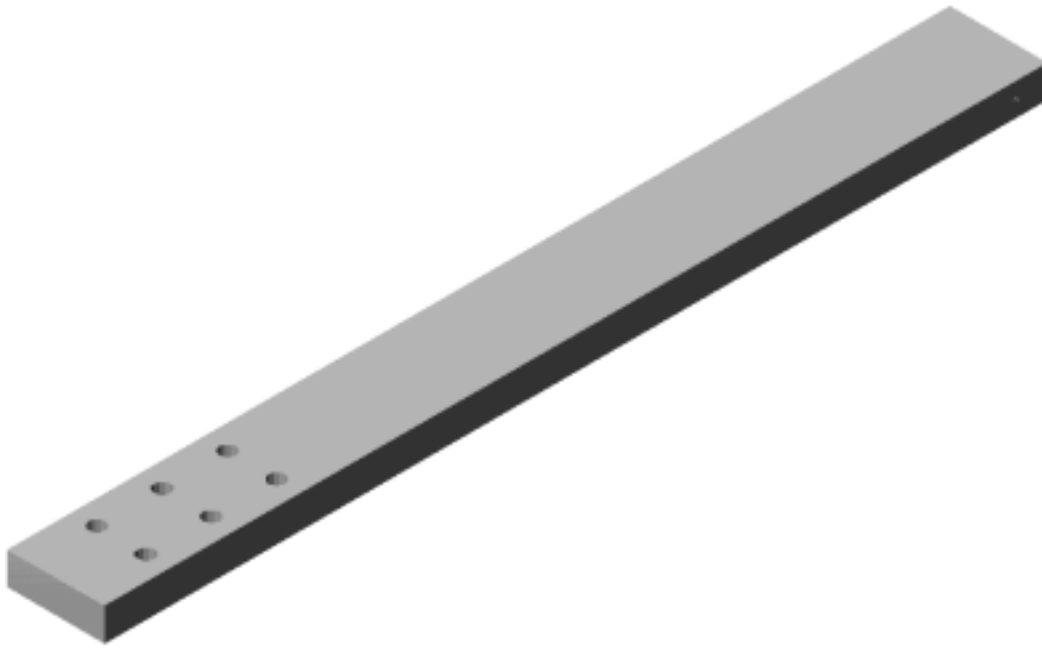
A2. Detailed Working Drawing of the Fixed-Fixed Beam.



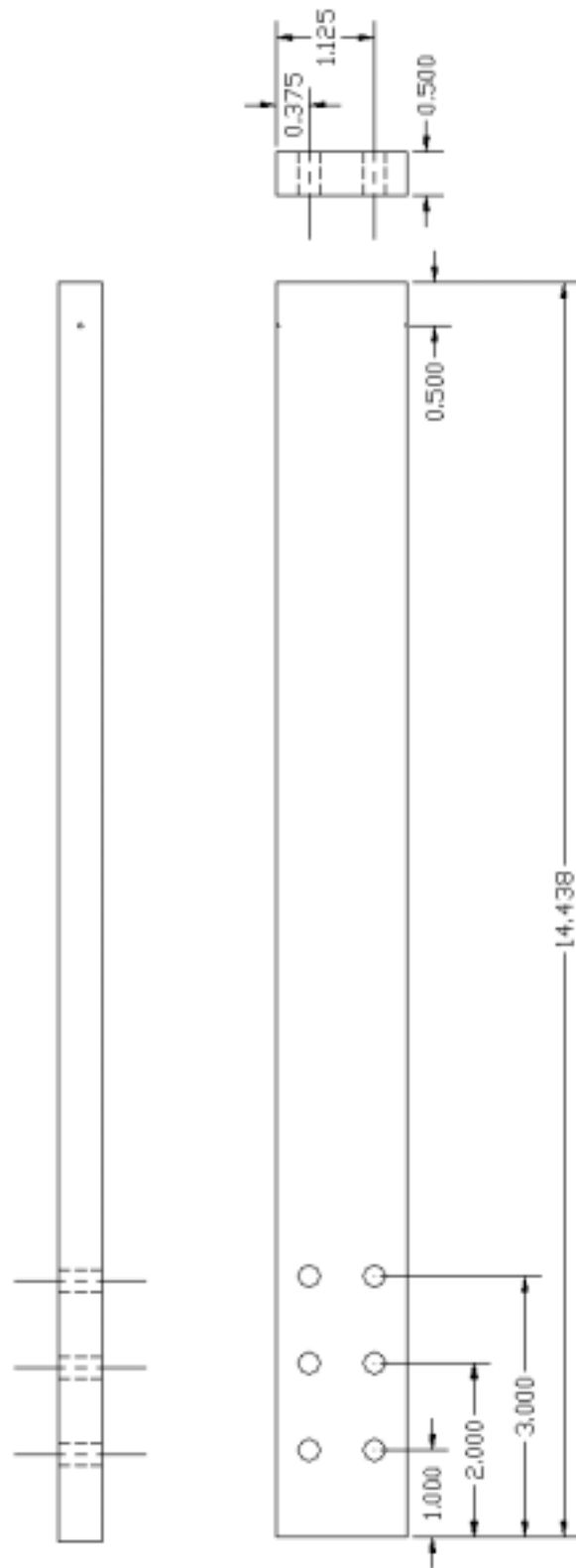
A3. 3-Dimensional Drawing of the Fixed-Free Beam.



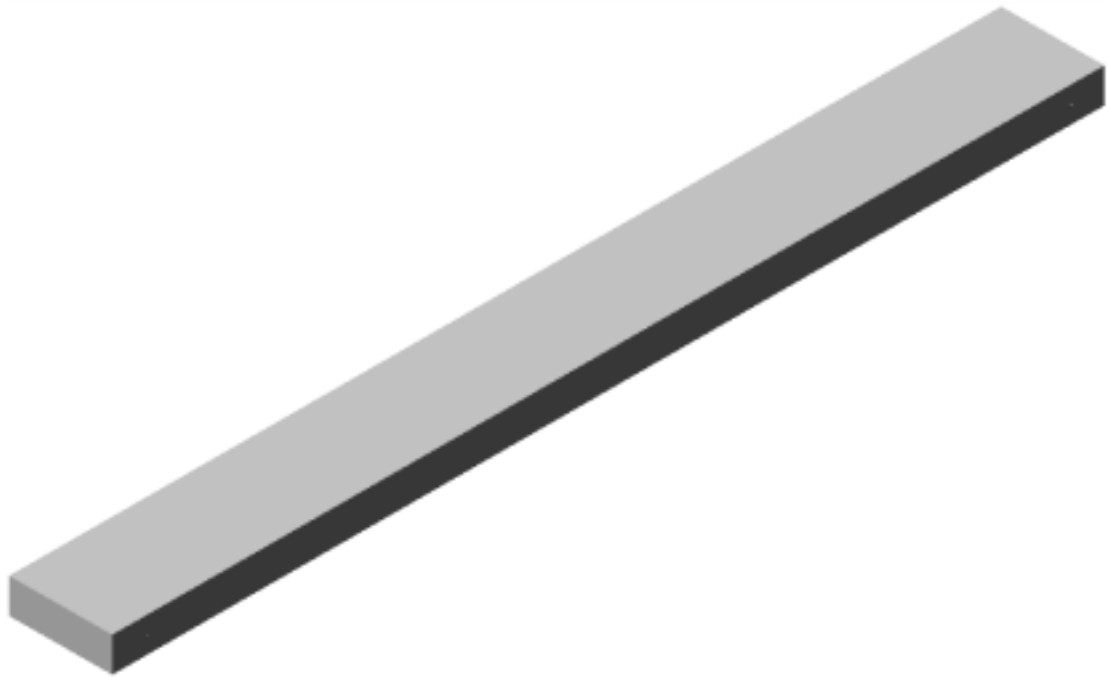
A4. Detailed Working Drawing of the Fixed-Free Beam.



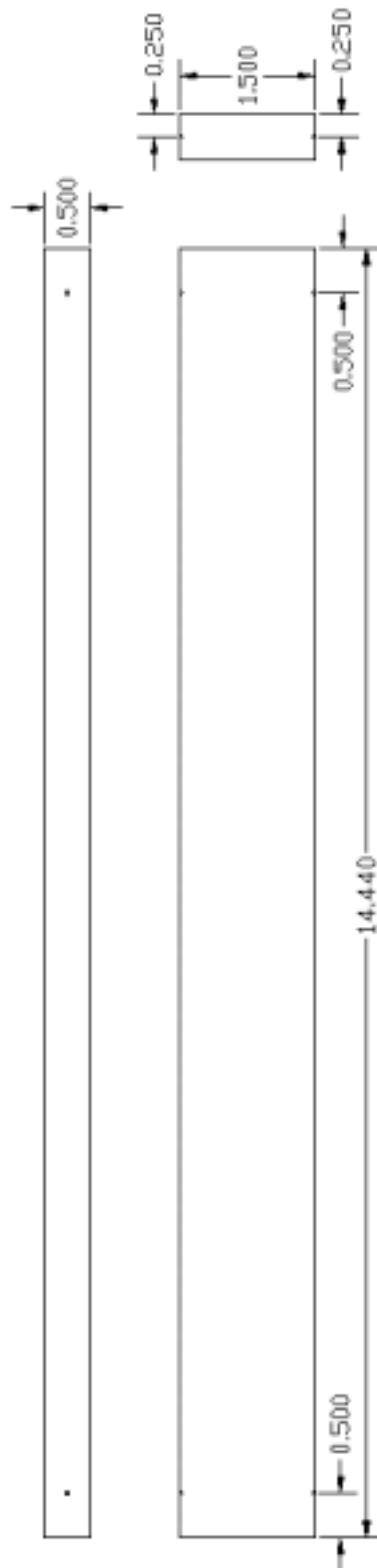
A5. 3-Dimensional Drawing of the Fixed-Simply Supported Beam.



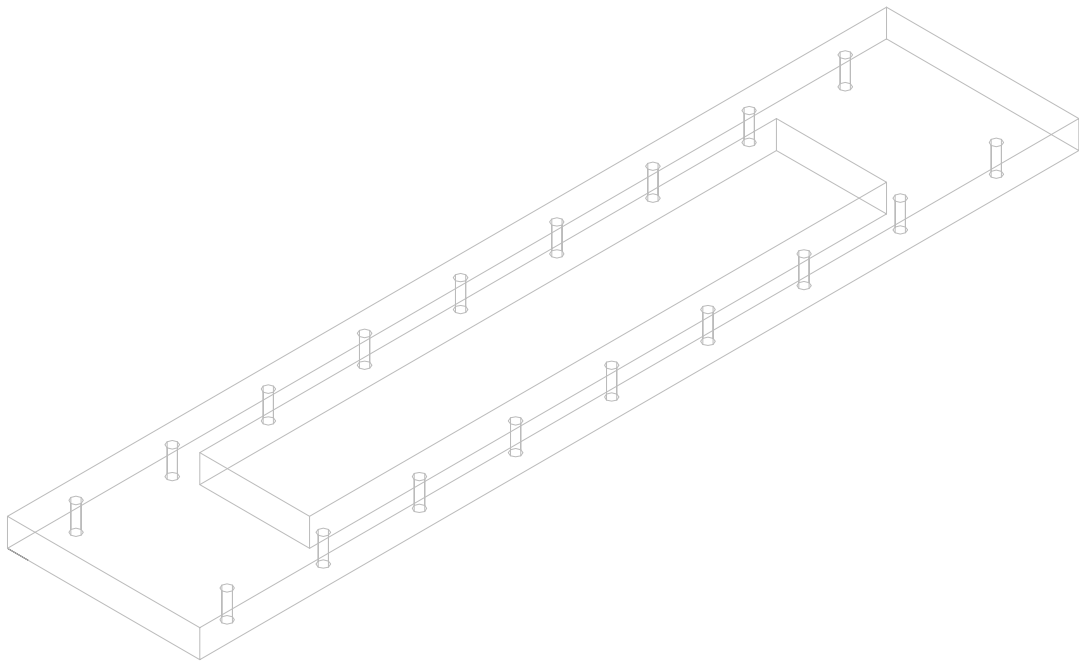
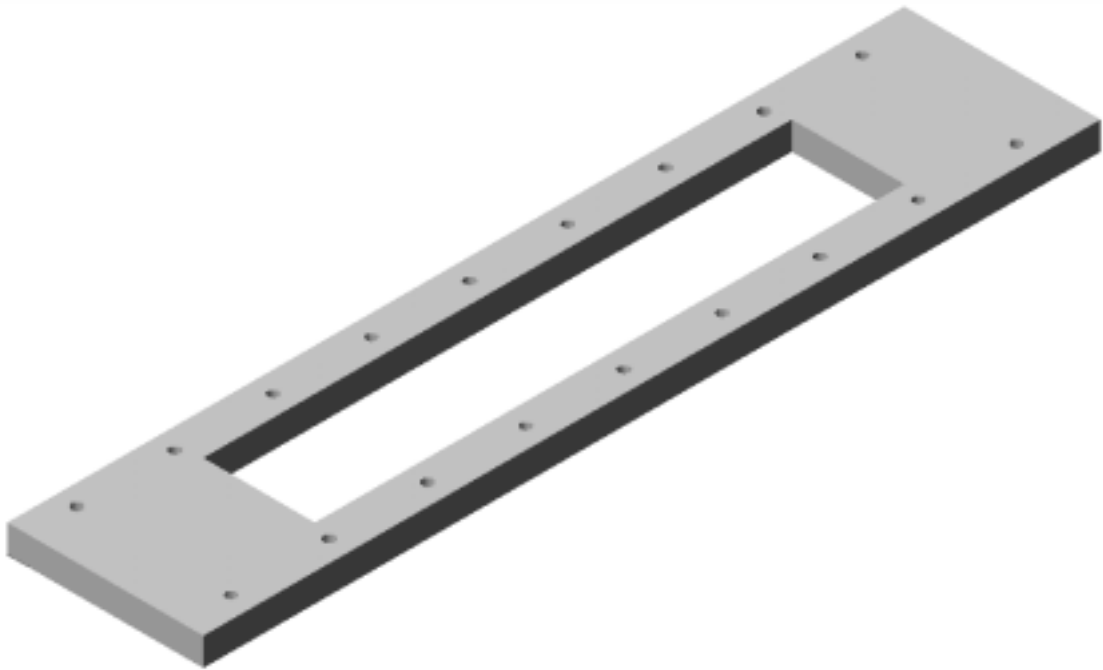
A6. Detailed Working Drawing of the Fixed-Simply Supported Beam.



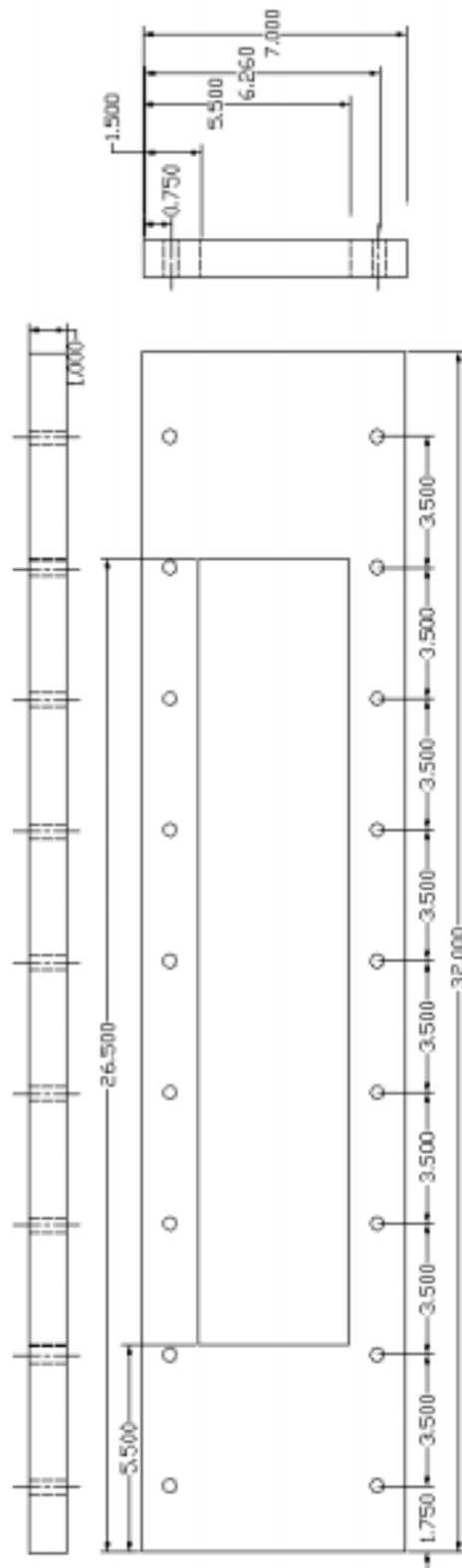
A7. 3-Dimensional Drawing of the Simply Supported-Simply Supported Beam.



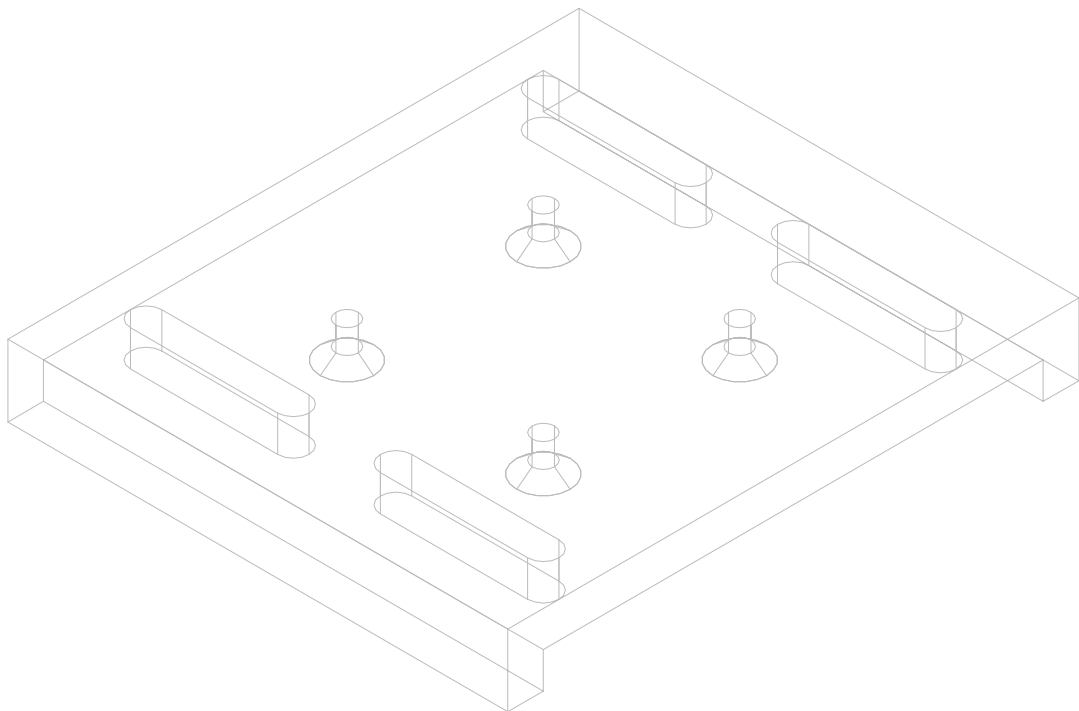
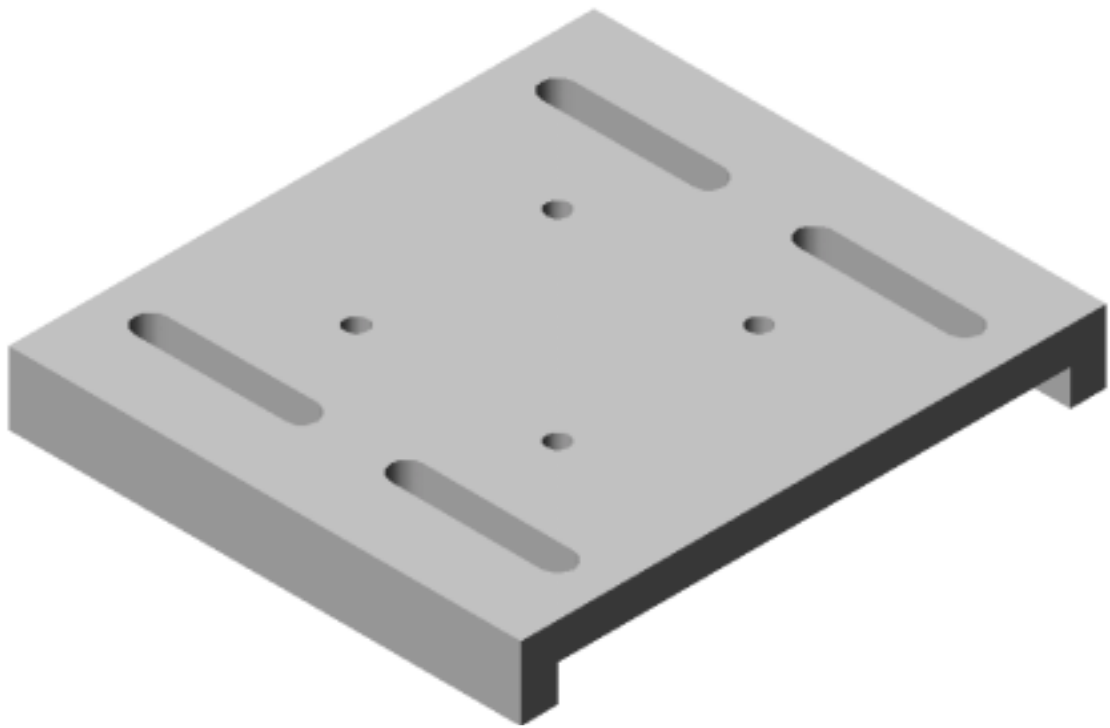
A8. Detailed Working Drawing of the Simply Supported-Simply Supported Beam.



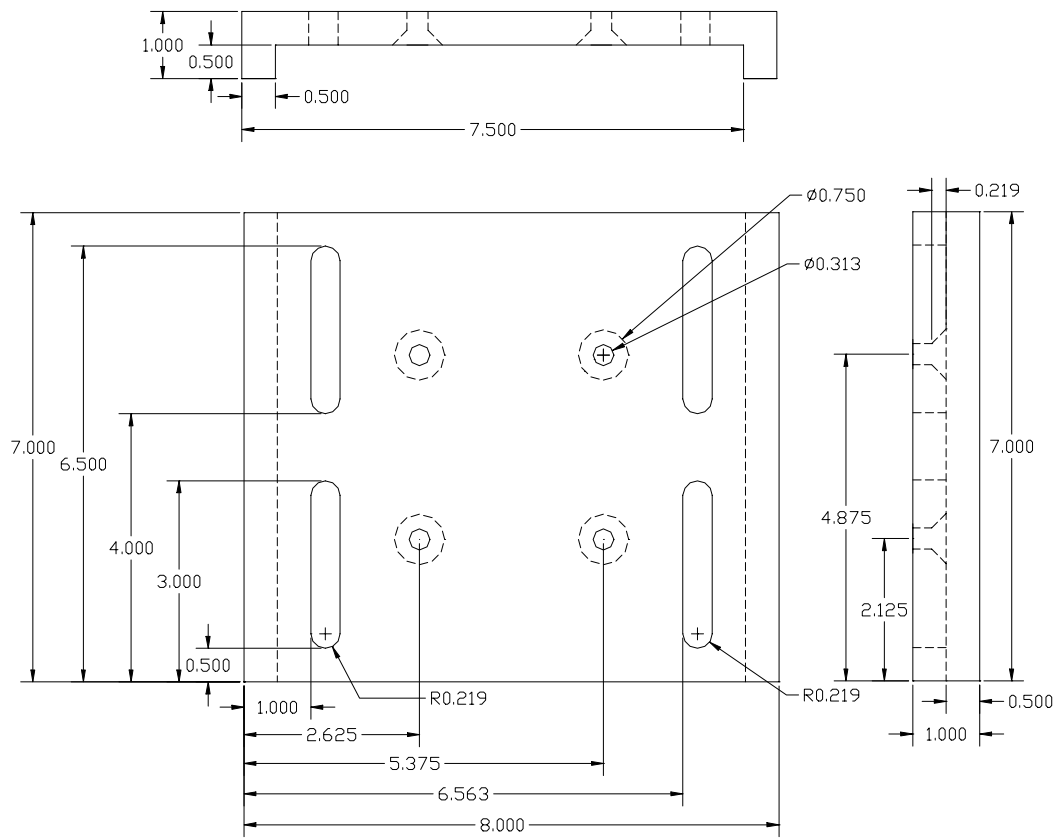
A9. 3-Dimensional Drawing of the Base.



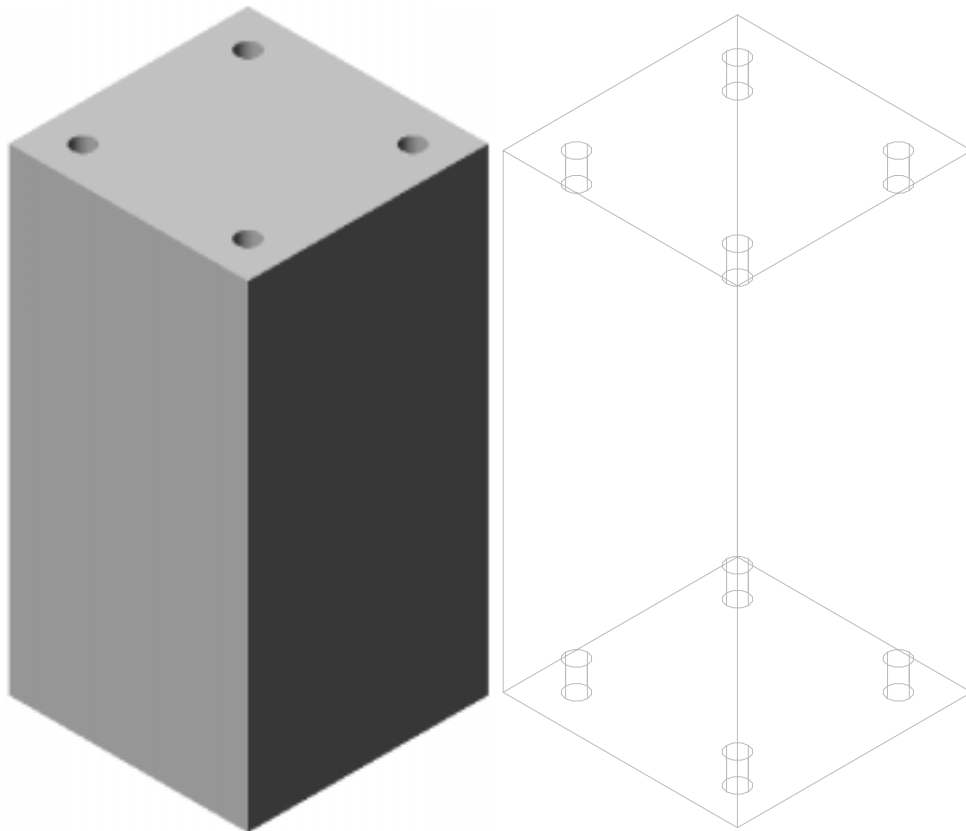
A10. Detailed Working Drawing of the Base.



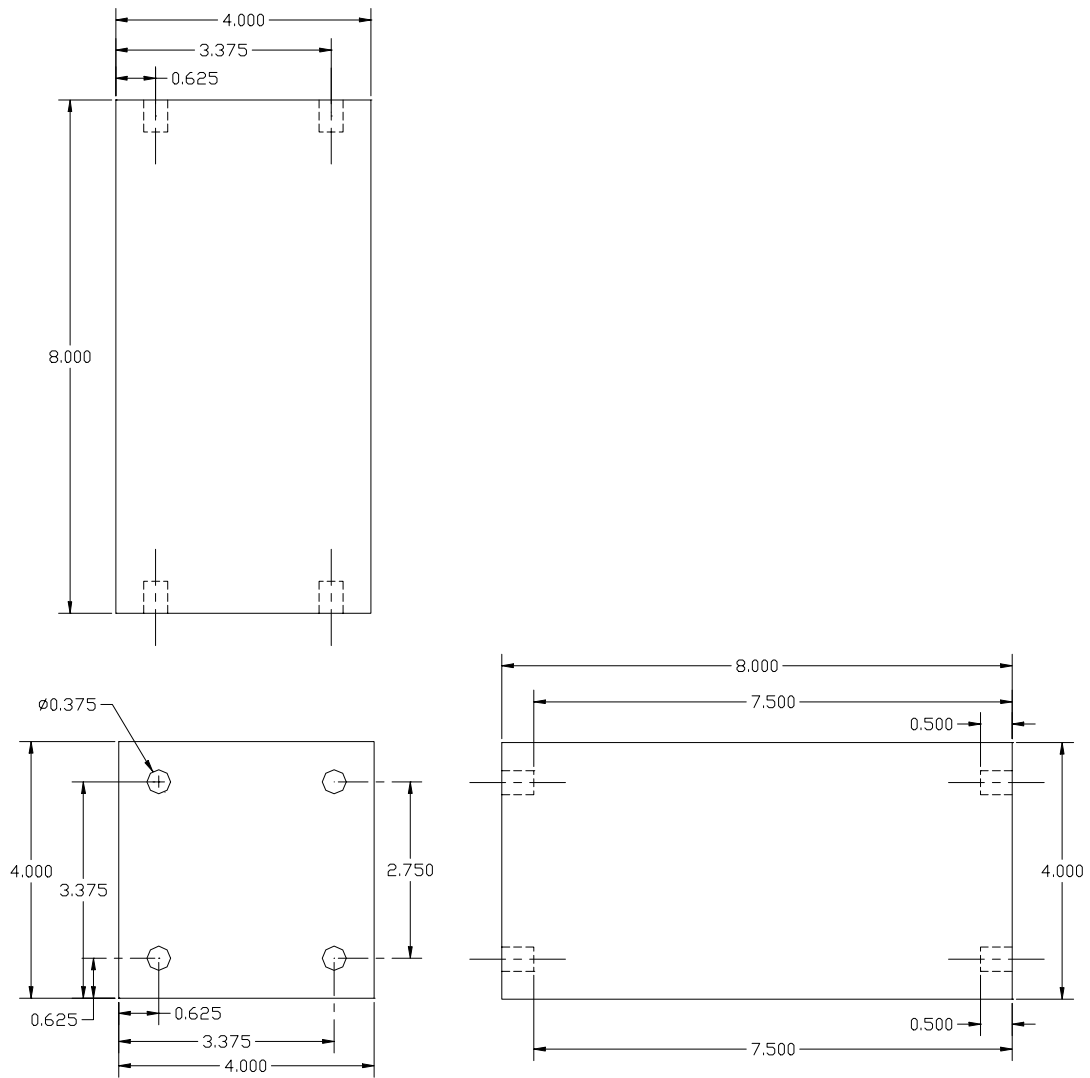
A11. 3-Dimensional Drawing of the Slide.



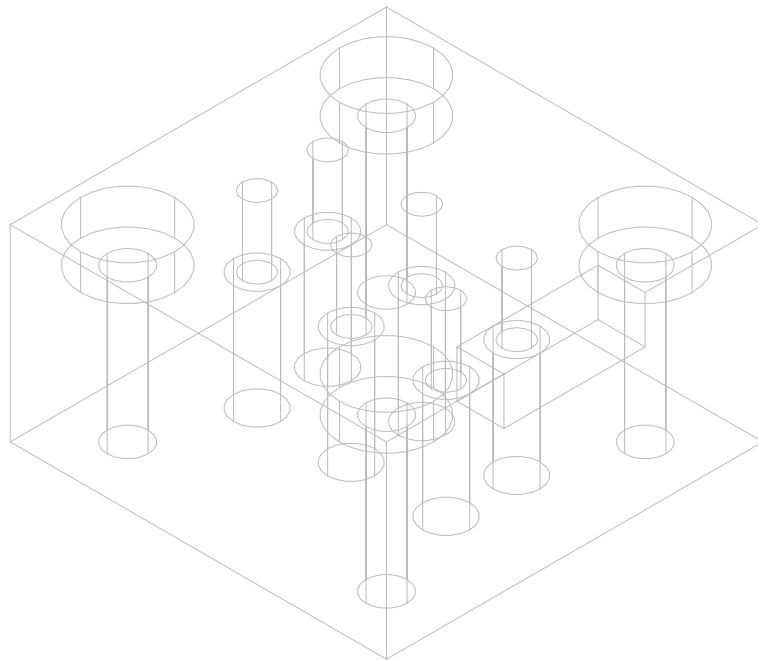
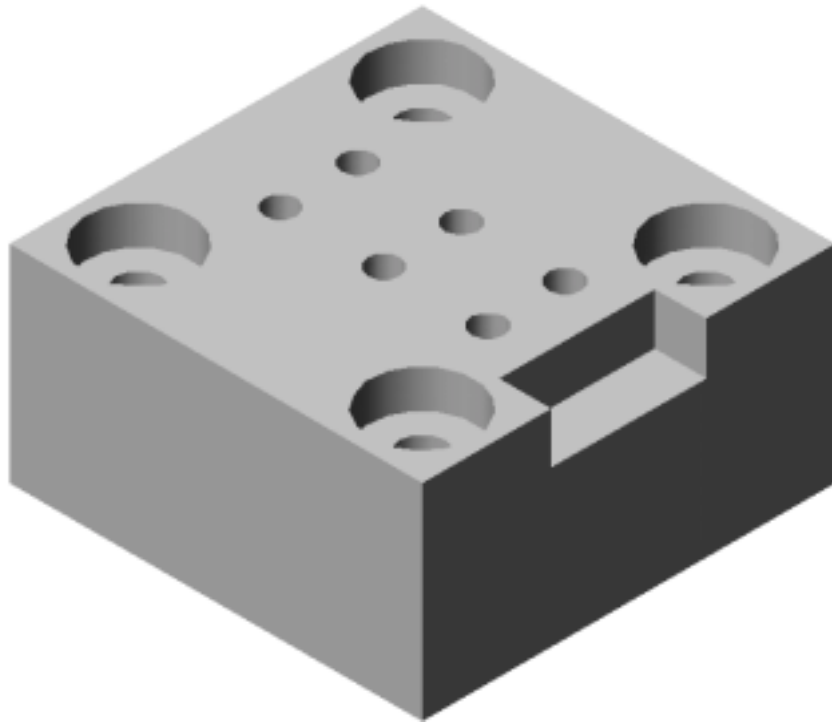
A12. Detailed Working Drawing of the Slide.



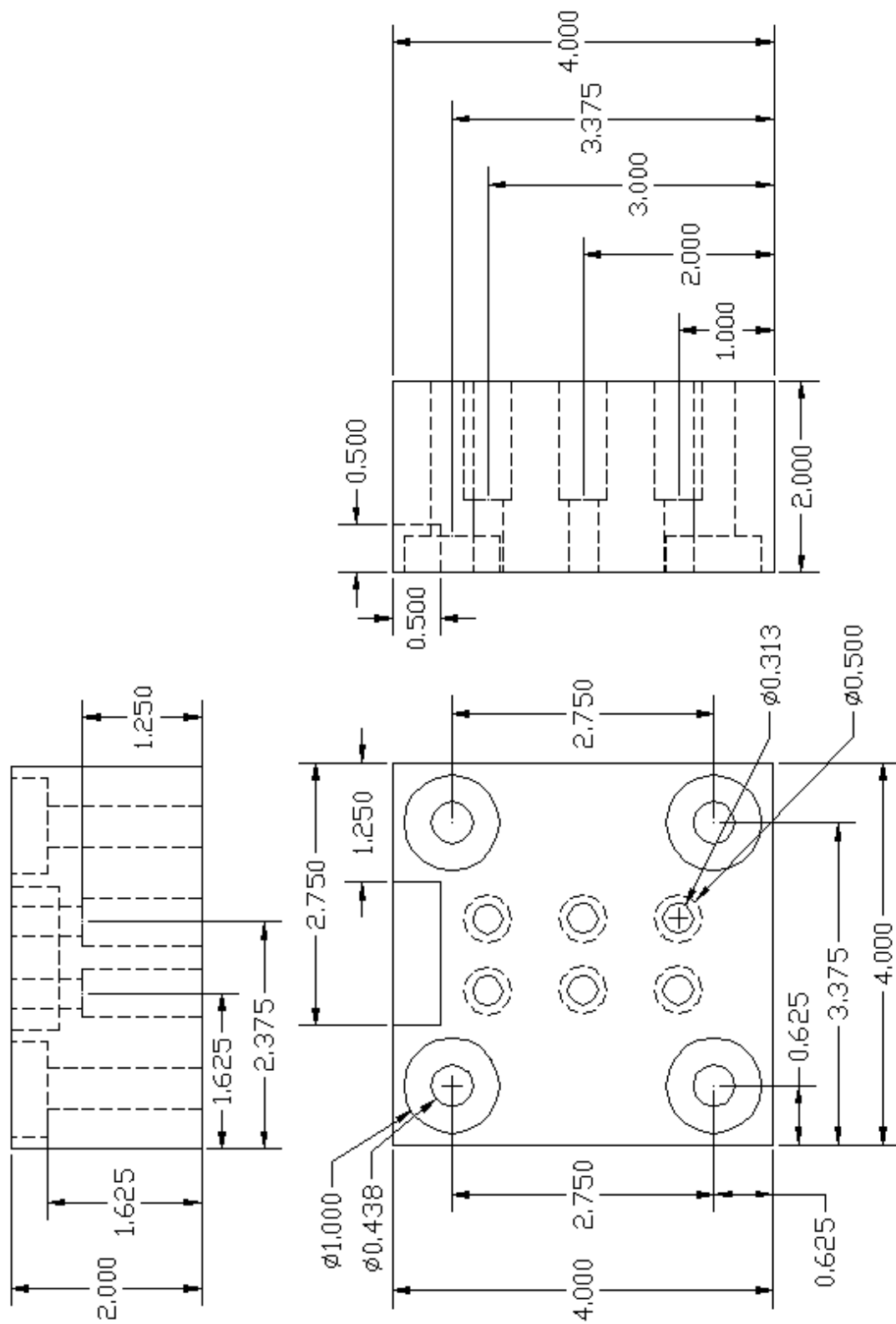
A13. 3-Dimensional Drawing of the Tower.



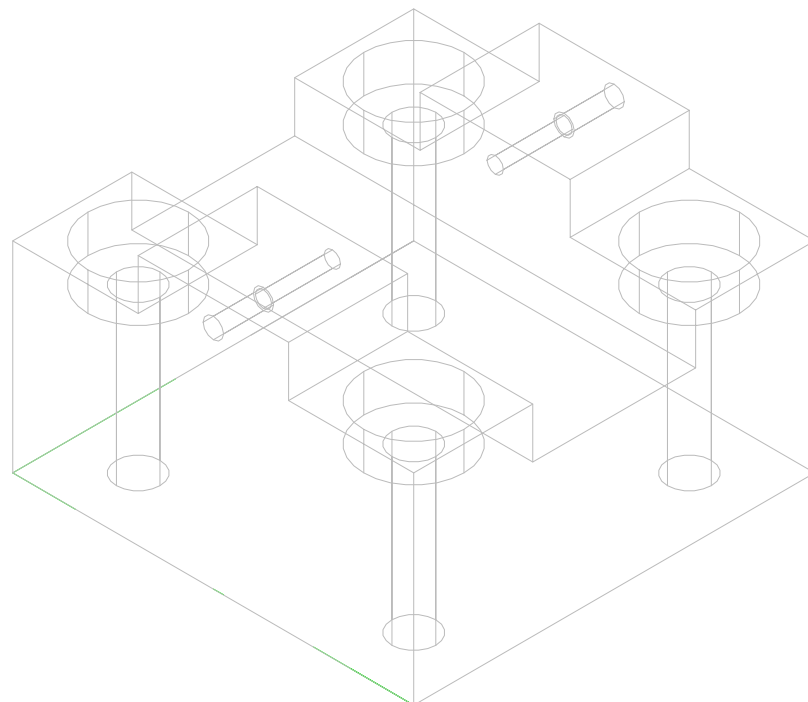
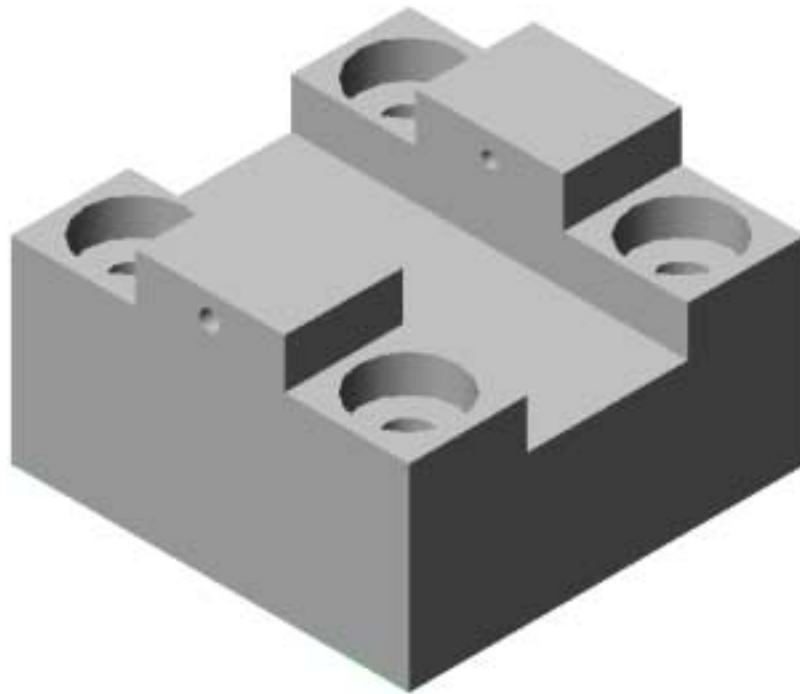
A14. Detailed Working Drawing of the Tower.



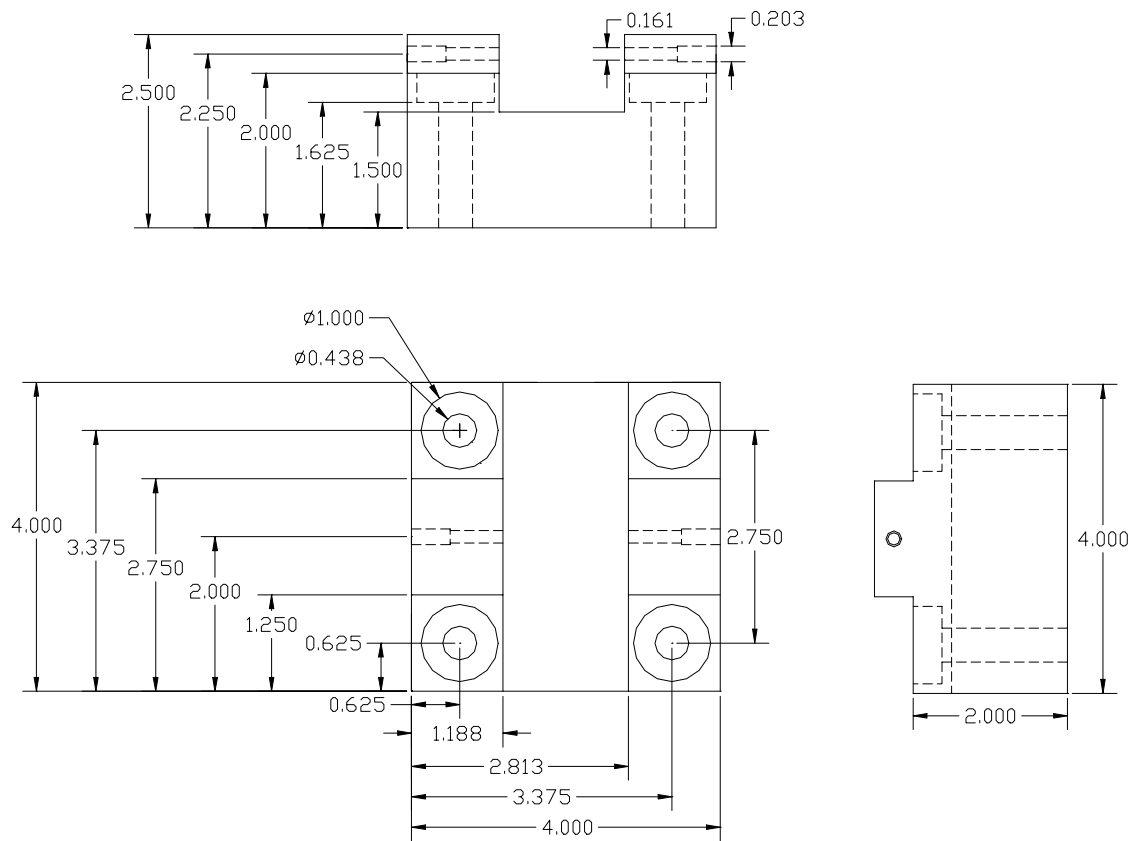
A15. 3-Dimensional Drawing of the Fixed End Condition.



A16. Detailed Working Drawing of the Fixed End Condition.



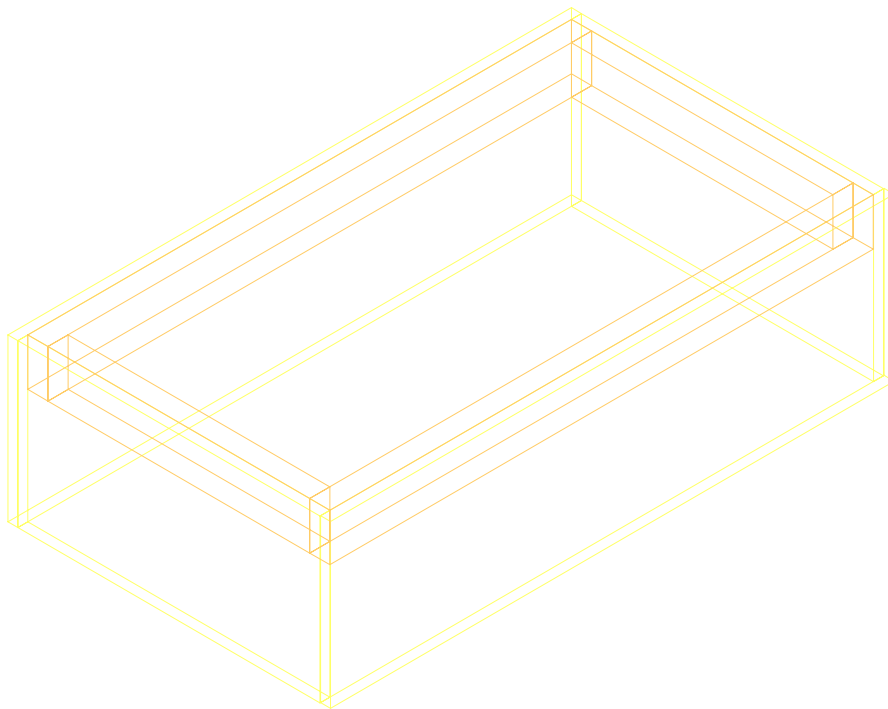
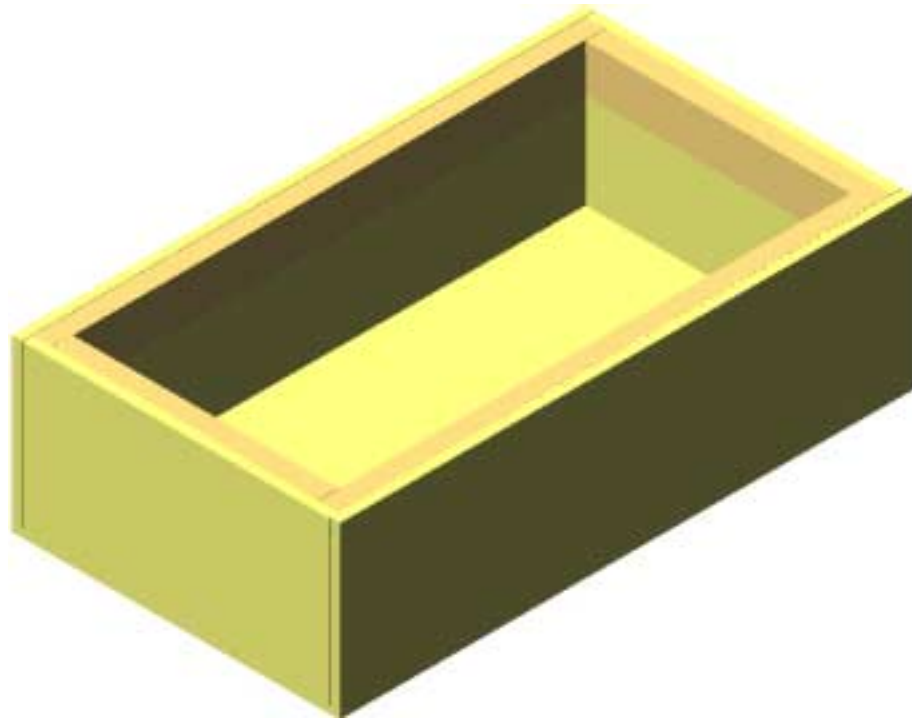
A17. 3-Dimensional Drawing of the Simply Supported End Condition.



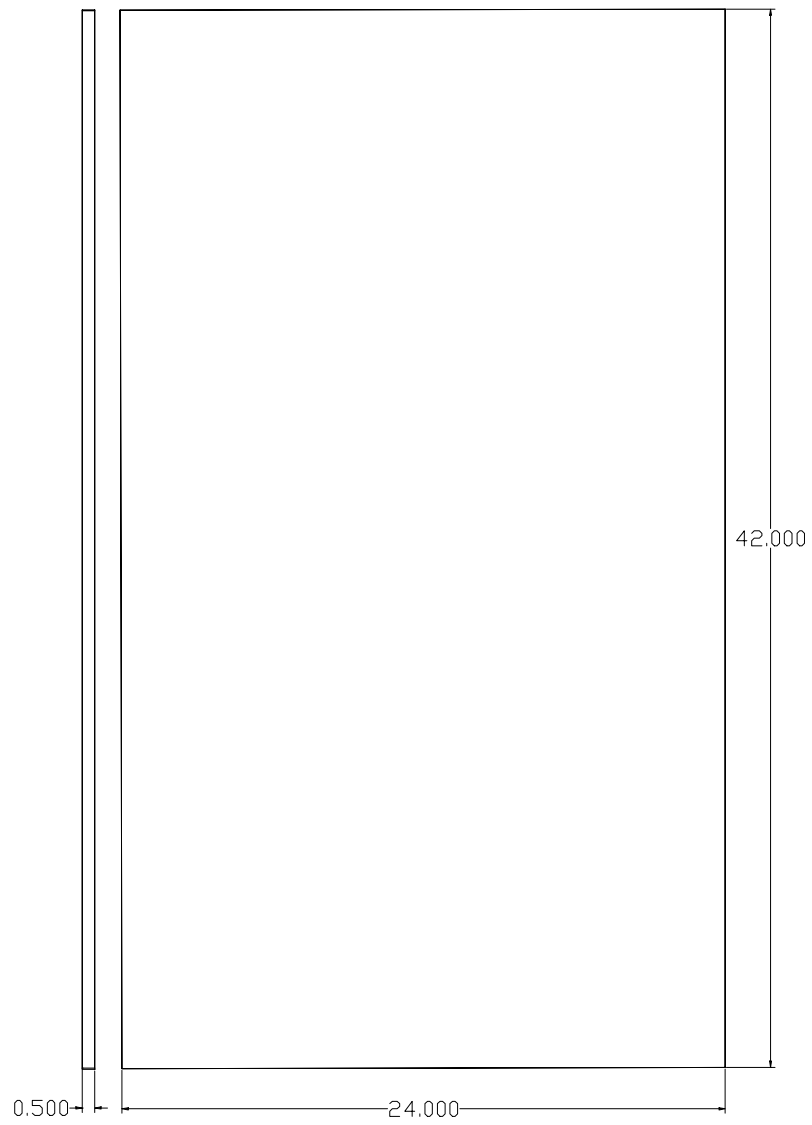
A18. Detailed Working Drawing of the Simply Supported End Condition.

Appendix B

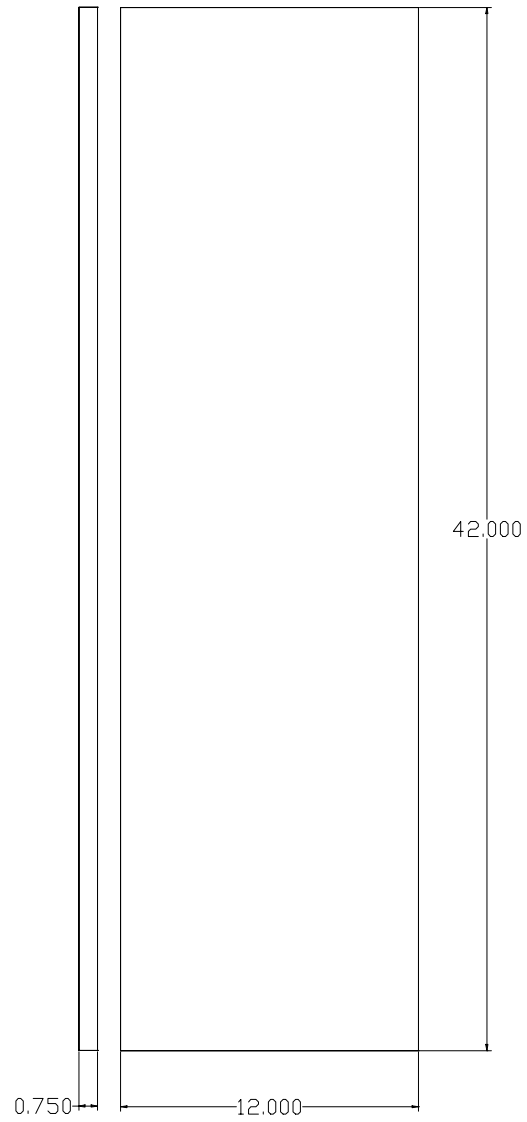
Assembly Drawings of the Baffled Enclosure



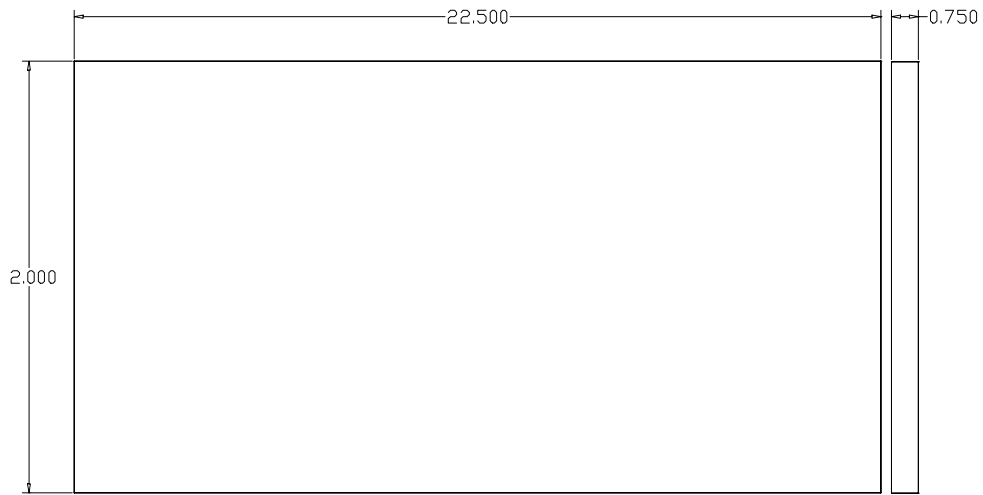
B1. 3-Dimensional Drawing of the Baffled Box.



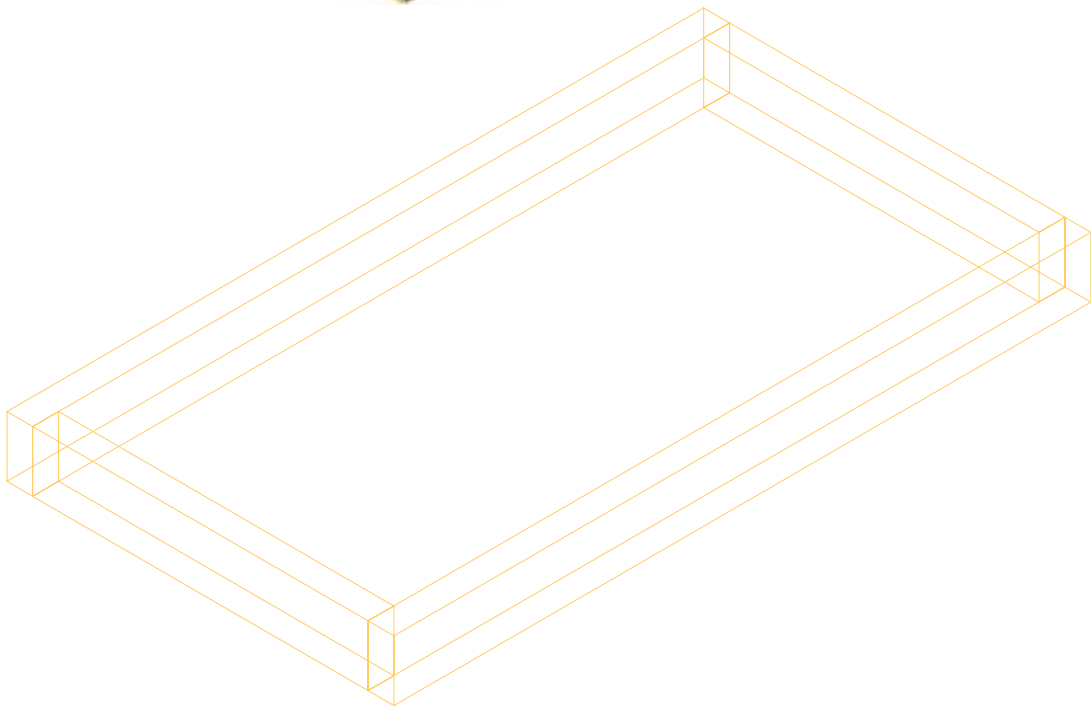
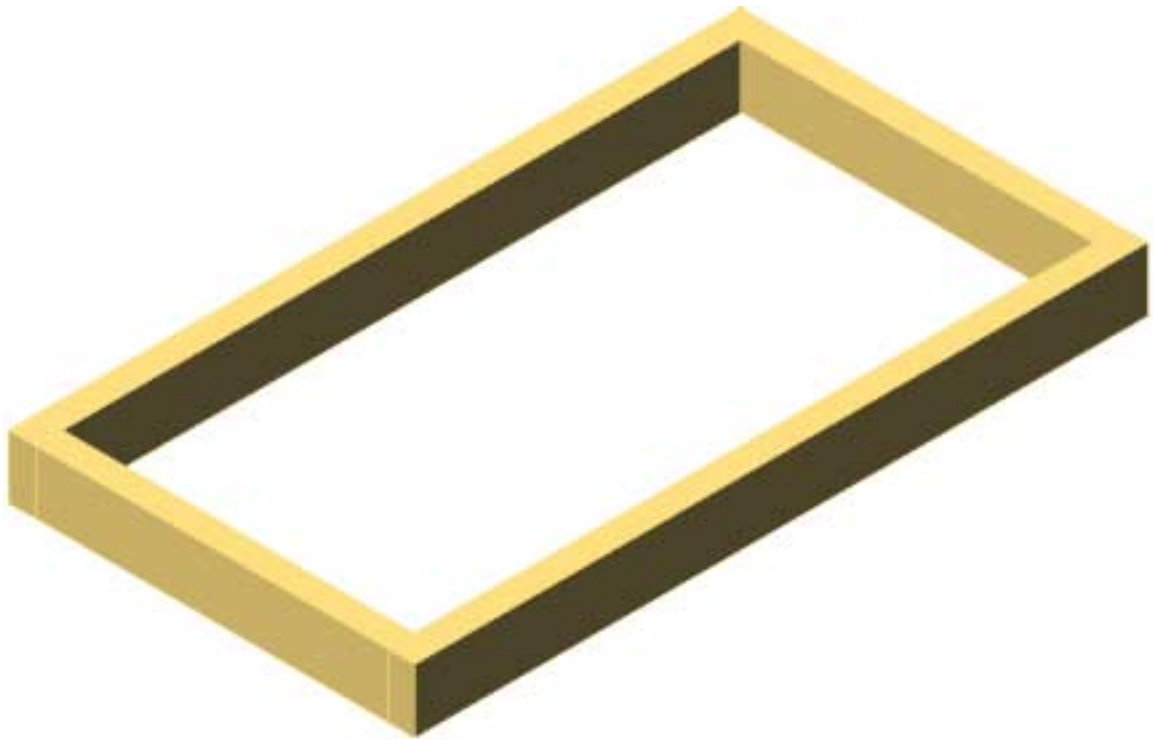
B2. Detailed Working Drawing of the Bottom.



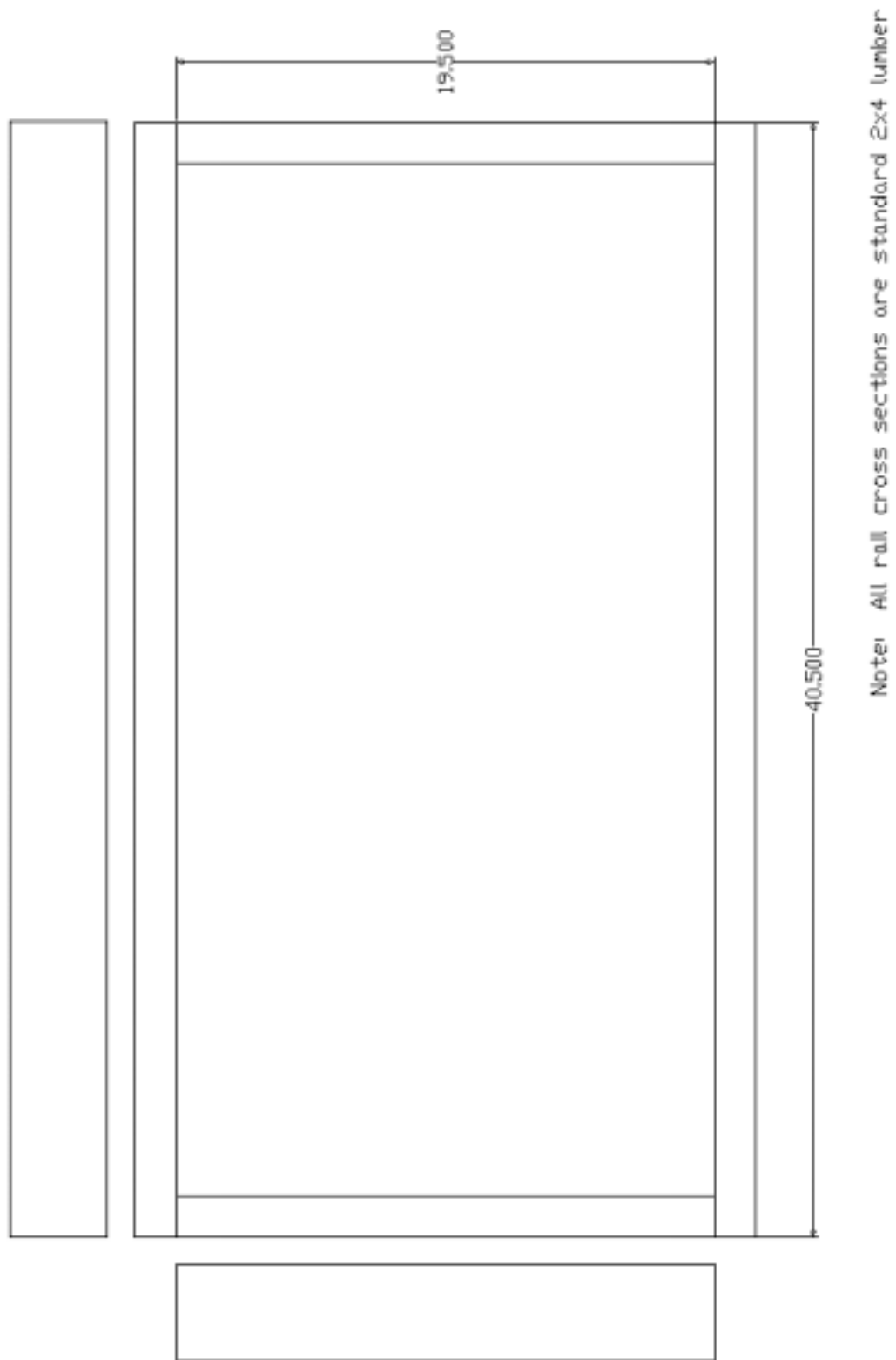
B3. Detailed Working Drawing of the Front and Back Sides.



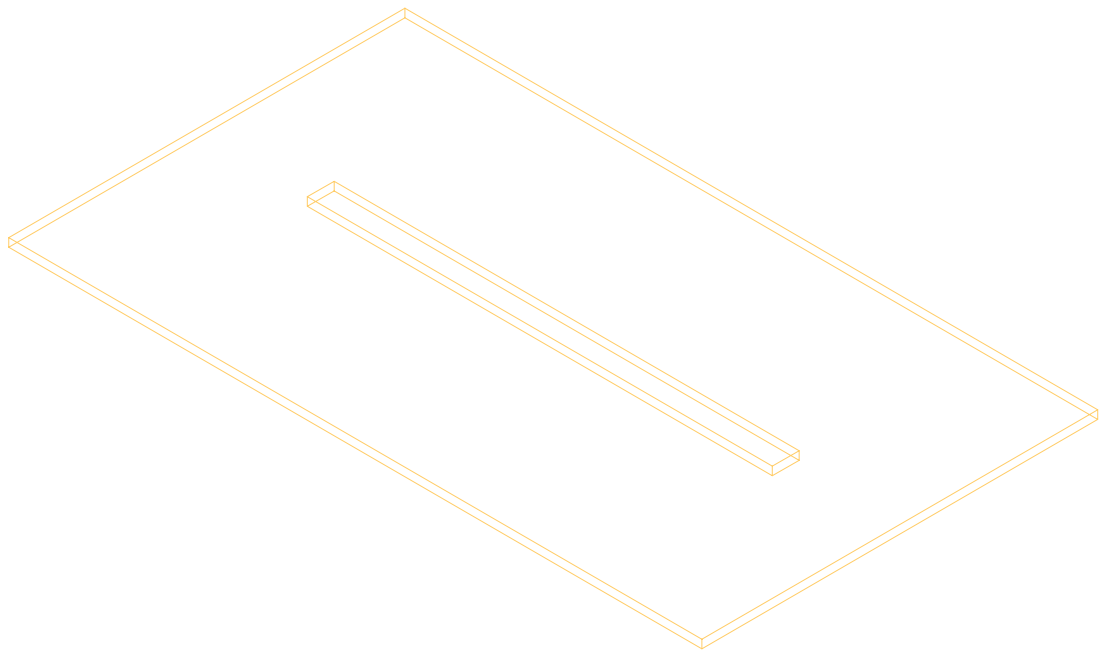
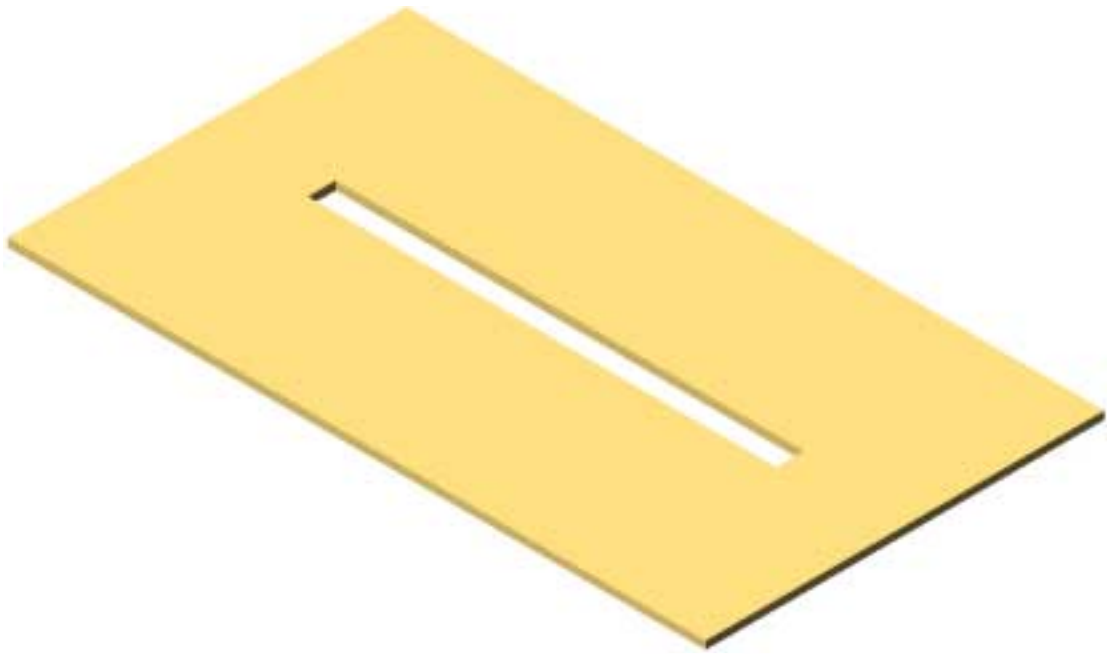
B4. Detailed Working Drawing of the Ends.



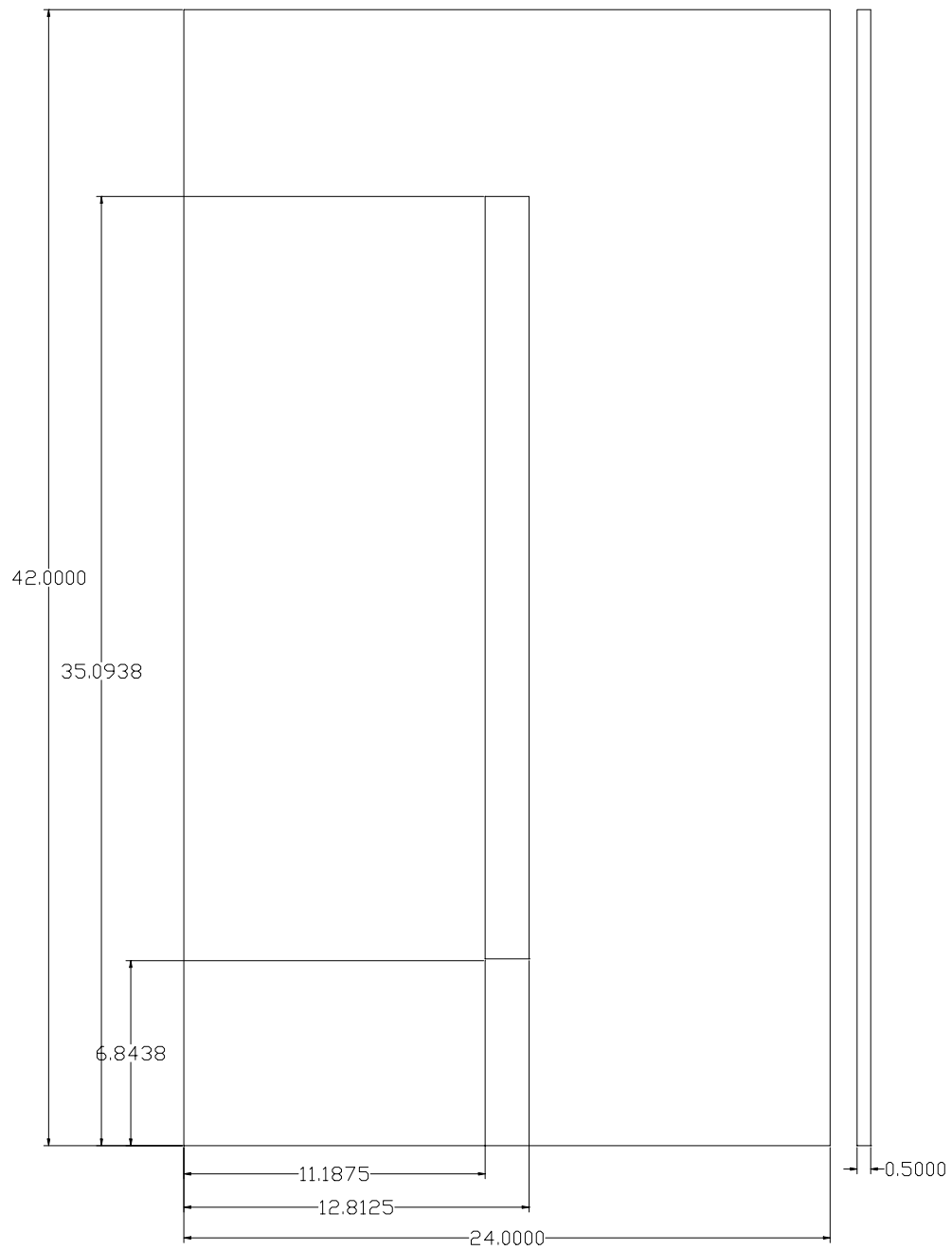
B5. 3-Dimensional Drawing of the Top Reinforcing Rail.



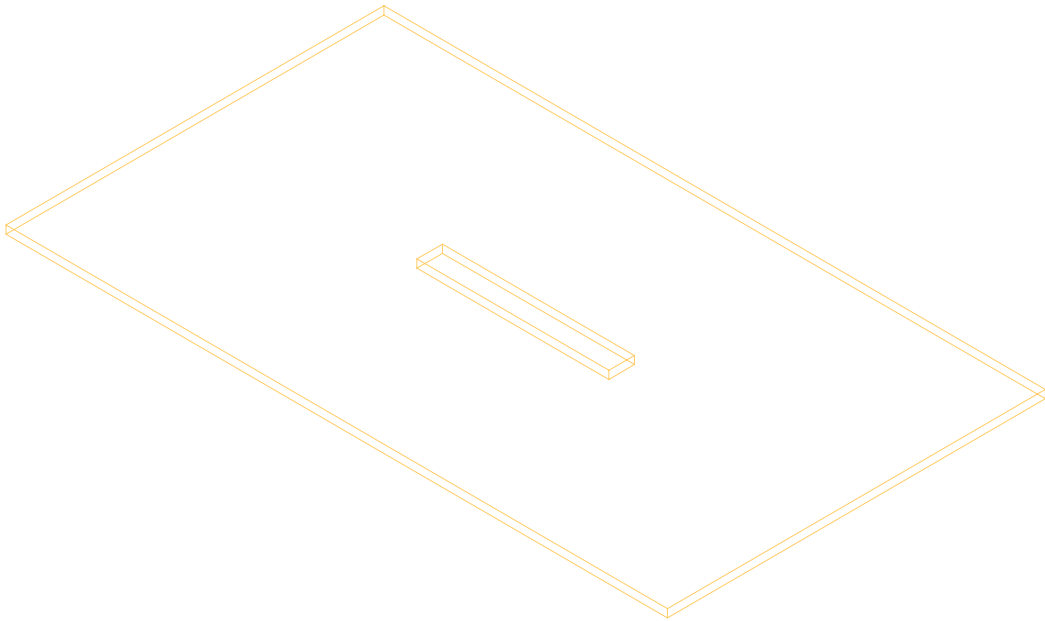
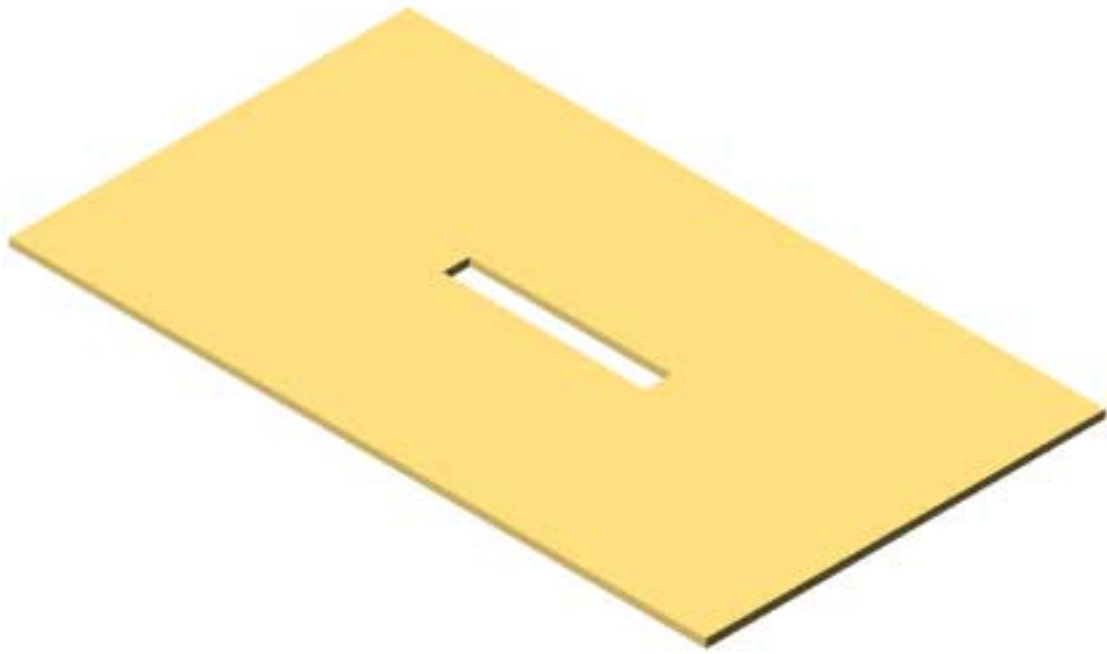
B6. Detailed Working Drawing of the Top Reinforcing Rail.



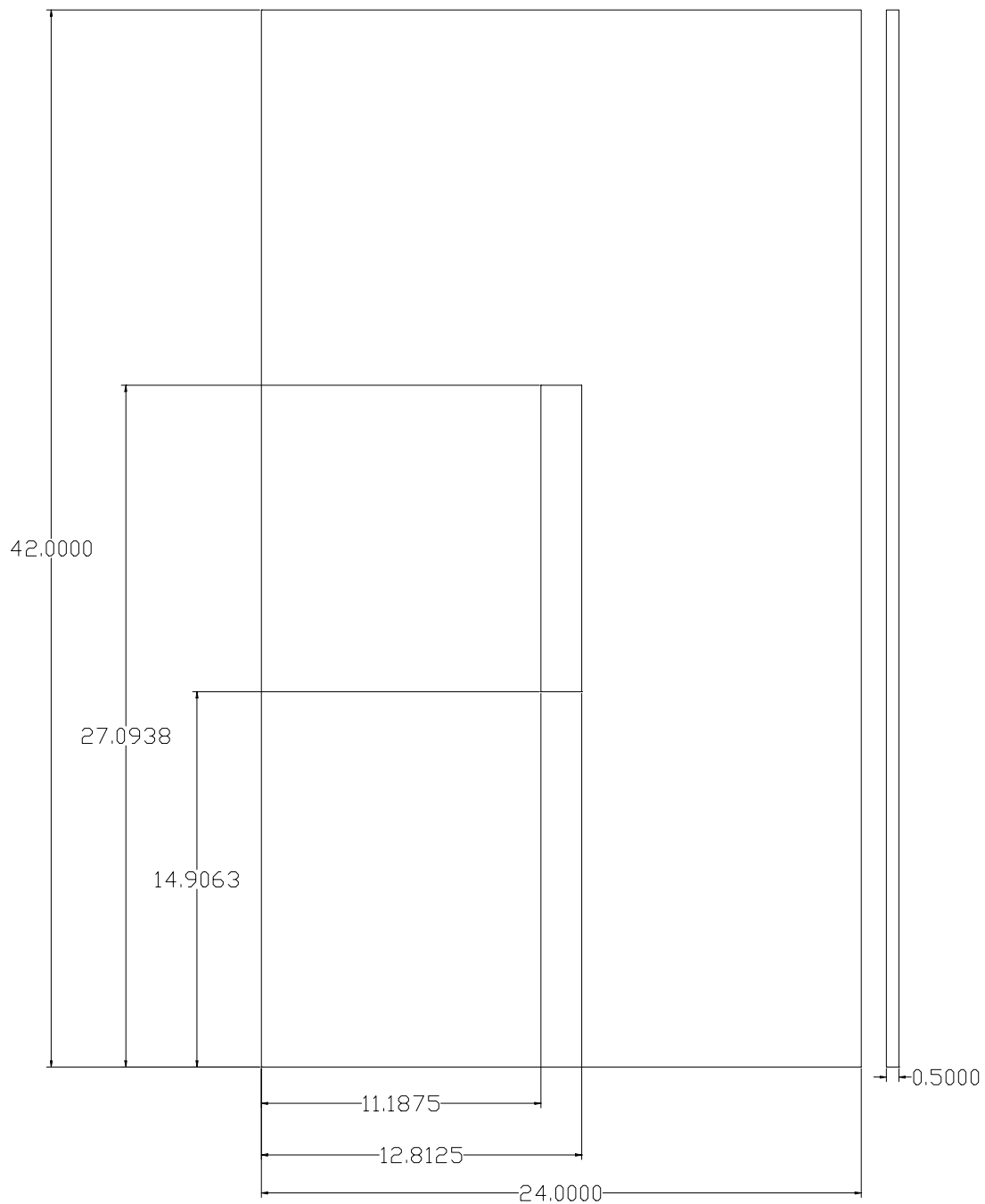
B7. 3-Dimensional Drawing of the Fixed-Fixed Top.



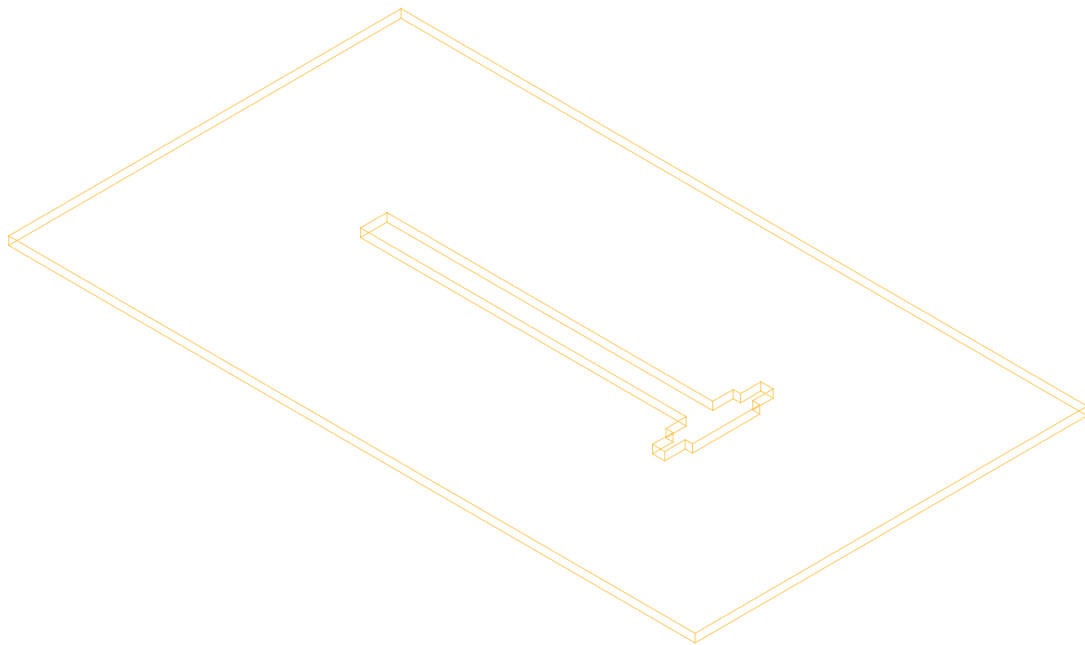
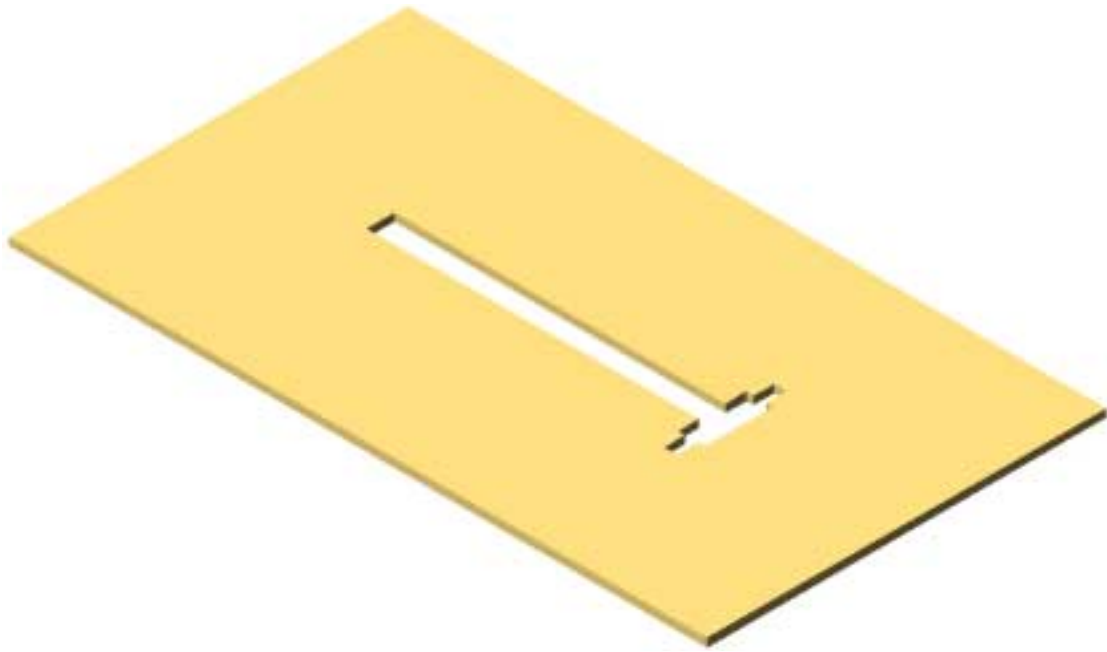
B8. Detailed Working Drawing of the Fixed-Fixed Top.



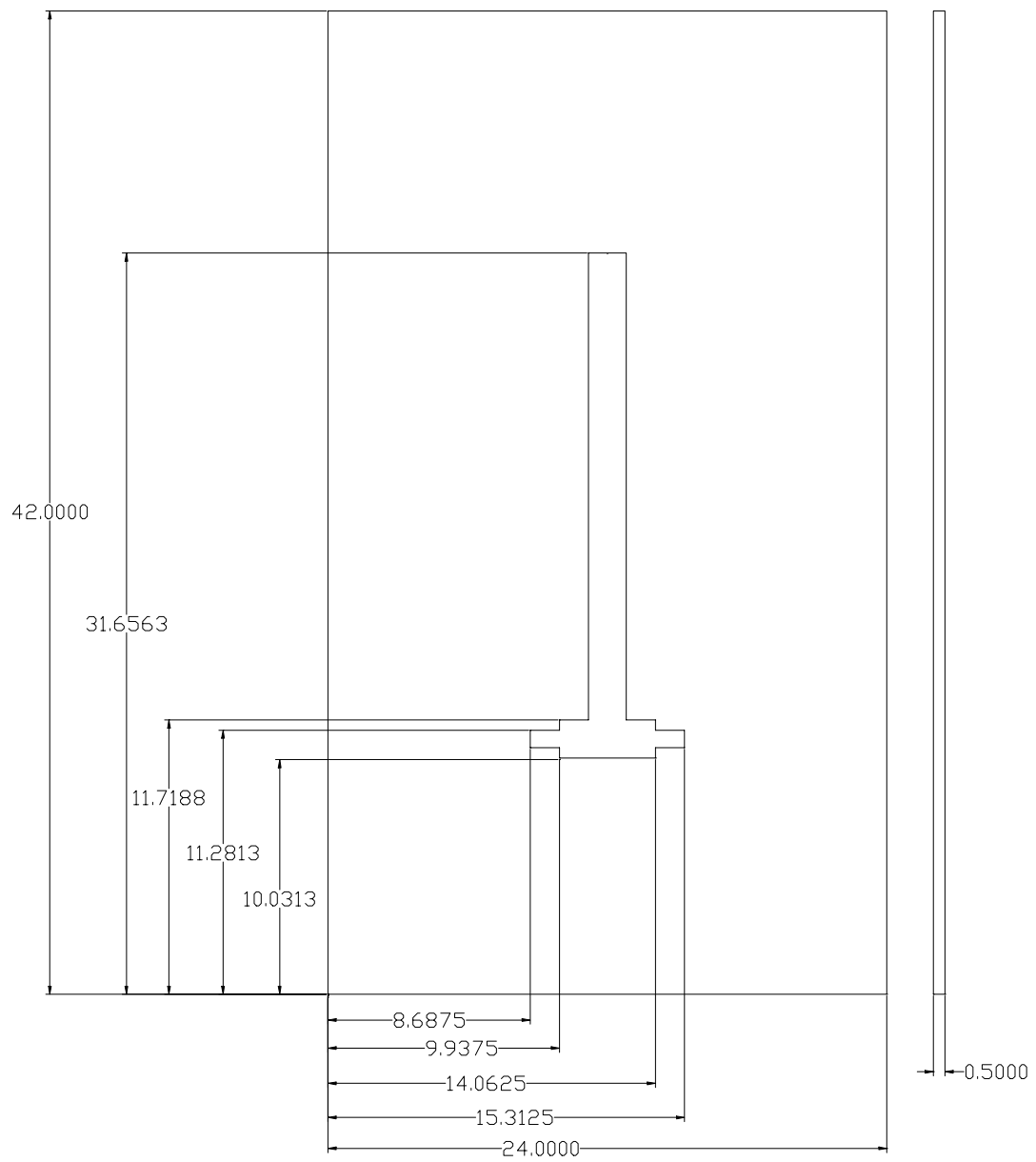
B9. 3-Dimensional Drawing of the Fixed-Free Top.



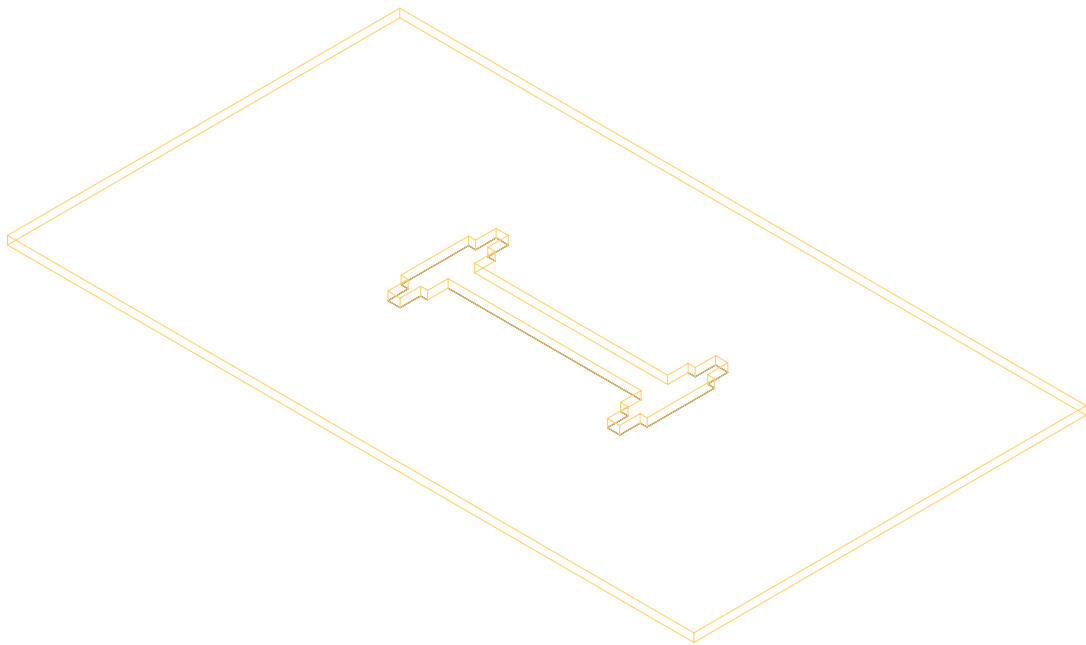
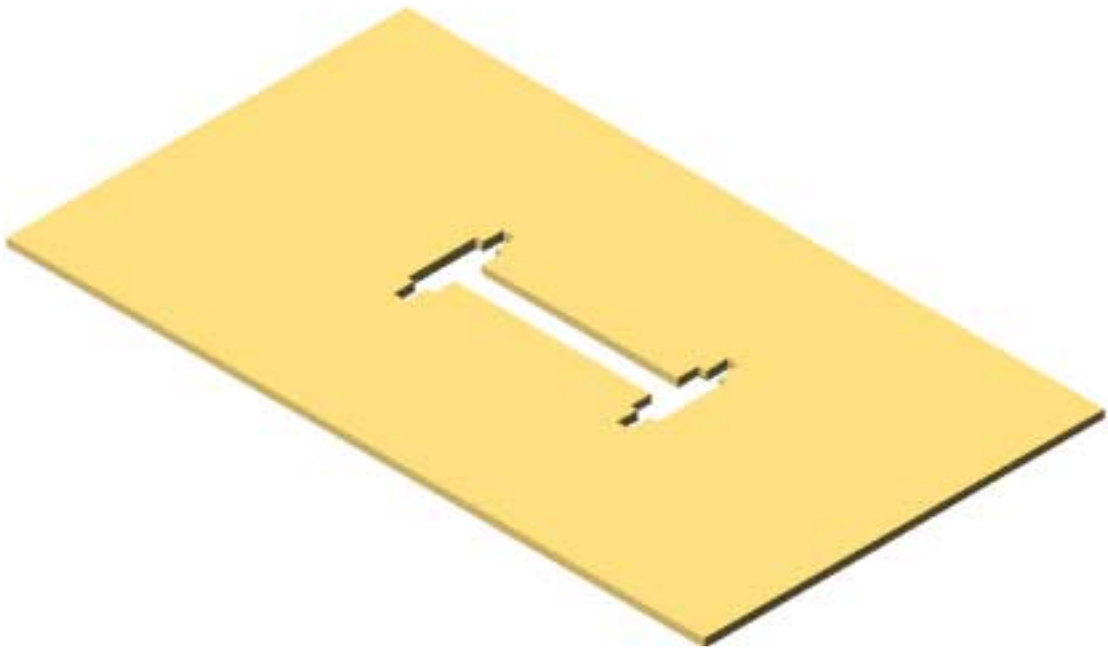
B10. Detailed Working Drawing of the Fixed-Free Top.



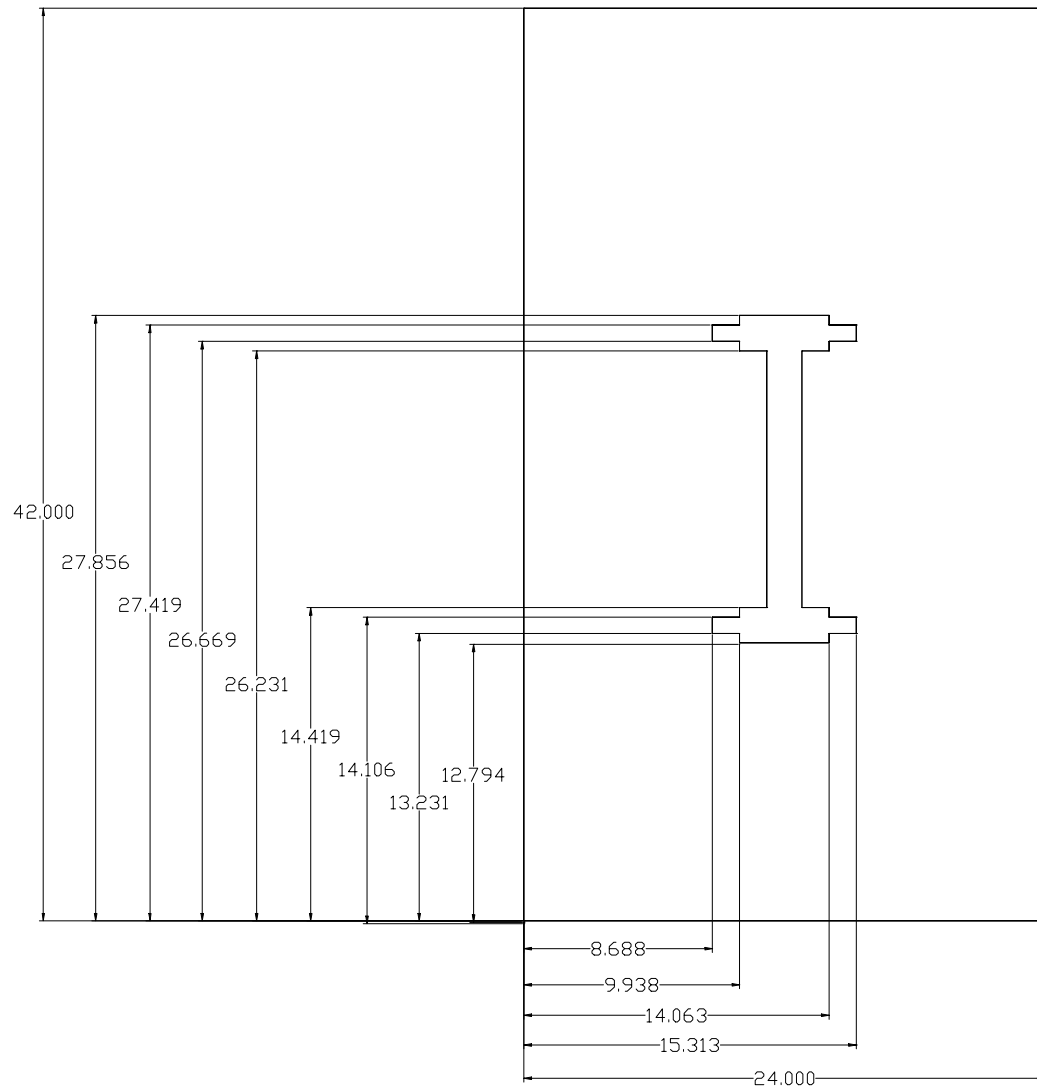
B11. 3-Dimensional Drawing of the Fixed-Simply Supported Top.



B12. Detailed Working Drawing of the Fixed-Simply Supported Top.



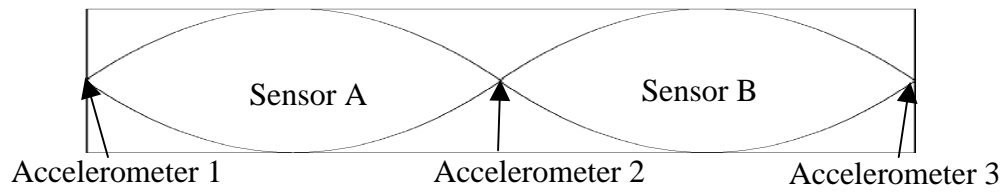
B13. 3-Dimensional Drawing of the Simply Supported-Simply Supported Top.



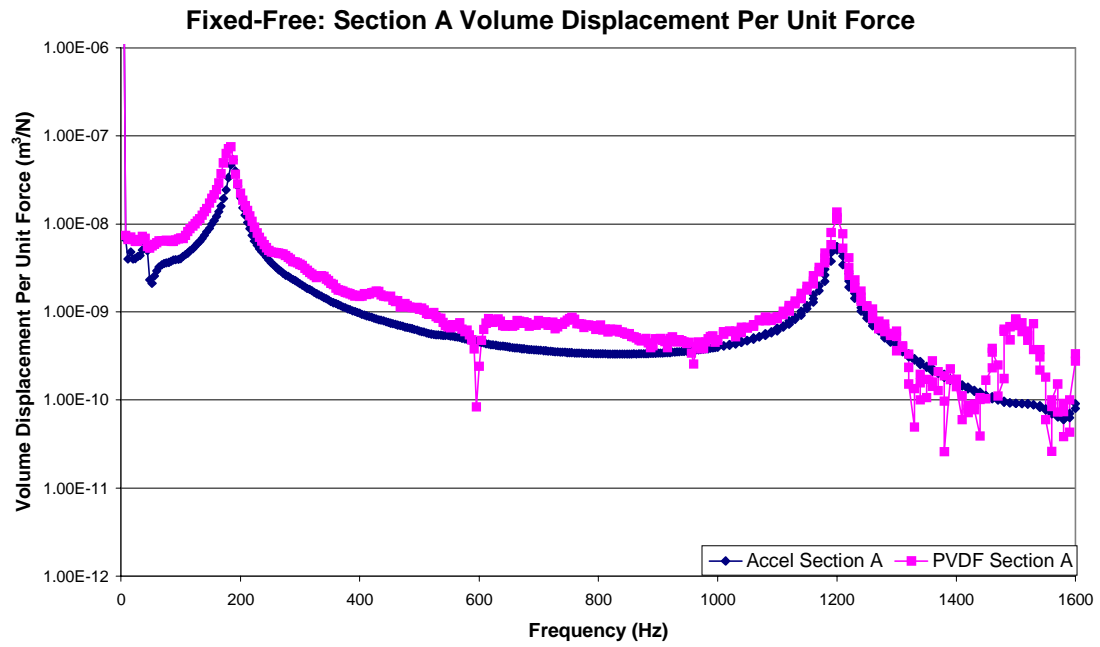
B14. Detailed Working Drawing of the Simply Supported-Simply Supported Top.

Appendix C

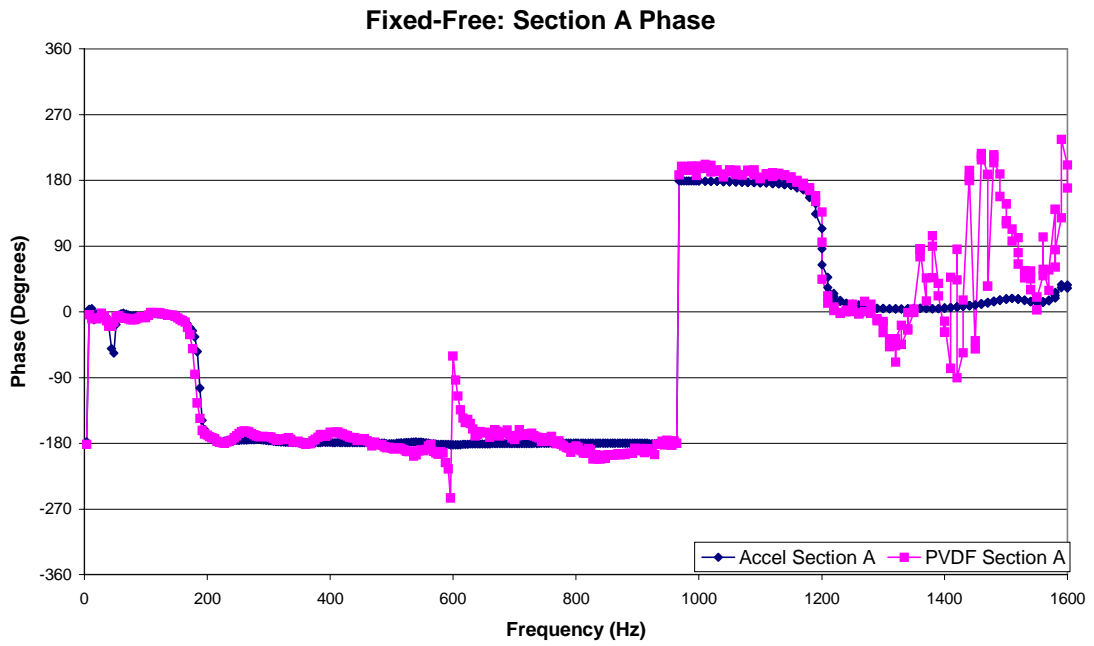
Volume Displacement per Unit Force, Phase, and Power Spectrum Plots for the Fixed-Free Beam



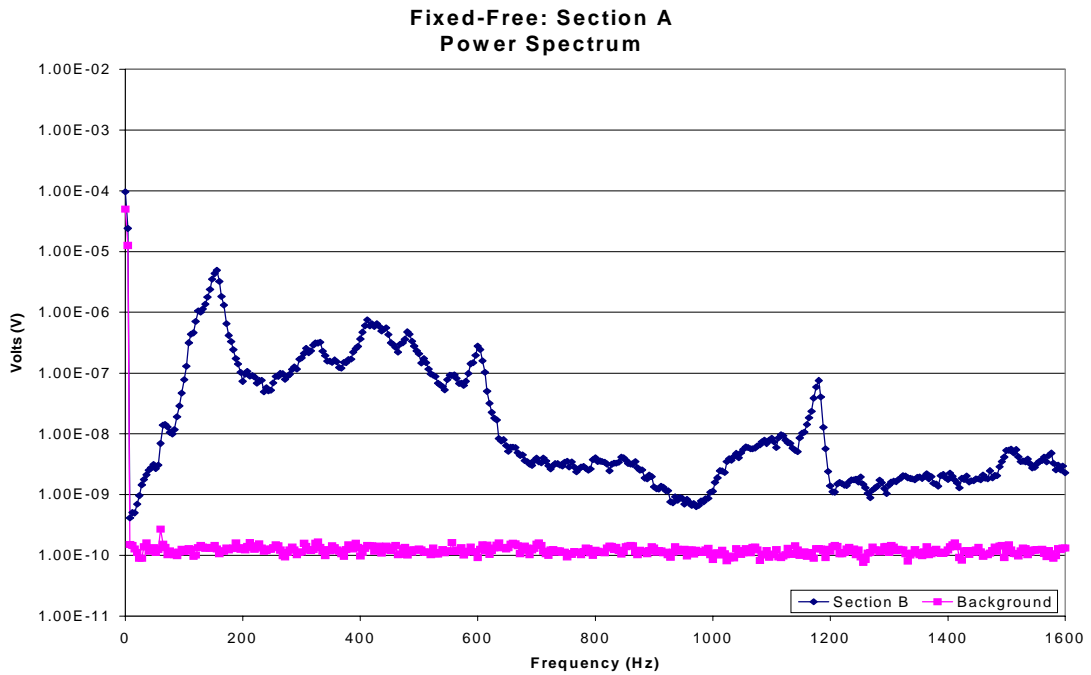
C1. Two Section Local Sensor Layout.



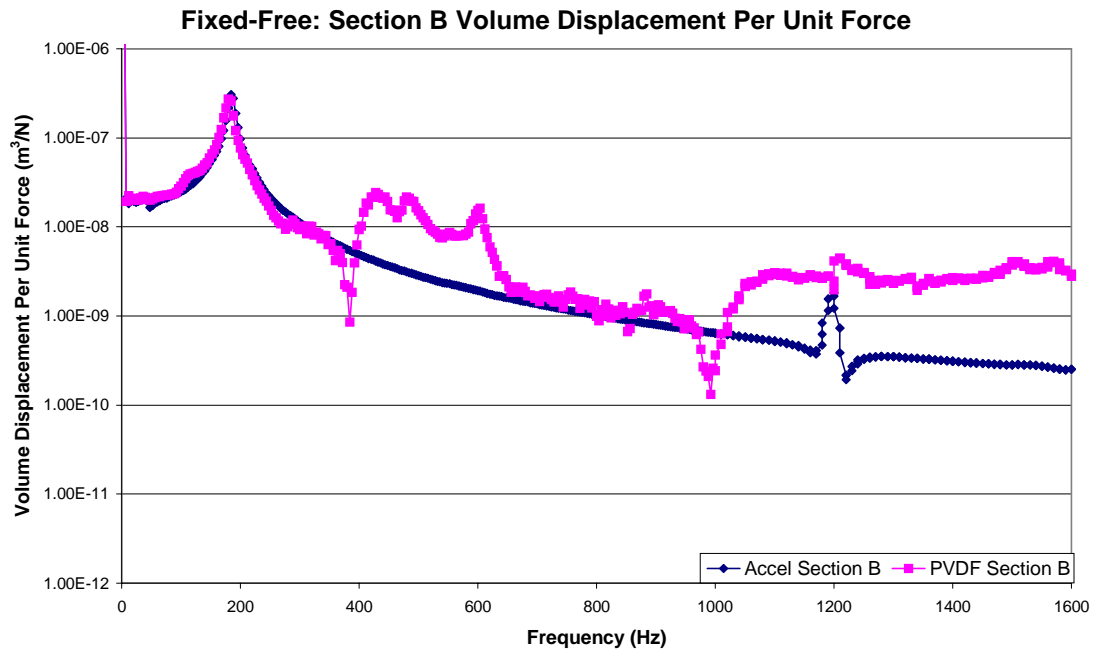
C2. Fixed-Free Volume Displacement for Section A of the Double Sensor.



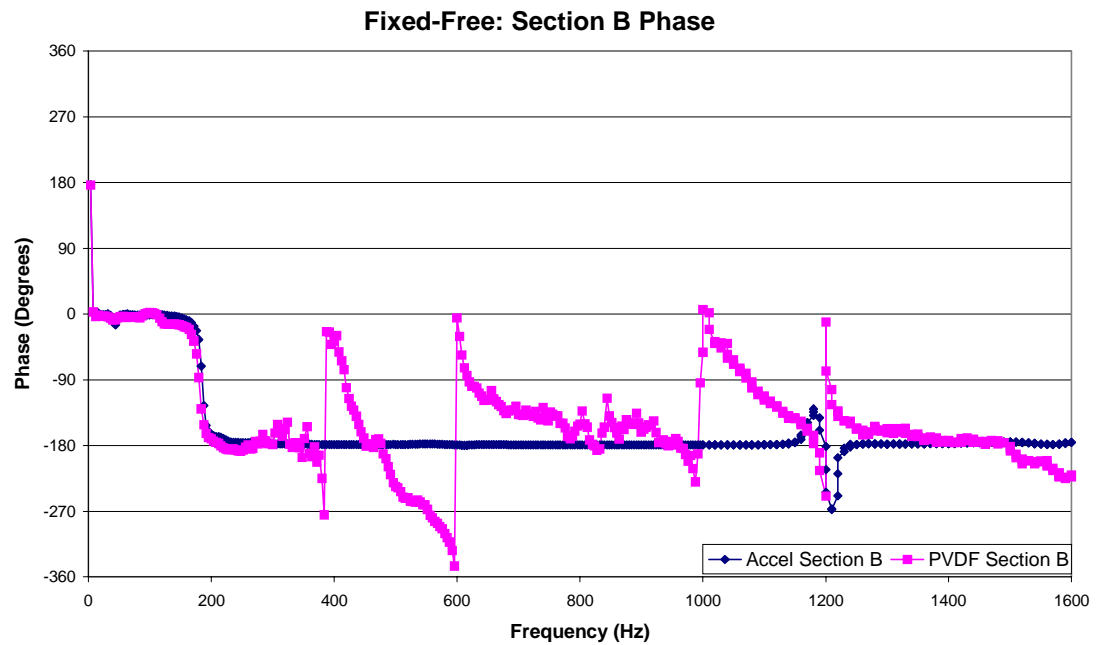
C3. Fixed-Free Phase for Section A of the Double Sensor.



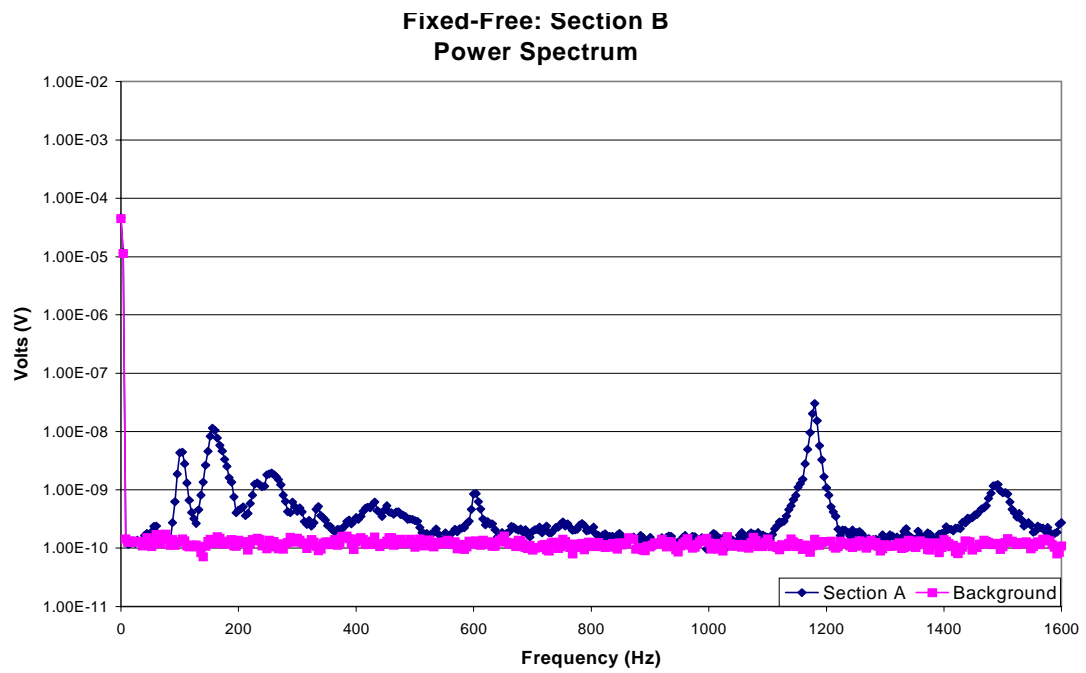
C4. Power Spectrum for Section A of the Two Section Local Sensor.



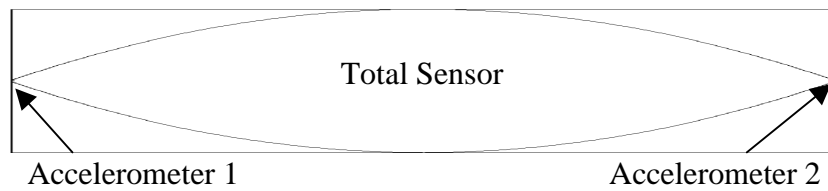
C5. Fixed-Free Volume Displacement for Section B of the Double Sensor.



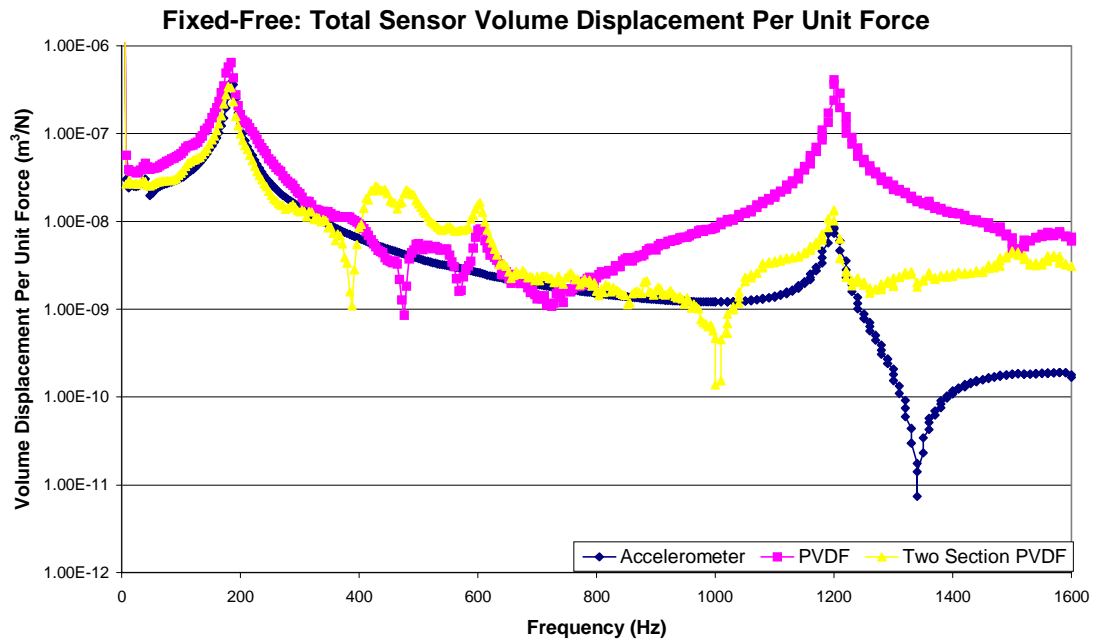
C6. Fixed-Free Phase For Section B of the Double Sensor.



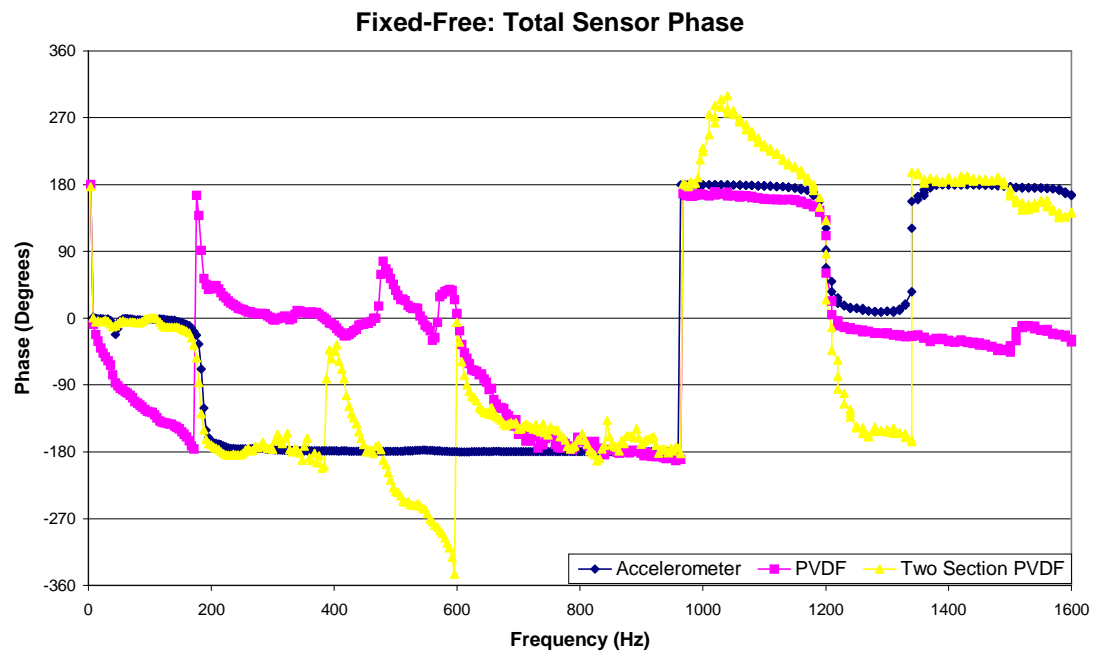
C7. Power Spectrum for Section B of the Two Section Local Sensor.



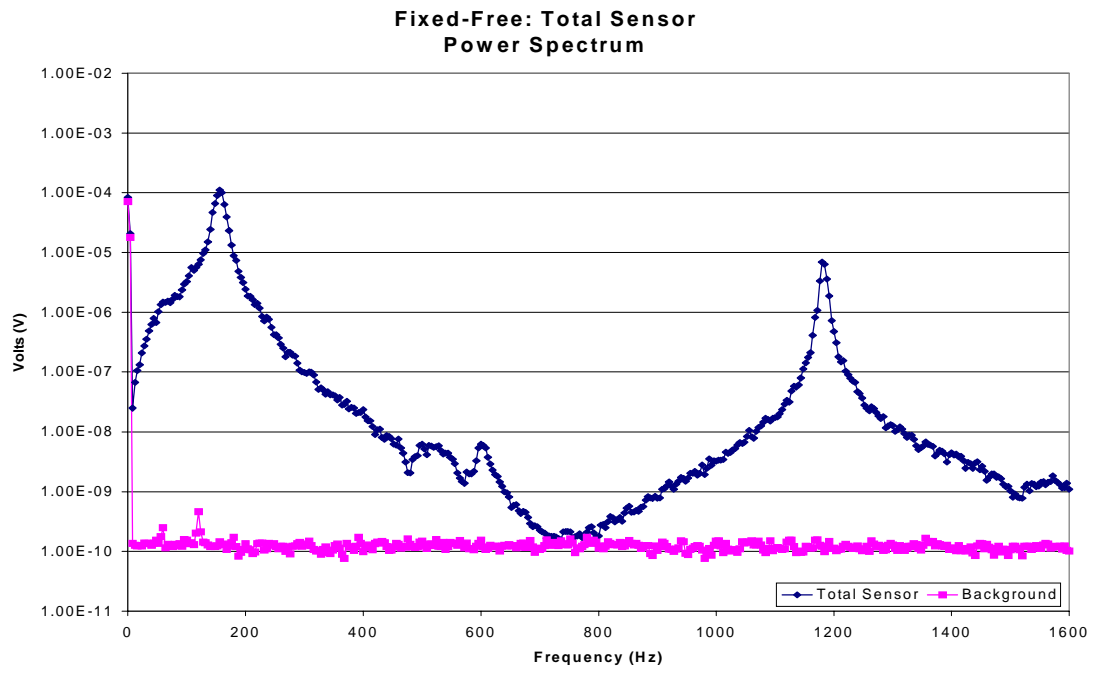
C8. Total Sensor Layout.



C9. Fixed-Free Total Volume Displacement.



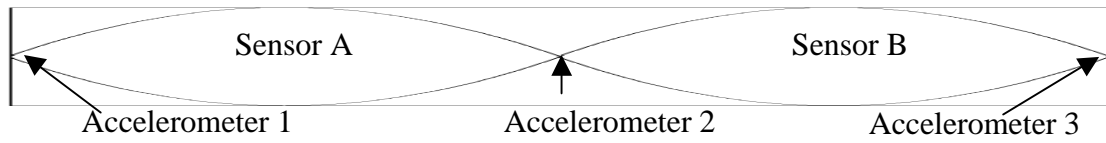
C10. Fixed-Free Total Phase.



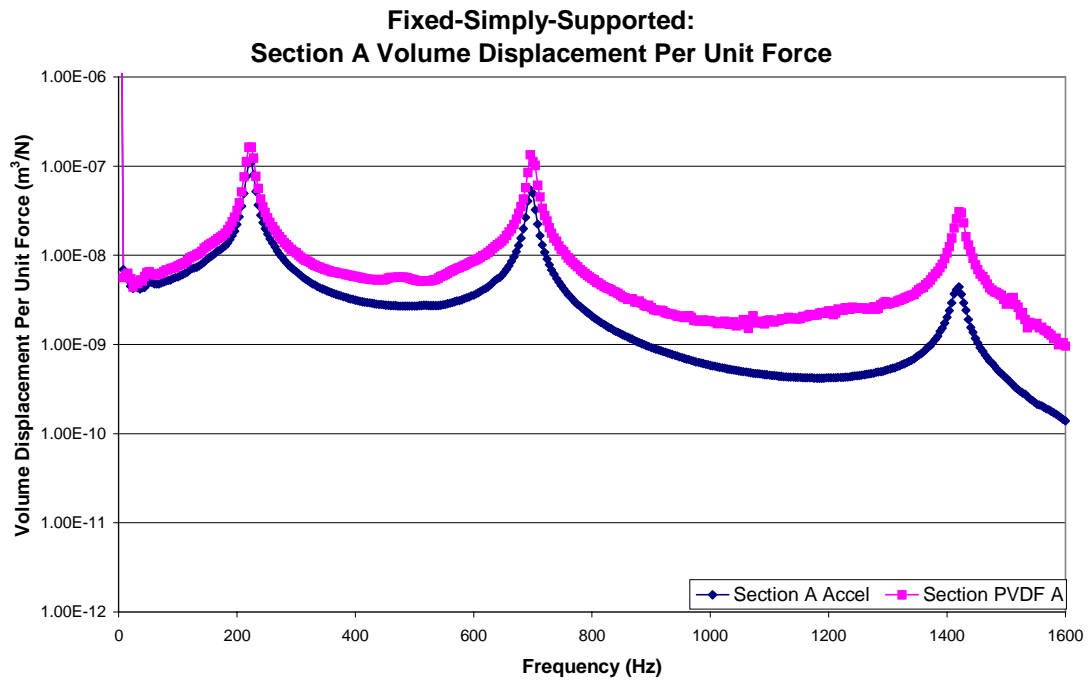
C11. Power Spectrum for the Total Sensor.

Appendix D

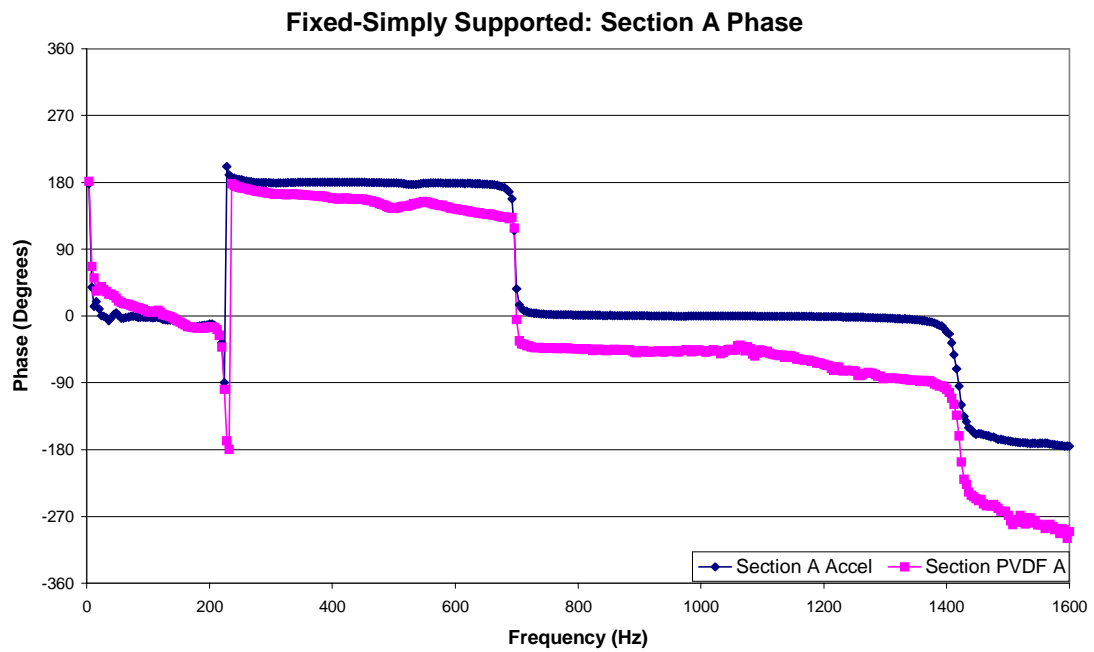
Volume Displacement per Unit Force, Phase, and Power Spectrum
Plots for the Fixed-Simply Supported Beam



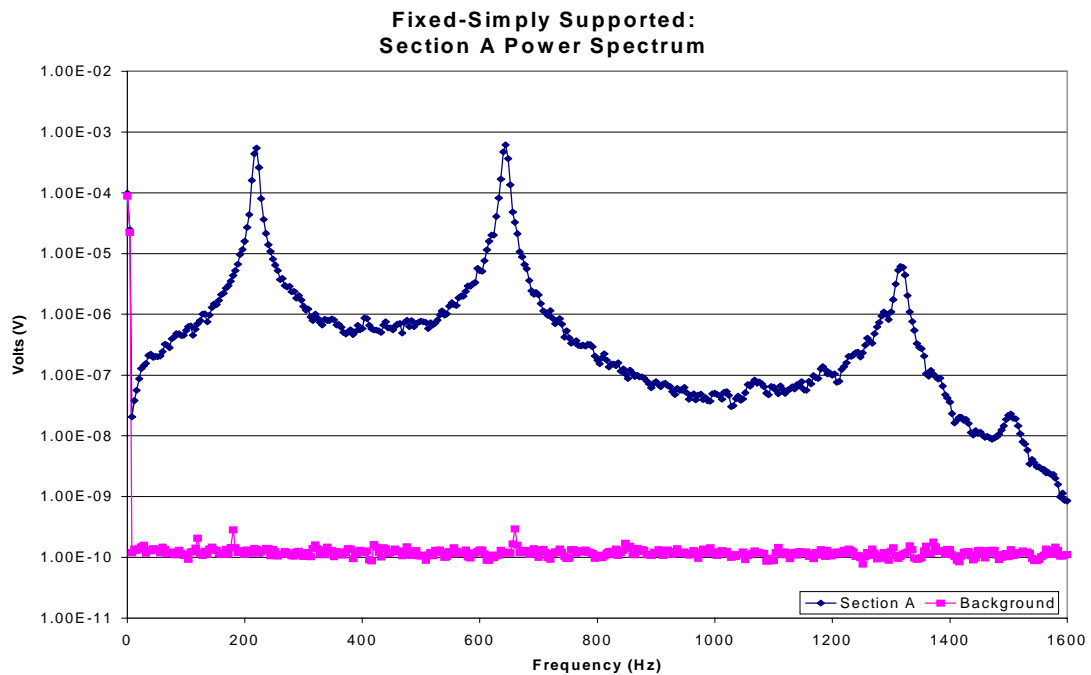
D1. Two Section Local Sensor Layout.



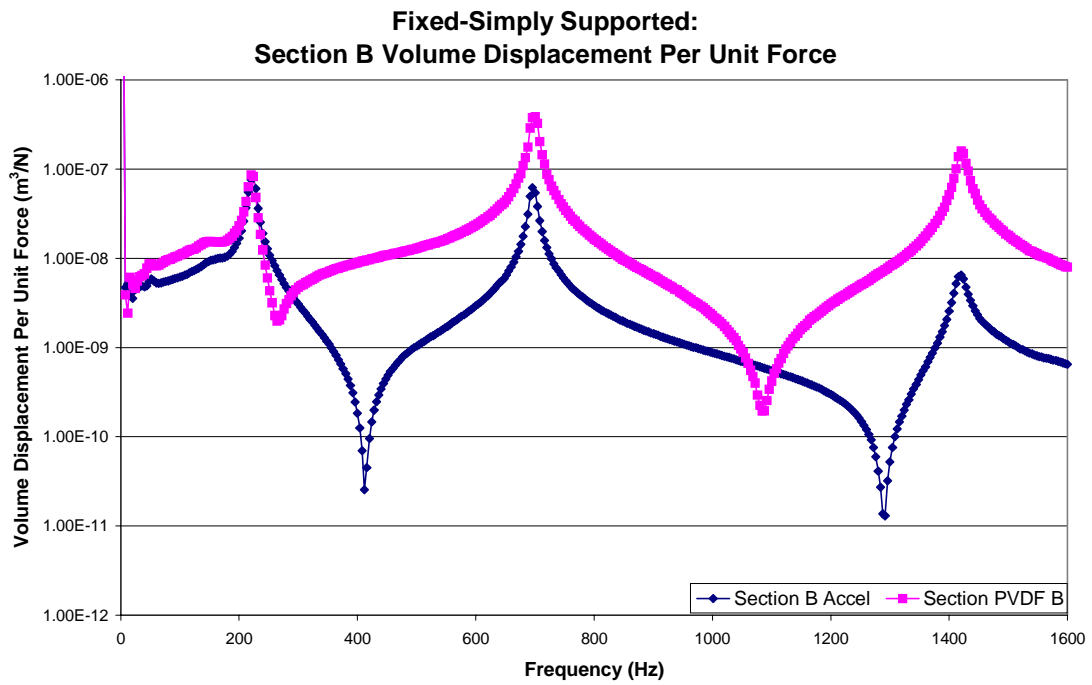
D2. Fixed-Hinged Volume Displacement for Section A of the Double Sensor.



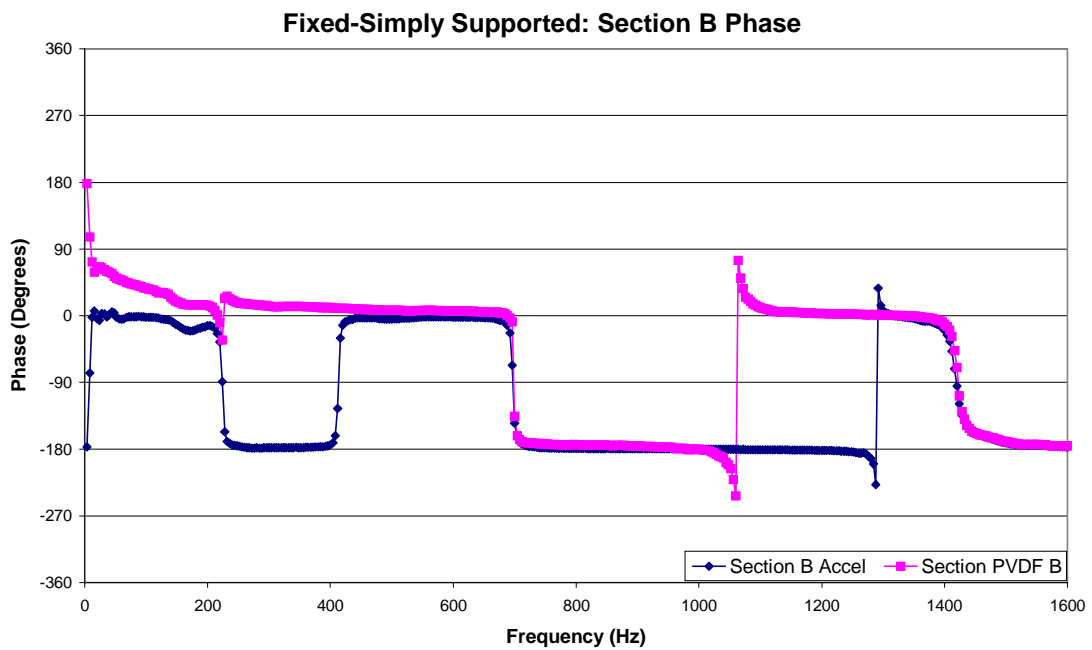
D3. Fixed-Hinged Phase for Section A of the Double Sensor.



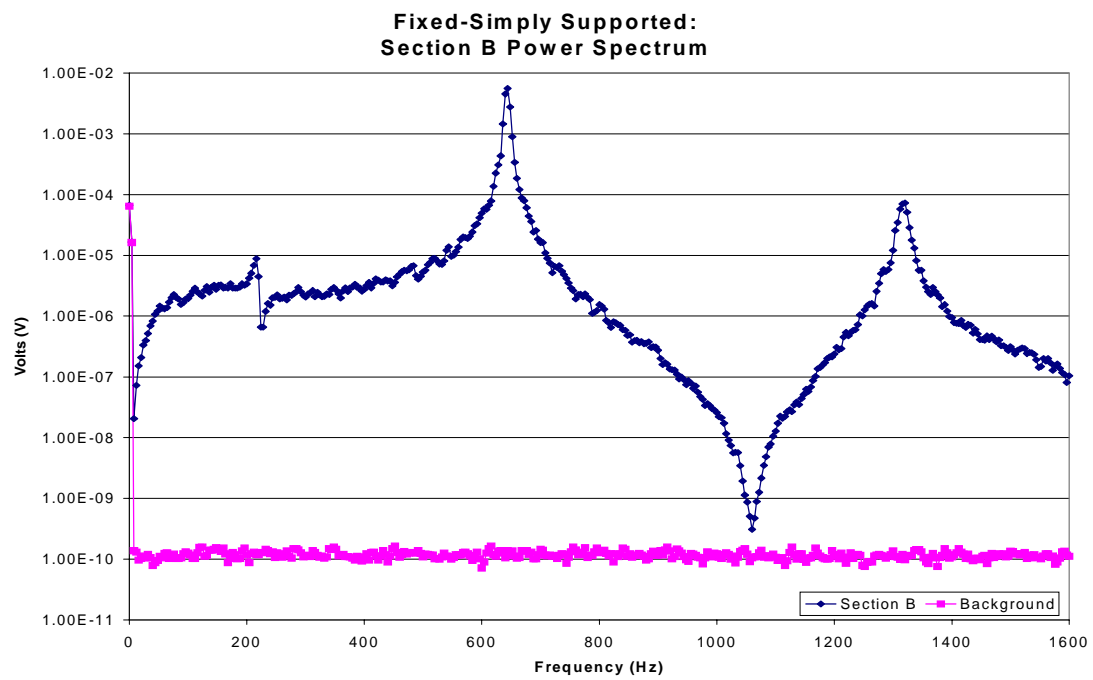
D4. Power Spectrum for Section A of the Two Section Local Sensor.



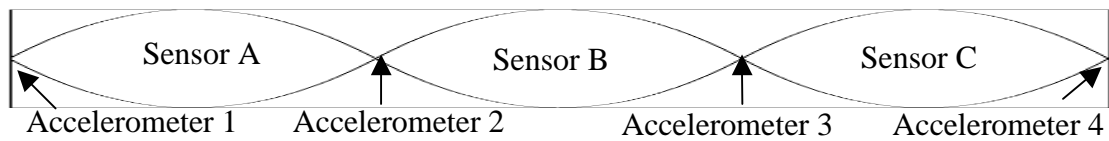
D5. Fixed-Hinged Volume Displacement for Section B of the Double Sensor.



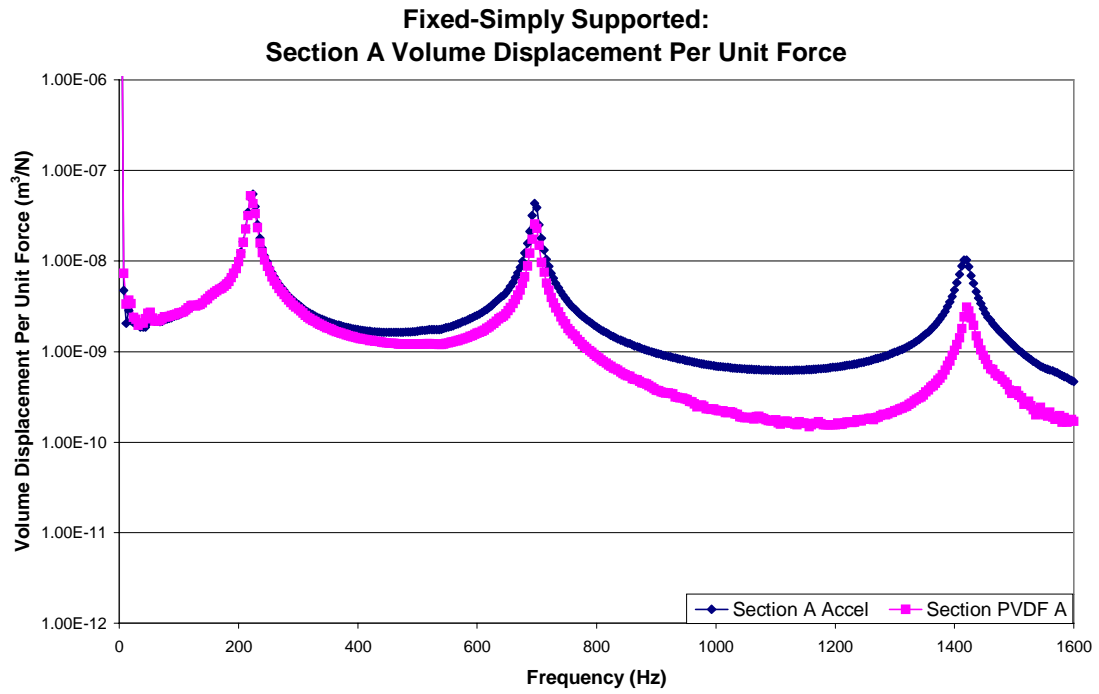
D6. Fixed-Hinged Phase for Section B of the Double Sensor.



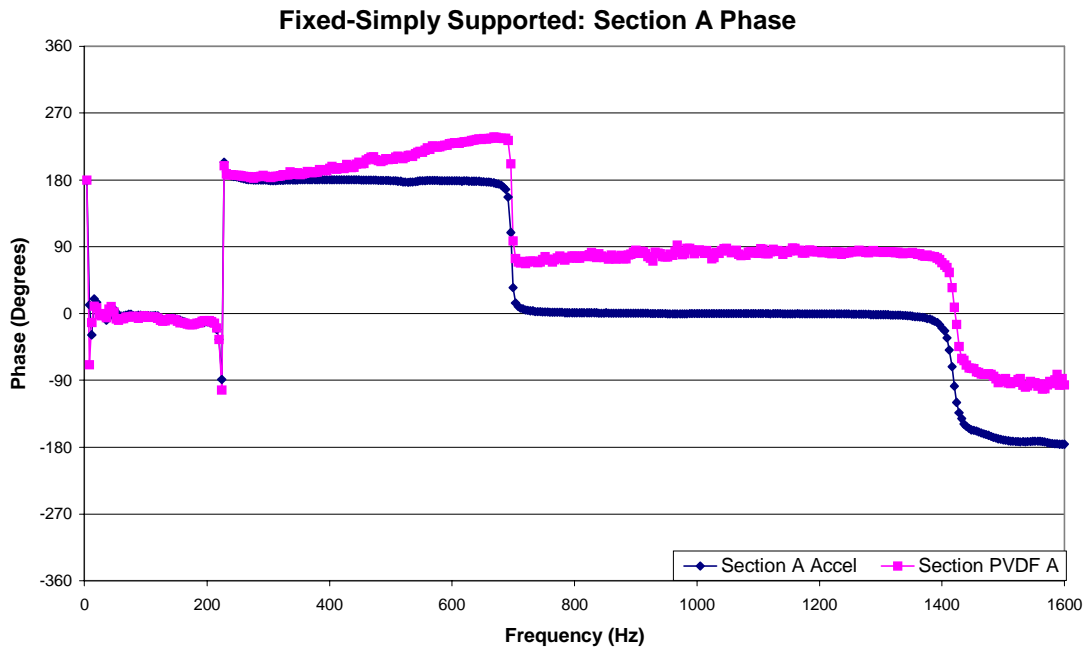
D7. Power Spectrum for Section B of the Two Section Local Sensor.



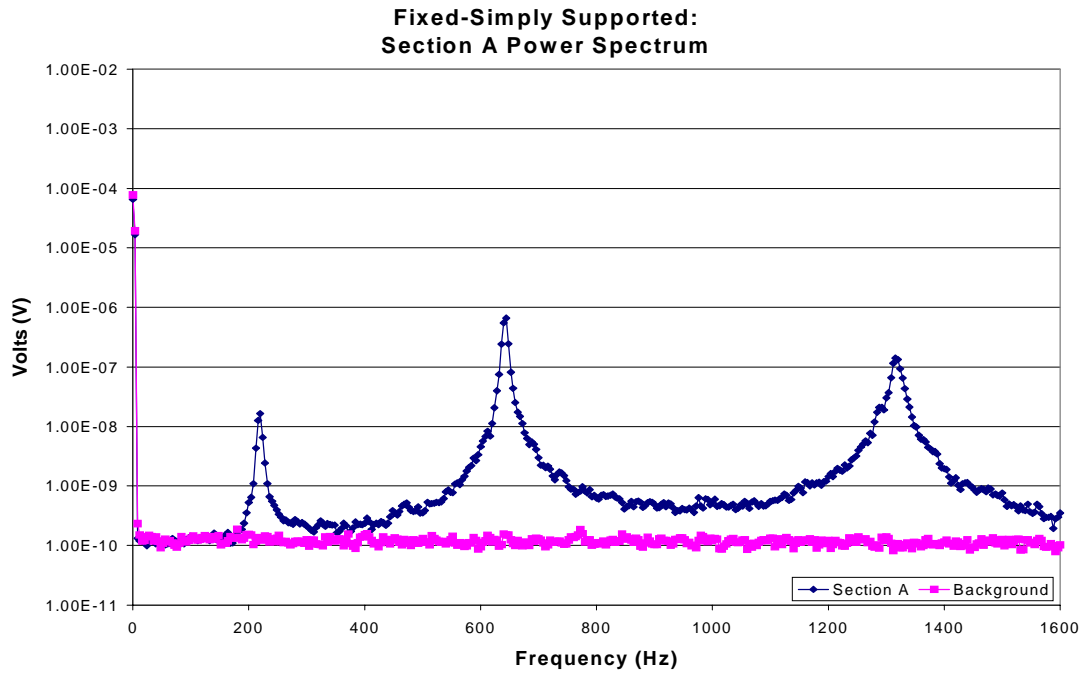
D8. Three Section Local Sensor Layout.



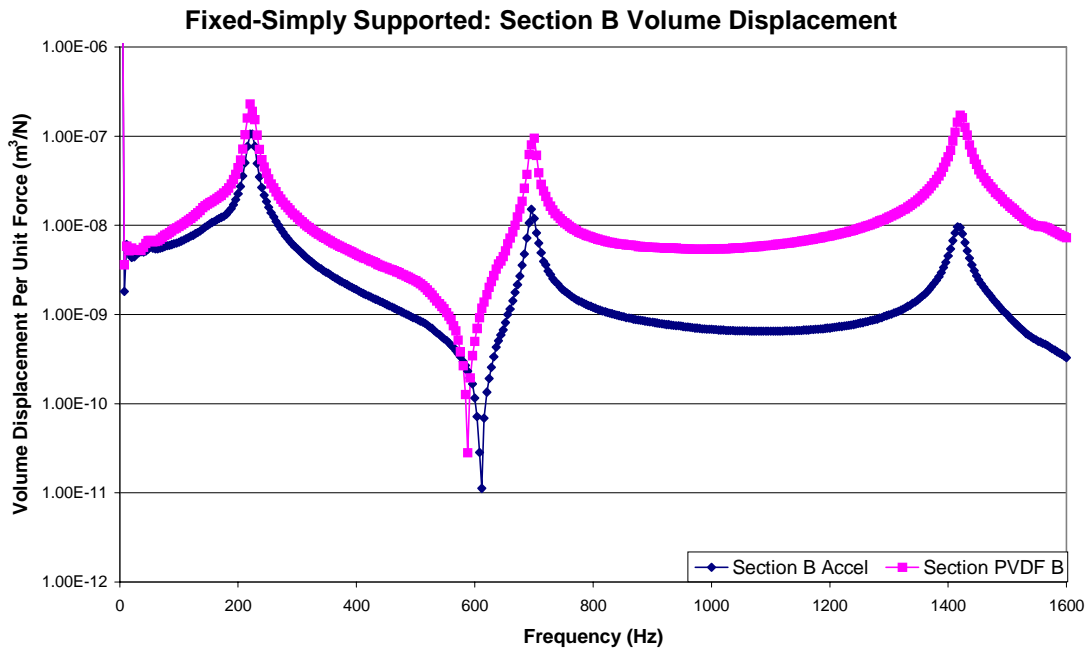
D9. Fixed-Hinged Volume Displacement for Section A of the Triple Sensor.



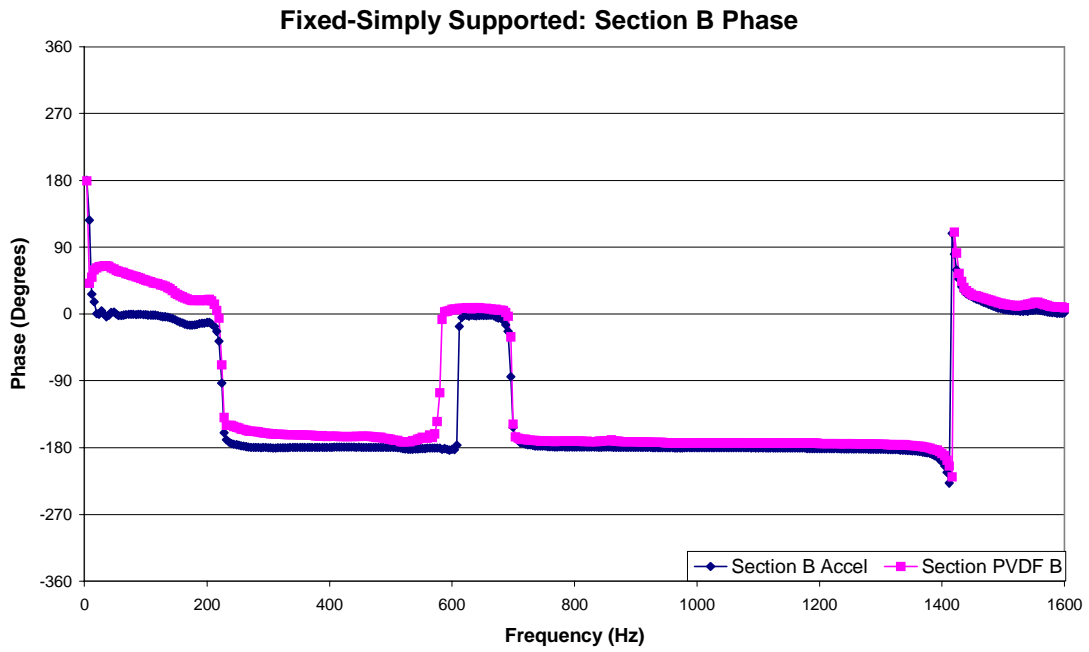
D10. Fixed-Hinged Phase for Section A of the Triple Sensor.



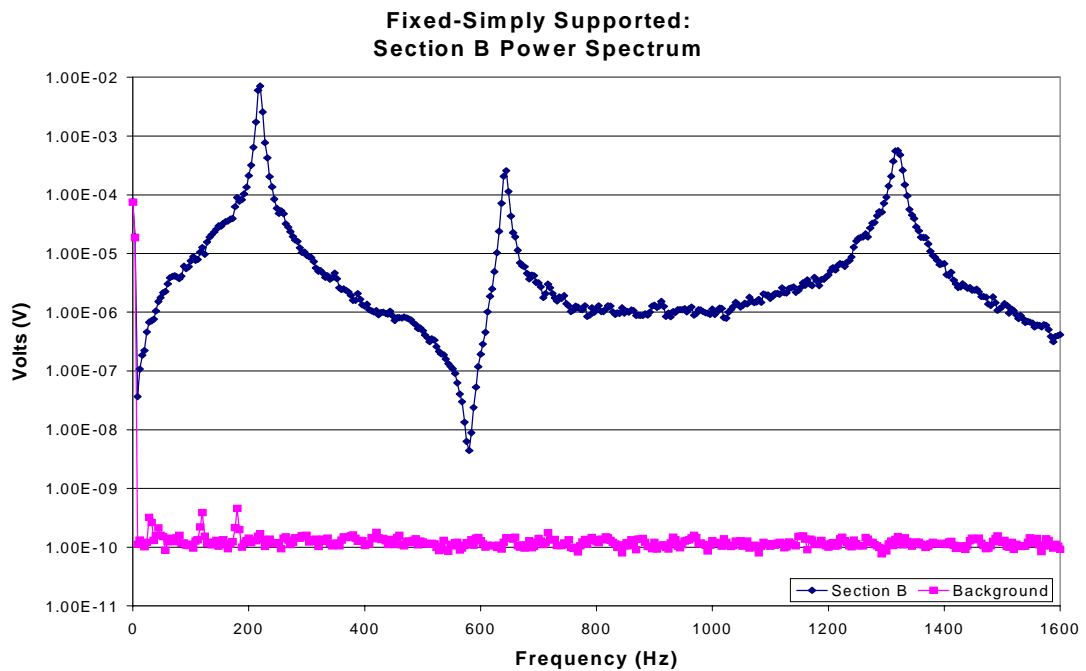
D11. Power Spectrum for Section A of the Three Section Local Sensor.



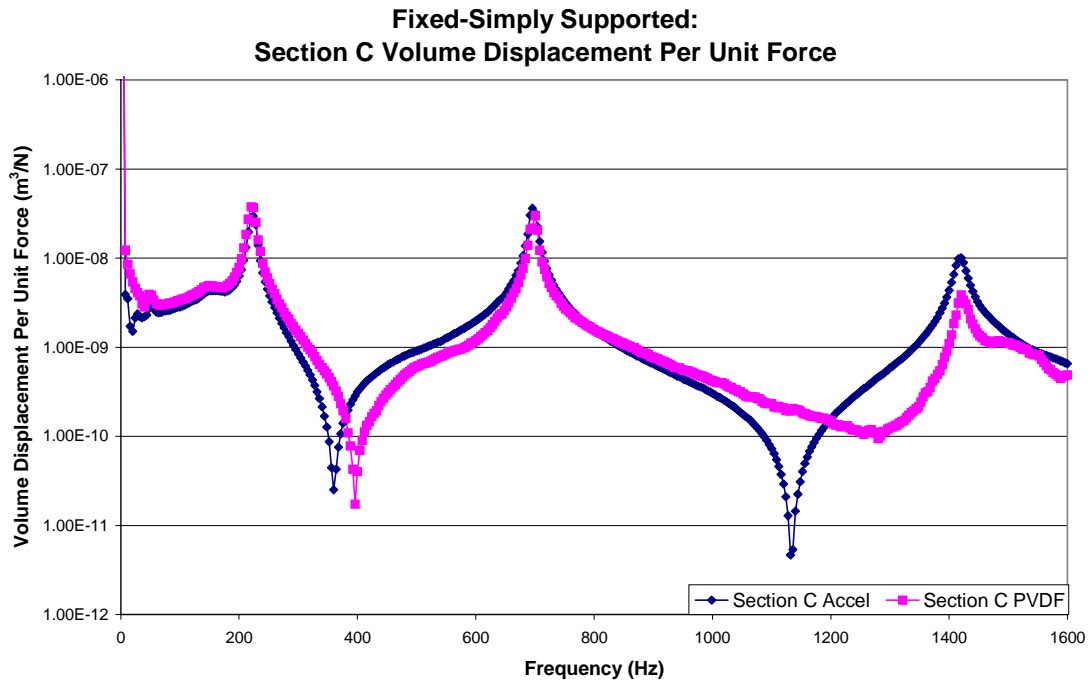
D12. Fixed-Hinged Volume Displacement for Section B of the Triple Sensor.



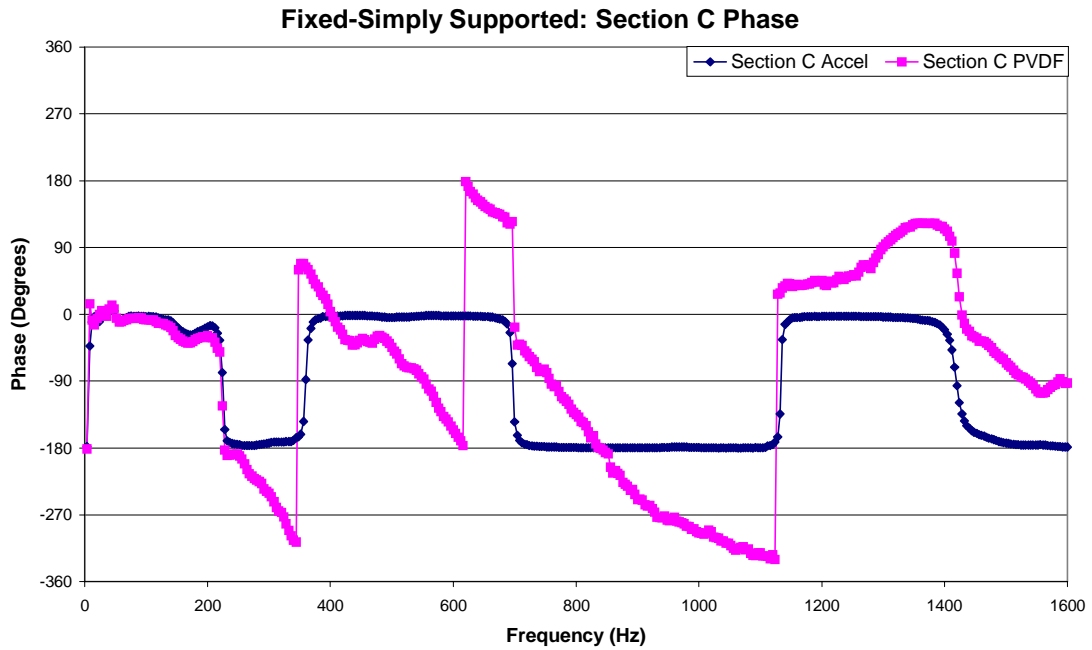
D13. Fixed-Hinged Phase for Section B of the Triple Sensor.



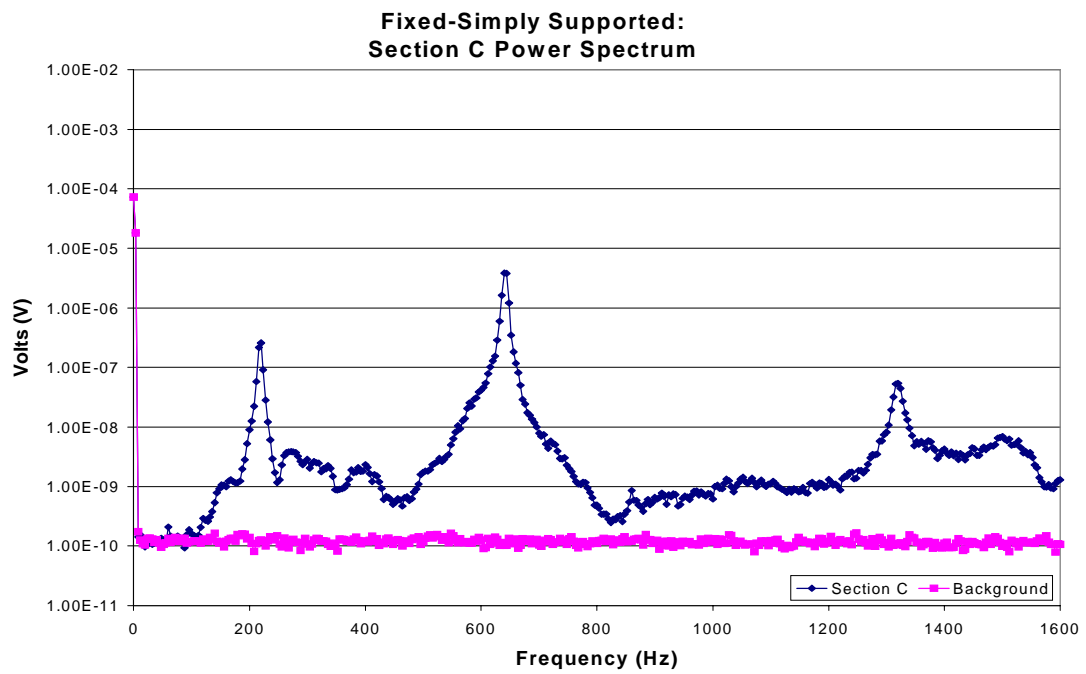
D14. Power Spectrum for Section B of the Three Section Local Sensor.



D15. Fixed-Hinged Volume Displacement for Section C of the Triple Sensor.



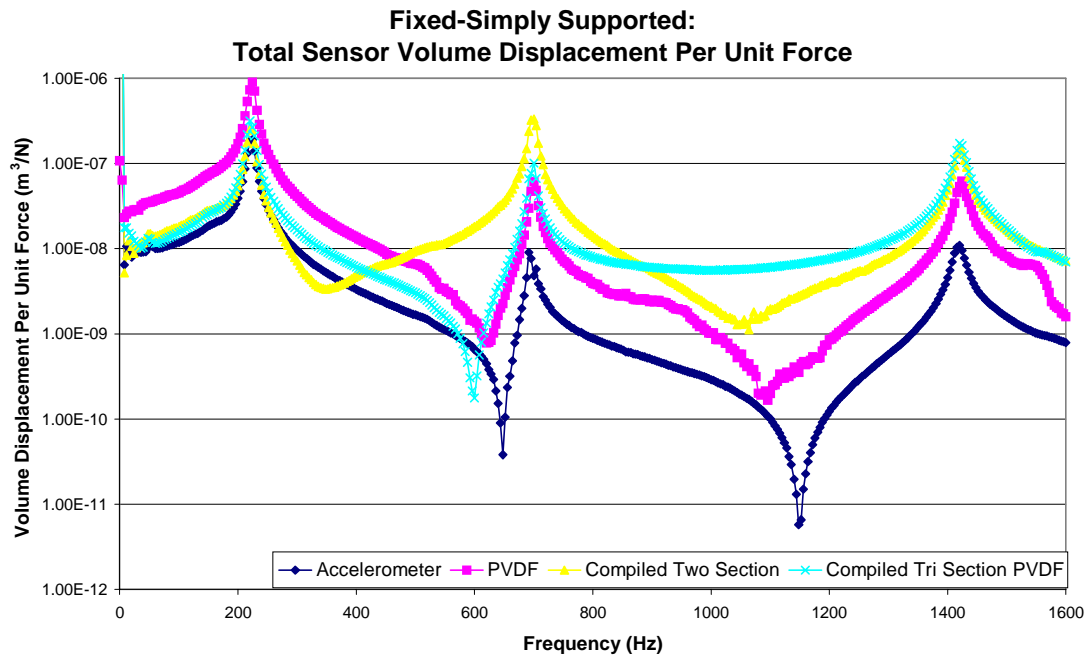
D16. Fixed-Hinged Phase for Section C of the Triple Sensor.



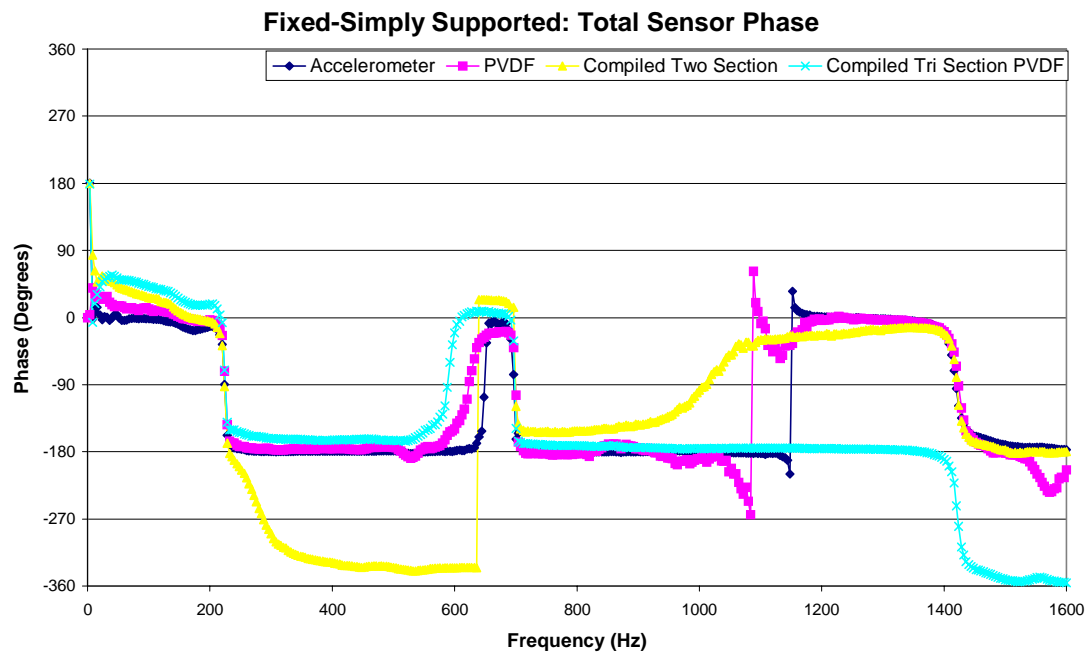
D17. Power Spectrum for Section C of the Three Section Local Sensor.



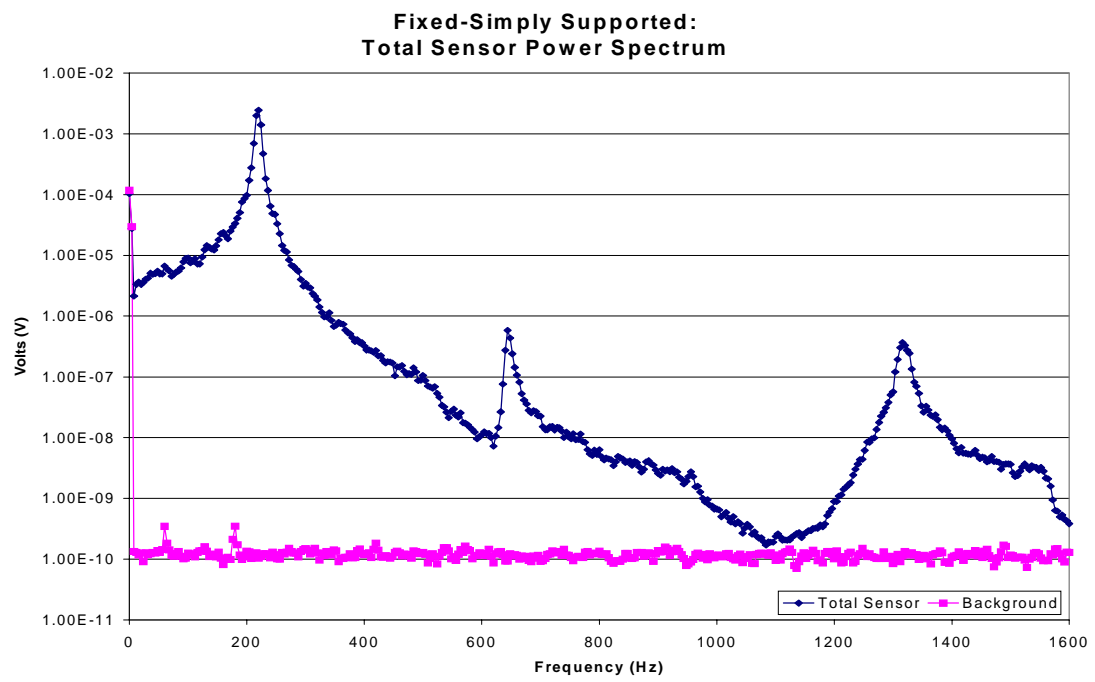
D18. Total Surface Sensor Layout.



D19. Fixed-Hinged Total Volume Displacement.



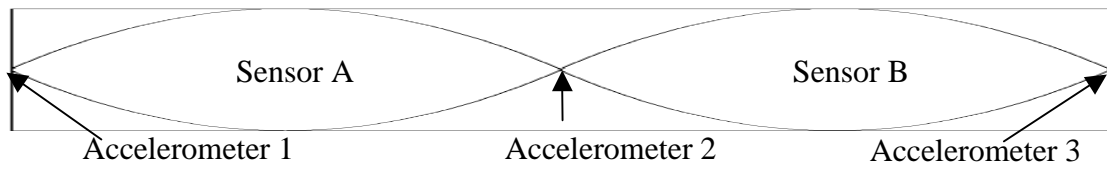
D20. Fixed-Hinged Total Phase.



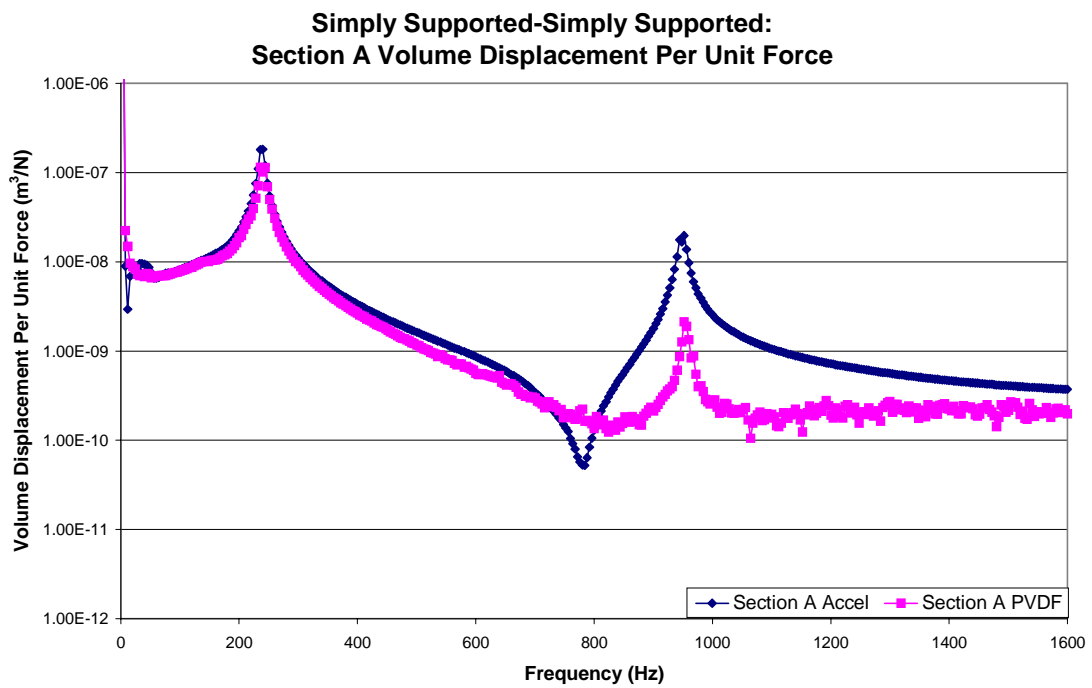
D21. Power Spectrum for the Total Sensor.

Appendix E

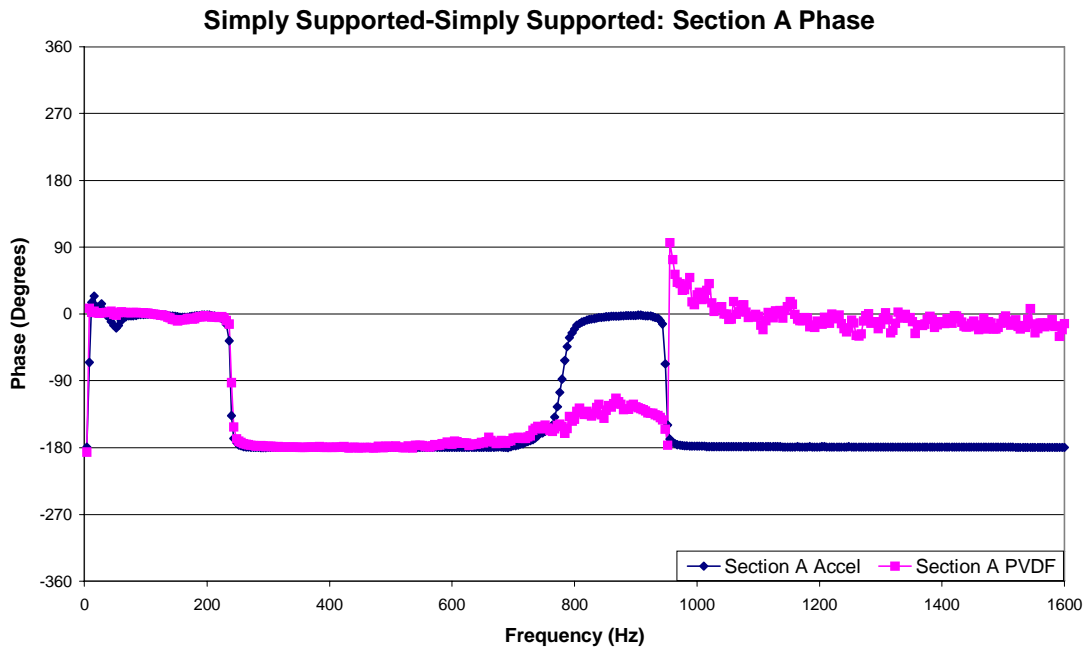
Volume Displacement per Unit Force, Phase, and Power Spectrum
Plots for the Simply Supported-Simply Supported Beam



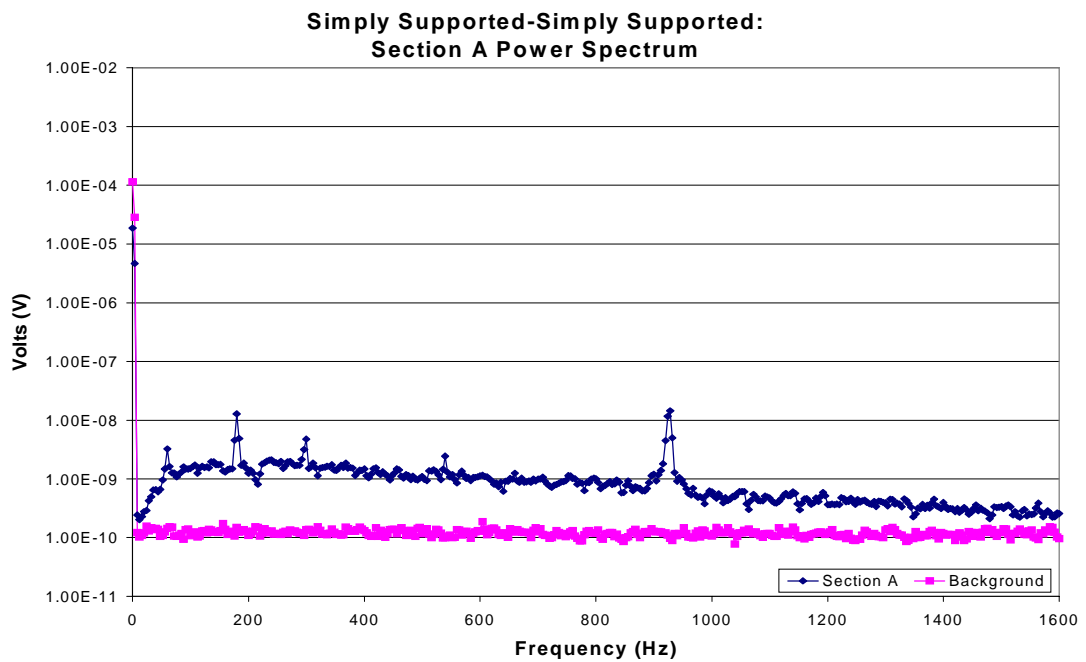
E1. Two Section Local Sensor Layout.



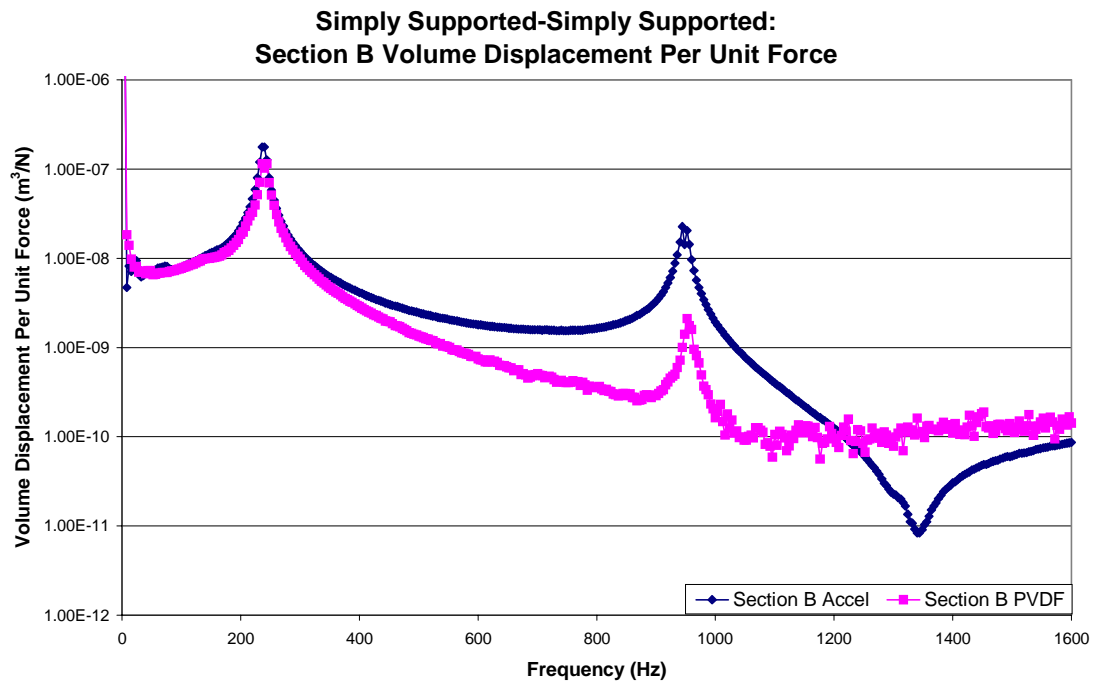
E2. Hinged-Hinged Volume Displacement for Section A of the Double Sensor.



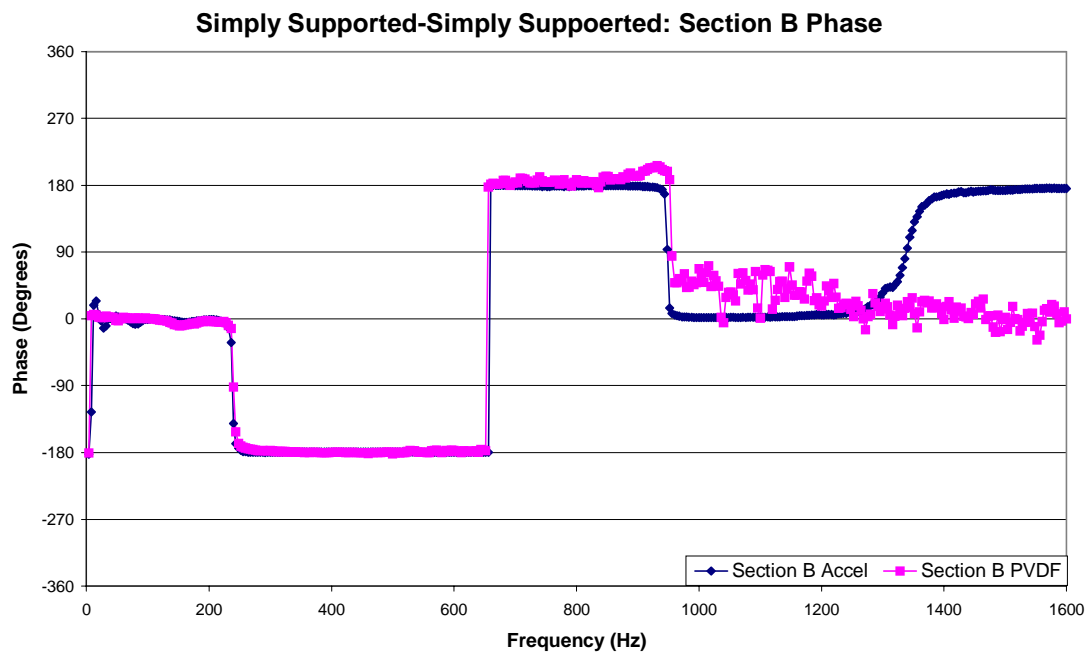
E3. Hinged-Hinged Phase for Section A of the Double Sensor.



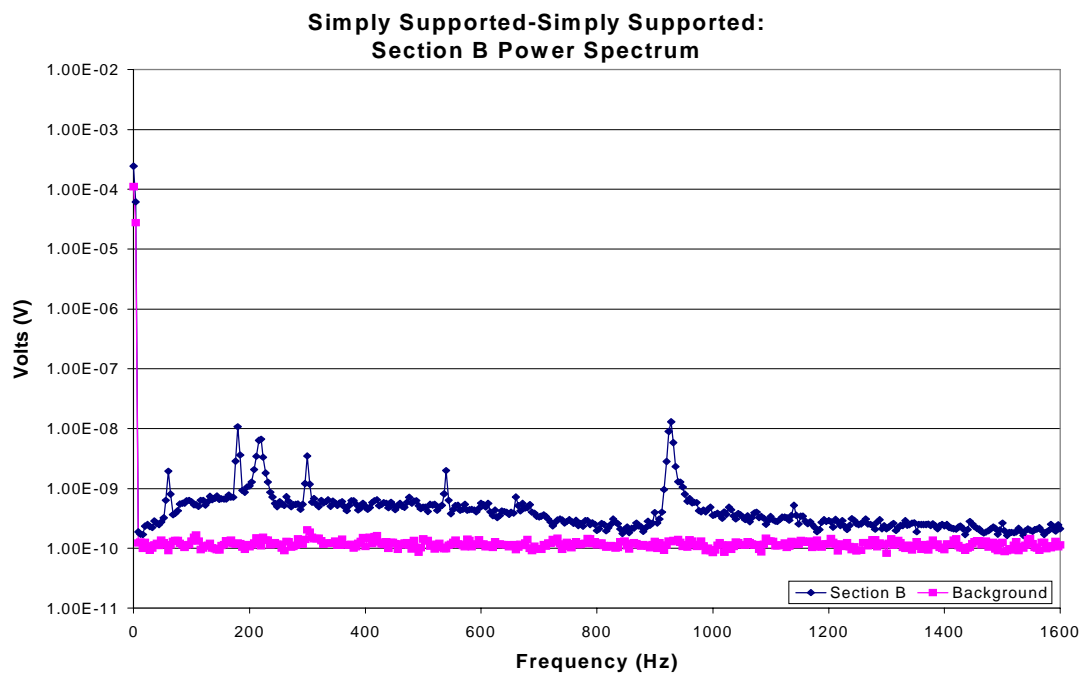
E4. Power Spectrum for Section A of the Two Section Local Sensor.



E5. Hinged-Hinged Volume Displacement for Section B of the Double Sensor.



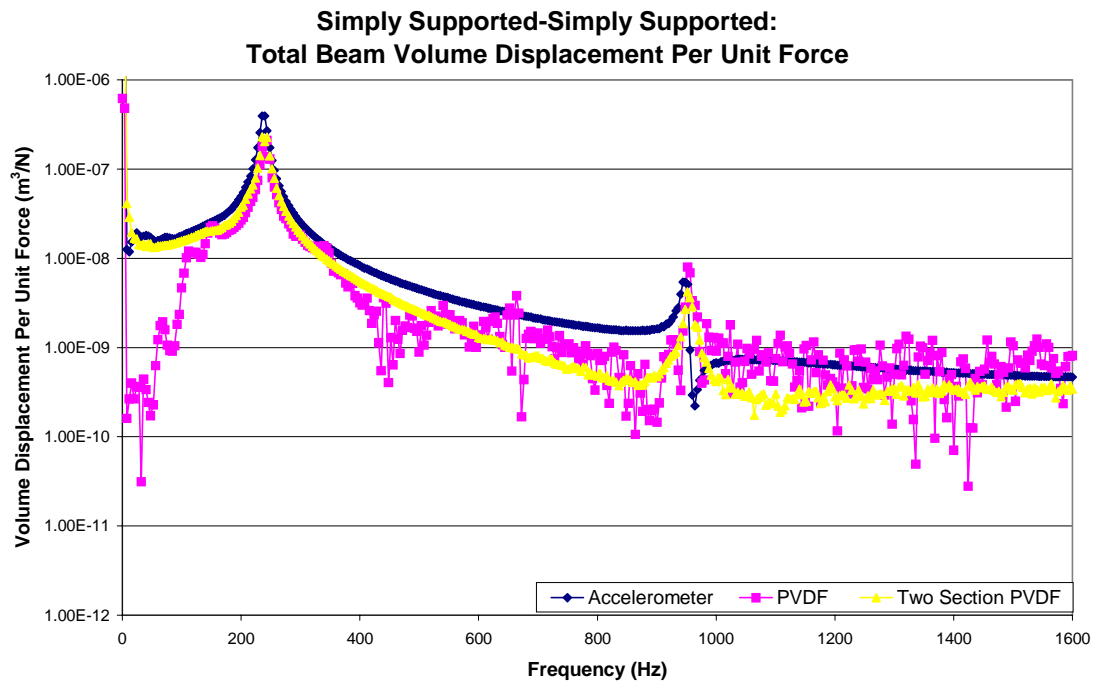
E6. Hinged-Hinged Phase for Section B of the Double Sensor.



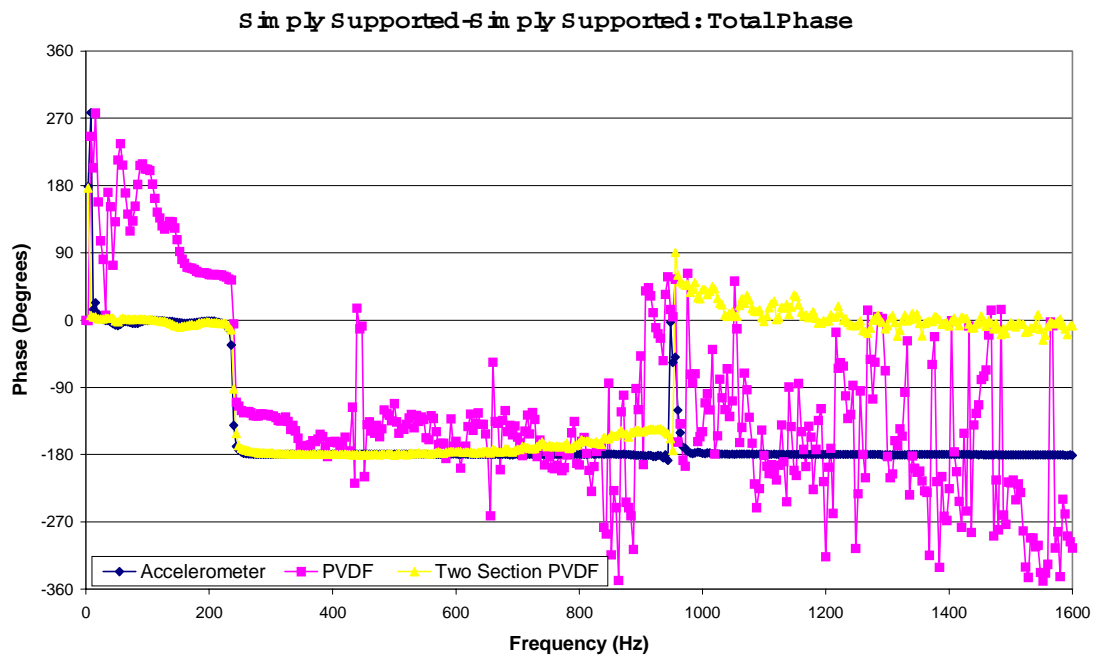
E7. Power Spectrum for Section B of the Two Section Local Sensor.



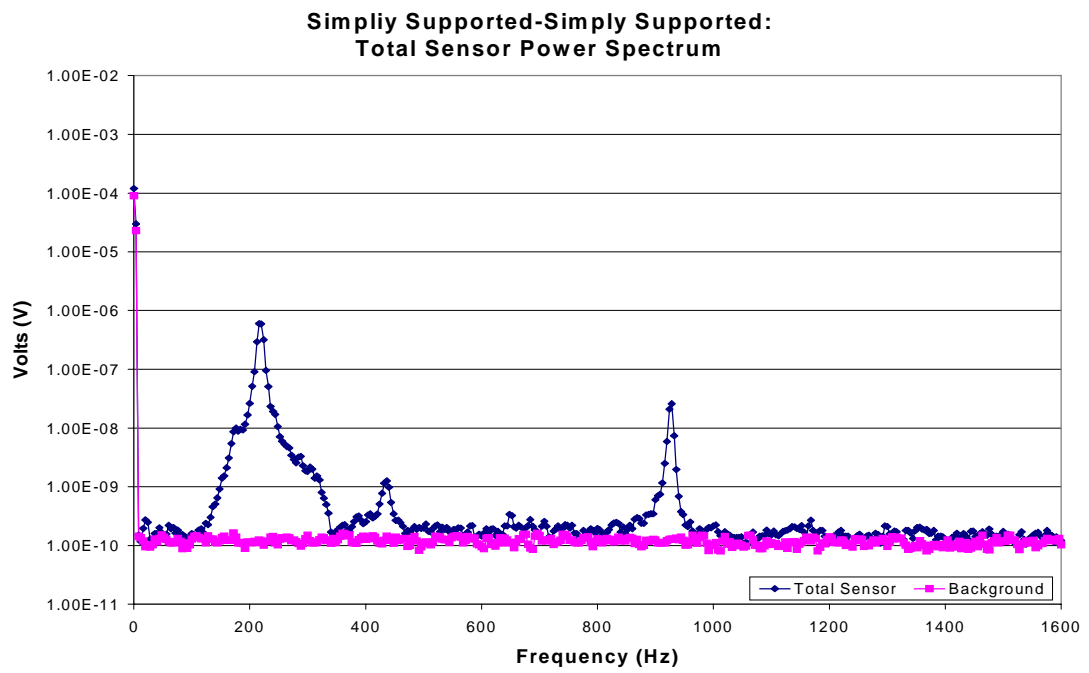
E8. Total Sensor Layout.



E9. Hinged-Hinged Total Volume Displacement.



E10. Hinged-Hinged Total Phase.



E11. Power Spectrum for the Total Sensor.